Master Thesis, Department of Geosciences

Microtextures of ultramafic pseudotachylyte fault veins from Corsica

an SEM-EBSD analysis

Petter Silkoset

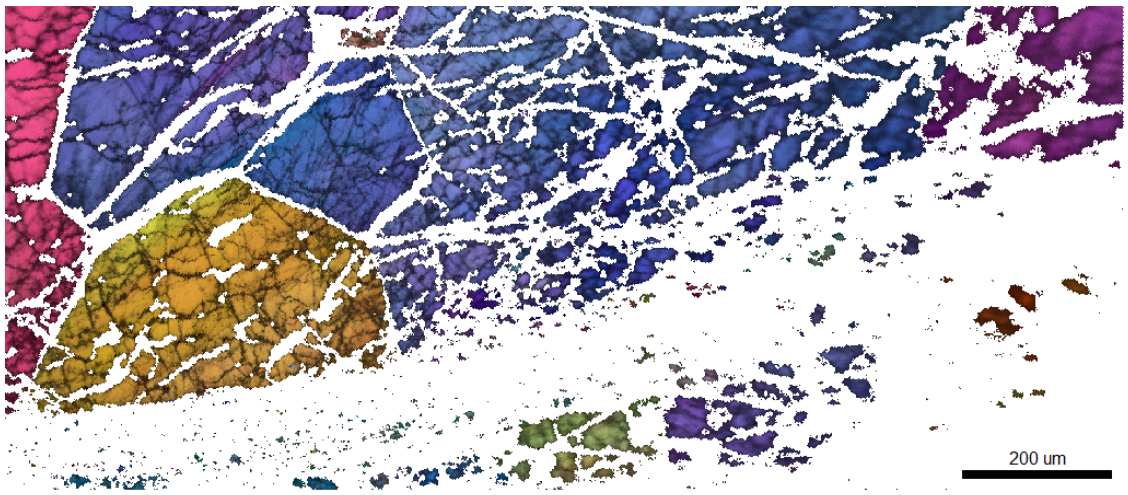

UNIVERSITY OF OSLO

FACULTY OF MATHEMATICS AND NATURAL SCIENCES

Microtextures of ultramafic pseudotachylyte fault veins from Corsica

an SEM-EBSD analysis

Petter Silkoset

Master Thesis in Geosciences

Discipline: Geology

Department of Geosciences and Centre for Physics of Geological Processes

Faculty of Mathematics and Natural Sciences

University of Oslo

March 2013

Tutors: Prof. Torgeir B. Andersen, Prof. Håkon O. Austrheim and Prof. John Wheeler

This work is published digitally through DUO – Digitale Utgivelser ved UiO

http://www.duo.uio.no

It is also catalogued in BIBSYS (http://www.bibsys.no/english)

Acknowledgements

More than anything, writing this thesis has been a process of continual learning instead of being a test of what I have learned so far during my studies. Learning how to find and use information, learning methods of analytical work, exploring anomalous software, how to interpret and apply fresh data to problems in earth sciences and finally how to write and present a scientific thesis. I consider myself lucky to be in a position where I could travel abroad and study aspects of tectonic development from field relations to micron-sized volumes, to me in a foreign country in an unfamiliar geological domain. I sincerely thank my supervisors Prof. Torgeir B. Andersen and Prof. Håkon Austrheim for this opportunity and for all the continued support, provision of samples and literature and helpful discussions during the course of my learning process. I will also thank my external supervisor Prof. John Wheeler from the University of Liverpool for introducing me to an aspect of analytical work that was completely unknown to me, and for pushing me in the right direction from the very beginning.

I will also like to direct special thanks to Anna Magraso from the department of Chemistry at the University of Oslo, and to Daniel Tatham and John MacDonald from the University of Liverpool, for helping me with all practical aspects of electron backscatter diffraction; from sample preparation to collection and treatment of data, and for being patient with me.

Further, I will like to thank Oliver Plümper at PGP for providing helpful insight and assessment of data, as well as introducing alternative methods in how to evaluate microstructures.

I will like to thank Berit Løken Berg for assistance with scanning electron microscope analysis and to Prof. Fernando Corfu for lending me an appropriate oven.

Warm thanks are also directed to all my fellow students at the institute of geosciences and study room colleagues at both the ZEB building and at PGP.

Finally, I will like to thank all my friends and family for the continued support, good company and fun times from start to end of this process. Cheers!

Abstract

Present-day subduction zones exhibit intense seismic activity in the descending oceanic lithosphere. The mechanism behind shallow earthquakes is generally well-understood and related to frictional stick-slip on fault planes. Earthquakes originating deeper, at intermediate (50-300 km) or at even greater depths (up to ~700 km) can generally only be studied by the seismic energies released from earthquakes in subduction zones. The mechanism(s) facilitating seismic failure at such depths are not fully understood. Direct investigation of the deformation products formed by seismic faulting at depth is generally restricted by a lack of exposed examples. Paleoseismicity recorded by pseudotachylytes in the high-pressure and low temperature blueschist- to eclogite facies subduction complex of Alpine Corsica provide insights into earthquakes formed under conditions of approximately 1.5-1.8GPa at ~450°C. Pseudotachylytes occur in both ophiolite gabbro and mantle peridotite, along and in vicinity of the fossil Liguro-Piemontese MOHO. Microstructural investigation using the SEM and electron backscatter diffraction (EBSD) technique has been applied in this pilot EBSD study of selected samples from Alpine Ligurian peridotite host rocks, fault rocks and ultramafic pseudotachylyte. The abundance of ultramafic pseudotachylyte on small faults suggests that peridotite retains its strength to great depths. The EBSD work shows that the peridotites record highly inhomogeneous crystal-plasticity. Intracrystalline deformation features in orthopyroxene and clinopyroxene with curved exsollution lamellae, mechanical twins and kink bands coexist with common undulous olivine, which also coexist with high temperature slip systems in olivine. The co-seismic deformation occurred during presence of free water, and pseudotachylyte generation surfaces are associated with pre-existing or possibly syndeformational heterogeneities in the peridotite. After seismic stress-drop, the peridotite largely returned to ambient conditions. Pseudotachylyte in the studied localities preserves delicate quench-texture, including spherulites, dendrites and chilled margins. A more comprehensive EBSD study involving both the wall-rock peridotite, damage zones adjacent to pseudotachylyte fault-veins and the pseudotachylytes themselves are necessary to provide a detailed understanding of the microstructures related to the subduction faulting.

Table of contents

1. Introduction

Subduction zones and the processes that occur along them are of major importance to our understanding of many aspects of Earth evolution. These processes range from controlling the surface topography to be the cause of natural disasters that may have great impact on civilization. The study of the activity within subduction zones is also crucial for understanding the mass transfer from mantle to crust, which is the principle way where new continental crust is created; and vice versa, subduction also controls transfer of material from the oceanic lithosphere to the mantle. Thus, both pathways of material transport are intimately associated.

Subduction zones exhibit intense earthquake activity and are the most seismically active domains on Earth, and the planes of descending hypocentres are known as Wadati-Benioff zones (e.g. Frohlich, 2006). The array of earthquakes that occur along the subducting plate may be frequent and damaging in some subduction zones as recently exemplified by the disastrous Tohaku (Mw-9.0, 2011) and Sumatra-Andaman (Mw-9.3, 2004) earthquakes (Lay et al., 2011; Lay et al., 2005). Earthquakes require a better understanding in order to predict their distribution, and are therefore of social as well as scientific relevance.

This thesis will assess activity on intermediate to deep earthquake faulting in subduction zones recorded by ultramafic pseudotachylytes, previously interpreted to have formed by earthquakes in the exhumed subduction complex of Alpine Corsica (Andersen and Austrheim, 2006; Austrheim and Andersen, 2004). The purpose of this study is to use microtexture fabric analyses in order to try to constrain a trigger mechanism for earthquakes that occurred in mantle lithosphere. An open question is why rocks that undergo burial to great depths in subduction zones develop strain localization, responding by slip at seismic velocities rather than by ductile continuous flow. The project concentrates on microtextures in previously mapped and sampled pseudotachylytes from an Alpine Ligurian mantle peridotite affected by blueschist- to lws-eclogite facies metamorphism. In this thesis mineral-name abbreviations are used according to Whitney and Evans (2010), which can be found in appendix 1.

Investigations by optical microscopy and scanning electron microscopy (SEM) are the main tools used in this thesis. Principles of electron backscatter diffraction (EBSD) was learned and applied in this pilot EBSD study of selected samples from Alpine Ligurian peridotite host

rocks, fault rocks and the ultramafic pseudotachylyte. This thesis focuses on the rheology of ol since it is the most abundant mineral in studied mantle rocks.

The EBSD method has been used to explore deformation mechanisms and distribution of grain sizes for ol within and adjacent to small and larger faults. These are important parameters during strain localization and faulting. Although the behaviour of ol is well reported in numerous experimental and case-studies its rheological behaviour related to deep earthquakes is scarce. Textural description of coexisting phases has been done and integrated into this general framework.

Stresses released during earthquake faulting in the Alpine Ligurian peridotites studied here have previously been estimated based on fault melting energy budgets (Andersen et al., 2008). Together, these estimates and the observations presented in this thesis will hopefully provide further insights into fault dynamics at depth, and help evaluate the generation of intermediate to deep earthquakes.

Subduction zone seismicity

Present-day seismicity

Present-day subduction zones exhibit intense seismic activity in the plunging oceanic lithosphere. The subducted lithosphere dips at an average angle of 45° where earthquakes occur along planar domains known as Benioff-Wadati zones, delineating the cold core of subducting slabs (e.g. Frohlich, 2006). Earthquakes occur below the Earth's crust to nearly 700km depth on these planar regions of seismicity, witnessing interfaces within the mantle that are seismically active (Kearey et al., 2009). The physical processes that allow the occurrence of deep earthquakes are not well understood. The brittle-frictional processes that operate to produce shallow seismic rupture, fracture and frictional sliding, appear to be suppressed by conditions at depth (Scholz, 2002).

A compilation of all seismic activity outside the coast of Japan from 1990 to the Mw-9.0 earthquake that occurred March 11, 2011 is shown on figure 1. The total depth range in this profile extends down to 150-300km depth, where deeper segments of the subducted slab are located further to the west, beneath continental Asia. The number of hypocentres down to 150km depth shows a relatively even distribution. Faulting occur more frequently on shallow solutions, but underlines that earthquakes do occur frequently along the slab interface (Frohlich, 2006). This raises a central question to why rocks in subduction zones undergo deep burial and respond by failure at seismic velocities. In particular, increasing pressure with depth tends to inhibit fracture and sliding, while increasing temperature promotes ductile flow (e.g. Scholz, 2002).

A wealth of similar information on seismicity from other subduction zones, regarding the depth distribution of earthquakes, shows that segments of a zone may change from seismically active to aseismic. The depth distribution of seismicity may vary between subduction zones and along strike within the same zone (Pacheco et al., 1993). This questions what factors control the uneven depth distribution, and if this may be coupled to some governing mechanism that facilitates seismic rupture at depth. The total depth range in which earthquakes are observed (<700km) can generally be subdivided into three zones. These zones are based on the depth of focus of the earthquake and a proposed geological process that allow their nucleation. They are termed shallow, intermediate and deep earthquakes (e.g. Green and Houston, 1995; Jung et al., 2004).

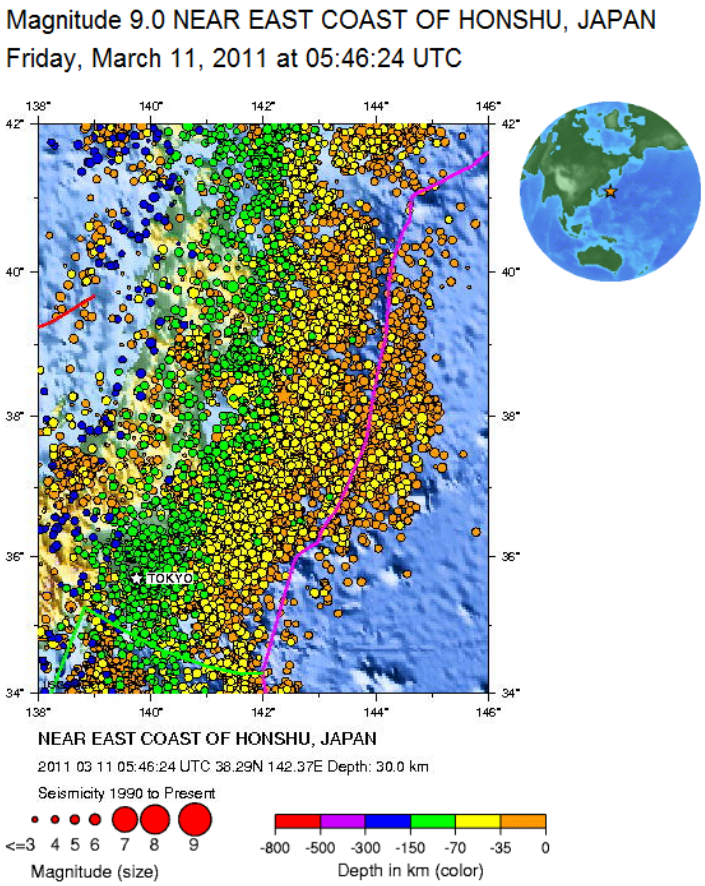

Figure 1: Historic seismicity from 1990 to the Mw-9.0 earthquake (orange star) that occurred on March 11, 2011, near the east coast of Honshu, Japan. The distribution of earthquakes from the proximal to the distal side of the ocean trench shows a progressive increase in depth (down to 150-300km depth) of the hypocentres from recorded earthquakes. Image taken from http://neic.usgs.gov/neis/eq_depot/2011/eq_110311_c0001xgp/neic_c0001xgp_h.html.

The mechanisms behind shallow earthquakes are generally well-understood and are related to downward flexure of the lithosphere, prompting brittle shear failure during creation of a fault, and frictional stick-slip on existing fault planes (e.g. Brace and Byerlee, 1966; Kearey et al., 2009). Such earthquakes are considered to originate on depths shallower than the extent of the seismogenic zone which depth vary from subduction zone to subduction zone, some 20-50km deep (e.g. Jung et al., 2004).

The difference in age between subducted plates, hence their thermal status, partly controls the depth to the base of the seismogenic zone. This influence the focus of depth and distribution along strike of the subduction zone (Tichelaar and Ruff, 1993). However, the existence of double Wadati-Benioff seismic zones (figure 2) in some subduction zones complicates the assumption that temperature alone can control the allocation of earthquakes at shallow to intermediate depths (Hasegawa et al., 1978). The seismogenic zone accurately describes generation of earthquakes within it, but at greater depths the governing deformation

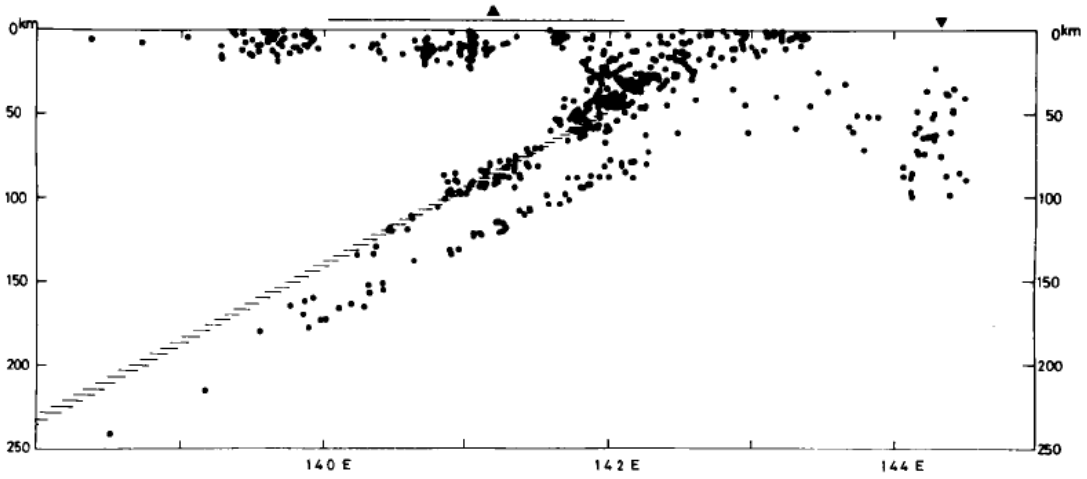

Figure 2: Focal-depth distribution of earthquakes in the central part of the Tohoku District projected on the vertical section in the E-W direction (solid circles). The hatched line marks the upper boundary of the slab interface. From Hasegawa et al. (1978).

mechanism is commonly assigned to crystal-plastic creep or flow, rather than brittle behaviour (e.g. Green and Houston, 1995; Scholz, 2002).

Deep earthquakes, at intermediate (~20-300km) or at even greater depths (300-700km) raise controversial hypotheses concerning their generation. Due to the progressive increase in pressure and temperature from the surface of the Earth towards its interior, it is considered that fracture and frictional sliding is strongly inhibited by extreme confining pressures (Frohlich, 2006). Increasing temperatures promote ductility, where minerals deform at a relatively low strain rate by generating and migrating lattice defects (Passchier and Trouw, 2005). Classic experiments on ol have shown that the shear stresses needed to overcome high confining pressure are far greater than that which can be sustained at high temperatures (Kohlstedt et al., 1980). It is unlikely that ductility alone can cause earthquakes, being a cohesion-preserving process.

Fossil seismicity

Both shallow and deep earthquakes released in either subduction zones or continental settings can be studied by the energies released on rupture by seismology. Direct observation of shallow earthquakes can be studied on fault scarps, damaged human infrastructure and regional vertical or strike-slip movements. Obviously, deep earthquakes cannot be studied in the same way. However, deep *fossil earthquakes* can occasionally be observed directly, complementary to the conventional seismological method (e.g. Sibson, 1975). The deformation products of fossil earthquakes formed by seismic faulting are restricted by a general lack of exposed examples, but are not an uncommon rock type (Sibson and Toy, 2006;

Spray, 1995). Thus, exhumed fault zones occasionally record deformation products formed by earthquake activity. During slip at seismic velocities, frictional heating may be sufficient to melt small portions of rock, which in turn may intrude along the fault plane and into pre-existing and syndeformational porosity, before quenching to produce *pseudotachylyte*. The presence of pseudotachylyte is one of the few definite indicators associated with a seismic event, and is an imprint of a 'fossil earthquake' (e.g. Cowan, 1999; Goldschmidt, 1943; Sibson, 1975).

Traditionally, as outlined by the behaviour of the seismogenic zone, earthquakes are considered to occur at depths generally less than this level. This is due to the overall change in rheology that takes place at depth (Scholz, 2002). On the other hand, earthquakes do extend below this conventional limit (figure 1 and 2). Investigation of exhumed metamorphic assemblages, incorporating fossil subduction complexes, has recently identified pseudotachylytes in upper mantle and lower continental crust (e.g. Austrheim and Andersen, 2004; Clarke and Norman, 1993). These reveal that pseudotahylytes occur at depths far exceeding the seismogenic zone. In addition, shear experiments at sub seismic velocities where materials deform under semi-brittle flow have been found to produce pseudotachylyte-like material (Pec et al., 2012). Such observations combined raise interesting questions regarding their generation, as the classic interpretation associates them with short-lived failure at seismic velocities, above the seismogenic zone.

The island of Corsica is an exceptional area for studying exhumed rocks that have undergone seismic failure on intermediate depths. Paleo-earthquakes are recorded by pseudotachylytes in the blueschist- to lws-eclogite facies Alpine subduction complex of Alpine Corsica (Andersen and Austrheim, 2006; Andersen et al., submitted; Andersen et al., 2008; Austrheim and Andersen, 2004). Here, abundant pseudotachylytes are exposed within both ophiolite metagabbro and mantle peridotite. Globally there have previously only been described a handful of examples of pseudotachylytes in ultramafic rocks. Apart from Alpine Corsica these occurrences are located at Hokkaido, Japan, at Holsnøy in the western Norway and from the Ivrea-Verbano zone in Italy (Lund, 2002; Morishita, 1998; Obata and Karato, 1995).

This thesis focuses primarily on pseudotachylytes found in mantle peridotite.

Pseudotachylyte

'Pseudotachylyte' was first described from the Vredefort Dome structure in South Africa (Shand, 1916). The name was used in order to describe a dark, fine grained glassy material occurring as veins and dike-like bodies in granite and Archean gneiss. He used the term due to the rock's imminent similarity to basaltic glass; tachylyte (Spray, 1995). Similar material was recognized by Goldschmidt (1943) in the Norwegian Caledonides, and he adopted the same term. Here, pseudotachylyte was found as veins and pockets along and in the vicinity of faults.

The Vredefort Dome is now recognized as one of the largest impact structures on Earth (e.g. Reimold et al., 2008). Many subsequent reports of pseudotachylyte, like that of Goldschmidt (1943), have been intimately associated with idle or active faults as well as from meteorite impacts. In addition, pseudotachylyte has occasionally been described from the basal slip surfaces in landslides, it has been produced as a result of frictional overheating during drilling, and in laboratory experiments at both seismic and sub seismic strain rates (e.g. Killick, 1990; Masch et al., 1985; Pec et al., 2012; Spray, 1987, 1988). This thesis focuses exclusively on pseudotachylytes found in exhumed fault zones.

Fault-related pseudotachylyte

Fault-related pseudotachylyte is not an uncommon rock type, and can be used to infer the past behaviour of faults (e.g. Cowan, 1999; Sibson, 1975). Of these, the bulk of recognized pseudotachylyte appears to have been generated in the upper continental crust seismogenic zone (Sibson and Toy, 2006). There is a general consensus that they originate by seismic slip that is localized, so that the temperature rise is sufficient to cause frictional heating and melting of the wall rocks (Magloughlin and Spray, 1992; Sibson, 1975; Spray, 1992). The melt is drained along the generation surface and into pre-existing and syndeformational fractures, eventually quenching and cooling to the temperature of the host rock, to produce veins of pseudotachylyte (e.g. Twiss and Moores, 2007). However, discoveries in lower continental crust and in subducted oceanic lithosphere, exceeding the base of the seismogenic zone (Austrheim and Andersen, 2004; Austrheim and Boundy, 1994; Clarke and Norman, 1993; Obata and Karato, 1995), raise interesting questions regarding the origin of seismic failure and associated pseudotachylyte. These are relatively scarce from literature. Whether their generation or preservation is commonly inhibited, or that they simply are not widely recognized remains largely unresolved.

Much of the currently available information on both shallow and deep-seated pseudotachylyte is derived from outcrops of limited extent which halt assessment of their lateral continuity

(Sibson and Toy, 2006). In addition not all dark, fine-grained fault rock is pseudotachylyte. Ultracataclasites and ultramylonites occasionally mimic the appearance of pseudotachylyte due to a comparable grey-black and flinty appearance, and by their occasional intrusive character (e.g. Passchier and Trouw, 2005). Fault-related pseudotachylytes, either generated by shallow or deep faulting or artificially generated in the laboratory, share some common features that distinguish them from other fine grained dark and/or intrusive fault rocks.

Characteristic appearance of fault-related pseudotachylyte

Fault rocks are traditionally classified according to style and intensity of deformation, and the ratio of clasts to matrix (e.g. Twiss and Moores, 2007). Of these, pseudotachylyte is dominated by an extremely fine-grained, cryptocrystalline to occasionally glassy matrix with variable but commonly minor amount of angular to thermally rounded wall rock fragments (Passchier and Trouw, 2005). Fine-grained cataclastites and mylonites may share some of these features, but are devoid of glass or other evidence of melting.

The most typical feature of fault-generated pseudotachylyte is knife-sharp contacts to wall rock and that veins commonly cut individual mineral grains (Passchier, 1982). Outside the contact there may be little sign of brittle deformation in wall rock, unlike that typically found along breccias and cataclasites (Magloughlin, 1992; Passchier and Trouw, 2005). The wall rock can, however, be highly fractured spatially related to faulting, but the pseudotachylyte commonly transects these features. Fault striations and slickenfibres are not present on pseudotachylyte-bearing faults since such mineral growth is obliterated due to the intense heat production (Swanson, 1992).

Pseudotachylyte usually occur in a characteristic geometric relationship where fault-vein(s) occur along the slip surface, coupled with irregularly spaced injection veins that ramify off it (Sibson, 1975). Patterns of pseudotachylyte fault- and injection veins have been used to interpret earthquake rupture dynamics (Di Toro et al., 2005). The two types of veins are distinguished by their lateral continuities and angular relationship (figure 3). Fault-veins lie along generation surfaces, which are predominantly planar to wavy. These may exhibit lenses and dilational pull-apart segments along strike (Curewitz and Karson, 1999). Injection veins branch off of these slip surfaces in all directions and are responsible for distributing and draining the melt through a larger volume of rock (e.g. Sibson and Toy, 2006). Individual pseudotachylyte fault-vein thicknesses are elaborate due to their lensoidal nature and loss of melt into injection veins. There is a vast amount of reported fault-veins that display

thicknesses <25mm, with peak occurrences around 10mm, whereas injection veins can be considerably wider (e.g. Passchier and Trouw, 2005; Sibson and Toy, 2006).

Figure 3: Schematic drawing showing the typical appearance of fault-generated pseudotachylyte. Fault-veins occur along generation surfaces with injection veins ramifying into adjacent wall rock. Both type of veins may occur several magnitudes wider or thinner, and often intertwine in complex networks. Modified from Curewitz and Karson (1999).

In case of later deformation in the ductile regime, pseudotachylyte does not commonly show evidence of stronger deformation than that undergone by surrounding rock (Passchier, 1982). However, if pseudotachylyte is reactivated and concurs with mylonite formation, pseudotachylyte is recognized by its homogeneous, fine-grained appearance with remnant injection-veins that cut the foliation at a steep angle (Sibson, 1980).

Despite the differences and similarities between pseudotachylyte and other fault rocks, positive identification is done by recognizing the evidence of a quenched melt phase (Magloughlin and Spray, 1992). Pseudotachylytes are suggested to form by melting at temperatures between 750-1600°C for various rock assemblages (Andersen and Austrheim, 2006; Austrheim and Boundy, 1994; Di Toro and Pennacchioni, 2004). However, these are hard to determine because pseudotachylytes may form by disequilibrium melting or super-heating of the host rocks (Di Toro and Pennacchioni, 2004; Passchier and Trouw, 2005). Characteristic textural evidence from both types of veins are very fine-grained, aphanitic material commonly with flow structures, chilled margins as well as thermally rounded and disintegrating wall rock fragments. The melt occasionally quenches to form glassy margins (e.g. Magloughlin, 1992; Sibson and Toy, 2006). Additional evidence of a highly localized melt phase is mineral grains formed by crystallization before quenching. These are called microlites that may arrange as spherulites, and can manifest as a sequence of increasingly complex shape from core to margin of a pseudotachylyte vein (Austrheim and Andersen, 2004; Lin, 1994; Magloughlin, 1992).

Most pseudotachylytes have a chemical composition that is almost identical to that of the host rock (Magloughlin, 1992). Cataclasites and mylonites often experience syndeformation

mineral growth and association with qz or cal veins or leaching by fluid circulation, and will often show a different composition than that of the host (Passchier and Trouw, 2005).

The occurrence and distribution of fault-related pseudotachylyte

There is currently an almost equal amount of reported pseudotachylyte occurrences in exhumed reverse and strike-slip systems, with a large discrepancy from normal fault systems. Of these, pseudotachylyte has been described in a variety of rock types with a vast predominance (>95%) from crystalline metamorphic and plutonic lithologies (Sibson and Toy, 2006). The low porosity and high competence of these rocks imply that this might be a pre-requisite to allow a great density of elastic strain to be stored prior to rupture. For this reason, pseudotachylyte is not normally associated with porous sedimentary or carbonate rocks. It is commonly assumed that these do not allow a great build-up of strain due to fluid content and dissocation, respectively, greatly lowering the effective normal stresses over faults (Passchier and Trouw, 2005). However, reports of pseudotachylyte in marble, northern Italy, suggest that other conditions might control melt production during faulting in carbonate rocks (Viganò et al., 2011).

There is a dominant portion of reported pseudotachylyte from felsic rock assemblages and only a handful of mafic and ultramafic occurrences (Sibson and Toy, 2006). This might be attributed to the appearance of typically thin, black and aphanitic quenched melts, and its striking similarity to mafic mineral assemblages, which make them hard to recognize.

Pseudotachylyte occur in various rock suites where the depth of generation span over a great range, from upper to lower continental crust as well as lithospheric mantle. Most of these are recorded from crustal levels ranging 2- ~15km, closely related to the depth to the base of the seismogenic zone (figure 4) (e.g. Sibson and Toy, 2006; Spray, 1987). As highlighted in the previous chapter, the extent of the seismogenic zone, for both continental and oceanic settings, is primarily controlled by depth. Figure 5 schematically display strength profiles for continental and oceanic lithosphere, where earthquakes and frictional heating are expected to occur in the brittle regime. Reports of pseudotachylyte in lower continental crust and in mantle lithosphere, occurring where crystal-plasticity is assumed to control deformation, give rise to the controversy concerning the origin of the heating, purely frictional or somehow related to viscous dissipation of heat (e.g. Braeck and Podladchikov, 2007; Kelemen and Hirth, 2007).

The pseudotachylytes explored in this thesis are shown on figure 4, and fall well below the base of the traditional interpretation of the seismogenic zone (compare with figure 5). The explored rocks in Corsica open a possibility to observe what controls their generation. The mechanism facilitating failure under these conditions is not properly constrained, and a range of possibilities has been proposed. The next section reviews deep earthquake trigger mechanisms with emphasis on two end-member processes concerning dehydration reactions and shear instabilities (Ogawa, 1987; Raleigh and Paterson, 1965).

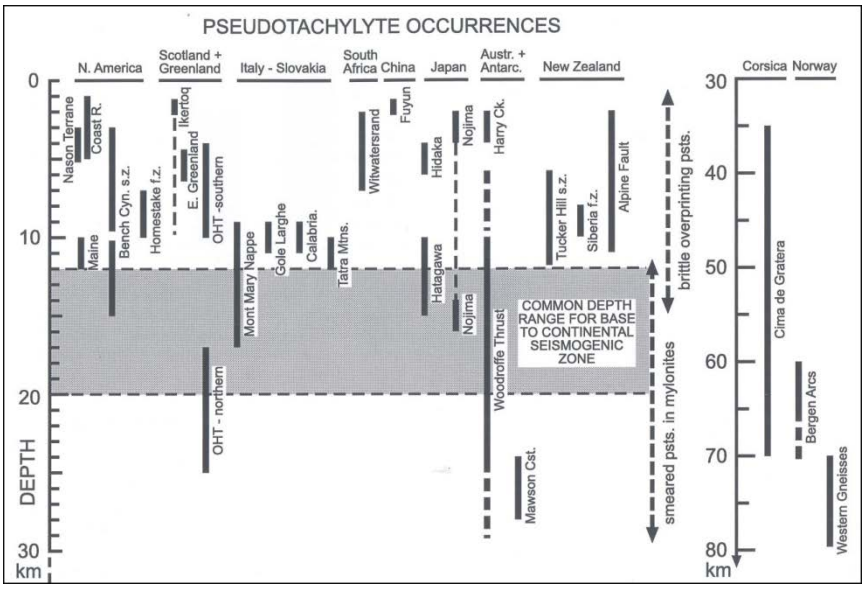

Figure 4: A compilation of estimated depths of formation for fault-generated pseudotachylyte. Note the change in depth scales between left- and right-hand groups and the location of Cima de Gratera, Corsica. From Sibson and Toy (2006).

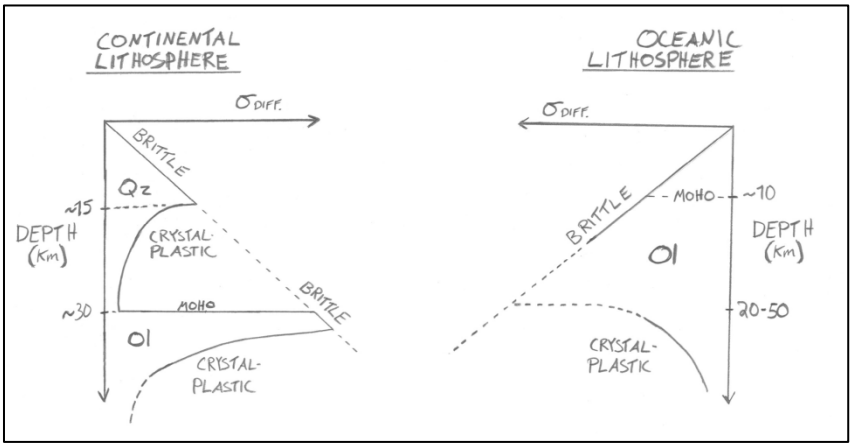

Figure 5: Schematically drawn strength profiles for continental and oceanic lithosphere, assuming qz and ol to control the rheology. Brittle failure follows that of Coloumb's criterion which is equivalent to a linear Mohr envelope. The seismogenic zone in continental settings occur at approximately 15km (but vary), whereas in oceanic lithosphere it varies greatly as a function of age (hence thickness).

Trigger-mechanisms for earthquakes at depth

> *"Studying geologic processes at high strain rates is difficult; events occur in seconds, and the energies released typically eradicate the earlier stages of rock transformation"* (Spray, 1995).

Intermediate and deep earthquakes occur at depths much greater than those commonly assigned to the seismogenic zone. High confining pressure render frictional failure unlikely and vast differential stresses therefore are required to induce failure (figure 6). Thus, brittle fracture and frictional sliding at great depth would require unrealistic rock strengths.

Since *"earthquakes occur because fault strength weakens with increasing slip or slip-rate"* (Rice, 2006) there have been proposed several mechanisms for how intermediate and deep earthquakes are triggered. These describe different rock-weakening processes that may cause rocks to fail in absence of low confining pressure. Many of them are overlapping with somewhat similar concepts (Frohlich, 2006; Green and Houston, 1995). The main mechanisms are briefly reviewed below.

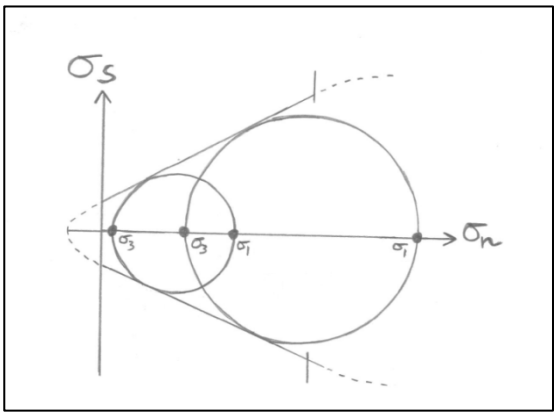

Figure 6: Mohr diagram showing critical states of stress in dry rock and the effect of low (small circle) and high (large circle) confining pressure. With increasing confining pressure, the critical Mohr circle shifts to the right, greatly increasing the differential stress required for failure.

- <u>'Phase transformations'</u>

  Earthquakes triggered by phase transformations concerns the densification of rocks with prograde metamorphism, such as basalt to eclogite transformation and ol to β-phase transformation. The dT/dP slope of phase boundaries for most mantle silicates is positive. If the T-P path of the descending lithosphere reaches the kinetic boundary at pressure below a critical value, metastable phase transformations are considered to occur instantaneously in a vast rock volume, causing earthquakes (e.g. Bridgman, 1945; Kirby et al., 1996; Liu, 1983).

- ‘Densification-induced anticrack failure’

  Experiments on metastable ol have shown that during the transition from ol to spl, nucleation of crack-shaped lenses of spl was oriented with their long axes perpendicular to the compression direction. This is opposite of tensile cracks, and were subsequently termed ‘anticracks.’ The exothermic reaction from ol to spl causes the reaction rate to increase, eventually joining anticracks at a fast rate to a critical density, causing fault growth similar to that of shallow earthquake growth (Burnley and Green, 1989; Green and Burnley, 1989).

- ‘Plastic instabilities’

  The mechanism of plastic instabilities suggests that earthquake events may be the result of instabilities in material undergoing plastic flow. At a particular strain rate, a critical temperature controls if the material is strain rate softening or strain rate hardening. At temperatures above this threshold, plastic flow is sustained, while at lower temperatures the material may undergo catastrophic plastic shear (Hobbs and Ord, 1988).

- ‘Shear heating’

  Frictional heating is often referred to as shear heating, because it is produced as rocks are sheared. Shear heating by viscous dissipation is different, but similar to that of the plastic instability mechanism. Rocks may deform plastically at low homologous temperatures, but heat is produced by the deformation. Here it is considered that the heat produced by shearing influences the strain rate, resulting in a stress drop by suppressing stable creep (Post, 1977). The effect on strain rate can be catastrophic if the deformed material is inhomogeneous (Ogawa, 1987). This mechanism will be discussed further below.

- ‘Dehydration embrittlement’

  The dehydration embrittlement mechanism concerns both dehydration of subducted hydrous rock, and the interaction between the released water and the adjacent anhydrous rocks (e.g. Jung et al., 2004; Raleigh and Paterson, 1965). The principal effect of this mechanism is to reduce the effective stress by increasing the pore fluid pressure – hence creating a stress-system similar to that of the “seismogenic zone.” This mechanism will be discussed further below.

Of the proposed mechanisms there are currently two which have recently been given much attention in relation to explain intermediate depth seismicity, and are supported by evidence from naturally deformed rocks. These two mechanisms are dehydration embrittlement and localized shear heating (e.g. Hacker et al., 2003; John et al., 2009; Jung et al., 2004; Kelemen and Hirth, 2007).

Dehydration embrittlement

Dehydration embrittlement refers to the weakening of rock actively dehydrating, whereas ‘hydration embrittlement’ is a more suited term for weakening produced by the presence of a free fluid phase produced at any distance from a body of rock, at any time (Barcheck et al., 2012). The model strictly involving in situ dehydration embrittlement has only been observed in experiments (Lee and Kirby, 1984), whereas the effect of a free fluid phase has been well reported to influence rock deformation (e.g. Green and Houston, 1995; Jung et al., 2004; Raleigh and Paterson, 1965). The released fluid will have an effect on the actively dehydrating rock as well as adjacent anhydrous lithologies in terms of fracturing and frictional sliding (Passchier and Trouw, 2005; Twiss and Moores, 2007).

The oceanic crust, its cover and the upper lithosphere may be extensively hydrated before arriving at the subduction trench (e.g. Hacker et al., 2003; Peacock, 2001; Reynard, 2012). Hydrothermal alteration at mid ocean ridges is enhanced by temperature gradients and extensive fracturing. Hydration of the oceanic lithosphere continues as the seafloor ages, and sediments are deposited onto it, which contains both pore and chemically bound water (Rupke et al., 2004).

Hydration of the lithosphere is commonly assigned to serpentinzation, which is attributed to accommodate the dominant portion of deeply subducted water (Reynard et al., 2010). In order for surface fluids to hydrate mantle rocks, fluids must first pass through the crust and its

sedimentary cover. Faulting at the outer rise is considered to promote serpentinization of deeper portions of the crust as well of the lithosphere (Hacker et al., 2003). Here, hydration possibly extends several kilometres below the oceanic crust (>15km) supported by seismic imaging (Christensen and Ruff, 1988; Ranero et al., 2003). Thus, old and mature lithosphere may become more hydrated than young, hot lithosphere due to the depth isotherm of serpentinization (Rupke et al., 2004).

As the subducted slab descends into the mantle, release of water will occur within the lithosphere as a function of pressure and temperature increase. Slab fluid release can be divided into three stages; release of water from subducted sediments, release of water from subducted crust, and finally from subducted lithosphere (Peacock, 2009). These processes are intimately associated with sediment compaction, metamorphic densification and equilibration (Rupke et al., 2004). At intermediate depth for a gentle geothermal gradient, reaction 1 and 2 is feasible for producing of a free fluid phase in the crust and cover at relatively early stages of subduction by following Spear (1993);

Prh-pmp → blueschist + water

Prh + cal → lws+ zo + H_2O + CO_2 (Reaction 1)

Ab + chl → gln + H_2O (Reaction 2)

and at increasing depth reaction 3 is suggested by Evans (1999);

Blueschist → eclogite + water

Gln + czo → omp + grt + H_2O (Reaction 3)

Dehydration of the upper lithospheric mantle, for both steep and gentle geothermal gradients is largely considered to occur through reactions 4 and 5 by following Brindley and Hayami (1965);

Srp → ol + silica + H_2O (Reaction 4)

Srp → ol + opx + H_2O (Reaction 5)

Dehydration of srp occurs at a wide depth range due to different srp minerals being stable at different intervals, down to a maximum of 600°C for atg (Reynard, 2012; Rupke et al., 2004).

The release of water by dehydration reactions will increase the pore fluid pressure in recently dehydrated and adjacent bodies of rock, lowering the effective stress. The effective stress is the result of reducing all applied normal stress components by an amount equal to the pore fluid pressure, while leaving the shear stress unchanged. Equation 1 (Twiss and Moores, 2007);

$$\sigma_n^{(eff)} = (\sigma_1 - \sigma_3) - P_f \qquad \text{(Equation 1)}$$

where $\sigma_n^{(eff)}$ is the effective normal stress, $(\sigma_1 - \sigma_3)$ is the differential stress and P_f is the pore fluid pressure, shows that the rock behaves as if the confining pressure was lowered by an amount equal to the pore fluid pressure. In this way the tensile strength of the rock is reduced (figure 7).

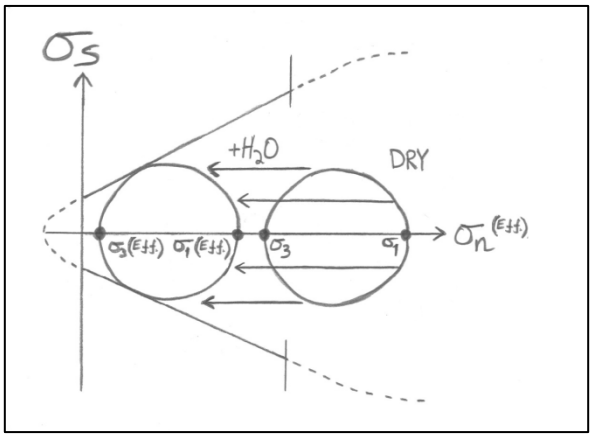

Figure 7: Mohr diagram with the effective stress plotted in the horizontal axis, showing the effect of pore fluid pressure on the fracture stability of rock. At large differential stress, an increase in pore pressure leads to shear failure. The fracture criterion remains the same, except that the normal stress is replaced by the effective normal stress.

This implies that dehydration releasing free water in subducted slabs could cause seismicity at depths otherwise inhibited due to extreme confining pressure. The main zone of intermediate depth epicentres correlates to inter-plate earthquakes occurring in crust and upper lithosphere where hydrous phases should be most abundant (figure 8) (Hacker et al., 2003).

Faulting at the outer rise may be sufficient to locally hydrate mantle lithosphere down to ~15km below the oceanic crust (Ranero et al., 2003) and matches that of seismological data (figure 2 and 8). However, the two-layered Wadati-Benioff zones observed in several subduction zones (figure 2) do not support failure by dehydration embrittlement occurring at the lower plane of seismicity. The lower plane of earthquakes are not accounted for by infiltration of water and serpentinization during faulting at the outer rise, because faulting nor

serpentinization is deep enough to match the region of intra-plate earthquake activity (Reynard, 2012; Reynard et al., 2010). This suggests that some other mechanism is responsible for nucleating earthquakes within anhydrous mantle.

Dehydration embrittlement is clearly an efficient mechanism. It facilitates brittle failure at high confining pressure, and suggests that externally released fluids will initiate earthquakes in other parts of the subducted slab. However, the pathways of fluid transport are not well constrained (e.g. Hacker et al., 2003; Peacock, 2009).

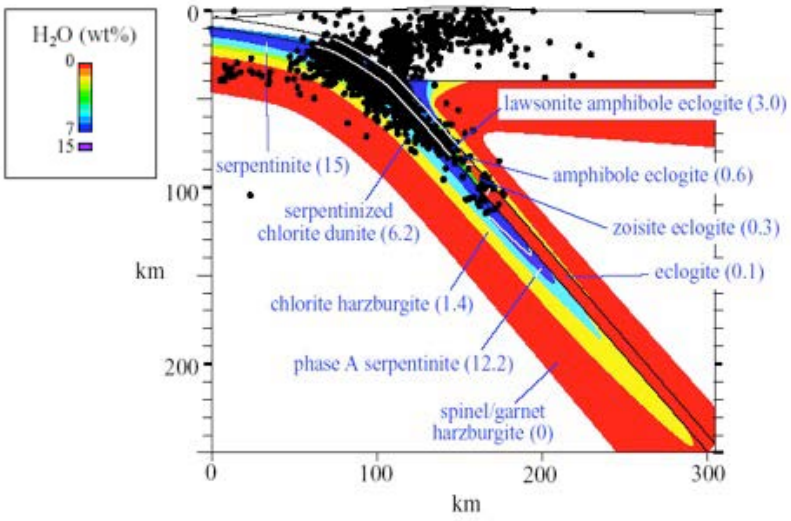

Figure 8: Correlation between seismicity (black dots) and phase transformations in the Costa Rica subduction zone. The subducted Cocos plate is 18Ma. Seismicity is projected 25km from either side of the section. The amount and distribution of water in the subducted plate is shown in color coding from 0-15wt% H_2O. Modified from Hacker et al. (2003).

Shear heating

In the absence of sufficient pore fluid pressures, shear heating proposes a mechanism in which rocks can fail by progressive thermal instability where ductile deformation in shear zones may lead to heating, thermal softening and weakening of rock (e.g. Braeck and Podladchikov, 2007; John et al., 2009; Ogawa, 1987). This mechanism requires that ductile deformation takes place before seismic rupture and therefore that no brittle failure takes place.

Below the seismogenic zone, as a function of temperature and pressure, most rocks may be characterized as viscoelastic where the rheology contains both viscous and elastic components (figure 5) (Braeck and Podladchikov, 2007). Viscoelastic materials behave elastic for short durations of imposed constant stress, and respond viscously during longer durations of imposed constant stress. In this way the strain includes an instantaneous recoverable elastic

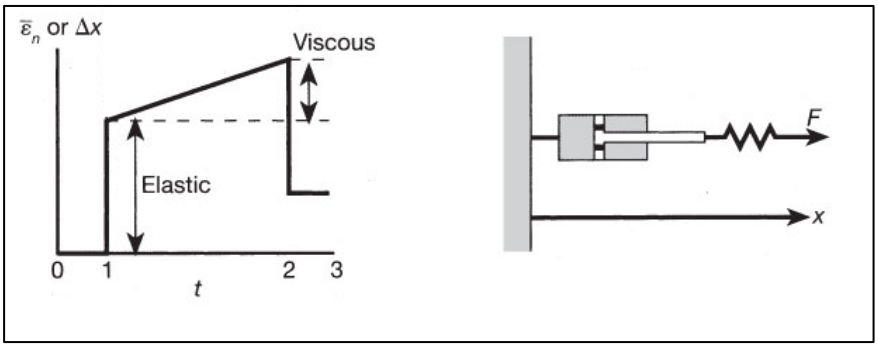

Figure 9: Characteristics of a viscoelastic material. Left: Stress versus time response to an imposed constant stress. Left: mechanical analogue. Modified from Twiss and Moores (2007).

deformation and a nonrecoverable viscous deformation (figure 9) (Twiss and Moores, 2007). This means that the viscous deformation by migration of lattice defects also has a component of stretching bonds along crystallographic planes in an ordered solid, which is not dissipated during continued deformation.

Shear heating (other than frictional heating) concerns heat production during viscous deformation (Ogawa, 1987). The temperature increase that arises from shear heating over time can be written as equation 2 by following Stüwe (2007);

$$\frac{dT}{dt} = \frac{\tau \dot{\varepsilon}}{\rho Cp} \qquad \text{(Equation 2)}$$

where T is temperature, t is time, ρ is density, Cp is heat capacity, τ is shear stress and $\acute{\epsilon}$ is strain rate. In heterogeneous materials the influence of shear heating along a weaker zone could result in a local temperature increase. In this way, a local increase in temperature will in turn have an effect on the rheology of the heated material. This concept has recently been revived in relation to intermediate and deep earthquakes by combined studies involving both field observations and numerical modelling (John et al., 2009; Kelemen and Hirth, 2007).

Self-localizing shear heating

Because of rock heterogeneity, preferential shear involving highly localized, narrow zones may occur in regions that already have the lowermost viscosity. A localised positive temperature perturbation by shear heating will lower the strength of the rock by further lowering the viscosity in the narrow band (Braeck and Podladchikov, 2007). In this way the temperature perturbation is amplified by shear heating, and the process become self-enhancing.

Depending on the competition between localisation of temperature and heat diffusion away from the narrow band, strain may be strongly or weakly, respectively, localized to the perturbed region (figure 10) (Braeck et al., 2009).

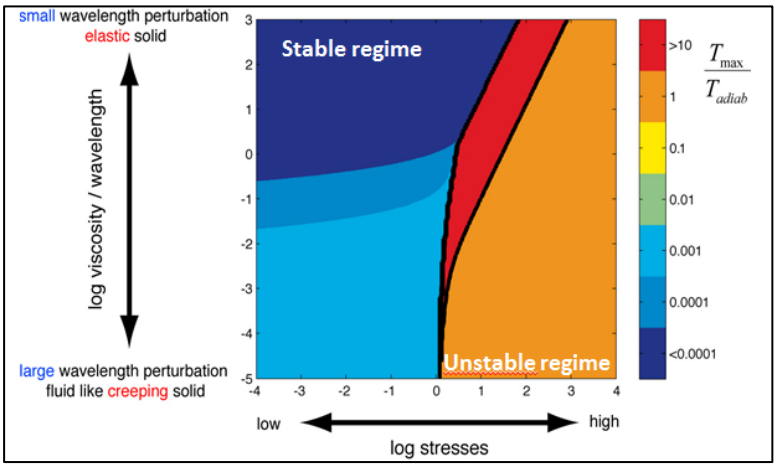

Figure 10: A contour plot of temperature rise in a viscosity-perturbed band, scaled by stress and viscosity. The blue region represents stable deformation processes and the red and orange regions represent areas of thermal runaway. The orange region is characterized by adiabatic thermal runaway, where the entire width of the initial perturbation in viscosity is heated by diffusion, weakly localising elastic strain. The red region is characterised by self-localizing shear heating, where elastic strain is highly localized in a zone much narrower than the initial width of the narrow band. Modified from (Braeck et al., 2009).

It is suggested that localized viscous deformation accompanied by rising temperatures feeds back positively and nonlinearly on the strain rate (Braeck and Podladchikov, 2007). At sufficiently high strain rates the release of stored elastic energy, due to the loss of strength in the heated band, can ultimately induce failure (e.g. Braeck et al., 2009; John et al., 2009). The temperature rises too rapidly to be diffused away from the shear zone and the shear instabilities become self-localizing. The elastic energy stored in the viscoelastic body of rock may thus be spontaneously released by the formation of such high-temperature shear instabilities (Braeck et al., 2009). The instability may be sufficiently great to produce intensely localized deformation and possibly failure at seismic velocities and subsequent generation of pseudotachylyte (e.g. John et al., 2009). A central question regarding the initial perturbation in viscosity must be addressed.

It is suggested that pre-existing fine-grained shear zones generated prior to and during the initial stages of subduction may be responsible for the perturbation (e.g. Kelemen and Hirth, 2007). There is geological evidence for shear zones (1-100µm ol) in shallow mantle peridotite (~5-10mm ol) (Jaroslow et al., 1996; Kelemen and Dick, 1995) where the reactivation of these zones may play a key role in the generation of intermediate-depth seismicity. These are

suggested to form by recrystallization and annealing of fault gouge during subduction, adapted from activity along oceanic transforms, in subduction-related thrusts and along faults at the outer rise (Savage, 1969). These zones are proposed to sustain for 10^8 to 10^9 years at shallow mantle temperatures (Kelemen and Hirth, 2007).

Using flow laws for ol and integrating the existence of fine-grained shear zones, numerical modelling has furthermore established the possibility of repeated, periodic earthquake-generation by viscous shear heating (Kelemen and Hirth, 2007), and that this mechanism may be responsible for intermediate-depth earthquakes.

2. Methods

Analytical techniques

The analyses of the Corsican samples were carried out at three institutes. Department of Earth, Ocean and Ecological Sciences, University of Liverpool; Department of Chemistry, research group for Functional Energy Related Materials (FERMiO), Forskningsparken, University of Oslo and finally in the Department of Geosciences, University of Oslo. In the study of the microtexture and mineralogy of the Corsican ultramafic pseudotachylytes and their wall-rocks, the following methods have been used;

1) Optical microscopy
2) Scanning electron microscopy (SEM)
3) Electron backscatter diffraction (EBSD)

Preparation for SEM and EBSD was done in a systematic study using the petrographic microscope for phase and texture determination. The microscope used was an Olympus BX 41 mounted with a Leica DFC 320 camera, for imaging and stitching mosaic layouts of faults and adjacent wall-rock relationships. Due to frequently observed highly strained, distorted grains where identification was proven difficult, determination was done using a SEM and energy-dispersive X-ray spectroscopy (EDS). Areas of interest for EBSD were selected on basis of this preliminary study and are covered in their respective chapters. Principles and setup of the SEM and theoretical background on electron-specimen interactions are covered in appendix 2.

Two different SEMs were used during the collection of EBSD-data and a third for backscattered electron (BSE) imaging and phase determination using EDS. In order to learn methods, a course for the use of EBSD was attended from the 13-17th of February, 2012, at the Department of Earth, Ocean and Ecological Sciences at the University of Liverpool. After the course (18-24th of February) initial analyses of samples from Corsica were carried out using a CamScan X500FE Crystal Probe field emission gun (FEG) with a Hamamatsu digital detector. Patterns were collected in high vacuum using an acceleration voltage of 20 kV, a beam current of 30nA and an emission current of 228µA. Patterns were indexed and processed using HKL Channel5, version 5.

Further EBSD analyses were done at the Department of Chemistry in the research group for Functional Energy Related Materials (FERMiO) at the University of Oslo. Analyses were

started in April 2012 and went on at spaced intervals to November 2012. The instrument put to use was an FEI Quanta 200 FEG-ESEM with a CD-200 Nordiff detector. Patterns were collected in low vacuum (40-80Pa) using acceleration voltages of 20-30kV and a beam current of 2-5nA. Patterns were indexed and processed using TSL/EDAX and TSL OIM version 6.1.

BSE imaging, phase analysis and investigation of dislocation densities were carried out at the 7th and 23rd of November at the Department of Geosciences at the University of Oslo. The type of instrument used was a JEOL JSM-6460LV SEM with a LINK INCA Energy 300 EDS from Oxford Instruments. Analyses were done using high vacuum and an accelerating voltage of 15kV.

In the following sections are the purpose, setup and use of EBSD, followed by the type of plots, commonly applied abbreviations and clean-up procedures that are used in this thesis. Two different software packages have been used to gather and post-process EBSD data. These are treated separately.

The chapter ends with describing specimen preparation prior to analysis for the analytical techniques that has been done.

An introduction to electron backscatter diffraction (EBSD)

The anisotropic optical properties of many minerals have given rise to measurement of crystallographic orientations in thin sections of rock by using a universal stage on a transmitted light microscope. Manual collection of orientation data using the universal stage has provided the basis for orientation maps and fundamental concepts on recrystallization mechanisms (e.g. Dingley and Randle, 1992). However, such measurements are time consuming and limited to a few crystal symmetries where the minimal measurable grain sizes are constrained by the thickness of the thin section, and by the optical limitation of the microscope (Mariani et al., 2008).

Over the years more automated systems have been explored which provide high resolution qualitative and quantitative 2D and 3D microstructural data. These include computer-integrated polarization microscopy (CIP), synchrotron X-ray tomography, serial-sectioning using a focused ion beam (FIB) in the SEM as well as electron backscatter diffraction (EBSD). Of these techniques EBSD is the more widely used in Earth Sciences (e.g. Prior et al., 2009; Schwartz et al., 2009; Zhou and Wang, 2007). It is fully automated and allows collection of

accurate and statistically meaningful crystallographic orientation data of minerals from most crystal systems. It is a relatively new technique; the first EBSD data from a rock was published by Kunze et al. (1994).

In literature EBSD is commonly addressed as backscatter Kikuchi diffraction (BKD) and electron backscatter patterns (EBSP) (e.g. Mariani et al., 2008). In this thesis, EBSD refers to the diffraction technique and EBSP refers to individual diffraction patterns. The network of diffraction lines that are exploited with EBSD forms an EBSP, frequently referred to in literature as a 'Kikuchi pattern.' These patterns may also be imaged in the transmission electron microscope (TEM) and by electron channelling in the SEM (e.g. Dingley and Randle, 1992; Wilkinson and Hirsch, 1997). This thesis uses exclusively EBSD in the SEM.

EBSD is based on the principle that electrons generated in the SEM are the source of a multi-directional population of elastically scattered electrons from a specimen. The scattered electrons create acquisitional data like on a normal backscatter image, but provide incomparable information due to the unique setup of the EBSD technique.

EBSD can be done on any kind of SEM that allow for rotation of its stage from the horizontal position, together with having sufficient space to host acquisitional equipment to detect and record EBSPs within its chamber. Specialized setups whereas the electron gun itself is tilted in relation to the stage do exist.

Principles and setup of EBSD

High-energy electrons of an electron beam generated from a field emission or thermionic electron gun travel down the electron column and interact with the target specimen in many different ways. For purposes of EBSD we are mainly interested in elastic specimen interactions (appendix 2). For this reason accelerating voltages are usually kept rather high (20-30keV) to increase the intensity of the signal, making it easier to record (Prior et al., 2009)

The trajectories of backscattered electrons

Once a population of electrons has undergone one or more events of elastic scattering within the target specimen, some eventually leave the surface of incidence as backscattered electrons. The ejected electrons are subject to path differences that lead to constructive and destructive interference (e.g. Zhou and Wang, 2007). Those that satisfy the Bragg equation for diffraction lead to constructive interference and describe conical trajectories of ejection for each lattice plane through equation 3:

$$n\lambda = 2d \sin\theta \qquad \text{(Equation 3)}$$

where θ is the diffraction angle, n is an integer (the order of diffraction), λ is the wavelength of the electron accelerating voltage and d is the lattice spacing (Hiltner and Krieger, 1969). In a two-dimensional section there will be four possible trajectories that satisfy the Bragg condition for diffraction (figure 11, A). In three dimensions the trajectories of electrons that satisfy the Bragg condition for diffraction define two cones that in turn generate two cones of diffracted electrons. In other words, every lattice plane generates two diffraction cones; one from the upper side and one from diffraction from the lower of the plane (Dingley and Randle, 1992). This is visualized on figure 11, B. The intensity of the cones is dependent on the electron accelerating voltage, the atomic species that define the plane the BSE arose from, the order of diffraction and by dynamical diffraction of numerous BSE (e.g. Dingley and Randle, 1992; Prior et al., 1999).

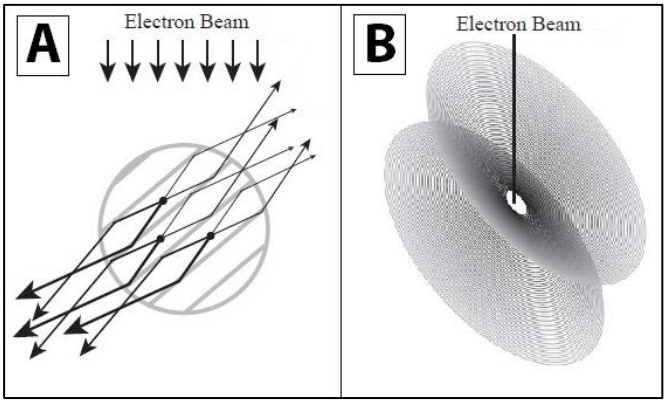

Figure 11: Schematic illustrations of electron trajectories. A) Two-dimensional section showing a single set of lattice planes giving rise to diffraction. Four scattered electron trajectories will satisfy the Bragg equation for each of the three source points shown here. The relative intensities of the diffraction directions are indicated by the thickness of the arrows. B) Diffraction cones in three dimensions for a single lattice plane. Two cones are generated; one from diffraction of the upper and one from the lower plane. Modified from Prior et al. (1999).

The Bragg angle for diffraction of electrons accelerated through 20-30keV is typically small, so that the opening angles of the two diffraction cones are close to 180° (Prior et al., 1999). Such diffraction cones approximate planes and appear as straight lines, and a network of diffraction lines forms an EBSP. In order to increase the amount of BSE and detect the conical trajectories of BSE a typical setup has been developed for use of EBSD in the SEM.

EBSD setup

The method of EBSD requires some additional equipment installed within the SEM chamber. A phosphor screen/film is positioned to intercept the conical trajectories of backscattered electrons (Venables and Harland, 1973). The phosphor is fluoresced by electrons ejected from the sample imaged by a sensitive charge coupled device (CCD) camera with its lens parallel to the screen on the distant side (e.g. Schwartz et al., 2009). Figure 12 displays the orientation of these components relative to the sample.

The configuration during EBSD holds an angle of incidence of 20° from the path of the electron beam and the specimen, the specimen consequently tilted 70° towards the phosphor screen. The sample inclination relative to the incident beam enhances the proportion of BSE that are able to undergo diffraction and escape from shallow depths in the specimen surface (e.g. Schwartz et al., 2009; Zhou and Wang, 2007).

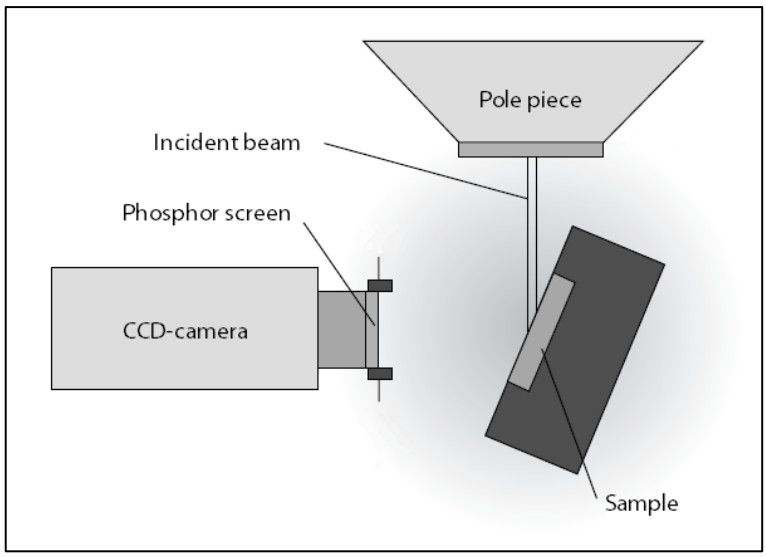

Figure 12: Schematic illustration of the arrangement and sample orientation for EBSD assembly in the SEM. Modified from Zhou and Wang (2007).

The resolution and quality of EBSPs

The multi-directional population of scattered electrons does not originate at one single point but within an activation volume (appendix 2, figure A.6). It is the size of this volume that controls the spatial resolution of the EBSD technique. The extent of the activation volume is dependent on incident electron energy where penetration depth generally increases with increasing accelerating voltages. By tilting the stage, increasing the number of BSE, it also minimizes the amount of electrons that are absorbed by the sample (Dingley and Randle, 1992; Prior et al., 2009). Figure 13 displays estimated source depths in an alumina sample tilted at 70° using 20keV.

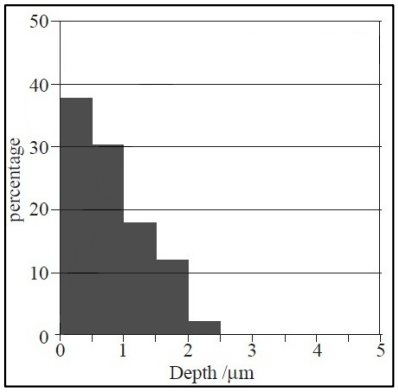

Figure 13: Estimated source depth for 2000 electrons in an alumina sample tilted at 70° at 20keV using Monte Carlo simulations. Modified from Prior et al. (1999).

The total depth of penetration in this scenario (figure 13) extends down to 2.5µm with a significant amount sourcing from depths <1µm. Electrons that penetrate deeper are likely to have their energies absorbed by the sample, and do not emerge as BSE. Due to the shallow penetration in which beam-specimen interactions take place this layer must be relatively strain free (e.g. Dingley and Randle, 1992; Tao and Eades, 2005; Zhou and Wang, 2007). Methods that are applied to ensure specimen purity are covered in the section concerning sample preparation.

Sample inclination make ejected electrons surface at some distance from their point of incidence. The difference in length causes blurring of individual diffraction bands (Prior et al., 1999). It should also be taken into account that the interactions producing EBSPs do not exclusively take place by elastic scattering. Electrons that interact with the sample experience numerous elastic and inelastic events until they are ejected as BSE, or until they lose sufficient energy to be able to emerge from the sample surface. There will be a population of BSE and emerged secondary electrons that have energies ranging from close to zero to that of the incident electron beam (Wilkinson and Hirsch, 1997). This gives rise to a diffuse

background signal on the phosphor screen. The background noise is corrected for by collecting an EBSP over a large area in scanning mode so that the signal from a large number of crystals is averaged and subtracted from the final EBSPs (e.g. Mariani et al., 2008; Schwartz et al., 2009). Figure 14 shows a typical EBSP of ol where background noise has been subtracted.

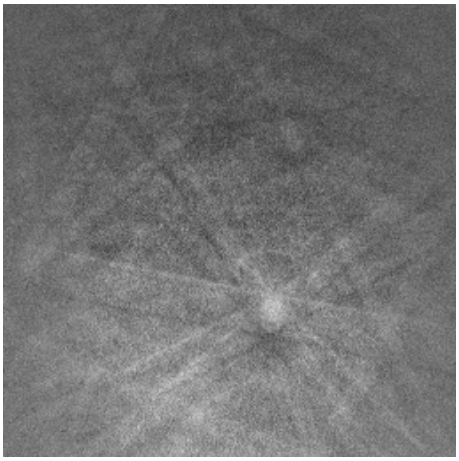

Figure 14: A captured live EBSP of ol with background noise subtracted. Note the variation in intensity for the individual diffraction bands, reflecting the distribution of scattered electron intensities and travel distance from the point of incidence. The EBSP was obtained at FERMiO, Forskningsparken (UiO) using 20keV and 2nA at a working distance of 8mm, acquired using EDAX/TSL.

The relative position of the sample, phosphor screen and camera also control the resolution and quality of EBSPs (e.g. Day and Quested, 1999). Figure 15 on demonstrates the setup and the calibration parameters. The projection of the source of BSE on the phosphor screen follows a trajectory perpendicular to it and generates the pattern centre (PC). It should project on the centre of the phosphor screen in order to properly assess EBSPs. The distance from BSE source to the phosphor screen is the detector distance (DD) which affects the angular resolution. A small DD is good for recognizing EBSPs but yield poor angular resolution. A large DD makes the diffraction bands harder to recognize, but the angular resolution is much better (e.g. Tao and Eades, 2005). The distance from electron gun to the specimen is called the working distance (WD) and governs the magnification (and spatial resolution). All three distances and the solid angles between them are calibrated in order for the acquisition software to properly evaluate the EBSPs (Prior et al., 2009).

To sum up, the depth of penetration, geometry of the activation volume, intensity of emerged electrons and calibration of the assembly within the SEM controls the resolution and quality of EBSPs. Problems with resolution and quality of EBSPs are further complicated by sample topography, sample tidiness and charging in nonconductive materials (minerals).

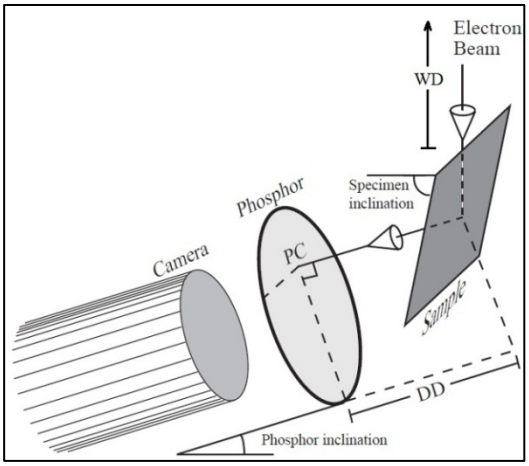

Figure 15: Schematic illustration of calibration parameters for EBSD assembly in the SEM. Calibration requires adjustment of the distances in between the individual units. WD is the working distance from electron gun to specimen, DD is the detector distance from specimen to phosphor screen and PC is the pattern centre on the screen. Modified from Prior et al. (1999).

Computer indexing

An EBSP is effectively a set of angles between planes recorded by the camera where indexing considers the position and orientation of bands with respect to the pattern centre (PC) (figure 15). Indexing is done automatically, initially by computerized band recognition that calculates the orientation and angles between planes that contain bands at the source point. Band recognition utilizes the Hough transform that translates the coordinates of identified bands (x,y) into 'Hough-space' (ρ ,θ). Equation 4 and figure 16 display this relationship by following Wilkinson and Hirsch (1997);

$$\rho = x\cos(\theta) + y\sin(\theta) \qquad \text{(Equation 4)}$$

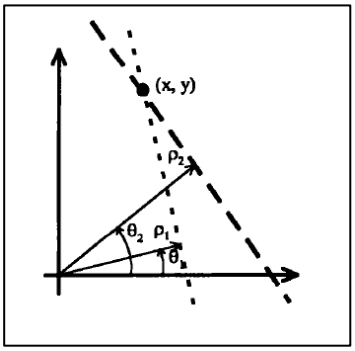

Figure 16: Hough parameters ρ, θ that define lines through the point (x,y). From Wilkinson and Hirsch (1997).

The calculations produce sinusoidal curves that intersect with coordinates ρ and θ, transforming the intensity of diffraction lines into points in Hough-space. Where diffraction lines interfere, higher intensities are recorded. Peak detection algorithms segment out high intensity peaks from the background, and in this way disregards possible false peaks (e.g. Duda and Hart, 1972).

Band recognition is an intermediate step in computer indexing. The Hough parameters define the locations of the prominent bands in the EBSP which is subsequently compared to a symmetry database. The symmetry database consists of crystal symmetry and unit cell dimensions that assess the recognized diffraction planes in three dimensions. The database has information on the relative intensity of diffracting planes investigated from existing X-ray data and atomic scattering calculations (e.g. Prior et al., 1999; Schwartz et al., 2009; Zhou and Wang, 2007). Further, the database suggests possible orientations of the crystals (minerals) for every single EBSP. Investigated crystal symmetries are chosen by the operator prior to analysis.

Assessment of whether the computerized indexing has indexed a pattern correctly requires manual comparison between an EBSP and the computerized, simulated bands. The simulated bands are overlain a captured EBSP (figure 17) and calibrated prior to analysis mapping. A good fit requires that all of the visible bands on the EBSP have been recognized, and that the computer simulation does not suggest bands that are not present on the EBSP. In order to correct for improper simulations, automated and/or manual configuration of the simulated

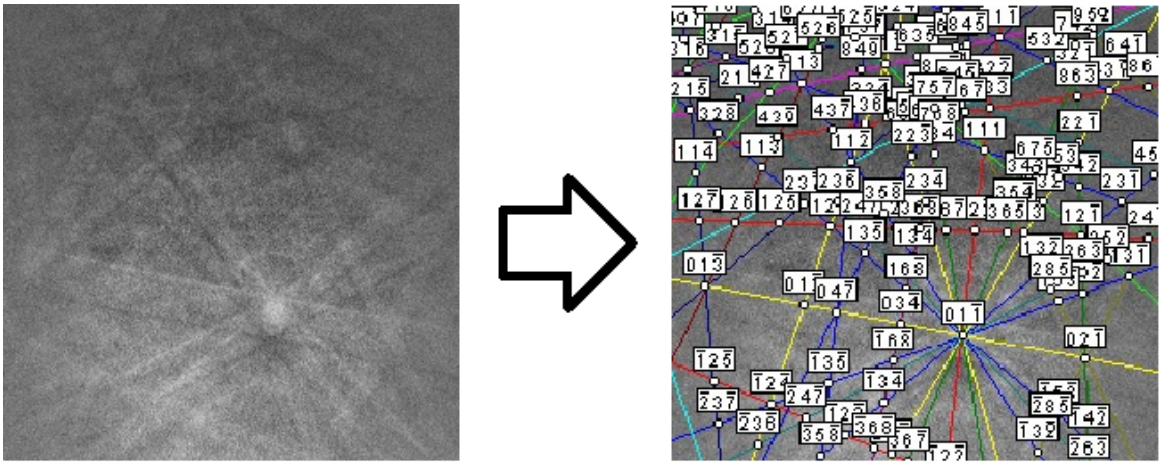

Figure 17: The image on the left is a captured live EBSP of ol (same as in figure 14) collected using 20keV and 2nA at a working distance of 8mm. The image on the right hand side displays the overlain computer simulation. In this scenario the detected bands has a large angular misfit (3°) prior to automated 'best fit' calibration and manual adjustment. All of the observed bands have been recognized, but some of the suggested bands are not present on the live EBSP. There are errors regarding the angles between bands in the upper left corner of the image.

bands is done by the operator. Additional parameters that help improve the angular fit are to resolve the resolution, the number of bands used for indexing, the number of reflectors and/or material dependence (Mariani et al., 2008).

Computerized band recognition and indexing constitute fully automated EBSD systems. Dedicated software packages can collect and index a pattern, store the data and move the beam to the next analysis point at a very fast rate (Prior et al., 2009). Orientation data are collected and stored at predefined points on a grid, which is consequently used to reconstruct and combine all the EBSPs over a scan area in relation to each other. In this way the microstructure is visualized by pixels containing information of the orientation of every analysed point. There are many ways in how to present the acquired orientation data. Colour-coded maps that represent orientations are widely used, commonly combined with plots and/or charts that together help investigate and explain the acquired orientations (or misorientations) (Wheeler et al., 2001).

EBSD data presentation

The following sections on data concepts and abbreviations, EBSD plots, EBSD maps and clean-up routines are based on HKL (2007); TexSEM (2009).

Data concepts and abbreviations

First off are some frequently used concepts and abbreviations related to presentation of EBSD data in this thesis. These are attributes that give information of the acquired datasets and are presented alongside with them. EDAX/TSL and HKL Channel 5 use different words for the same type of data measurements, and will be grouped accordingly.

- Mean Angular Deviation (HKL Channel 5)
  Angular misfit (EDAX/TSL)

The mean angular deviation/angular misfit are numbers that expresses how well the simulated EBSP overlays the actual EBSP. The actual and simulated EBSP are displayed on figure 17. The numbers are given in degrees, specifying the average misfit between detected and simulated diffraction bands.

- BC - Band Contrast (HKL Channel 5)
  IQ - Image Quality (EDAX/TSL)

The band contrast/image quality is an EBSP quality factor, derived from the Hough transform that describes the average intensity of the patterns with respect to the overall intensity within the EBSP. The values are scaled to a byte (0-255) in this thesis.

- CI - Confidence Index (EDAX/TSL)
  No equivalent for HKL Channel 5?

This parameter is calculated during automated indexing of a diffraction pattern. For a given diffraction pattern, several possible orientations may be found which satisfy the diffraction bands detected by the image analysis. The software ranks these orientations (or solutions) using a voting scheme based on equation 5;

$$CI = (V_1 - V_2)/V_{IDEAL} \qquad \text{(Equation 5)}$$

where V_1 and V_2 are the number of votes for the first and second solutions, and VI_{DEAL} is the total possible number of votes from the detected bands. The confidence index ranges from 0 to 1. A CI of -1 is given to EBSPs that could not be analysed (nonindexed).

- Step size (same for EDAX/TSL and HKL Channel 5)

The step size refers to the spacing between every individual scan point within the scan area (by how much the electron beam was moved between each pixel). A step size less than the minimum grain size is needed for recognizing, and eventually restoring misindexed points.

EBSD plots

The presentation of EBSD plots is relatively similar for both HKL Channel 5 and EDAX/TSL. Different reference systems had to be accounted for.

- PF - Pole figure

Pole figures display how plane normals and crystal directions are arranged relative to the specimen. The type of projection and which plane normals are to be investigated are entered by the operator. The pole figures are contoured for easier assessment of the data. In this thesis the following parameters was used for plotting contoured pole figures:

-HKL Channel 5:

Stereographic projections of poles to [100], [010] and [001] are plotted in the upper hemisphere. The pole figures were contoured using a Gaussian half-width of 10° with a resolution of 5° without symmetry inversion.

-EDAX/TSL:

Stereographic projections of poles to [100], [010] and [001] are plotted in the upper hemisphere. The pole figures were contoured using a Gaussian half-width of 10° with a resolution of 5° without symmetry inversion.

- Inverse pole figure (IPF)

Inverse pole figures show which crystallographic directions align with the specimen axes. The operator decides which sample direction(s) to consider. HKL Channel 5 and EDAX/TSL utilize different reference systems, where HKL uses X, Y, Z whereas EDAX/TSL uses the Transverse Direction (TD), Rolling Direction (RD) and Normal Direction (ND) for the exact same directions. In this thesis, a reference system from that in EDAX/TSL was adopted on all datasets. The parallel (Y, RD), transverse (X, TD), and normal (Z, ND) direction of the sample is used on both HKL Channel 5 and EDAX/TSL datasets. As a consequence, HKL datasets are rotated accordingly. This produces parallel [100], transverse [010] and normal [001] inverse pole figures that show which crystal directions in the crystal lattices are aligned with the axes of the sample reference frame. The sample reference frame is indicated with a shear direction on every dataset.

- Misorientation profiles

Misorientation profiles give the amount of misorientation along a user-defined line through the scan area. In this thesis the amount of misorientation is displayed between points along the line compared to the first point (origin) of the line. The starting point is given in the figure description on these profiles.

- Grain size presentation

Grains are identified and characterized based on grain definition parameters from the operator. These parameters are discussed in the next section concerning EBSD clean-up routines. In this thesis, grain sizes are presented in tables displaying the number of grains identified and

their diameter. Diameters are averaged for every table in order to investigate systematic differences between datasets. Grains terminating at the edges of datasets are not included in calculations.

- Misorientation angle distribution

Misorientation angle distributions give the distribution of grain boundary misorientations. The misorientation angle distribution displays the amount of misorientation between grains that touch (correlated/neighbouring), randomly selected grains that do not touch (uncorrelated/random-pair) and calculated random distributions (MacKenzie distribution) (Mackenzie and Thomson, 1957). Statistical differences between the correlated/neighbouring and the uncorrelated/random-pair distributions, relative to the calculated random distribution, give insight into physical processes that may give rise to the acquired distribution (Wheeler et al., 2001).

Due to different clean-up routines using HKL Channel 5 and EDAX/TSL the misorientation angle distributions between the two softwares were highly dissimilar. These issues will be assessed in the section on clean-up routines and in chapter 6.

EBSD maps

Datasets of the scan areas are presented as maps. The datasets can be cropped in order to focus on an area of interest within a scan. Cropping of datasets collects indexed data from the selected area which can be assessed and plotted independent of the original dataset.

The presentation of EBSD maps is relatively similar for both HKL Channel 5 and EDAX/TSL. Different words are used to describe the same type of maps and will be grouped accordingly.

- IPFC map - Inverse pole figure component map (HKL Channel 5)
  IPF map - Inverse pole figure map (EDAX/TSL)

For inverse pole figure maps/component maps, each indexed pixel is coloured according to an automatically coded unit triangle of the inverse pole figure (see previous section). In this thesis are inverse pole figure maps/component maps with respect to the normal direction of the sample. This produces [001] inverse pole figure maps/component maps that show which crystal directions in the crystal lattices are aligned normal to the sample reference frame.

- BC map - Band contrast map (HKL Channel 5)
  IQ map - Image quality map (EDAX/TSL)

The values are scaled to a byte (0-255) in this thesis and are visualized on the dataset of the scan area. This scale is mapped in greyscale from black to white over the dataset, where black represent low values and white represent high values. This type of presentation gives qualitative information on the strength of the recorded bands for every single point. Any distortion to the crystal lattices within the diffracting volume will produce lower quality (more diffuse) diffraction patterns.

- TC map - Texture component map (HKL Channel 5)
  HL map - Highlighted map (EDAX/TSL)

Texture component maps/highlighted maps are created on basis of a fixed point within a grain entered by the operator. All other points within the grain are compared to that single point, and gives deviation in orientation presented in RGB colours for the whole grain.

EBSD post processing and clean-up

In order for an EBSD dataset to give reasonable information of the analysed area, clean-up is a crucial step in order to allow proper assessment and analysis. It is also an important procedure for reproducing a texture that has not been captured. Misindexing is more of a problem than nonindexing, and parameters are usually set to effectively eliminate the former whilst minimizing the latter.

The automated pattern indexing is generally quite effective in identifying the orientation from an EBSP, however at times difficulties identifying some orientations do occur. An example is at grain boundaries, where EBSPs often are made up of two superimposed diffraction patterns from both crystal lattices. This may produce incorrect solutions. Uneven topography of the sample surface may also lead to erroneous results, while residue from polishing or even dust gathered during storage will inhibit indexing due to shadowing effects. The symmetry for some minerals mimics several crystal systems and are prone to systematic misindexing. Orthorombic systems, valid for both ol and opx, also seem to have an effect on the automated indexing algorithms. Even though exclusively ol was set to be indexed in this thesis, scattered indexation does occur within opx for most datasets.

Clean-up algorithms are integrated in both software packages and offer methods which attempts to alter faulty orientations based on input from the operator. These methods change

orientation data, so care has been taken to avoid introducing artificial trends into the datasets. The type of clean-up was done differently for the two software packages and will be covered separately.

Grain identification parameters for both softwares were set to 10°. This means that whenever adjacent domains with internally consistent orientations are separated by interfaces ≥10°, these are considered as multiple grains. If domains with internally consistent orientations are separated by interfaces ≤10° these are classified to belong to the same grain.

Clean-up routines for HKL Channel 5

Clean-up/noise reduction was done in a display-software called *Tango* which is one of several in-built platforms in HKL Channel 5. Clean-up was done on all raw datasets before they were cropped. Due to the limited stay at the University of Liverpool the applied clean-up method could not be altered at a later stage.

Step 1 – Applying a band contrast (BC) threshold

By truncating the lower end of the BC in the datasets this removes faulty domains and their orientation data. The strength of the recorded diffraction bands is typically very low at grain boundaries due to interference between crystal lattices on both sides, and this is an effective method for cleaning these. The datasets presented in this thesis was applied a threshold where mapped band contrasts range from 5-255.

Step 2 – Wild spikes extrapolate

Wild spikes are measurement points with a wrong indexing solution; spikes may occur where no or only very poor quality EBSP are generated (e.g. grain boundaries, cracks, dislocation clusters, voids, inclusions or damages on the sample surface). Wild spikes are identified as single pixels that differ in orientation from all neighbours. This clean-up method removes all isolated, faulty orientations without altering other orientations in the dataset.

Step 3 – Zero solution extrapolate

Zero solutions are EBSPs that could not be indexed by the automated indexing algorithms. These manifest as voids in the dataset that does not contain any orientation data. Data points removed by step 1 (BC threshold) and 2 (wild spikes extrapolate) also leaves zero solutions in the dataset. Extrapolation of zero solutions grows existing orientation data into voids on the basis of the number of neighbouring points, and is for all practical purposes a risky grain

growth experiment. However, this clean-up routine was applied using transparent RGB colour coding so that dilated grain sizes could be compared with the identified band contrast, which define the extent of individual grains. The level of zero solution extrapolation is set by the operator and range from 1-8 neighbours. The datasets in this thesis were cleaned using 6 neighbouring points at one step at a time (single iteration).

Clean-up routines for EDAX TSL 6.1

Clean-up/noise reduction in EDAX/TSL was applied on all raw datasets before they were cropped. No control on image quality in comparison to grain dilation could be assessed. Special clean-up procedures were done in order to not grow grains outside of their boundaries. Clean-up was done on all raw datasets before they were cropped.

Step 1 – Grain confidence index (CI) standardization

This clean-up method changes the CI of all points in a grain to the maximum CI found among all points belonging to the grain. It essentially enables pixels with low CI, yet having an orientation similar to that of the surrounding measurements, to be distinguished from a point with a low CI where no correlation exists between the point and its neighbours. The grain tolerance angle was set to 10° and the minimum grain size was set to that of the step size for each respective dataset.

Step 2 – Neighbour Orientation Correlation

This method is performed on data points with a CI less than a user defined value. If a particular point has a CI less than the minimum value, then the CIs' of the nearest neighbours are checked to find the neighbour with the highest CI. The orientation and CI of the particular point are reassigned to match the orientation and CI of the neighbour with the maximum CI. For all practical purposes, this method "closes" gaps inside grains without growing them into cracks or pores. The grain tolerance angle was set to 10°, the minimum CI was set to exclude low quality EBSPs (0.15 for all datasets) and the clean-up level was set to 4. This clean-up procedure was done multiple times until the number of data points changed per clean-up was reduced to <100pts.

Step 3 – Applying a confidence index threshold

This method applies a filter which effectively removes all data points that have a CI value lower than a user defined value. Misindexed points that were not cleaned up by step 2 (neighbour orientation correlation), as well as single, isolated pixels with faulty orientations,

are excluded from the dataset using this procedure. This method greatly reduces data points at and within grain boundaries, and helps reducing the number of scattered points within nonindexed phases. However, some misindexed pixels with relatively high CI values do occur throughout most of the datasets presented in this thesis.

Step 4 – Pseudosymmetry

Ol possesses pseudo-hexagonal symmetry along the *a*-axis (100) due to oxygen stacking (e.g. Fliervoet et al., 1999; Soustelle et al., 2010). Every map was thoroughly checked for systematic misindexing after applying the CI-threshold. Datasets that exhibited misindexing errors were cleaned up with rotations of 60° around (100) with a tolerance angle of 5° (55°-65°). Figure 18 displays the situation before and after applying this clean-up method.

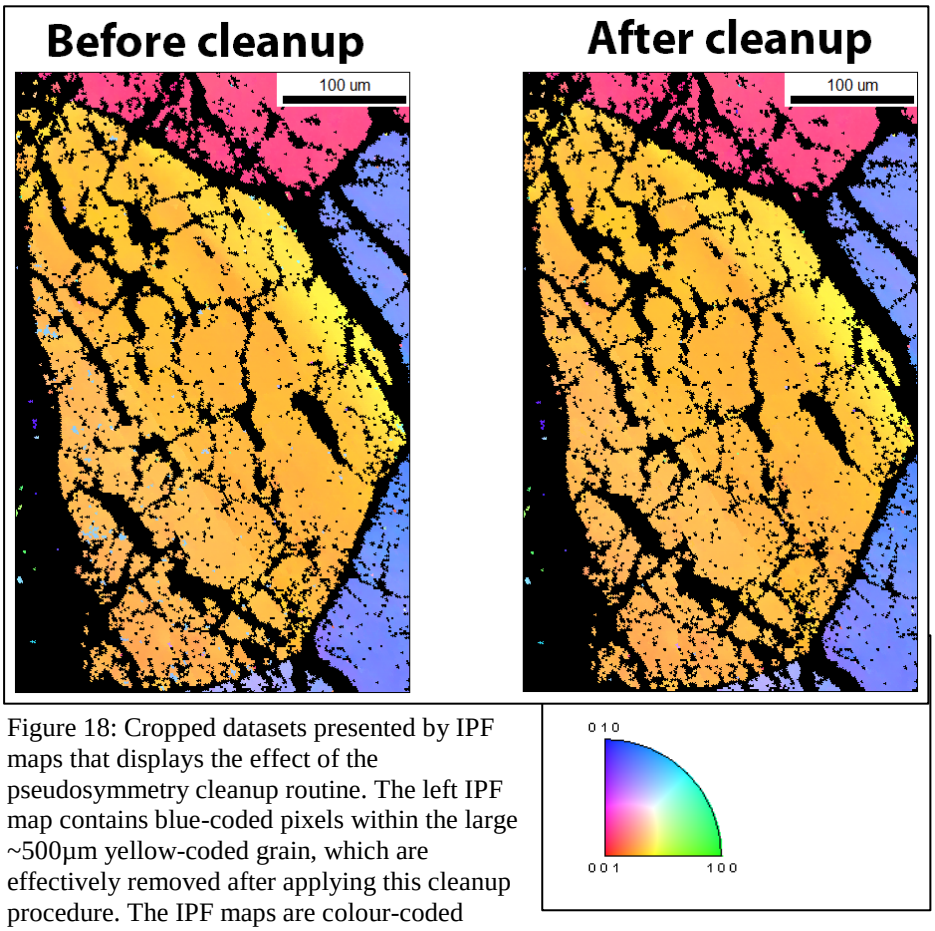

Figure 18: Cropped datasets presented by IPF maps that displays the effect of the pseudosymmetry cleanup routine. The left IPF map contains blue-coded pixels within the large ~500µm yellow-coded grain, which are effectively removed after applying this cleanup procedure. The IPF maps are colour-coded according to the unit triangle in the bottom right.

Specimen preparation

Samples COR-06-03D, COR-04-06 and COR-05-06C analysed with EBSD had been cut and prepared as polished thin sections prior to the work of this thesis. Other samples from 2003 and 2006, included here for textural descriptions, had also been cut and prepared as polished thin sections prior to the work of this thesis for Andersen and Austrheim (2006); Austrheim and Andersen (2004). Additional samples were collected in the field in autumn 2012 (COR-6/12 and COR-10/12), and were cut and prepared as polished thin sections at the Department of Geosciences, University of Oslo.

Due to the shallow penetration and ejection of BSE, additional preparation of samples has to be done prior to EBSD analyses. Samples need to have pristine crystal lattices which extend from the very surface in order to collect good quality EBSPs (e.g. Dingley and Randle, 1992). Chemical-mechanical polishing is required in order to remove the uppermost few µm of surface damage produced by mechanical polishing from preparing samples as polished thin sections (e.g. Mariani et al., 2008). This also helps smoothen the specimen surface even further – EBSD suffers from shadowing effects caused by topography due to the sample being tilted.

Chemical-mechanical polishing was done using colloidal silica, which combines the effect of mechanical polishing with etching. This was done on all samples prior to EBSD analyses. Samples were polished using SYTON® (colloidal silica), which is a mix of 30-50% 0.05µm suspended amorphous silica in 50-60% water (DuPont, 2005). The polishing cloth put to use had an abrasive size of 0.02µm. The total duration of polishing varied between samples. Due to the rough nature of mafic rocks they were polished for at least an hour, up to three hours. If there were difficulties obtaining EBSPs, multiple polishing runs were done.

EBSD specimen prep., University of Liverpool

Thin sections were carbon coated after polishing with SYTON®. In order to increase the conductivity between the sample and sample holder, a layer of colloidal graphite (graphite in a water-based solution) was applied onto the edges, and a few mm onto the top of the thin sections. These procedures were done in order to reduce/eliminate the effects of charging using high vacuum.

EBSD specimen prep., Forskningsparken, University of Oslo

The SEM used at FERMiO, Forskningsparken, had a coupled phosphor screen and camera mounted on a retractable arm, which was inserted for purposes of EBSD. In optimal position, at low working distance, the phosphor screen was very close to the sample mount. The width of a normal thin section exceeded the width of the sample mount, and the operator in charge requested that the thin sections were to be cut in half prior to analyses. Samples were cut by hand using a diamond-knife and re-polished with SYTON® in order to remove any added surface damage. After polishing, samples were glued to sample mounts using silver paint, and trails of silver paint were affixed from the sample mount onto the edges of the thin sections. This was done in order to reduce/eliminate charge at low vacuum conditions (e.g. Reed, 2005).

SEM specimen prep., Department of Geosciences, University of Oslo

The sample stuff from sample COR-04-06 was polished and subsequently oxidized in air for 40 min at 900°C in order to decorate dislocations and grain boundaries in ol (Karato, 1987; Kohlstedt et al., 1976). After oxidation the sample was cut and prepared as a polished thin section.

Samples investigated purely by BSE imaging were carbon coated and affixed to the sample mount using carbon tape. This was done in order to reduce effects of charging at high vacuum conditions (e.g. Reed, 2005).

Deformation mechanisms

Deformation in rocks is a process where grains change shapes and sizes. Information on deformation conditions, processes during deformation and properties after deformation can be obtained in microstructures preserved in deformed mineral grains (e.g. Vernon, 2004).

This chapter gives an overview of the current understanding on intracrystalline deformation mechanisms. The principles described here are used to recognize and interpret texture and microstructures in the Corsican peridotites and ultramafic pseudotachylytes. These are described and interpreted in chapter 5 and in chapter 6.

Viscous deformation

Viscous deformation is a process where rock undergoes permanent strain without loss of cohesion on grain scale. Thus, crystals deform without the formation of open cracks inside grains or along grain boundaries. The onset of viscous deformation is largely dependent on temperature, weakly so on confining pressure (e.g. Twiss and Moores, 2007). Viscous deformation in rocks can usually be described with a power-law rheology, where the strain rate is proportional to the differential stress with a power exponent from 1 to 5. Crystals deform internally without brittle fracturing by the movement of lattice defects, which are grouped into point defects and line defects (e.g. Passchier and Trouw, 2005; Twiss and Moores, 2007).

Diffusion creep

Point defects are missing or extra lattice points (molecules or atoms) known respectively as interstitials and vacancies, which presence or absence distort the crystal lattice (figure 19). In nature, vacancies are more common than interstitials because their formation requires lower energy (Vernon, 2004). The mobility and migration of these result in diffusive mass transport,

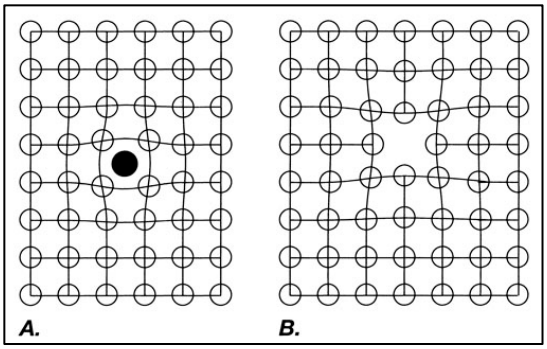

Figure 29: Point defects in a crystal lattice, distorting crystal structure. A) An interstitial, represented by the black circle. B) A vacancy, represented by the lack of an atom. From Twiss and Moores (2007).

known as *diffusion creep*. There are several types of processes that envelop diffusion creep, and all arises from thermal motions of atoms driven by a gradient in chemical activity (Passchier and Trouw, 2005). Thermal migration of atoms concern point defects, where interstitials flow towards surfaces of minimum stresses, and vacancies flow towards surfaces of maximum stresses (figure 20). The rate at which diffusion occur through material is a function of temperature (e.g. Vernon, 2004; Weertman and Weertman, 1975). Two main types of solid state diffusion creep processes can be distinguished. These are termed *Nabarro-Herring creep* and *Coble creep*. Additional diffusive processes are activated with the aid of a fluid phase, or if deformation occurs along grain boundaries accommodated by sliding.

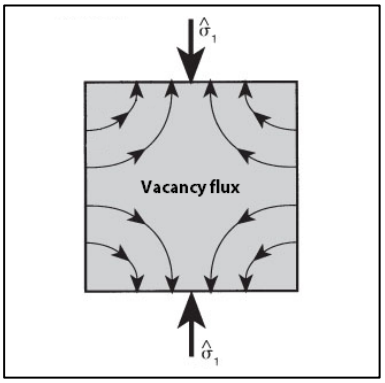

Figure 30: Migration paths for diffusion creep. Vacancies migrate towards surfaces of high stress, whereas point defects migrate in the opposite direction. From Twiss and Moores (2007).

Nabarro-Herring creep, also known as volume diffusion, concerns diffusion of atoms through crystal lattices like that explained above. If a differential stress is applied to a crystal, vacancies are generated at interfaces of lower compressive stress, and migrate towards the areas of higher compressive stress where they are destroyed (Twiss and Moores, 2007). Nabarro-Herring creep is only effective on high homologous temperatures. For ol, this type of mechanism is considered to exclusively occur as the homologous temperature (T/T_m) approaches 1 (e.g. Weertman and Weertman, 1975).

Coble creep, also known as grain boundary diffusion, acts on the same principle as Nabarro-Herring creep although diffusion also occurs along grain boundaries. Diffusion along grain boundaries is more rapid than through a crystal lattice (Vernon, 2004). The activation energy for this type of creep is roughly two thirds that for Nabarro-herring creep, and is consequently activated on lower temperatures than Nabarro-Herring creep (Twiss and Moores, 2007).

Another type of diffusive mechanism is activated during high compressive stresses with the aid of an intergranular fluid. This type of diffusion is called ***solution creep***. Solution creep is in principle very similar to that of coble creep, although diffusion occurs by dissolving mineral grains at faces under high compressive stresses. These subsequently diffuse through a fluid phase that wet grain boundaries, rather than diffusion on the grain boundaries themselves (Twiss and Moores, 2007). Thus, this process can be activated at even lower temperatures. With the presence of fluid this mechanism dominates over coble creep, and the rate of diffusion is greatly enhanced (Vernon, 2004). If deformation occurs by sliding on grain boundaries, with no voids in between grains, grains may change shape accommodated by diffusion. This type of diffusion is called ***grain boundary sliding*** or superplasticity (e.g. Twiss and Moores, 2007).

The grain sizes needed diffusive mechanisms to occur is considered to be relatively small, since progressive deformation by this mechanism increases the pathways for diffusion, hence slowing down the diffusive process (e.g. Passchier and Trouw, 2005; Vernon, 2004). They are considered grain-size dependent mechanisms, and diffusive mass transport mainly occurs at low stresses and at high temperatures (Twiss and Moores, 2007).

Dislocation creep

At moderate to high stress regimes, crystal lattices deform by the movement of line defects. Line defects arise from shearing one lattice point at a time along a glide plane. Shearing an entire row at a time would require unrealistic stresses, since all atoms above the glide plane would have to be lifted at the same time before settling at the next lattice site (e.g. Wenk and Bulakh, 2008). The process of shearing one lattice point at a time introduces *dislocations* which separates sheared from unsheared parts of the lattice (e.g. Passchier and Trouw, 2005). Thus, dislocations are parts of the crystal which does not match the ideal configuration of the respective mineral. A permanent change in shape is achieved by the movement of these defects through the crystal, by a change in the relative positions of molecules or atoms. The motion of dislocations is probably the most important mechanism for producing ductile deformation in crystalline materials (e.g. Passchier and Trouw, 2005; Twiss and Moores, 2007; Vernon, 2004; Wenk and Bulakh, 2008).

Dislocation geometry

There are two principle types of linear defects that occur in crystal lattices; edge and screw dislocations (e.g. Passchier and Trouw, 2005). These can interconnect in dislocation loops (figure 21). Both types of dislocations mark the boundary between sheared and unsheared part

of the lattice, called a dislocation line. Edge dislocations manifests as an extra half lattice plane in the crystal. Screw dislocations exist where part of a crystal is displaced over one lattice distance, and is therefore twisted. These types of dislocations are distinguished by whether the sheared part of the crystal has moved perpendicular or parallel to the dislocation line (e.g. Wenk and Bulakh, 2008).

Both types of dislocations are characterized by a Burgers vector (b) which indicates the direction and minimum amount of lattice displacement. The Burgers vector is parallel to the glide plane, perpendicular to an edge dislocation, and parallel to a screw dislocation (figure 21). Because a dislocation line marks the boundary on a glide plane between slipped and unslipped portions of the crystal lattice, it cannot simply stop inside the crystal (Passchier and Trouw, 2005). It must either continue to the edge of the crystal where it ends at a step in the lattice, or it must form a closed system within the crystal called a dislocation loop, such as in figure 21, in which edge and screw dislocations are interconnected.

Curvature of a dislocation results from offsets along the dislocation line. The offsets can be short segments of edge dislocation type, called jogs, in a screw dislocation or short segments of screw dislocation type, called kinks, in an edge dislocation (e.g. Twiss and Moores, 2007).

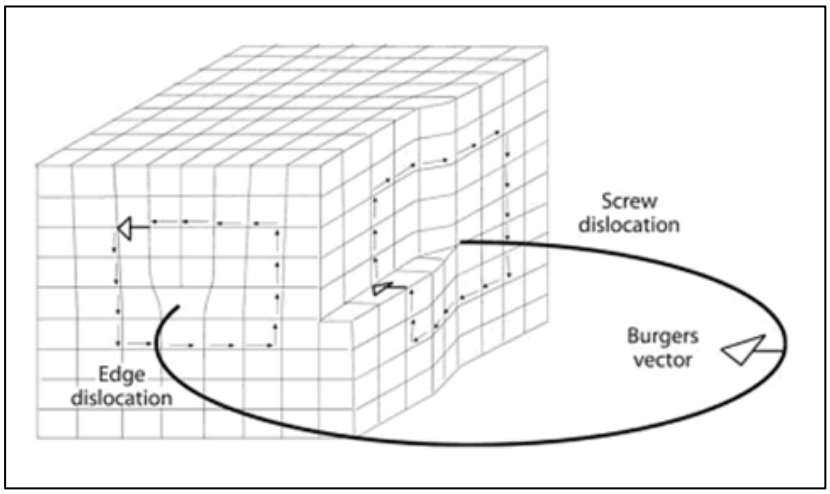

Figure 21: A dislocation loop displaying simple dislocation geometry. The dislocation line is indicated as the black solid circle, and the direction of the Burgers vector with open arrows. Edge dislocations are extra half lattice planes in the crystal, perpendicular to the dislocation line. Screw dislocations produce a helical surface around the dislocation line, and can be of a left or right character. From Passchier and Trouw (2005).

The motion of dislocations

Ductile deformation can occur in crystal lattices by the propagation of tremendous numbers of dislocations through the lattice, prompting permanent change in the shape of the crystal,

without destroying the solid crystalline structure. Intracrystalline deformation by glide of dislocations alone is known as dislocation glide (e.g. Passchier and Trouw, 2005).

The events in which bonds are switched occur all along the dislocation line and are accompanied by propagating kinks or jogs along it (e.g. Passchier and Trouw, 2005; Twiss and Moores, 2007). A set of parallel slip planes, coupled with a slip direction, is together known as a *slip system* (figure 22).

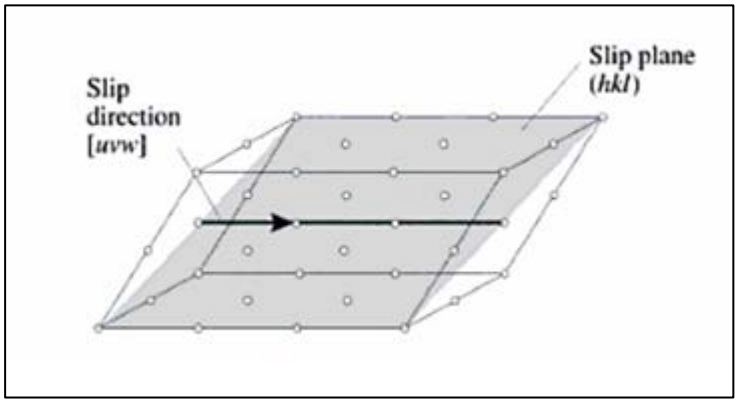

Figure 22: Slip direction [uvw] and slip plane (hkl) defining a slip system. From Wenk and Bulakh (2008).

When an axial force is applied (F) to a crystal in a cross-sectional area (A), only that component of F that is resolved on the slip plane (A cos ψ) and in the slip direction (cos λ) causes shear deformation, leading to a relationship for the resolved shear stress (τ) by following Rosbaud and Schmid (1925);

$$\tau = \left(\frac{F}{A}\right) \cos\psi \cos\lambda \qquad \text{(Equation 6)}$$

Deformation only occurs if the resolved shear stress reaches a critical value (τ_c). This is referred to as the critical resolved shear stress (CRSS). The type of slip system(s) that will be active in a crystal depends on the magnitude of a CRSS necessary to move a dislocation, and on the magnitude of the stress field in the grain (Passchier and Trouw, 2005).

The magnitude of the CRSS is strongly dependent on temperature, but is also influenced by strain rate, differential stress and the chemical activity of components that influence the strength of specific bonds in a crystal, such as volatiles and water (e.g. Passchier and Trouw, 2005; Wenk and Bulakh, 2008).

A slip system is defined by a slip plane and a direction of slip (the Burgers vector) within this plane, as indicated on figure 22. These elements are indicated by Miller indices of the slip

vector followed by the indices of the plane (e.g. Vernon, 2004). For any specific plane and direction, the notation [direction](plane) is used in this thesis. Different minerals activate different slip systems according to their dependence on factors described above. As a result, the type of dominant slip system that is active in a crystal changes with metamorphic condition, and the configuration of stress (e.g. Passchier and Trouw, 2005).

Ol has a very complex behaviour that is strongly dependant on temperature. Classic experimental deformation of ol were conducted by Ave'Lallemant and Carter (1970), and they proposed that activated slip systems follows a linear relationship between temperature and strain rate. Their results are presented in figure 23.

The experimentally determined activation of slip systems in ol are further discussed in chapter 6. More recent studies has shown that the slip systems presented on figure 23 can activate under a wide range of conditions (e.g. Jung et al., 2006; Karato and Jung, 2003; Katayama and Karato, 2006; Tommasi et al., 2000).

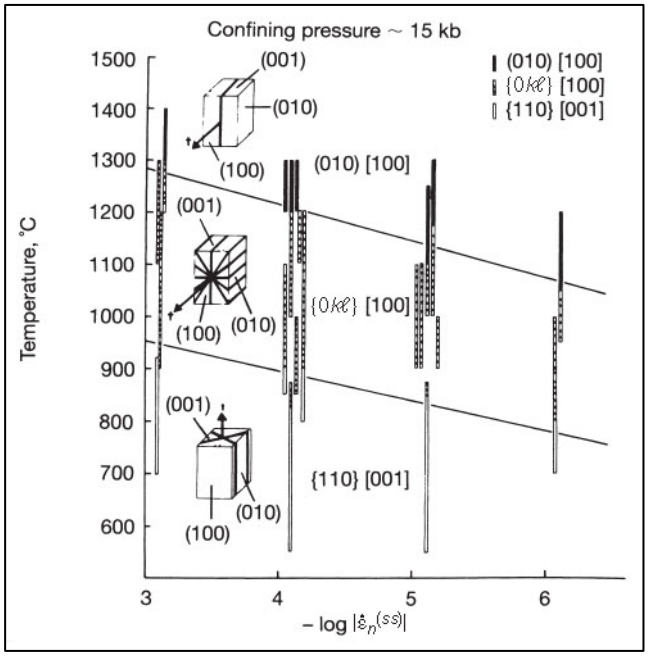

Figure 24: Experimentally derived slip systems that operate in ol as a function of temperature and strain rate at 1,5GPa. The blocks represent ol crystals on which active slip planes (solid lines) and slip directions (arrows) are indicated. From Ave'Lallemant and Carter (1970).

Edge dislocations glide only on planes that contain both the dislocation line and the Burgers vector. When different concurrent activated slip systems intersect in a crystal, such as that encountered in the temperature range of ~900- ~1200 °C on figure 23, or when dislocations are pinned by secondary phases in the crystal lattice, migrating dislocations may become

entangled and obstruct further movement (e.g. Wenk and Bulakh, 2008). Such tangles may inhibit deformation by building up a pile of dislocations behind the pinned front, working as a strain hardening mechanism (Passchier and Trouw, 2005). However, they can leave the original glide plane by adding or subtracting atoms from the edge of the extra half-plane in a process known as dislocation climb. This effectively displaces the dislocation, and allows it to bypass blocked sites. The combined processes of dislocation glide and dislocation climb is known as *dislocation creep*. Deformation used to describe deformation by dislocation creep is termed *crystal-plastic deformation* (e.g. Passchier and Trouw, 2005; Vernon, 2004).

Crystal-plastic deformation mainly occurs under moderate to high stress regimes, and is a grain size insensitive deformation mechanism since dislocations may form in minerals of all sizes (e.g. Twiss and Moores, 2007).

Dislocation generation and annihilation

A crystal can be imagined to possess a certain amount of internal strain energy, which is at its minimum when the lattice is free of dislocations (Passchier and Trouw, 2005). When applying deformation, dislocations are introduced to the lattice and the internal strain energy is increased by local changes in the distance between atoms. The increase in internal energy is proportional to the increase in total length of dislocations per volume of crystalline material, also known as the *dislocation density* (e.g. Twiss and Moores, 2007).

One would imagine that when propagating dislocations eventually deposit an extra half-plane at one edge of the crystal lattice, the dislocation density would progressively reduce during deformation. Thus, in order to sustain an arbitrary amount of ductile deformation there must be some kind of mechanism for generating dislocations (Twiss and Moores, 2007). A common mechanism is called the *Frank-Read source* (Frank, 1980) in which a nucleating

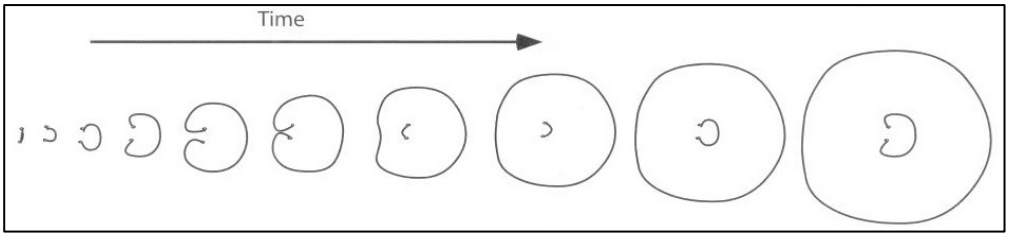

Figure 24: Schematic illustration of a Frank-Read source that multiplies dislocations around obstacles. A dislocation segment pinned on both ends, with the Burgers vector in the plane of the solid line, is displaced under influence of a differential stress in the crystal. With increasing shear stress on the crystal, the dislocation tends to bow out more and more from the pinning points, eventually pivoting around them and annihilates upon closure. By this process all of the material within the dislocation loop has slipped one lattice spacing, and a dislocation segment is left between the original points. From Passchier and Trouw (2005).

dislocation is pinned on both ends, and starts propagating in a bulging fashion. It eventually forms a dislocation loop with the original dislocation segment preserved (figure 24). With many sources such as this operating throughout a crystal there is potential for continuous creation of new defects (e.g. Twiss and Moores, 2007).

Crystal lattices have an overall tendency to adopt low-energy configurations, which provides an effective force that governs the systematic movement of migrating and newly created dislocations (Passchier and Trouw, 2005). During deformation, dislocation generation and annihilation will operate in junction to minimize the total free energy in the system. Dislocation generation and annihilation mechanisms such as Frank-Read sources and dislocation creep, respectively, will compete until deformation stops. Dislocation annihilation will progress towards an equilibrium situation after deformation has stopped (Passchier and Trouw, 2005). Two umbrella terms called *recovery* and *recrystallization* is commonly used to cover mechanisms that help reduce dislocation density.

Recovery and recrystallization

In response to recovery, dislocations tend to concentrate in planar zones in a crystal. In this configuration the dislocation density is decreased in other parts of the lattice (e.g. Wenk and Bulakh, 2008). As previously outlined, one of the most important processes for annihilating dislocations is the climb of edge dislocations. Figure 25 displays migration paths related to recovery. The onset of recovery often manifests as zones in the crystal that have approximately uniform extinction, that grade into other similar crystal sectors with slightly different orientations. These transitional zones are known as deformation bands, and can be

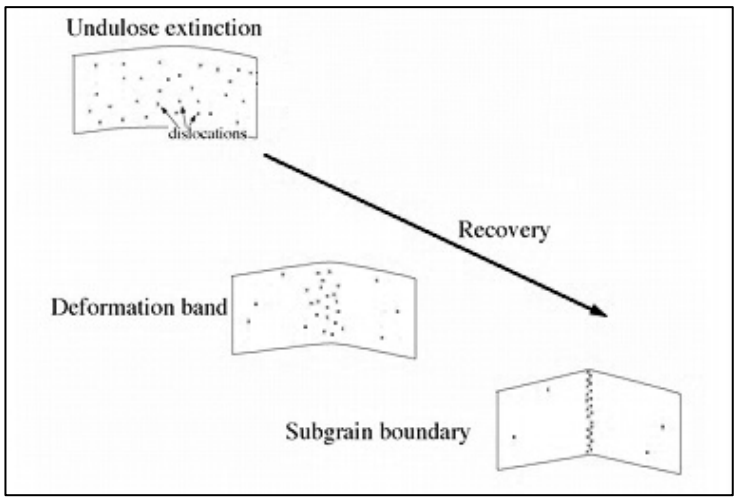

Figure 25: Schematic illustration of processes related to recovery, starting from undulose extinction in the upper left. With increasing grade of recovery, dislocations are concentrated in deformation bands and eventually in subgrain boundaries. Modified from Passchier and Trouw (2005).

regarded as an early stage of reorganizing equally distributed dislocations (Passchier and Trouw, 2005). A common process of higher order recovery is the arrangement of edge dislocations of the same sign on different parallel slip planes into dislocation walls that align dislocations over one another. These networks are known as *tilt walls* or *subgrain boundaries* (e.g. Passchier and Trouw, 2005; Twiss and Moores, 2007).

Such boundaries separate crystal fragments known as subgrains. These can be equant or elongate, and are slightly misoriented with respect to the crystal lattice of the host grain by discrete, sharp, low relief boundaries. These misorientations are usually small (<5°), where the greater the density of dislocations in a subgrain wall, the larger the angle of tilt (e.g. Vernon, 2004). During progressive deformation, these boundaries can become larger due to a continuous increase in density of dislocations within the wall, and marks the onset of one out of several processes of recrystallization. Recrystallization is called dynamic if it is synchronous with deformation and static if it occurs in the absence of deformation. There are in principle three different mechanisms of recrystallization that can operate during deformation, depending on temperature and/or flow stress (e.g. Twiss and Moores, 2007). These processes are schematically displayed on figure 26 and will be reviewed in the following sections.

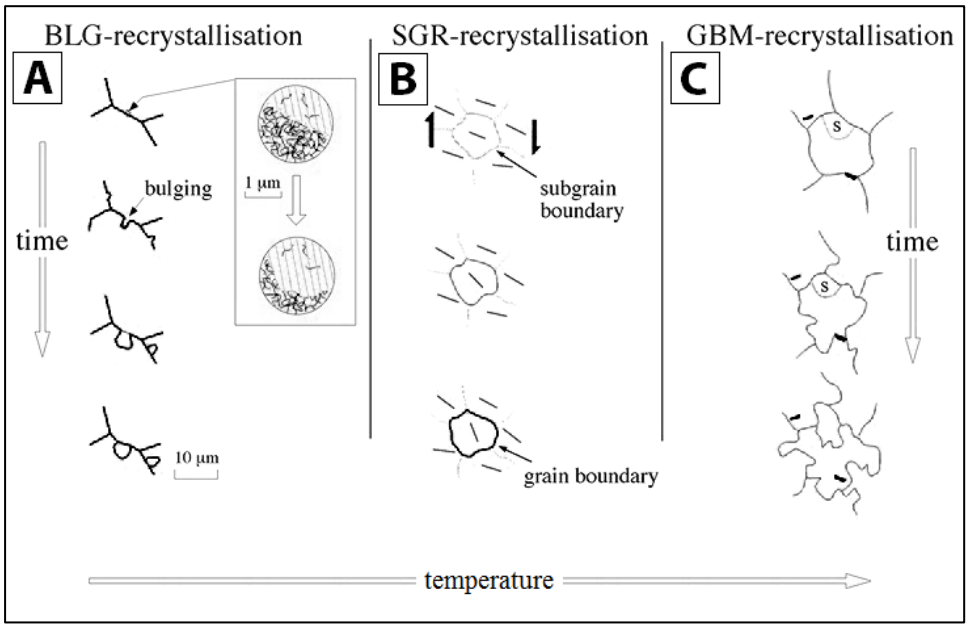

Figure 26: Schematic illustration of three mechanisms of recrystallization, as a function of time and temperature. A) Bulging (BLG) recrystallization. The upper grain migrates into the lower, more strained grain indicated by the boxed area. This mechanism eventually leaves new, unstrained grains on the grain boundary between the two. B) Subgrain rotation (SGR) recrystallization where diffuse lines indicate subgrain boundaries and solid lines indicate grain boundaries. Bars in the subgrains indicate lattice orientation. C) High temperature grain boundary migration (GBM) where grain boundaries are represented as solid lines and a subgrain is noted with (s). See text for explanations. Modified from Passchier and Trouw (2005).

In general, recrystallization is a way of reorganizing material assisted by a change in grain size, shape and orientation within the same mineral without altering its chemical composition (e.g. Vernon, 2004). One of these is a process that occurs when dislocations are continuously added to subgrain boundaries, increasing the angle of tilt as described above. In such cases, the angle that define the subgrain relative to the host grain increases to an extent where the subgrain can no longer be classified as part of the same grain. By definition, any subgrain wall that has progressively developed an angle greater than 10° is regarded as a new grain (neoblast) in a process called *subgrain rotation (SGR) recrystallization* (e.g. Passchier and Trouw, 2005; Twiss and Moores, 2007). After this amount of lattice rotation the grain boundary is no longer represented by a dislocation wall (figure 26, B). The implication of forming new, isolated grains is that the newly formed high-angle boundary is very mobile and allows atoms or ions to transfer across them, to the contrary of immobile subgrain boundaries (Vernon, 2004).

Working at slightly different conditions than SGR-recrystallization is a type of recrystallization where grain boundaries themselves start migrating. In the case of two adjacent crystals where one has a high dislocation density and the other a low dislocation density, material in the unstrained crystal may cross the grain boundary and add to the strained crystal (e.g. Twiss and Moores, 2007). In this way the grain boundary migrates into the more strained region and leaves unstrained, newly migrated domains behind it. This will locally displace the grain boundary on expense of the strained crystal. The implication of this type of recrystallization is that the grain boundary that separate the two crystals may increase in length, hence increasing the total free energy of the crystal aggregate, but is cancelled and outpaced by the total free energy lost by the removal of dislocations (Passchier and Trouw, 2005).

There are two types of recrystallization that involve the movement of grain boundaries, working at both lower and higher temperatures than SGR-recrystallization. The low-end temperature process is called *bulging (BLG) recrystallization* (figure 26, A). It occurs during high strain rate and concerns a type of highly localized grain boundary mobility (Passchier and Trouw, 2005). It is characterized by small independent ‘bulges’ along the grain boundary that are separated from the host grain to form subgrain boundaries, eventually evolving into grain boundaries (figure 26, A). The process can also occur or by the migration of a true grain boundary (Twiss and Moores, 2007). BLG recrystallization mostly occurs along the boundaries of old grains and at triple junctions (Passchier and Trouw, 2005).

At relatively high temperatures, grain boundary mobility increases to an extent where entire grains and its subgrains can be consumed by advancing grain boundaries sweeping in all directions (Twiss and Moores, 2007). This is called *high temperature grain boundary migration (GBM)* and is commonly active at the same time as SGR recrystallization, but once true grain boundaries have developed these may also become highly mobile (figure 26, C) (Vernon, 2004).

Lattice preferred orientations

In many deformed rocks the lattice orientation of crystals is not randomly distributed, but arranged in a systematic way (Passchier and Trouw, 2005). Deformation by dislocation glide and dislocation creep initiates slip systems, as described above, that produce characteristic *lattice preferred orientation (LPO)* for specific minerals (e.g. Mainprice and Nicolas, 1989; Tullis, 1977). LPO is progressively amplified due to rotation of individual crystals towards an orientation as a result of slip on their particular slip systems (figure 27).

A larger amount of rotation means a higher order of LPO. The pattern LPO that develops for a particular mineral in an initially randomly oriented polycrystalline aggregate, depends on the slip systems that are active during formation, and on the geometry of the externally applied deformation (e.g. Twiss and Moores, 2007). Coaxial deformation produces fabrics that are symmetric with respect to the principal axes of finite strain, whereas noncoaxial deformation tends to produce asymmetric fabrics.

The type of slip system(s) that will be active depends on their CRSS, which is in turn dependent on metamorphic and deformational condition (e.g. Passchier and Trouw, 2005). Usually, more than one slip system can operate in a mineral and the CRSS of each slip system changes with temperature and chemical activity of certain components, as previously outlined.

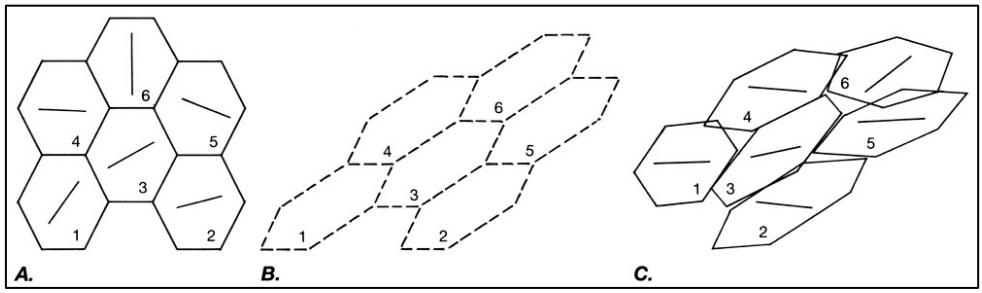

Figure 27: Schematic illustration of producing LPO in crystals. A) An undeformed polycrystal where the lines in each crystal show the orientation of a single slip plane. The slip direction is in the plane of the diagram. B) The form of the polycrystal, given that it deformed homogeneously. C) An approximation of the homogeneous form of the deformation given that the crystal glide on the single slip plane indicated in A. From Etchecopar and Vasseur (1987).

Over time, these conditions may change thereby producing unique fabrics for each scenario. Commonly, LPO give information on the finite strain (Schmid, 1994). LPO patterns can be modified by both dynamic and static recrystallization based on the activity of sweeping grain boundaries, as well as from nucleation of new grains (e.g. Humphreys and Hatherley, 1995; Jessell, 1987; Shelley, 1979).

In general, the strength of crystallographic preferred orientation increases with increasing strain at constant flow parameters and temperature (Lister and Hobbs, 1980). Deformation by diffusion creep does not produce preferred orientations because it is not associated with any preferred plane or orientation in crystals. Because of this, diffusion creep will distort and eventually randomize pre-existing LPO if it works as the dominant deformation mechanism after arrangement of dislocations by creep

LPO is distinguished from shape preferred orientation (SPO) because grains deformed under dislocation creep are not considered passive spheres, and will deform according to which slip planes are active. SPO is easily overprinted and only contain information of the finite strain (Passchier and Trouw, 2005).

Twinning and kinking

Some minerals deform by *mechanical twinning*, also known as deformation twinning, in addition to dislocation creep and glide (e.g. Egydio-Silva and Mainprice, 1999; Jensen and Starkey, 1985). Twinning always operates in specific crystallographic directions, and is characterized as wedge-shaped segments in a mineral grain which orientation deviates from that of the host. Twinned structures may be related to the original structure by a mirror reflection across the twin plane, or by rotation of the original structure about an axis normal to the twin plane (Twiss and Moores, 2007; Wenk and Bulakh, 2008). Kinking resembles twinning, but is not limited to specific crystallographic directions. It typically operates in crystals with one or few individual slip systems.

In general, both kinking and twinning occur in the lower temperature range of deformation, and can only accommodate a limited amount of strain (Passchier and Trouw, 2005).

3. Geological setting

General Corsican geology

Corsica is located in the northern corner of the Western Mediterranean between two Cenozoic oceanic basins, the Liguro-Provencal to the west and the Tyrrhenian Sea to the east (figure 28). Corsica is subdivided into two principal geological domains; the western Hercynian Corsica and an eastern Alpine Corsica. Corsica and Sardinia together are traditionally regarded as a microblock between the southern France and Northern Iberia until Middle Oligocene, when rifting and eastward drifting in the Liguro-Provencal basin took place (Rollet et al., 2002). The western Hercynian Corsica is correlated with the Maures-Esterel basement in southern France, whereas Alpine Corsica is often regarded as the southern extension of the western Alps, through the Western Liguria and Voltri Group Alpine Units (e.g. Durand-Delga et al., 1997; Jolivet et al., 2003).

Hercynian Corsica comprises mostly intrusive and volcanic rocks. These intruded into mid Paleozoic (Ordovician-Silurian) basement of migmatittic orthogneisses which are the oldest rocks on the island (Rossi and Rouire, 1980). These rocks are occasionally exposed as undifferentiated pockets along the geographically central domain of the island, isolated by a series of plutonic intrusions and associated volcanic and volcano-sedimentary covers. The intrusions are Carboniferous to Permian granitoids, associated with Permian volcano-sedimentary sequences that together constitute the dominant portion of the western side of the island (Malavieille et al., 2011). These rocks are only slightly affected by Alpine deformation and also include a reduced and incomplete Mesozoic to Mid-Eocene sedimentary cover (Michard and Martinotti, 2002).

The transition between Hercynian and Alpine Corsica occur along the Balagne ophiolite section consisting of unmetamorphosed pillow lavas (figure 29). A thin autochthonous cover on the Hercynian basement can be found along the Alpine front (e.g. Malavieille et al., 2011). The Tenda massif (figure 29) is one of several imbricated slices of Corsican-derived continental crust that rests directly upon more pristine granitoids (Molli et al., 2006). The eastern termination of this sliver marks the East Tenda Shear Zone (ETSZ) (figure 28 and figure 29) and the lateral transition between Hercynian basement, reworked massifs and the high pressure low temperature (HP-LT) Ligurian Alpine Corsica (Malavieille et al., 2011). The Tenda massif and the ETSZ locally contains relict HP-LT fabrics in form of blueschist assemblages, but are dominantly characterized by greenschist-facies exhumation-related tectonites (e.g. Jolivet et al., 1990; Maggi et al., 2012; Molli and Tribuzio, 2004).

Alpine Corsica can roughly be divided into two separate units. The lowermost unit named the 'Schistes Lustrés' is a variably metamorphosed composite nappe derived from the Western Tethys, which also crops out in the western Alps (Jolivet et al., 1990; Lahondere and Guerrot, 1997; Molli, 2008). It includes variably altered mantle ultramafics, gabbros, pillow lavas and associated metasediments, with imbricated slices of European continental crust. This unit is largely characterized by subduction related metamorphism and deformation during the Alpine orogeny (e.g. Fournier et al., 1991; Jolivet et al., 2003). Prograde metamorphism ranged from low-grade blueschist to lws-eclogite and variable degree of retrogression at greenschist facies conditions (Brovarone et al., 2011b; Brunet et al., 2000; Fournier et al., 1991).

The second unit comprises the uppermost low to nonmetamorphosed 'Nappe Supérieure.' This nappe includes the Balagne, Macinaggio and Nebbio sequences (figure 29). These are ophiolites with attached continental-derived calciferous and siliciclastic flysch (Malavieille et al., 2011). This nappe and its contacts with the underlying units are locally unconformably sealed by lower Miocene sediments of the St. Florent, Aleria and Francardo basins (e.g. Cavazza et al., 2001; Egal, 1992).

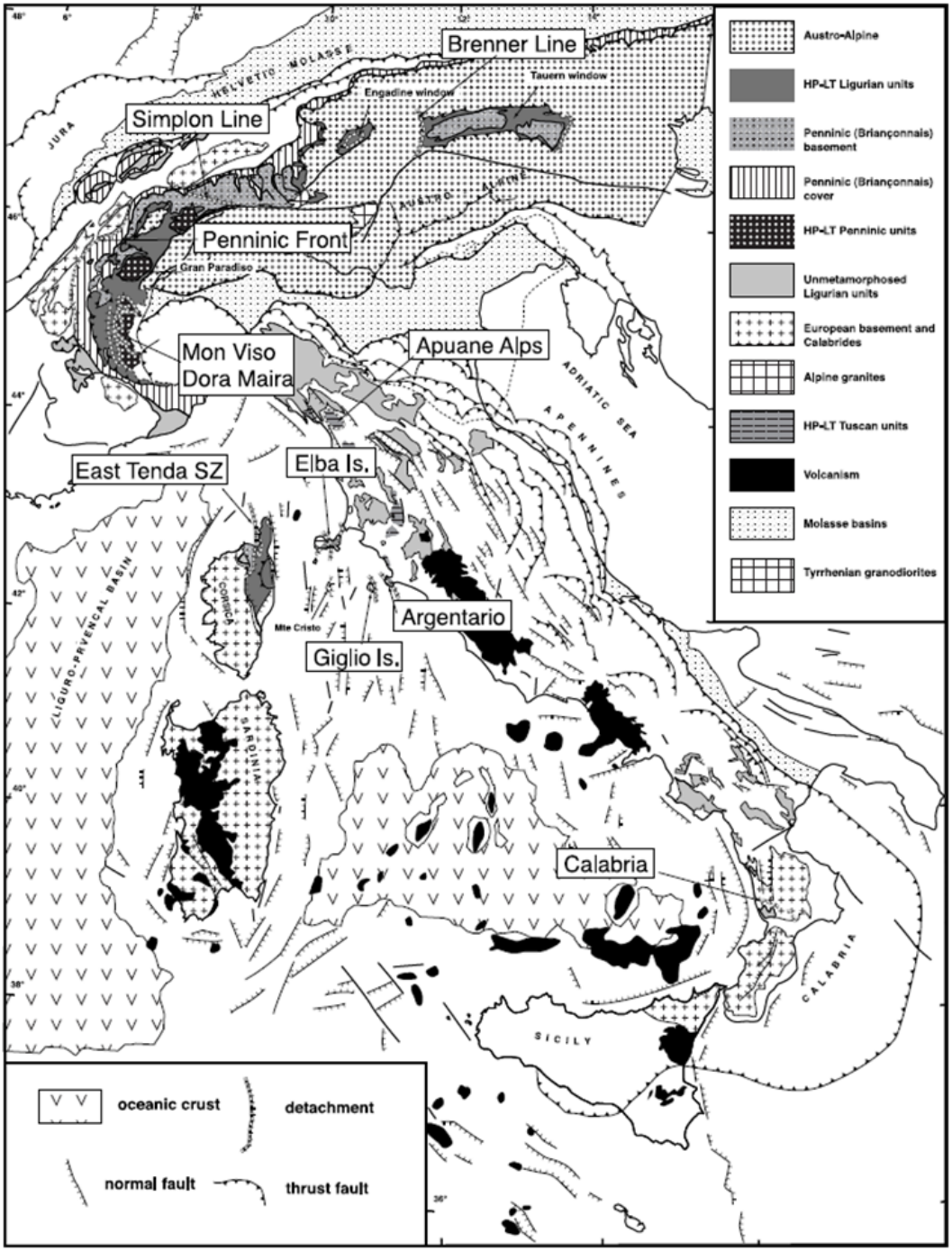

Figure 28: Tectonic map of the Alpine-Tyrrhenian region. From Jolivet et al. (2003).

Alpine Corsican geology

The pseudotachylytes described in this study are located in the HP-LT complex of Alpine Corsica, in the Schistes Lustrès unit (Austrheim and Andersen, 2004). Similar HP-LT terrains are found on the other flank of the Tyrrhenian Sea, in the Tuscan archipelago and the Calabrides (figure 28), altogether considered a southern prolongation of the Alps (Jolivet et al., 2003). The pseudotachylytes in the Schistes Lustrés unit occur in blueschist to eclogite facies ophiolite gabbro and mantle peridotite, on the south-southwestern slope of Cima di Gratera at Cape Corse. Figure 29 displays simplified tectonic and tectono-metamorphic maps of Alpine Corsica and a schematic geological cross-section demonstrating the position of the main units (Malavieille et al., 2011).

The Schistes Lustrés unit is structurally juxtaposed on the eastern Corsican margin and consists of several thrust sheets folded in an open antiform-synform pair (figure 29). These trend roughly N-S and has an amplitude of about 5 km. The eastern constituent has developed in a doubly plunging axial depression along the 50 km long Cap Corse-Castagniccia antiform (Malavieille et al., 2011). The western synform, where the Nebbio sequence is located, rests directly upon the ETSZ. Both limbs of the Cap Corse-Castagniccia antiform have been reworked by high angle normal faults that are responsible for a steep regional morphology. Within the antiform, four distinct lithological assemblages can be recognized from top to bottom; descriptions from Brovarone et al. (2011b); Malavieille et al. (2011); Ravna et al. (2010).

(1) – An ep-blueschist, distal oceanic unit mainly consisting of ophiolites and associated metasediments with minor continent-derived slices. These rocks are exposed along the two limbs of the antiform.

(2) – A lws-blueschist unit that is largely characterized by metaophiolites and metasediments. It contains a greater fraction of slices of continental crust than the uppermost unit. This unit contains vast volumes of serpentinites enveloping local pockets of metagabbros and peridotites, which hosts pseudotachylytes at Cima di Gratera.

(3) – A lws-eclogite unit of metaophiolites coupled with slices of continental crust and associated metasediments. These are exposed along Défile du Lancône and in Monte San Petrone.

(4) – The lowermost position consists of car-bearing metasediments which crops out in the axial culminations of the northern- and southern Cap Corse-Castagniccia antiform.

All Alpine Corsican units display HP-LT metamorphism attesting their involvement in subduction to different depths, with increasing grade from the west to the east (Brovarone et al., 2011b). The dominant fabric in the Tenda massif is greenschist facies exhumation-related tectonites, but it locally contains relict blueschist assemblages within its internal regions and along the ESTZ (Maggi et al., 2012). The peak metamorphic conditions in the Cap Corse Alpine region are recorded by lws-eclogites cropping out in (3) at Défile du Lancône. P-T conditions are controversial but suggested to have been stable within a window ranging from 335-420°C at 1.9-2.6GPa (Ravna et al., 2010) and 500-540 °C at 2.3GPa (Brovarone et al., 2011b). These temperature estimates are important for determining the minimum temperature-rise (ΔT) in relation to the formation of pseudotachylytes (see section on previous work).

The age of the earliest metamorphic event related to eclogitisation is not properly constrained, and extends from the Late Cretaceous (Sm-Nd of 84 ± 5Ma) (Lahondere and Guerrot, 1997) to the Early-Mid Eocene (U-Pb of 53.7 ± 7.7Ma) (Maggi et al., 2012) with intermediate values from Early Paleocene to Early Eocene (Ar^{40}/Ar^{39} of 65-55Ma) (Brunet et al., 2000).

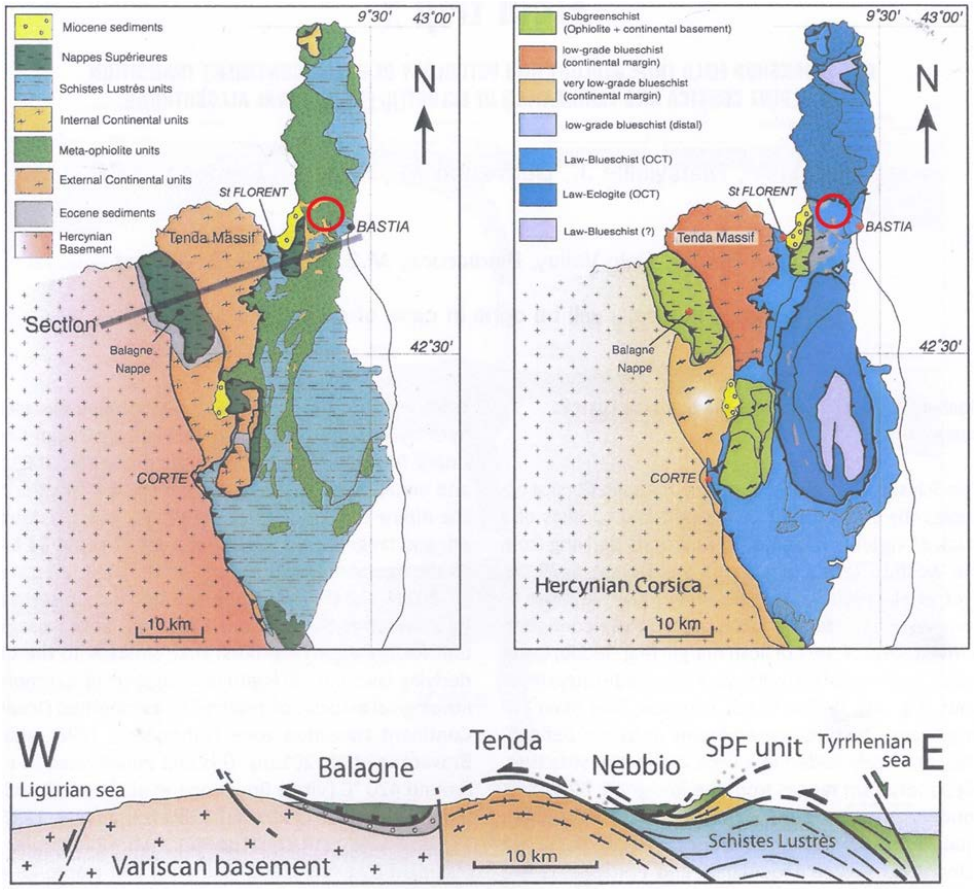

Figure 29: Simplified tectonic (left) and tectono-metamorphic (right) maps of Alpine Corsica and related schematic geological cross-section. The red circle marks the occurrence of the studied ultramafic pseudotachylytes. Modified from Malavieille et al. (2011).

The syn-high-pressure kinematic indicators and structures are mostly associated with an E-W direction of transport. These display dominant top-to-the-west shear sense and can be observed all along the boundary between the Hercynian and Alpine Corsica (e.g. Egal and Caron, 1988; Fournier et al., 1991).

Tectonic constraints

The present geometry and metamorphic conditions of the Corsican nappe stack provide first order constraints on the role of the Corsican segment of the European continental margin prior to, and during the initial stages of the Alpine orogenic history (Mattauer and Proust, 1975). The lithological association of ophiolitic and continental basement rocks in Alpine Corsica, also extensively documented in the Western Alps, has recently been attributed to the more distal part of a fossil Tethyan inherited Ocean-Continent Transition Zone (OCTZ) (figure 30) (Brovarone et al., 2011a; Mohn et al., 2010). This type of margin is characterized by continental and oceanic lithosphere separated by extensive regions of exhumed mantle, locally overlain by continental extensional allochtons (Lavier and Manatschal, 2006; Peron-Pinvidic and Manatschal, 2009). This is similar to what is observed in the lithological units (2) and (3) in the Cap Corse-Castagniccia antiform.

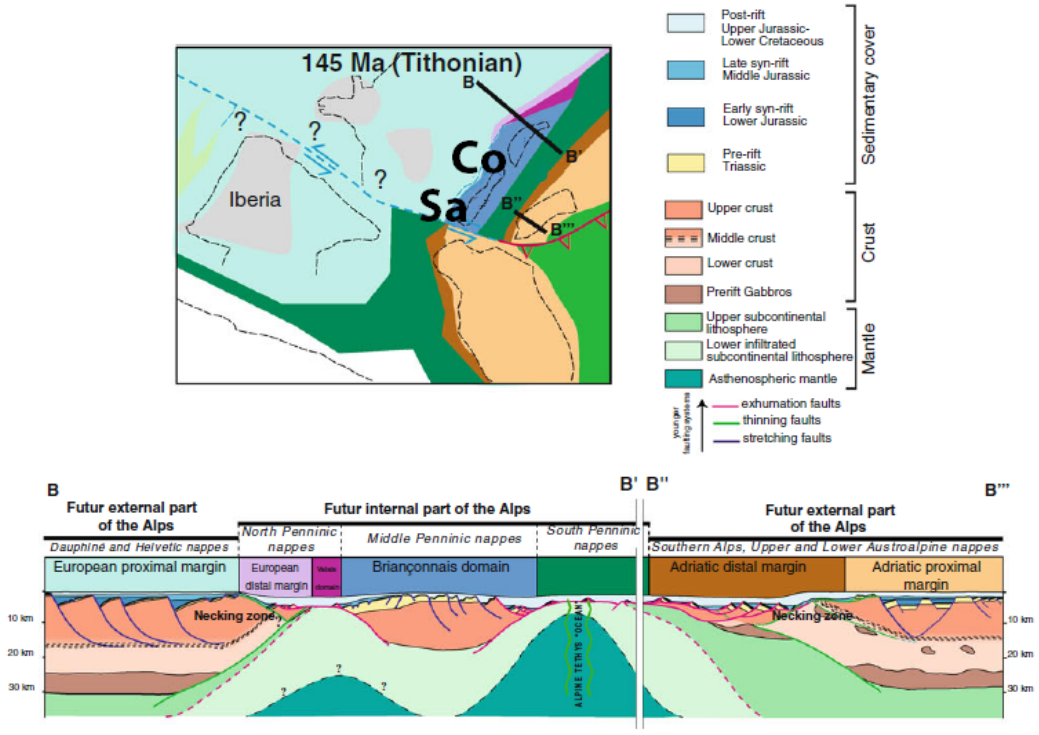

Figure 30: The distribution of major Alpine tectonic units and their paleogeographic position during late Jurassic (Tithonian). Corsica and Sardinia is marked as Co and Sa, respectively. The cross sections shows the late Jurassic crustal structure through the Alpine Tethys along the marked sections B-B' and B''-B'''. Modified from (Mohn et al., 2010).

The convergence between the margins of Adria and Europe suggests progressive underthrusting of the Ligurian oceanic lithosphere and the distal European continental margin in a framework of east-dipping subduction (figure 30) (e.g. Malavieille et al., 2011; Mattauer and Proust, 1975; Molli et al., 2006). A possible scenario, following Ravna et al. (2010) is shown on figure 31 that starts in the late Cretaceous. Austrheim and Andersen (2004) attributed formation of the pseudotachylytes in the Cima di Gratera area to this subduction. The event of eastward subduction ended with the arrival of thick Corsican crust blocking subduction during Eocene (Molli, 2008).

From the Eocene and onward the Adria plate started subducting, forcing Ligurian slab tearing, flip in subduction polarity and a reorganization of the accretionary complex. Units undergoing subduction continued their way up the subduction channel and eventually reached the accretionary complex, the last units to be involved in thrusting being the Tenda massif and neighbouring imbricated slices (Malavieille et al., 2011; Ravna et al., 2010). The Nappe Supérieure was subsequently emplaced on top attested by the presence of olistoliths occurring below its basalts (Egal, 1992). At 33Ma the regime of subduction changed in the Mediterranean region as a whole (Ravna et al., 2010). The opening of the Liguro-Provencal basin and rotation of the Corsican-Sardinian microblock commenced (Rollet et al., 2002), succeeded by eastward retreat of the Adrian slab and opening of the Tyrrhenian Sea.

The event related to extension is reflected in Corsica by the presence of crustal-scale shear bands. These evolved in time from a ductile to a brittle regime in which major thrusts were reactivated as extensional shear zones, truncated by east-dipping normal faults (Jolivet et al., 1991). This configuration, coupled with erosion, completed the exhumation and juxtaposition of the HP-LT metamorphic domains with the low-grade Nappe Supérieure, and ensued development of the Miocene basins (Egal, 1992; Jolivet et al., 2003).

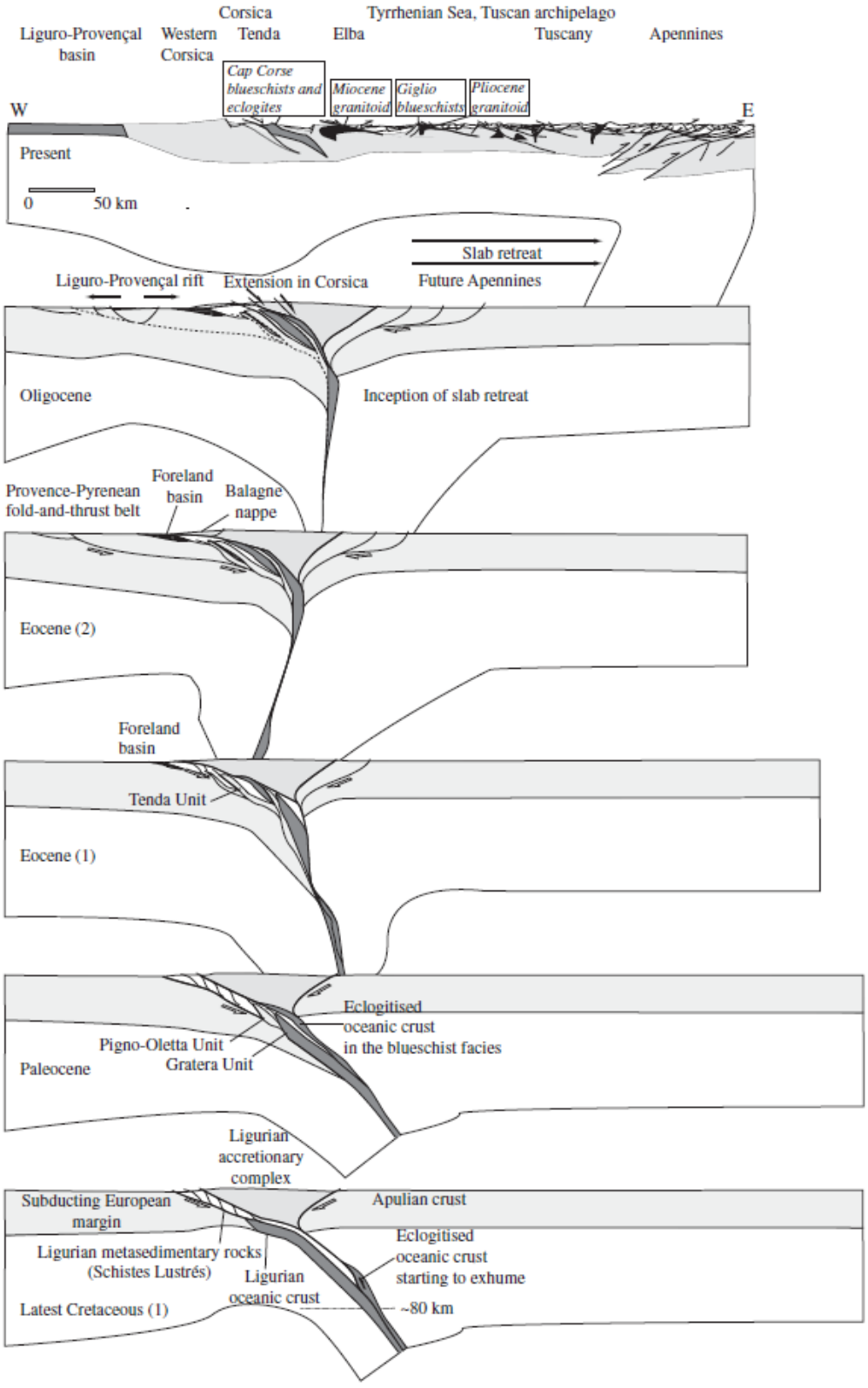

Figure 31: A model of tectonic evolution for the Alpine HP-LT metamorphic subduction complex. The formation of the studied Corsican pseudotachylytes is attributed to early stages of this subduction (Austrheim and Andersen, 2004). See text for details. From Ravna et al. (2010).

Previous work

The pseudotachylytes in the Schistes Lustrès unit was discovered and first described by Austrheim and Andersen (2004). Initial work mapped out the extent of the pseudotachylyte-bearing gabbroic and peridotite bodies and arranged textural and mineralogical description of fault, injection veins and host rocks.

Additional work by Andersen and Austrheim (2006) expanded on textural descriptions and mineralogical data, and provided field observations that highlighted the frequency of pseudotachylyte within the least altered mantle peridotites. The mineralogy of pseudotachylytes was used to determine crystallisation (1300-1400°C) and quench temperatures (1200°C) of veins, and minimum disequilibrium melting temperatures for wall rock (>1750°C), in relation to conditions of 1.5GPa and 470°C (ΔT=minimum 1280°C). The time for individual pseudotachylytes to solidify was estimated based on vein thicknesses and temperature rise from ambient conditions. Earthquake magnitude in relation to energies required to melt peridotite and produce commonly observed vein thicknesses were estimated to Mw-7. The porosity and low total analyses within the pseudotachylytes were used to estimate water content prior to solidification (4wt%).

Further work (Andersen et al., 2008) focused on stresses released during coseismic faulting. These estimates were based on wall rock melting temperature, pseudotachylyte vein thicknesses and offset markers over a gabbroic vein in peridotite. Minimum estimates associated with a single rupture-event were calculated to range from a few MPa up to 580MPa with an average of >200MPa.

Extensive sampling was done during all field campaigns. An important observation is that all rocks preserve some evidence of hydration prior to seismic faulting, by inclusions of tlc, clc and srp in opx and ol (Deseta et al., submitted). This is supported by porosity in the pseudotachylytes representing fluids dissolved in the primary ultramafic melt (Andersen and Austrheim, 2006). An on-going study by Natalie Deseta (unpublished PhD work in progress, Wits University, South Africa) focuses on the mineralogy, fluid budget and petrology of the pseudotachylytes in both peridotite and gabbro.

This thesis focuses primarily on previously gathered samples and some collected in the field during autumn 2012. Previously gathered samples COR-04-06 and COR-05-06C where stress release during coseismic faulting are estimated (Andersen et al., 2008) have been selected for

extensive analyses using EBSD. Sample COR-06-03D, devoid of pseudotachylytes, has been analysed by EBSD and used to represent the ultramafic host.

The field trip during autumn 2012 focused on sampling pseudotachylyte injection veins (COR-6/12) and well preserved peridotite (COR10/12). These samples have not been analysed using EBSD, but are included for textural description. The locations of previously gathered (2003, 2006) and recently gathered (2012) samples are shown on figure 32.

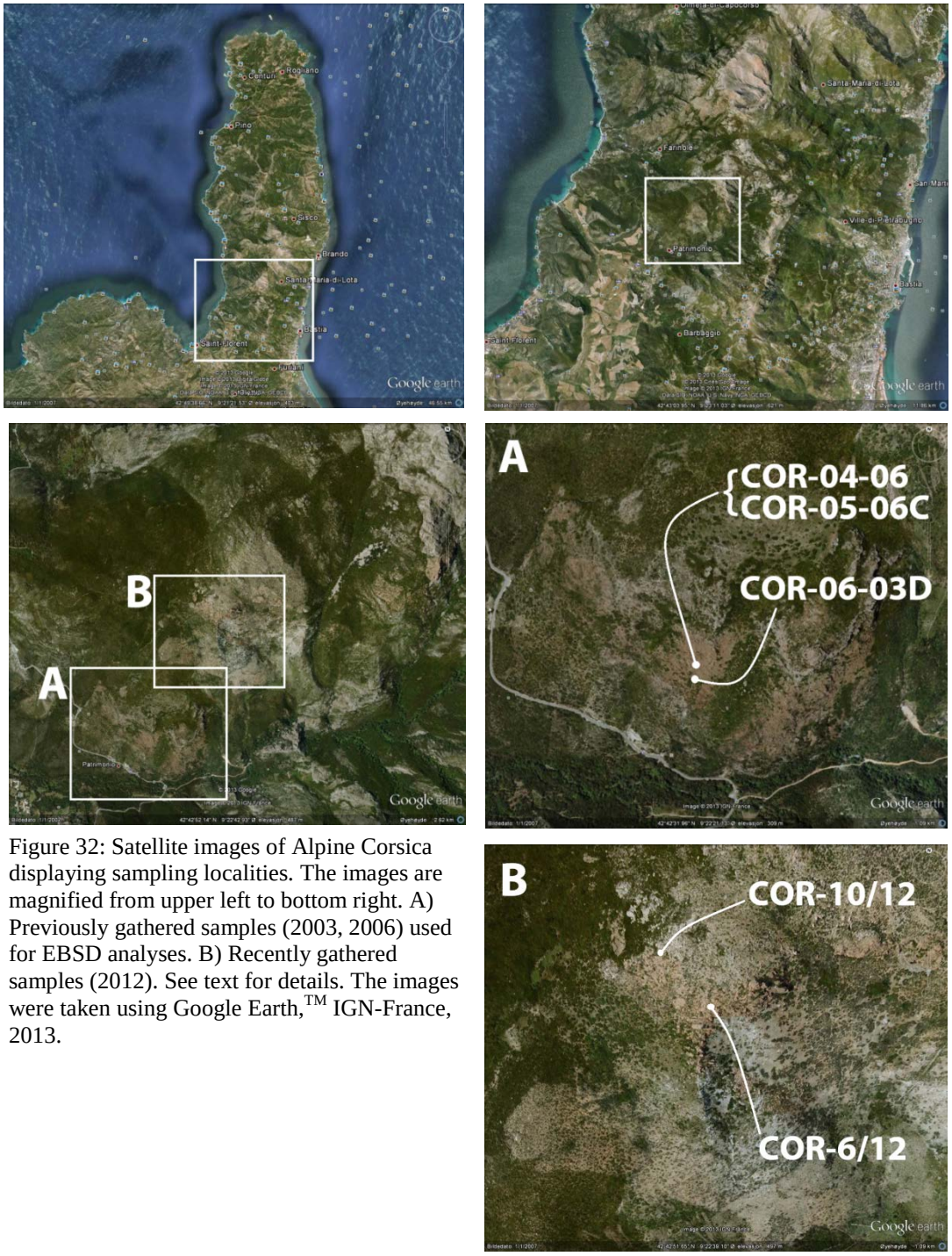

Figure 32: Satellite images of Alpine Corsica displaying sampling localities. The images are magnified from upper left to bottom right. A) Previously gathered samples (2003, 2006) used for EBSD analyses. B) Recently gathered samples (2012). See text for details. The images were taken using Google Earth,™ IGN-France, 2013.

4. Field relations

Field mapping and observations are not an essential part of this study. A field trip for reconnaissance in both Hercynian and Alpine Corsica was done during 23-28th of September 2012. Three days were spent in the cliff side of Cima di Gratera where samples of pseudotachylyte injection veins and peridotite host rock were gathered for textural description.

The studied pseudotachylytes occur in both gabbros and peridotites on the SSW- slope of Cima di Gratera in the Cape Corse region of Alpine Corsica (Austrheim and Andersen, 2004). They are preserved in the least altered portion of the rocks and are found in great abundance along the interface between peridotite and overlying gabbros. The lowermost part of the cliff, below the peridotites, hosts foliated serpentinites. The pseudotachylytes in both gabbro and peridotite display a polyphase slip history and will be described separately. Figure 33 displays the SSW-slope of Cima di Gratera and the positions of gabbro, preserved peridotite bodies and serpentinite (Andersen et al., submitted).

On outcrop scale the peridotites occur in variably hydrated lenses up to 140m thick and 850m long along a continuous, gently dipping horizon which can be traced approximately 2,5km in the hillside. The lithological boundary between gabbro and peridotite/serpentinite has previously been interpreted to constitute the paleo-MOHO within the Liguro-Piemontese

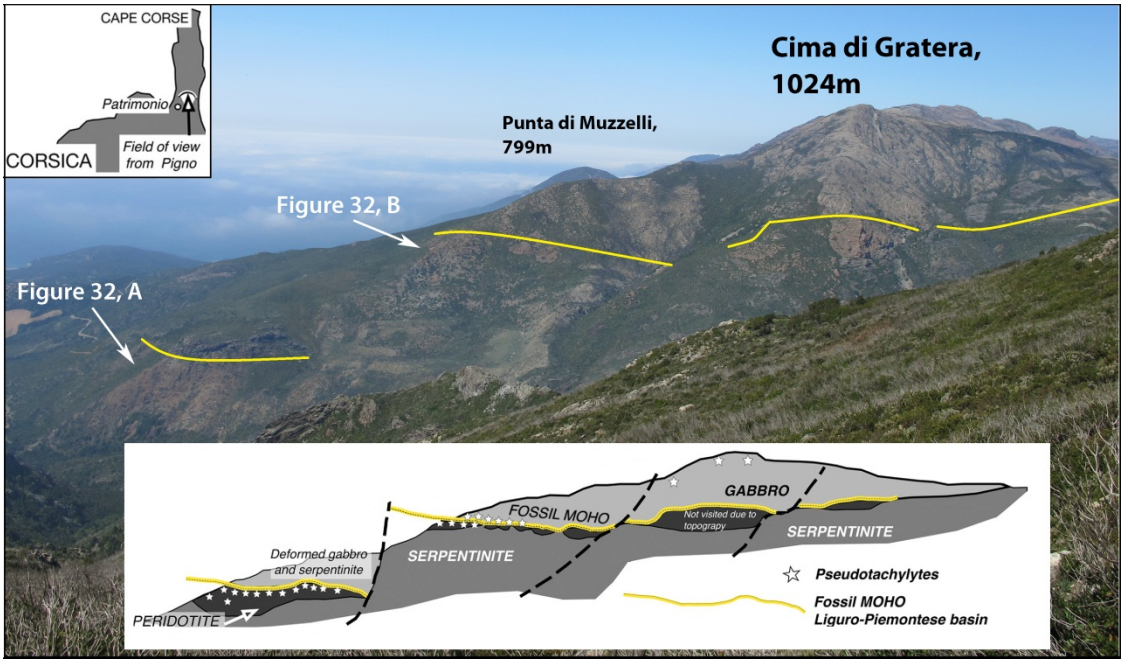

Figure 33: View onto the SSW-slope of Cima di Gratera and schematic illustration of the main lithological units, highlighted with line drawings. The fossil MOHO of the Liguro-Piemontese oceanic basin is marked in yellow and the occurrence of pseudotachylytes is presented as white stars. The sampling localities from figure 32 are indicated with arrows. Modified from Andersen et al. (submitted).

oceanic basin, now exposed in the Schistes Lustrés composite nappe (Andersen et al., 2008). The gabbro constitutes the summit at Cima di Gratera. The fossil MOHO, indicated on figure 33, is offset by later normal faults that together with the regional dip are responsible for distributing the peridotite-gabbro interface at different heights in the cliff side. This array of faults extends into and truncates the middle Miocene St. Florent basin, on the far western limb of the Cap Corse-Castagniccia antiform (Malavieille et al., 2011).

Metagabbro

The metagabbros resting directly atop the fossil MOHO display foliated domains with gln which constitute anastomosing networks around lenses with more primary magmatic textures (figure 34, A). In general, however, the gabbro massif of Cima di Gratera is remarkably well preserved with abundant examples of both primary igneous structure and mineralogy (Fournier et al., 1991). The foliation strike N-E and defines a lineation direction towards the E (figure 34, B). Uphill and away from the contact the gabbro is relatively heterogeneous and range from massive magmatic to cumulate-layered with transitional domains between the two. Magmatic layering is, however, locally well preserved (figure 34, C). Commonly, the gabbro

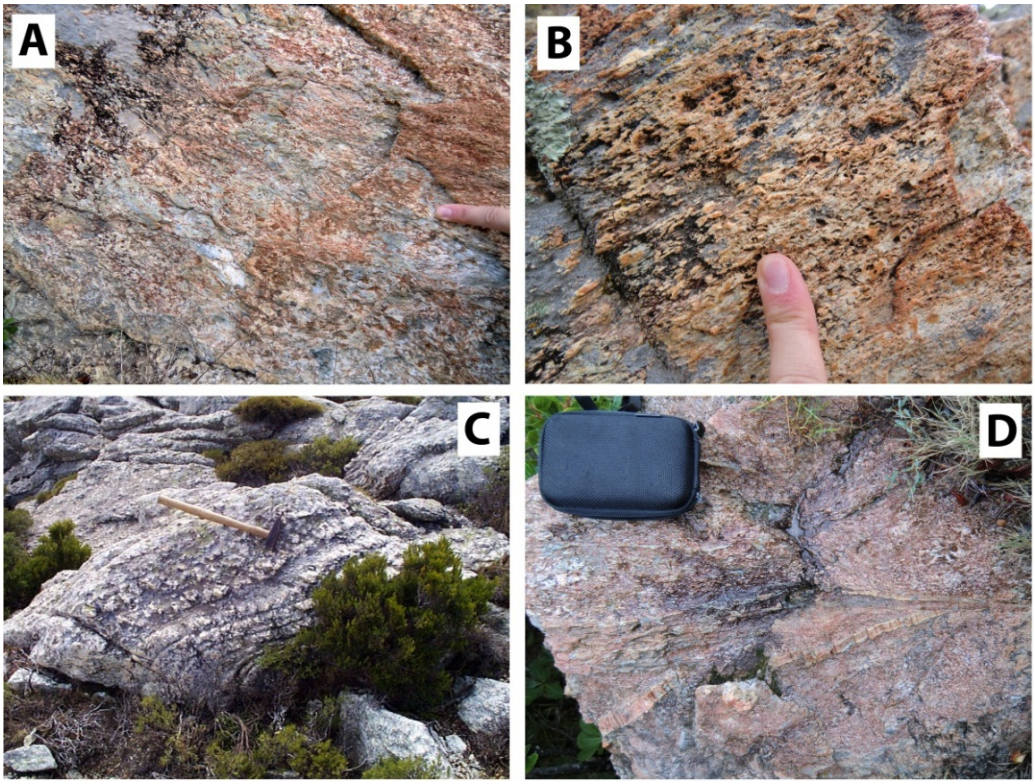

Figure 34: A) Foliation in gabbro (top left-bottom right) enveloping lenses of more magmatic fabrics. Thin pseudotachylytes strike subparallel to the foliation. B) The foliation defines a lineation towards the east, to the right-hand side of the image. C) Well preserved magmatic layering in gabbro. Hammer 30cm for scale. D) Magmatic textured gabbro, where individual pseudotachylyte fault-veins and injection veins are wider and better preserved than in foliated gabbro. The satchel is 13cm for scale. Most fault-veins strike subparallel to the foliated domains and to the paleo-MOHO.

is variably hydrated and varied-textured, with poorly defined domains of coarse and finer grained gabbro. In general the gabbro is pl-rich and large parts are perhaps best described as a leucogabbro (Fournier et al., 1991).

At the scale of outcrop, pseudotachylytes have positive relief with respect to their host rock. Gabbro-hosted pseudotachylyte veins on weathered surfaces are dark bluish-grey to black, occasionally brown, and usually forms single discrete fault-veins and injection-networks. On fresh surfaces these are glassy and black to greenish and aphanittic. Comminuted, disintegrated wallrock clasts, flow banding and chilled margins can be observed. Individual fault-veins are usually <3 cm while the extent of fault zone-networks near the paleo-MOHO up to meters in width. The majority of gabbro-hosted pseudotachylyte strikes subparallel to the paleo-MOHO and to the foliation in the gabbro. Some measurements made during field reconnaissance on gabbro-hosted pseudotachylyte near the paleo-MOHO are presented in figure 35.

Pseudotachylytes occur in well preserved igneous protoliths and in variably deformed terrains. They are commonly reworked and distorted in the foliated domains (figure 34, A). The least deformed gabbro domains spectacularly preserve pristine fabrics of pseudotachylytes relative to those in foliated domains (figure 34, D) (Austrheim and Andersen, 2004).

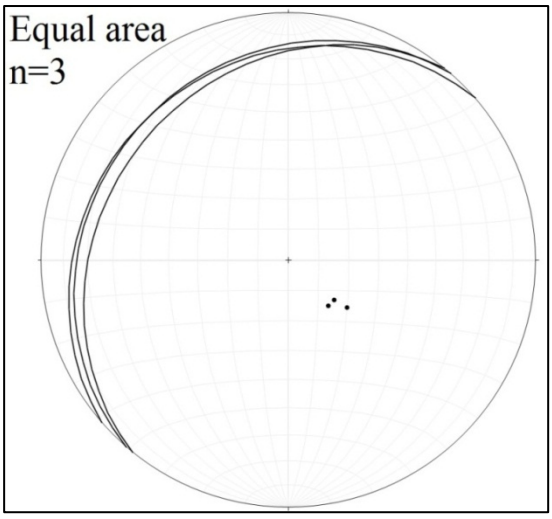

Figure 35: Orientation of a few gabbro hosted pseudotachylyte fault-veins (n=3). These strike subparallel to the foliated domains in the gabbro and to the paleo-MOHO at the interface between mafic and ultramafic bodies. All stereonets are plotted using Rick Allmendinger's Stereonet 8, from http://www.geo.cornell.edu/geology/faculty/RWA/programs/stereonet.html.

Peridotite

The peridotite lenses form a discontinuous horizon along the paleo-MOHO (figure 33). They are engulfed in serpentinites below with gabbros above. The weathered surfaces of the peridotite is commonly orange to brown, and may be massive and smooth, but are more commonly rough with an appearance dominated by veins and fractures. As a whole, the lenses record variable degrees of hydration through common veins of srp that occur on meter to millimetre scale throughout the bodies. However, some constraints can be put on the events related to hydration. Pre-earthquake hydration is evident as veins of srp as well as inclusions of tlc in opx and srp in ol (Austrheim and Andersen, 2004). Post-earthquake hydration is evident as static hydration and syn-kinematic alteration, producing the vast serpentinite body that engulf the peridotite lenses (figure 33). Generally, post-earthquake hydration records a progressive character witnessed by foliated serpentinites at some distance from the lenses that transition into statically hydrated domains at the margin of the peridotites. The magmatic fabrics at the margins of these lenses are partly preserved, and record statically hydrated pseudotachylytes (figure 36, A). These are devoid in the foliated serpentinites underneath.

The best preserved, least altered cores of the peridotite bodies are mostly without obvious stratification or banding. At rare locations, a vague compositional banding of alternating pyroxene-rich and ol-rich domains can be observed (figure 36, B and figure 36, C). The thicknesses of the arranged layers vary from outcrop to outcrop. Sampling of COR-10/12 was done on the fresh surface on figure 36, B, where thin bands could be recognized and suited for investigation with the optical microscope. The banding in all observed outcrops is subparallel to the paleo-MOHO, and to the foliation in the gabbro. In the majority of outcrops however, a compositional banding is not evident and dominantly attest to a ‘deformational banding.’ This banding is defined by close-spaced, subparallel faults and fractures, and the interplay between these (figure 36, D).

Ultramafic pseudotachylyte weather to a tan/rust-red to brown colour, but on fresh surfaces is black to grey and aphanittic. Fresh ultramafic pseudotachylyte injection-veins observed in the field and in hand specimen occasionally display comminuted wallrock clasts and flow banding.

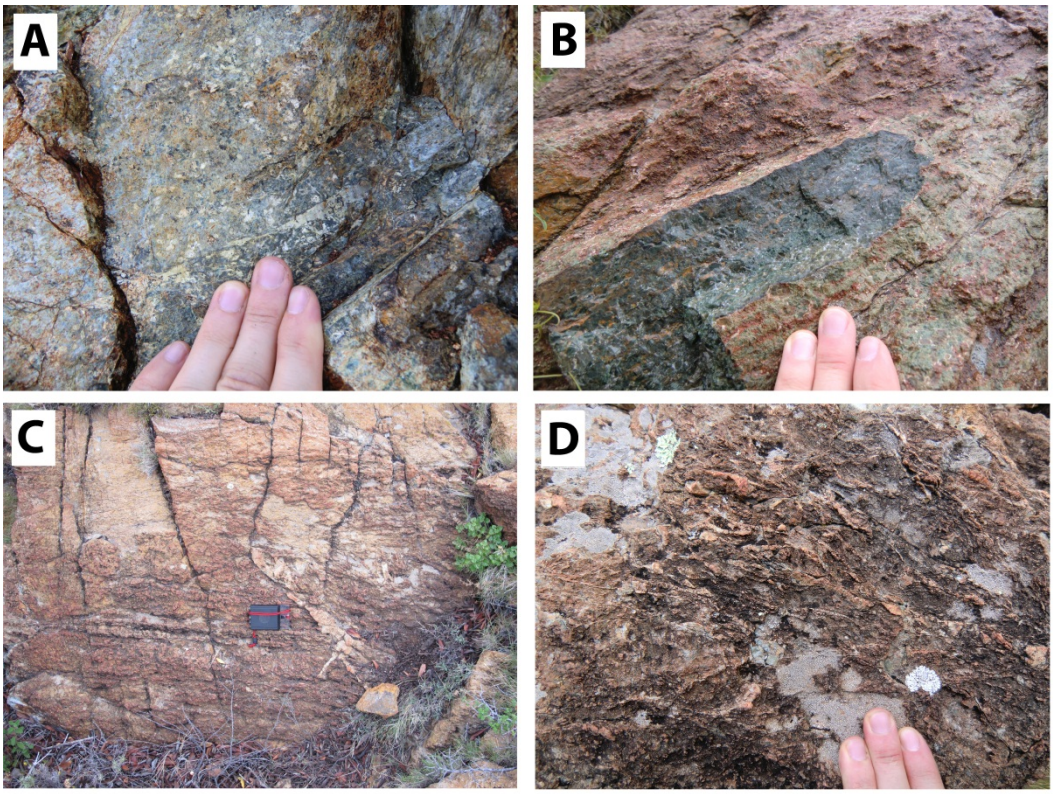

Figure 36: A) Statically hydrated peridotite where remnant magmatic fabric can be recognized. Pseudotachylyte fault- and injection-veins are conjointly hydrated and are preserved as grey to green veins. B) Small-scale, discontinuous compositional banding (bottom left-top right) of alternating pyroxenes and ol domains in peridotite. The fresh surface is the sampling locality of COR-10/12. C) Compositional banding in peridotite (lower half of image) cut by later fractures and injection veins. Compass is 11cm for scale. D) Commonly recognized 'deformational banding' constituted by close-spaced fault-veins and fractures in the interior of peridotite bodies.

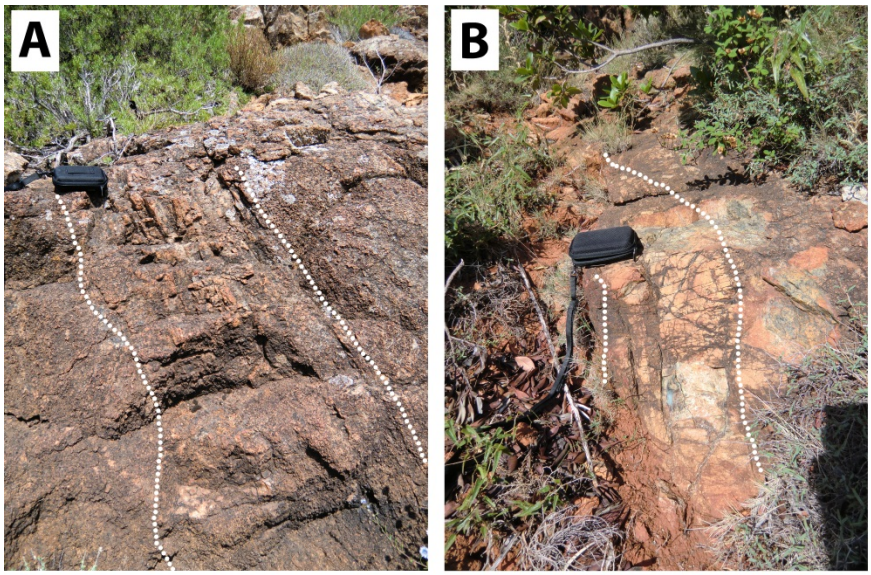

Figure 37: A) Fault-zone approximately 0.5m wide. The amount of pseudotachylyte is most abundant along the fault core. B) Thick segment of a pseudotachylyte fault-vein with maximum thickness of 38cm. This fault can be traced almost continuously across the peridotite body. The satchel is 13 cm for scale.

Fault- and injection veins display a more dramatic nature in the peridotite relative to the gabbro. This is witnessed by a considerably higher frequency of faults, their spacing denser and by individual fault- and injection veins anastomosing and cross-cutting each other (see gabbro, figure 34 A and D, and compare with figure 36, D). Some pseudotachylyte veins in the interior of the peridotite bodies are up to 0,5m in thickness and similar thick veins have not been observed in the gabbro. Injection vein networks typically ramify at a high angle off of faults and fault-zones, frequently clustering and intertwining along subparallel close-spaced faults. They occasionally record generation by radial expulsion from single interfaces (see later description). Ultramafic pseudotachylyte have been observed in isolated fault-zones <0,5m wide (figure 37, A), as single fault veins <38 cm wide (figure 37, B) and occasionally as fault- and injection-swarms decorating entire outcrops (figure 40). Most commonly, the lower and middle interior of the peridotite lenses, relative to the paleo-MOHO, display dense networks of cm-sized fault- and injection veins. These are unevenly spaced and distributed like that on figure 36, D and figure 37, A.

Sampling localities for fault rocks analysed with EBSD

The position of gathered samples relative to the peridotite bodies are shown on figure 32. Here, fault samples COR-04-06 and COR-05-06C were gathered in proximity of the core in one of the presently westernmost peridotite lenses. An array of thin and steep pseudocahylyte fault-veins offsetting a gabbroic vein were sampled and used for estimating strain-averaged stresses during a single rupture-event (Andersen et al., 2008). Some measurements on these faults were made during field reconnaissance and are presented on figure 38.

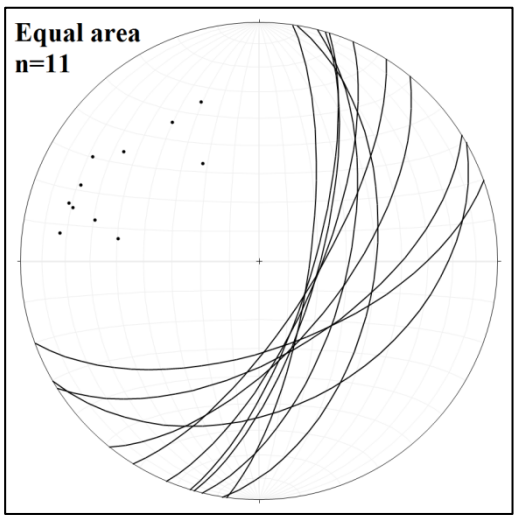

Figure 38: Peridotite-hosted, thin and steep pseudotachylyte fault-veins offsetting a gabbroic layer (n=11).

The array of faults can be traced for several meters and does not show any evidence of later offset or reactivation. The sampling localities of samples COR-04-06 and COR-05-06C are displayed on figure 39. The fault on where sample COR-04-06 was drilled has an orientation of 031/59 with an apparent slip of 0.8 cm. Sample COR-05-06C is a hand piece from a fault with multiple strands that has an orientation from 024/59 to 039/64. This fault zone has an apparent slip of 18.3 cm (Andersen et al., 2008). Slip estimates are uncertain due to lack of piercing points.

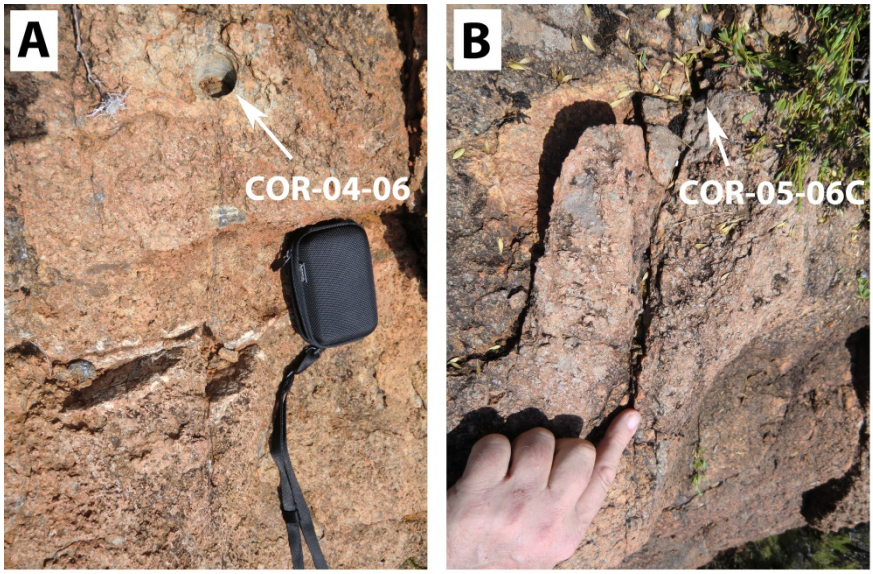

Figure 39: Sampling localities for fault rocks investigated using EBSD. A) Location of drill core sample COR-04-06. The apparent offset is 0.8cm. The apparent offset is 18.3cm. B) Location of hand piece sample COR-05-06C. The satchel is 13cm for scale. See text for orientations.

On higher levels within the peridotite bodies, adjacent to the contact to the gabbro, there is a salient change in the orientation and appearance of faults. Field observations attest that the amount of pseudotachylyte increases sharply towards the fossil MOHO at distances approximately 20 m or less from the interface. Within this domain it is difficult to recognize single, isolated faults even though the pseudotachylyte vein boundaries appear sharply defined. Most commonly a cluster of faults strike along the same fault trace and their respective damage zones extend several centimetres into wall rock. These fault zones contain numerous anastomosing faults that are crisscrossed by injection veins and pockets of melt. The outcrop on figure 40 crops out approximately 20 m in vertical distance from the interface between gabbro and peridotite, and display some of the features encountered when approaching it. Such outcrops are frequently encountered in lateral extent, beneath the fossil MOHO. Despite the apparent polyphase slip history and melt expulsion frequently portrayed

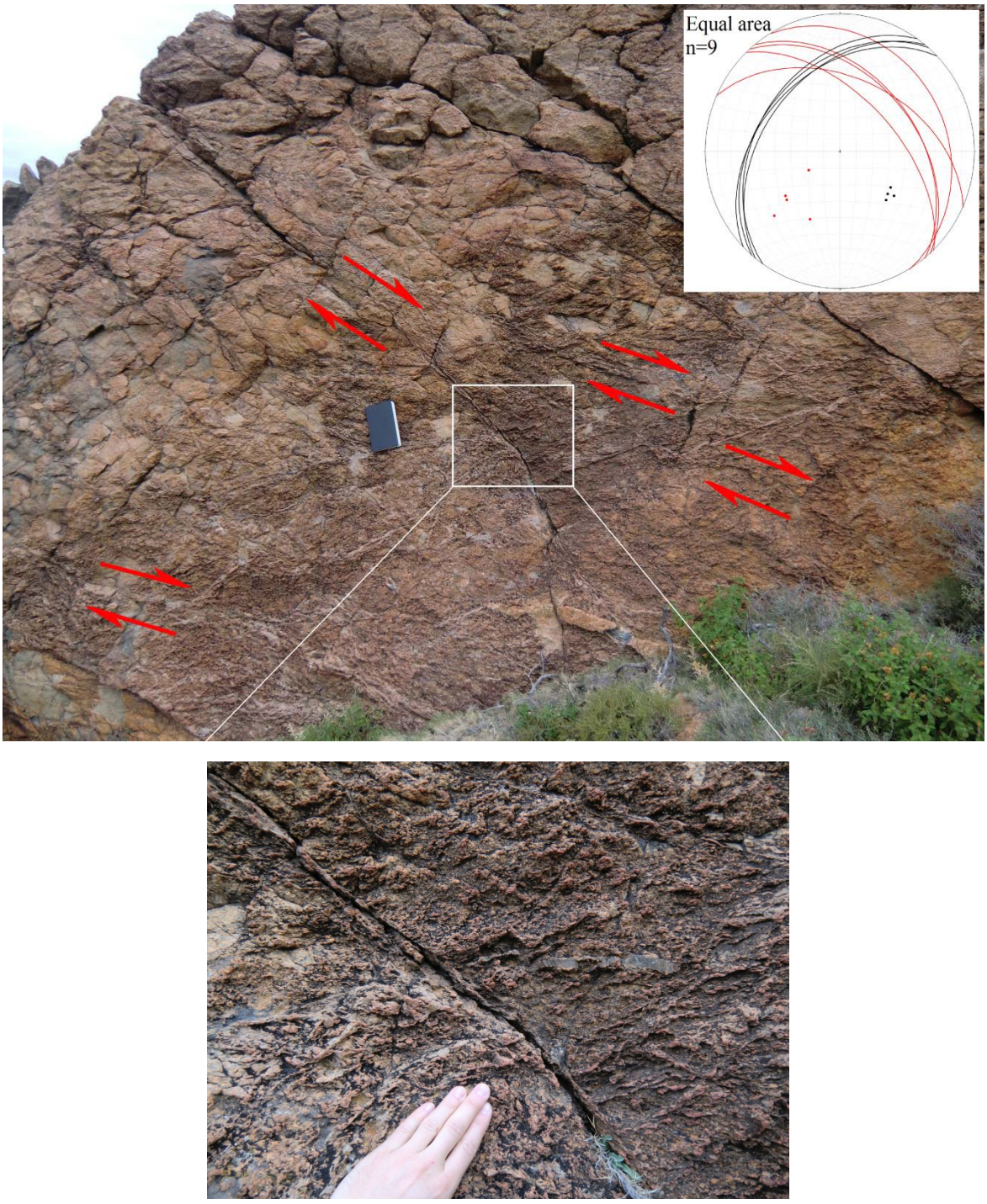

Figure 40: Pseudotachylyte fault- and injection vein networks in peridotite beneath the fossil MOHO. The upper, smooth surface has undergone less weathering than the lower pseudotahylyte-swarmed host. The outcrop is <20m in vertical distance from the paleo-MOHO. Two set of fault populations can be recognized. The orientation of fault-veins (n=9) is shown on the stereogram as poles and great circles. The shear direction of the most recent faulting event, striking N-W, is shown with red arrows, and marked with red on the stereogram. These are offsetting faults that align subparallel to the foliation in the gabbro, striking N-E. The book is 21cm for scale. The white square encloses the fault core of the central prominent fault. It displays fault core, antecedent faults and adjacent wall rock, displaying dextral sense of shear with numerous injection-veins radiating out from the fault plane. Sample COR-6/12 was gathered at the fresh surface in the injection vein below the squared area.

in fault zones, there have been recognized two orientations along which faults occur beneath the paleo-MOHO. Here, the dominant set of ultramafic pseudotachylytes is subparallel to it and to the foliated gabbros. A later set forms an array of faults that cut these, striking towards the NW. Figure 40 display one of several outcrops where both populations are exposed rather spectacularly. The set of most recent faults record similar strain markers and splaying, indicating concurrent generation. Compare stereoplots on figure 35 and figure 40 for the correlation in orientation between gabbroic and antecedent peridotite-hosted fault veins.

The MOHO-parallel fault (figure 41, A) is defined as a several meter wide damage zone in which massive pseudotachylyte approach 1 m or more in cumulative thickness. A single major fault plane is difficult to recognize. Domains of massive pseudotachylyte are spaced by dense networks of mutually criss-crossing fault- and injection veins that transition into breccia with pseudotachylyte matrix (figure 41, B). These fault-veins show the same relationship as elsewhere in the peridotites, and are later cut by an array of more recent faults. Based on the draping of foliation and orientation of shear bands it is suspected that these constitute top-W deformation (figure 41, C). The thick aggregates of pseudotachylyte are overlain by a 1 m thick foliated transitional zone before the true gabbroic domain is apparent (figure 41, A). The substantial melt production along the 1-2 m MOHO interface (figure 41, A) and adjacent peridotite wall rock (figure 40) indicate that the amount of produced melt was very high. Andersen et al. (submitted) suggests that if the earthquake(s) involved occurred along a 1m wide slip zone it could have had a displacement of up to 19 m. Such an earthquake might have been on the order of Mw-8, with a rupture length that far exceeds the seismogenic zone.

Below the paleo-MOHO, additional conspicuous structures are observed at uneven intervals. These are small-scale expulsive branches that resemble three dimensional ‘star-patterns’ that radiate from defined fault planes (figure 42). Such explosive network veining might represent reminiscent “explosive melt-production” (Andersen et al., submitted). These are similar to the dense networks of fault- and injection veins in wall rocks beneath the fossil MOHO (figure 40), although on a smaller scale. Both types of structures demonstrate that the amount of melt stored on fault-vein generation surfaces are much smaller than the total volume generated during rupture, and are swiftly distributed through large volumes of rock. This attests to the melt being effectively drained from fault planes into pre-existing and syndeformational porosity. The ultramafic melt must have had an extremely low viscosity upon formation (Andersen and Austrheim, 2006; Suzuki and and collaborators, 2001).

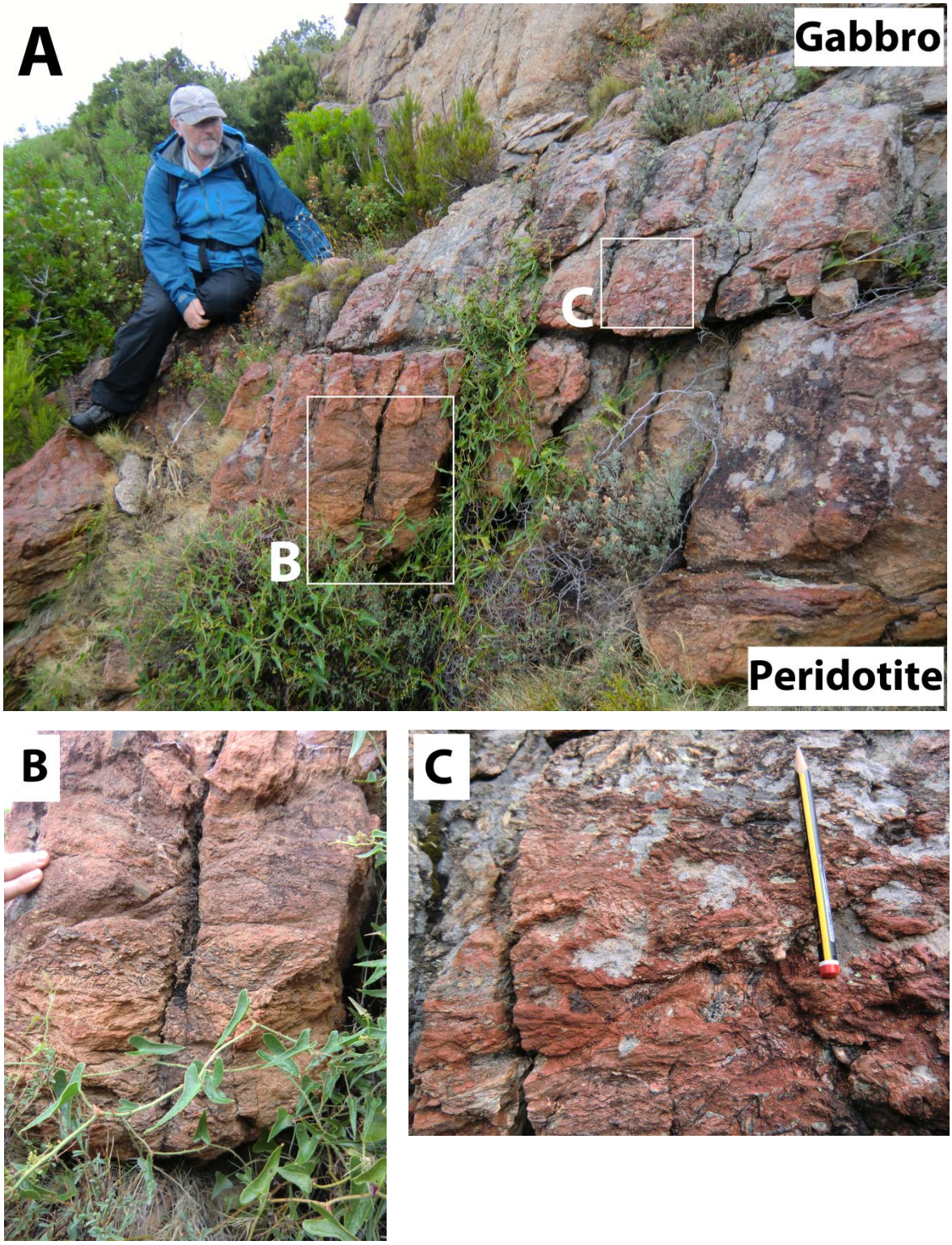

Figure 41: A) Paleo-MOHO parallel fault where massive pseudotachylyte approach 1m in cumulative thickness. No single fault plane can be recognized. The transitional zone from peridotite to gabbro is strongly foliated. B) Massive pseudotachylyte spaced by fault-and injection veins that transition into breccia with pseudotachylyte matrix. C) Shear bands at the base of the peridotite-gabbro transitional zone. These attest to top-W deformation.

Figure 42: Explosive radial network-veining from a single interface. From Andersen et al. (submitted).

A compilation of all measured faults in peridotite taken during field reconnaissance are presented on figure 43. Three principle orientations can be observed. A population of faults strike NE, subparallel to the MOHO and to the foliated gabbros, with a more recent event that cut these striking NW (figure 40). The third population is steeper and strike roughly N-S (figure 38).

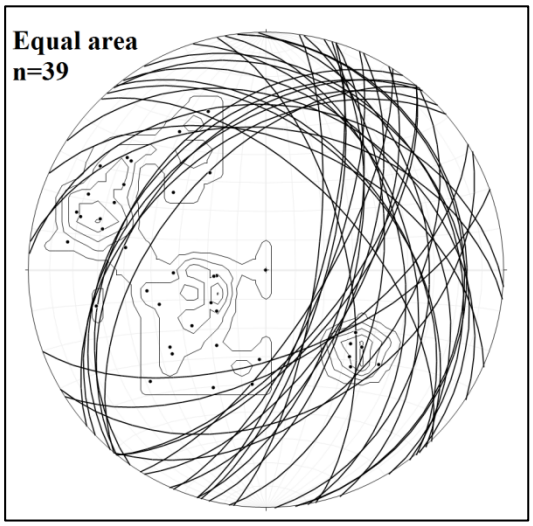

Figure 43: All measured peridotite-hosted pseudotachylyte fault-veins (n=39). The densities of poles are contoured using 1% area and show three prominent populations. See text for details.

Observations done in the cliff side of Cima di Gratera attest that a large volume of frictional melts has been swiftly distributed through vast bodies of rock. Intuitively, the amount of pseudotachylyte is much higher in peridotite relative to gabbro. In peridotite, the amount of melt stored along individual faults can be very high, but is more often allocated in damage zones that may extend several meters into wall rock. A polyphase slip history is evident on numerous outcrops. The amount of pseudotachylyte increases dramatically close to the gabbro-peridotite interface, and vanes into the overlying gabbro massif.

5. Results

Petrography and layout of ultramafic host rocks

The peridotite host rock samples have individually been sampled within 10-20m of heavily faulted domains and are devoid of pseudotachylytes. The composition of the peridotite varies from locality to locality and mainly differ based on the amount of pl. Samples COR-06-03D and COR-10/12 have been used to represent two separate host ultramafics. Both samples have been sampled, spatially, within a few hundred meters (figure 32 and figure 33). Their approximate compositions are plotted on figure 44. The mineralogy is consistent in both samples where relative amounts record ol ≈ opx > cpx > pl > spl. The ultramafics contains spl as a minor phase that is unevenly scattered through both samples. Several generations of fractures and veins of srp are distributed through the rock suites. Fractures are commonly associated with mag in both samples. None of the investigated host ultramafic samples (COR-06-03D and COR-10/12) show any sign of high pressure mineral assemblages.

Earlier work on the EMP has put constraints on the mineral compositions where ol ($fo_{\sim 90}$) and opx ($en_{\sim 87}$) are highly magnesian, the pl ($an_{\sim 94}$) is highly calcic and both cpx ($wo_{\sim 45}en_{\sim 50}\, fs_{\sim 5}$) and spl ($\leq$37wt% Cr_2O_3) are enriched in Cr (Andersen and Austrheim, 2006; Austrheim and Andersen, 2004).

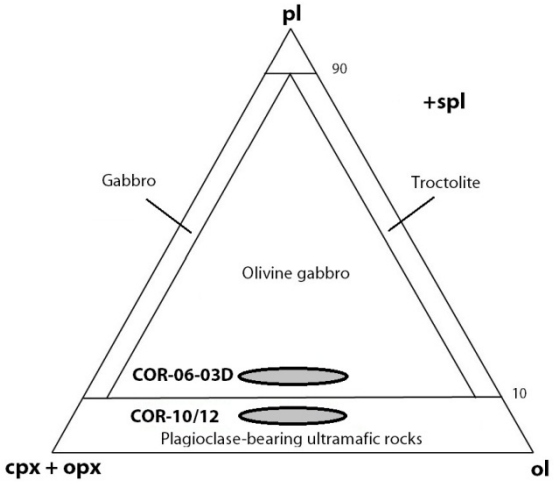

Figure 44: A subdivision of the Streckeisen diagram plotted in pl-px-ol space, showing the bulk composition of both Corsican ultramafic host rocks. Modified from (Winter, 2010).

Sample COR-06-03D

Sample COR-06-03D contains approximately ~15% pl and plots as an ol gabbro (figure 44). The pl is highly calcic (Austrheim and Andersen, 2004) and will be referred to as a spl-melagabbro. Grain sizes are consistent through the sample in which opx > ol > cpx > pl > spl. Opx and cpx record annealed poikiloblasts of ol (figure 55) and other minor unidentified inclusions. Abundant fracturing and veins of srp transect all phases.

Both opx and cpx commonly show exsollution lamellas of each other. An example of immiscibility is shown on figure 46. Pl is often thoroughly altered into cloudy, fine grained minerals (figure 49). The reaction is often progressive, where alteration initiates at grain rims and/or along cleavage planes and fractures that extend through the grain(s). Occasionally, complete transformation has taken place with no trace of the former pl, and cloudy aggregates constitute individual grains. Typical breakdown products are a more ab-rich component and minor phases unidentifiable using the optical microscope and EDS (figure 49). Pl grains that retain much of their original shape and composition commonly display carlsbad twinning in addition to polysynthetic twins. Spl is occasionally rimmed by chl (figure 48).

Sample COR-10/12

Sample COR-10/12 contains approximately ~5% pl and plots as a pl-bearing ultramafic (figure 44). It can be subdivided based on the relative amounts of cpx and opx (figure 45). It is slightly richer in opx and will be referred to as a pl-spl-lherzolite. The pl-spl-lherzolite contains more cpx relative to the spl-melagabbro. Grain sizes are consistent through the sample in which ol ≈ opx ≈ cpx > pl >spl. Opx and cpx record annealed poikiloblasts of ol

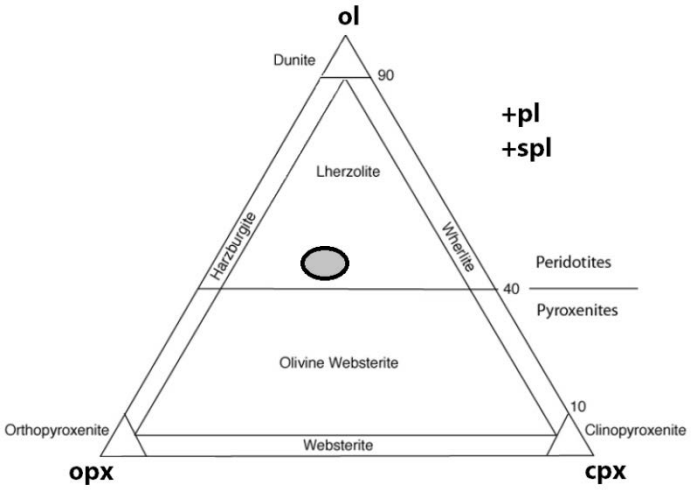

Figure 45: A subdivision of the Streckeisen diagram plotted in ol-opx-cpx space, showing the composition of the pl-bearing ultramafic host rock. Modified from (Winter, 2010).

(figure 47). Ol contains minor inclusions. Abundant fracturing transects all phases, but the sample is devoid of veins of srp. Spl does not show a reaction rim like that in the melagabbro. Similar to the spl-melagabbro, both cpx and opx commonly show exsollution lamellas of each other (figure 52, B), and pl is commonly broken down into fine grains. Pl that retains its original shape and composition display polysynthetic twins and carlsbad twins (figure 47).

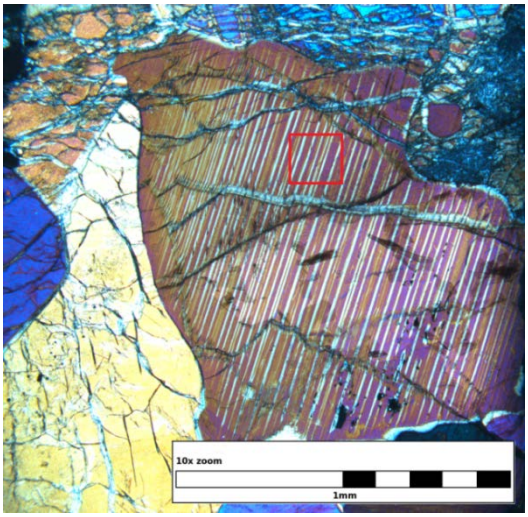

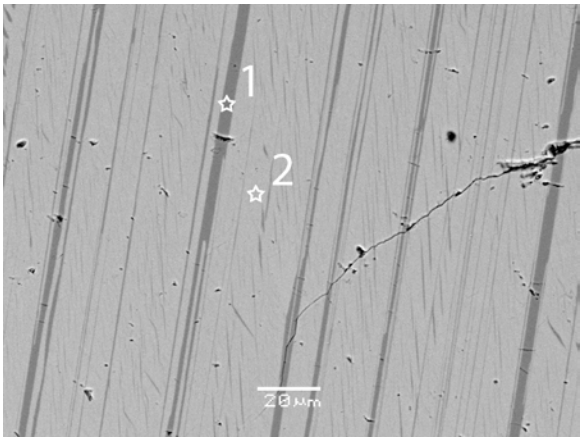

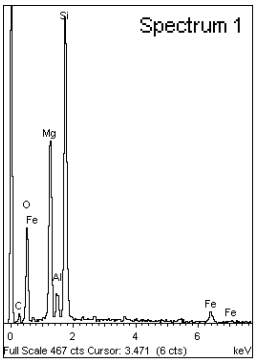

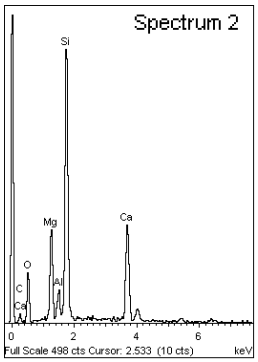

Figure 46: Micrograph in cross-polarised light, BSE image and EDS point-analyses of opx exsollution lamellas in cpx. The red square encloses the area in which the BSE image and analysis were taken. The wide opx lamellas (top-bottom) lie within and parallel to cleavages in cpx. Opx has also exsolved in microfractures that are oriented at an angle to the cleavages. Images and analyses from sample COR-06-03D.

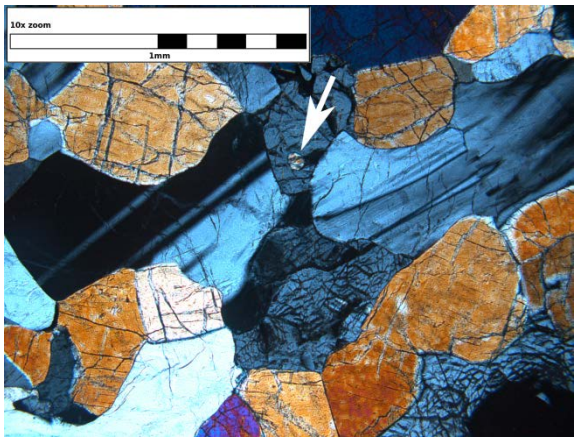

Figure 47: Micrograph in cross polarised light of carlsbad and polysynthetic twins in pl. The arrow points to an ol poikiloblast in opx. From sample COR-10/12.

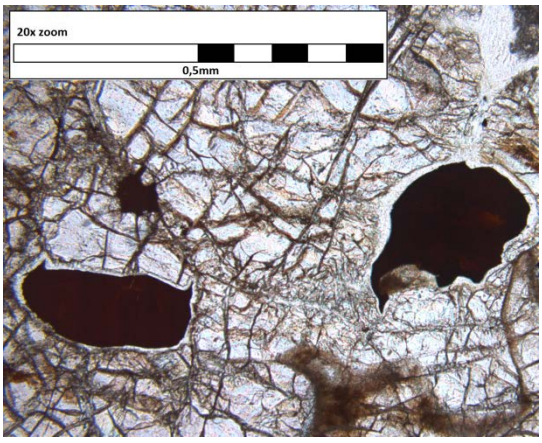

Figure 48: Micrograph in plane-polarised light of reaction rims of chl surrounding spl. From sample COR-06-03D.

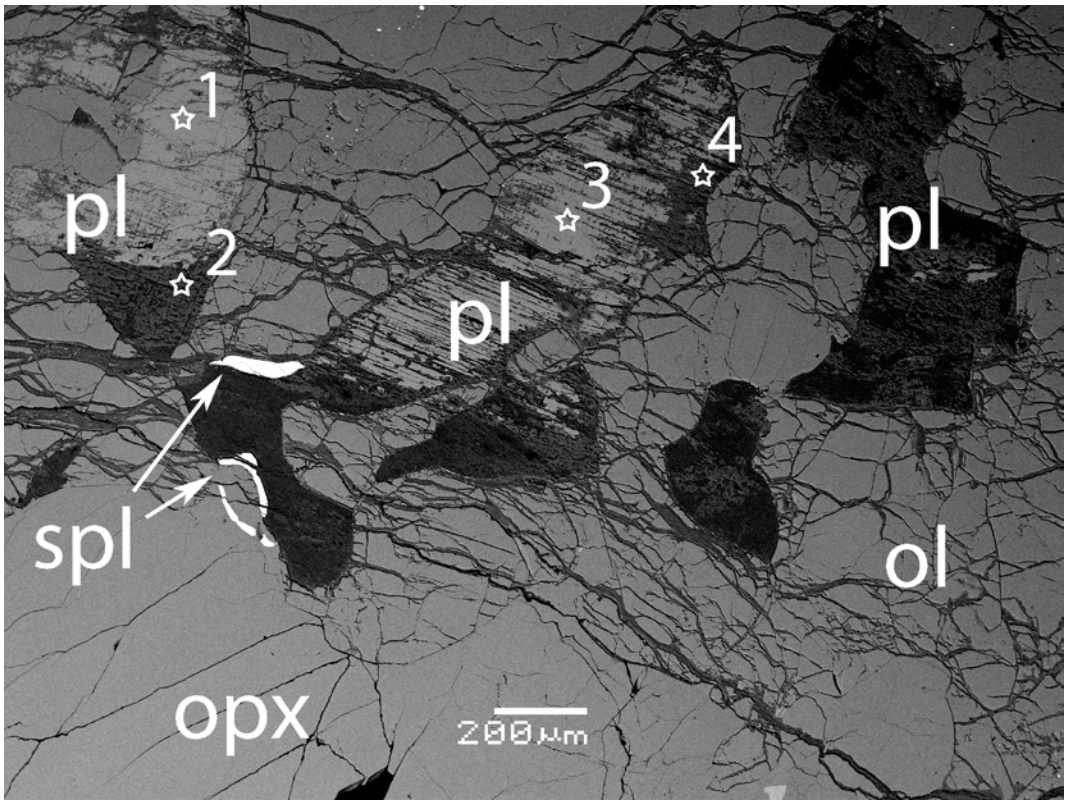

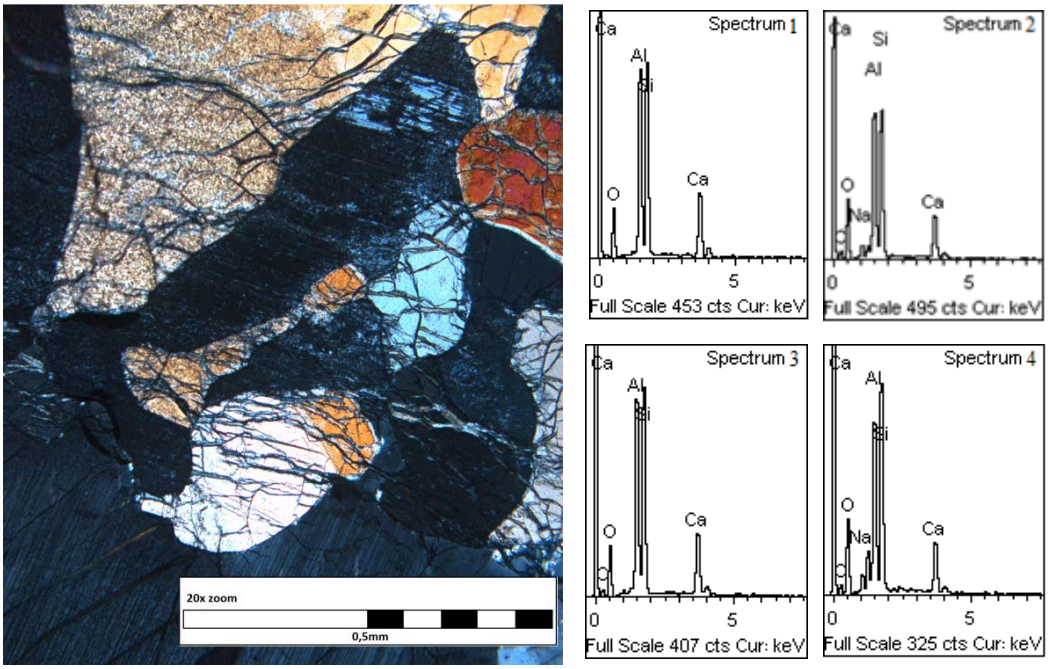

Figure 49: BSE image, micrograph in cross-polarised light and EDS point analyses of commonly observed breakdown of pl in both host ultramafics. The three marked pl grains on the BSE image show three steps of progressive reaction, from left to right. Point analyses 1 and 3 displays typical an-pl while point analyses 2 and 4 show influx of Na to a more ab-rich phase. Images and analyses from sample COR-06-03D.

Structures and textures

Both ultramafic host rocks display similar structures and textures and will be assessed together.

Compositional banding

Both samples record a vague elongation and alignment of opx and cpx with intervening ol that compose a weak and inconsistent compositional banding (figure 50). This has also been observed on outcrop scale (figure 36, B and figure 36 C, chapter 4). Grain sizes of opx, cpx and ol vary from fine- to coarse-grained (<1mm-8mm) and constitute smaller and larger aggregates along the vague banding. Spl are typically distributed unevenly through both samples, but often reside along grain boundaries and in triple junctions.

The spl-melagabbro record large grains of opx (5-8mm) separated by mixed bands of dominantly ol with minor cpx, pl and spl (figure 51, A). Grain sizes of these range from <0,5mm-3mm along their long axes. All phases are slightly elongated subparallel to the vague banding. The latter domain containing ol, cpx, pl and spl is extensively criss-crossed by fractures and veins of srp (figure 51, A). Fractures transect all phases and are associated with mag, enveloped by brown discoloration as seen on figure 50.

The pl-spl-lherzolite displays a large array of grain sizes for ol and opx+cpx, similar to the spl-melagabbro. In contrast to the spl-melagabbro, however, the sampled pl-spl-lherzolite does not record the same large, isolated opx nor any convincing evidence of hydration (figure 51, B). Ol constitute the largest grains (≤8mm). The pl-spl-lherzolite is slightly richer in cpx compared to the spl-melagabbro. Cpx share an approximate uniform grain size with opx. Both range in size from ≤1mm to 5mm along their long axes. Pl and spl are minor phases where

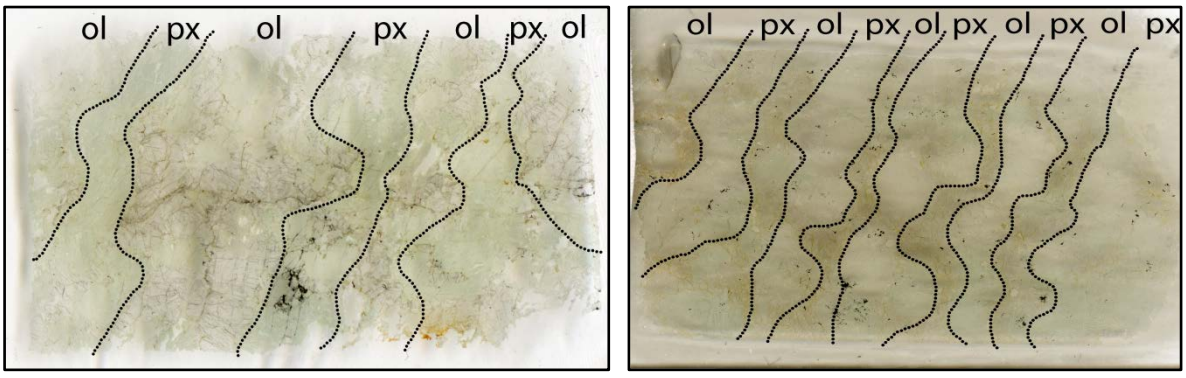

Figure 50: Scanned thin sections of host rock COR-10/12 (left) and COR-06-03D (right) displaying weak and inconsistent compositional bandings. Ol-rich domains are easily recognized by numerous fractures that strike both subparallel and normal to the banding. These are enveloped by brown discoloration. Both samples are cut perpendicular to the banding observed in the field.

grain sizes vary, generally ≤2mm and ≤0,5mm, respectively. All phases are elongated subparallel to the vague and inconsistent compositional banding (figure 51). Fractures transect all phases and are associated with mag, enveloped by brown discoloration (figure 50).

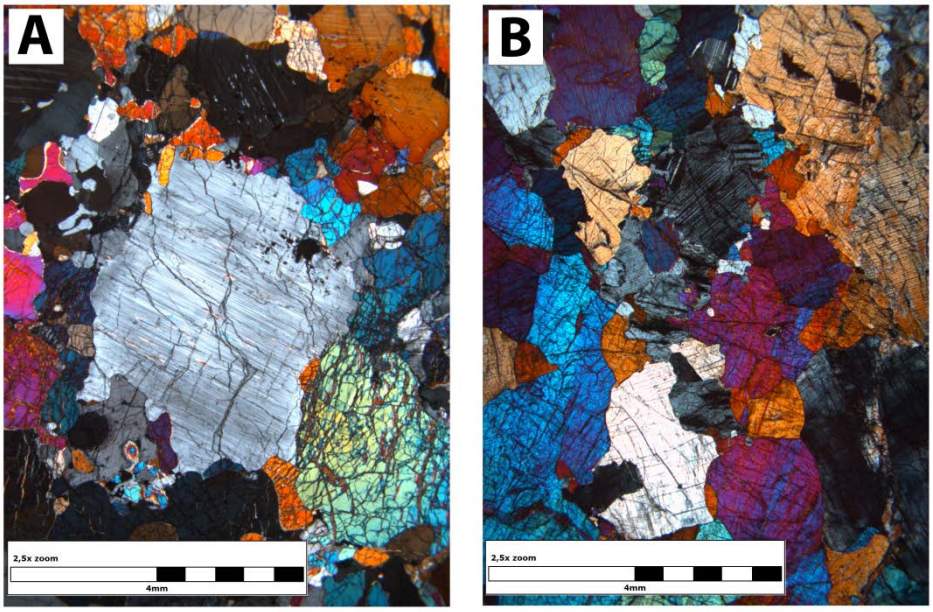

Figure 51: Micrographs in cross-polarised light of weak, inconsistent compositional banding in both ultramafics. A) Spl-melagabbro. B) Pl-spl-lherzolite. The orientation of compositional bands and elongation of grains (roughly N-S on images) can be compared to the scans of the thin sections on figure 50.

Fractures and sheared bands

Both ultramafic host rocks contain fractures and bands that offset individual mineral grains. This is more pronounced in the pl-spl-lherzolite. Fractures align both subparallel to the vague compositional banding and at a high angle to it (figure 52). There has been found no evidence of pseudotachylyte along these in the ultramafic host rock samples.

The fractures typically transect and offset all phases along a sharp interface. These bands are occasionally hair-thin and identified due to offset grains along a planar to wavy line (figure 52, A). Other bands are wide (<0,5mm) and contain peeled-off, sheared and prolate clasts of ol, opx, cpx and pl. Cpx transected by any population of these bands are occasionally sheared, evident by the orientation of exsollution lamellas (figure 52, B). Spl are found within and along these features, but does not show any evidence of offset nor alignment in relation to the band(s).

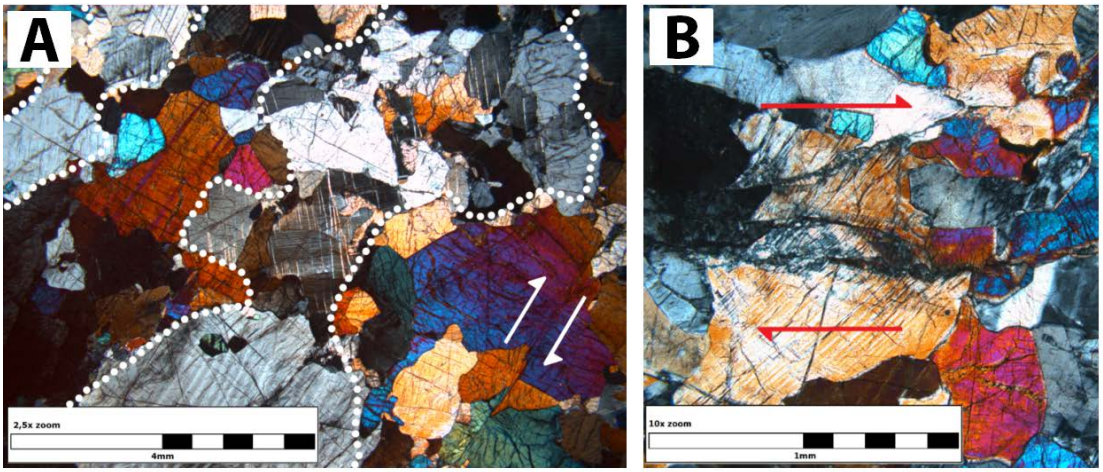

Figure 52: Micrographs in cross-polarised light of typical appearances of bands that transect grains. A) Hair-thin fracture offsetting ol grains in the lower right-hand corner. The fracture is subparallel to the compositional banding, marked by white dotted lines. Note deformation twinning in both opx and cpx. B) Fracture transecting compositional banding at a high angle. The appearance of exsollution lamellas in cpx attest to shear along the fracture. Both images from sample COR-10/12.

Microstructures

Both ultramafics display protogranular, modified equilibrated textures with variable grain boundary migration. Both samples display unequal amounts of relatively strain-free grains and those which show pronounced undulatory extinction, development of tilt walls and subgrain boundaries. Grain junctions vary from polygonal to dihedral and grain boundaries are straight to highly interlobate.

Some phases display kink bands, twinning and folding. Out of these, opx and less frequently cpx record kinking. Kinked grains often contain a single kink-band through the centre of grains, typically normal to already exsolved lamellas (figure 53 and 55). The immiscibility between opx and cpx is highly exaggerated along kinks. This is evident by high densities of exsollution lamellas radiating along the kink and out from it, and along exsollution lamellas that have already developed in the host (figure 55).

Opx grains occasionally display curvature and folding evident by the orientation of cpx lamellas (figure 54). Both pyroxenes record deformation twinning (figure 52) Deformation twins have also been observed in pl (figure 47).

Grain boundaries in both samples are planar to lobate and occasionally join up in triple junctions. These are frequently modified polygonal. Grain boundaries between dissimilar phases are dominantly serrated to highly interlobate (figure 56), can also be observed on figure 51 and figure 52). The latter is well developed along the vaguely compositionally

Figure 53: Micrograph in cross-polarised light of a kink in opx, oriented subperpendicular to pre-existing exsollution lamellas. The immiscibility between opx and cpx are exaggerated along it and radiates out from it. From sample COR-10/12.

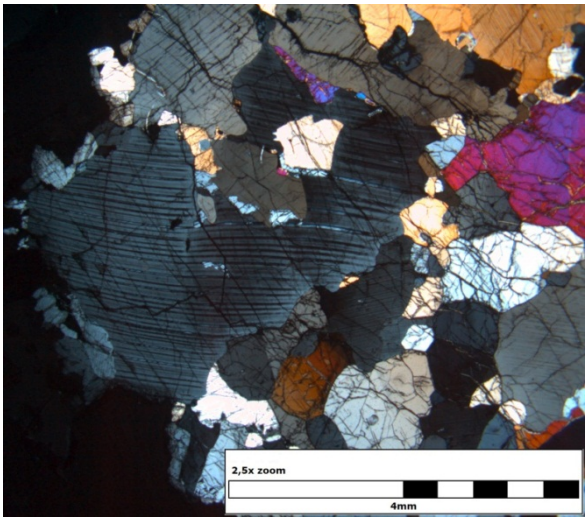

Figure 54: Micrograph in cross-polarised light of folded opx evident by pyroxene immiscibility. From sample COR-06-03D.

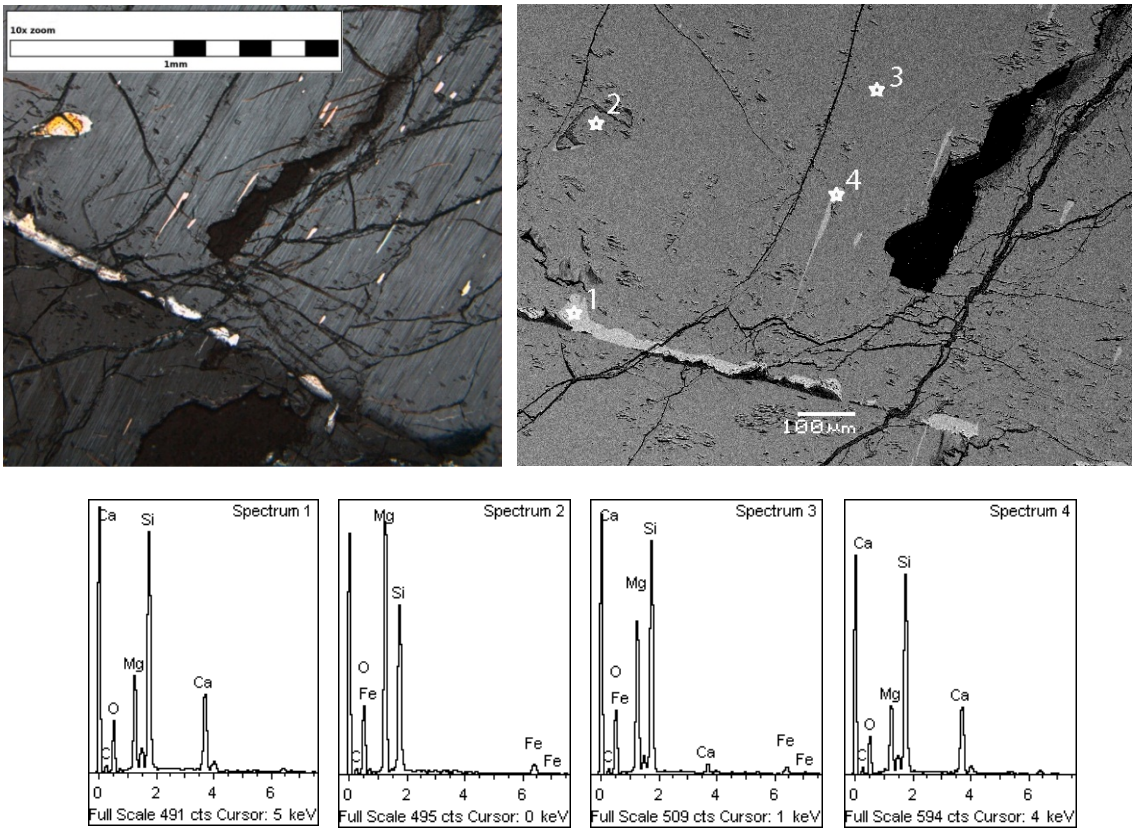

Figure 55: Micrograph in cross-polarised light and BSE image with EDS point analyses over a kink in opx. EDS point-analyses show opx with cpx exsollution lamellas radiating along and out from the kink. Spectrum 1 and 4 shows cpx exsollution lamellas. Spectrum 3 displays the opx host while spectrum 2 confirms ol as an annealed poikiloblast within the opx grain. Images and analyses from sample COR-06-03D.

banded interface, displayed on figure 56, A and figure 56, C. Some evidence of strongly serrated boundaries in ol grains have been observed in both samples. Pl exclusively displays highly interlobate grain boundaries in the extent of the thin sections for both samples (figure 47 and figure 49).

Both the spl-melagabbro and pl-spl-lherzolite displays variable development of tilt walls in ol, opx and pl, and eventually development of neoblasts in ol. This is generally well expressed in ol for both samples. Neoblasts are rarely observed in other phases. A few dislocation walls have been observed in pl and opx. These are typically poorly developed and are recognized as domainal close-spaced lineaments that have uneven extinction angles. This is visualized in opx on figure 56, C.

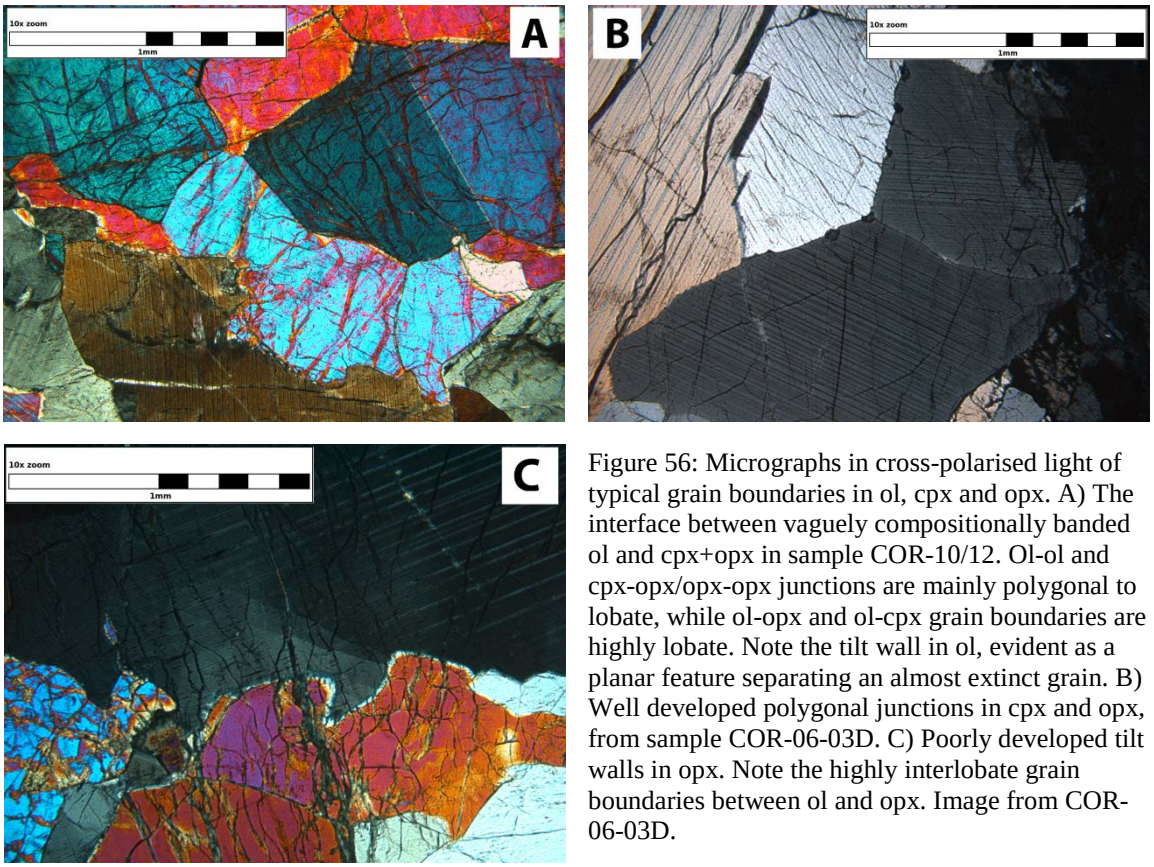

Figure 56: Micrographs in cross-polarised light of typical grain boundaries in ol, cpx and opx. A) The interface between vaguely compositionally banded ol and cpx+opx in sample COR-10/12. Ol-ol and cpx-opx/opx-opx junctions are mainly polygonal to lobate, while ol-opx and ol-cpx grain boundaries are highly lobate. Note the tilt wall in ol, evident as a planar feature separating an almost extinct grain. B) Well developed polygonal junctions in cpx and opx, from sample COR-06-03D. C) Poorly developed tilt walls in opx. Note the highly interlobate grain boundaries between ol and opx. Image from COR-06-03D.

EBSD on host rock

The ultramafic host rocks exhibit protogranular textures with relatively coarse grain sizes. Two analysed areas was mapped at scattered locations through sample COR-06-03D to investigate dislocation walls (area 1.1 and area 1.2) and one over an ol aggregate (area 1.3).

Area 1.1

Dislocation walls in an ol grain in the spl-melagabbro was investigated using EBSD and is displayed on figure 57. The location of analysis relative to the macrofabric is shown in appendix 3. The acquisitional parameters and the properties of the post-processed dataset are displayed in table 1.

Software	EDAX/TSL
Step size	3.0µm
Working distance	12.0mm
Avg. angular misfit	0.96°
Avg. image quality	96.38
Indexed fraction	0.815
#Indexed points/grains	155444 / 5

Table 1: Acquisition parameters and properties for area 1.1.

Lattice rotation is confined to three close-spaced tilt walls that are located in the centre of an elongated ol grain, 4mm along its long axis. Nonindexed phases are opx. The dislocation walls individually display <7° rotation which is insufficient to classify any of them as a subgrain boundary. These represent an early stage of recovery where dislocations eventually align into one dislocation wall (e.g. Passchier and Trouw, 2005). The tilt walls align subparallel to each other and are slightly curved. The amount of lattice rotation is largest over the middle dislocation wall.

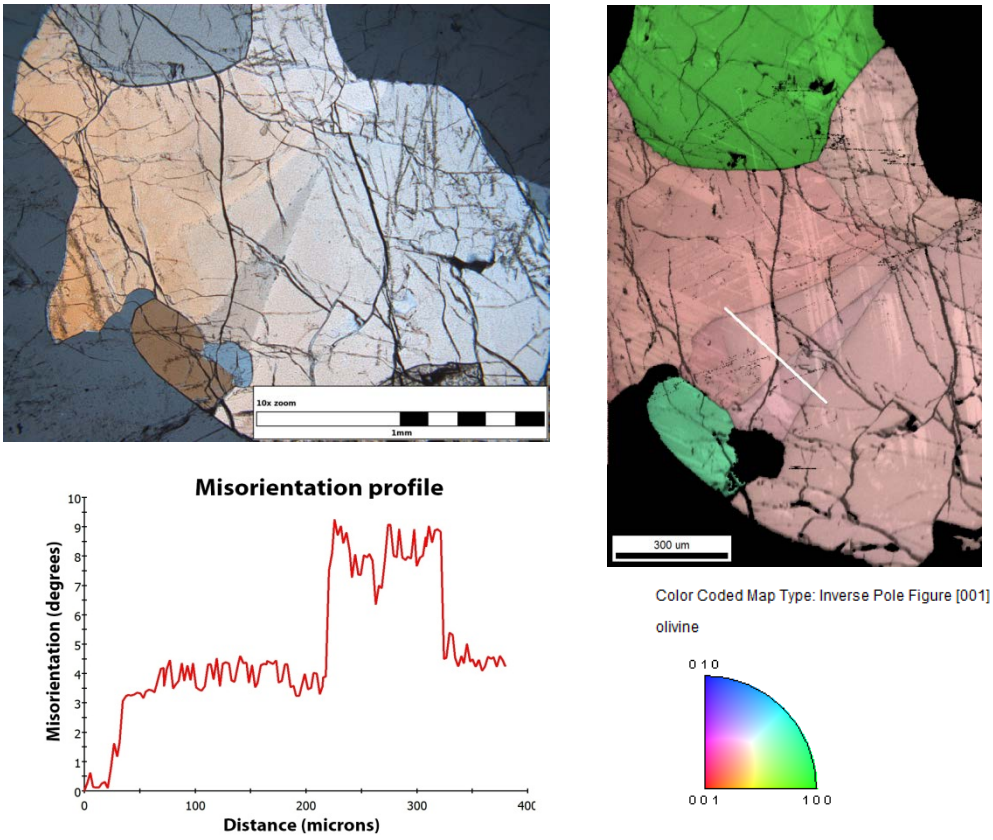

Figure 57: Area 1.1; Micrograph in cross-polarised light, IQ+IPF map and misorientation profile across dislocation walls in an ol grain in sample COR-06-03D. The IQ+IPF map is colour coded according to the unit triangle. The amount of lattice rotation along the white line on the IPF map, from upper left to bottom right, is displayed on the misorientation profile. Three shifts in misorientation represents three tilt walls that individually are rotated 3°, 6° and 5° from left to right, respectively. The total amount of lattice rotation between the two domains separated by tilt walls is ~4,5°.

Area 1.2

Dislocation walls in an ol aggregate in the spl-melagabbro was investigated using EBSD and is shown on figure 58. The location of analysis relative to the macrofabric is displayed in appendix 3. The acquisitional parameters and properties of the post-processed dataset are displayed in table 2.

Software	HKL Channel 5
Step size	5.0µm
Working distance	8.0mm
Mean angular deviation	0.35°
Avg. band contrast	79.01
Indexed fraction	0.862
#Indexed points/grains	30458/5

Table 2: Acquisition parameters and properties for area 1.2.

The ol aggregate display straight to interlobate grain boundaries between five <3mm ol grains. The nonindexed area in the upper right is opx. The central enclosed nonindexed area is pl, evident by breakdown to fine grains (figure 58). The upper central ol grain contains two subparallel dislocation walls where the amount of lattice rotation is sufficient (>10°) to classify the lower as a grain boundary. The neoblast is surrounded by high-angle grain boundaries. This attests to SGR-recrystallization. The newly formed grain boundary terminates into triple junctions on both ends. The neoblast has an interlobate high-angle grain boundary on the distal side from the dislocation wall. Adjacent ol display equilibrated textures.

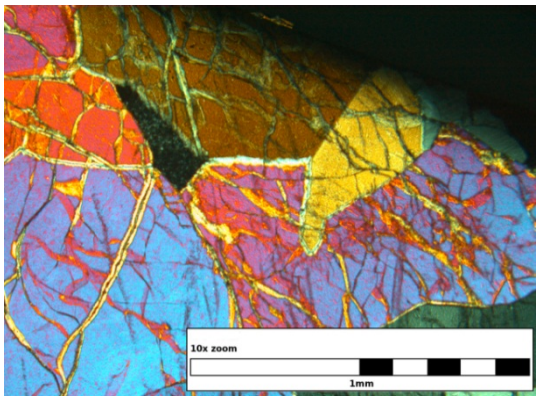

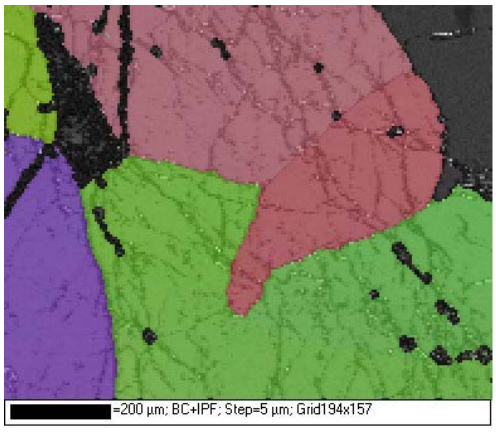

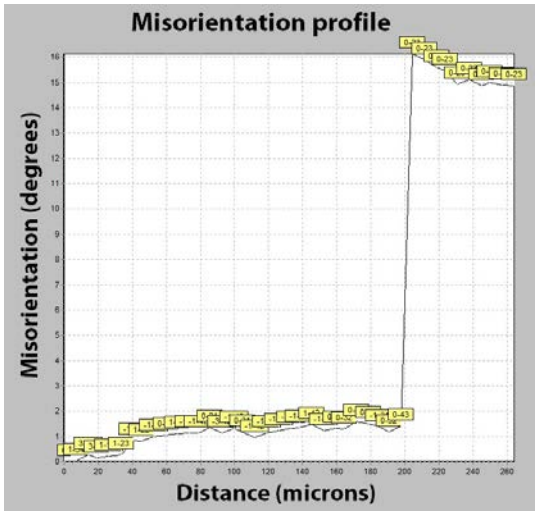

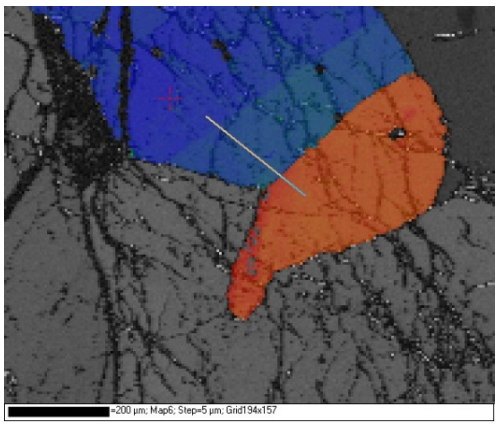

Figure 58: Area 1.2; Micrograph in cross-polarised light, BC+IPFC map, BC+TC map and misorientation profile in an ol aggregate in sample 06-03D. The area display dislocation walls and modified polygonal as well as highly interlobate grain boundaries in ol. The misorientation profile shows the amount of misorientation along the grey line, from upper left to bottom right, on the BC+TC map. The amount of lattice rotation is ~15° over the dislocation wall defined by colour coding.

Area 1.3

An attempt to estimate ultramafic host rock texture was done on an ol aggregate shown on figure 59. The location of analysis relative to the macrofabric is displayed in appendix 3. The acquisitional parameters and the properties of the post-processed dataset are displayed in table 3.

Software	EDAX/TSL
Step size	1.0µm
Working distance	12.0mm
Avg. angular misfit	1.31°
Avg. Image quality	77.91
Indexed fraction	0.668
#Indexed points	1018681

Table 3: Acquisition parameters and properties for area 1.3.

The ol aggregate displays straight to interlobate grain boundaries that link up in polygonal to modified polygonal junctions. Nonindexed phases are dominantly opx and minor spl, as well as fractures with srp that run subparallel to the vague compositional banding (figure 59).

Large grain sizes imply that few individual grains can be indexed, which is controlled by the magnification in which the EBSD data is acquired. This has particular importance for orientation data that by rule of thumb is more precise the more individual grains are projected in the dataset, and caution should be taken when assessing the projections.

The clean-up method (chapter 2) strongly altered the number of grains used for projection due to abundant nonindexed veins of srp. This is highlighted in table 3 that shows that the software has used 76 individual grains for projection, when counted individually on the IPF map there are only 13 grains. These share 6 dominant colour-coded orientations on the IPF map. This is reflected on the PF, where 6 intensity maxima are plotted.

The PF and IPF display few scattered intensity maxima, but both align poles to [010] subparallel to the vague compositional banding, whereas poles to [100] and [001] scatter.

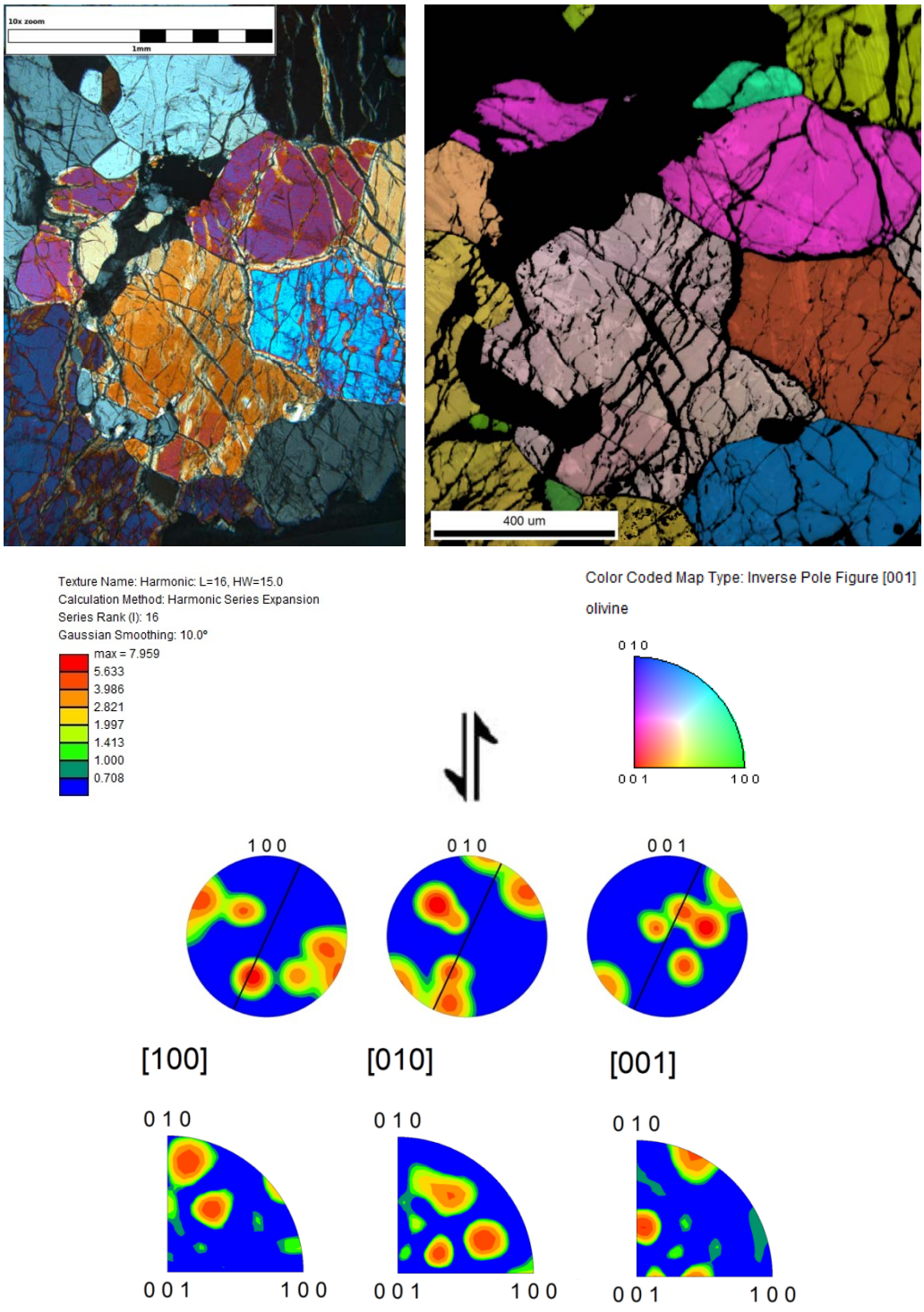

Figure 59: Area 1.3; Micrograph in cross-polarised light, IQ+IPF map, contoured PF and IPF of the three principle crystallographic axes of an ol aggregate in sample COR-06-03D. The IPF+IQ map is colour coded according to the unit triangle. The calculation parameters and the intensity of the PF are shown below the micrograph. The solid line on the contoured PF displays the orientation of the vague compositional banding. Poles to [100], [010] and [001] on the IPF corresponds to the parallel, transverse and normal direction, respectively, relative to the reference direction marked by shear direction (arrows). See text for discussion.

Fault rocks

Distribution and appearance of pseudotachylyte

The ultramafic pseudotachylytes are dark and glassy when observed using the optical microscope, found to sharply cut individual mineral grains and older veins or deformation zones in wall rock. Thin sections reveal that single faults observed in the field typically contain numerous hair-thin pseudotachylyte veins (figure 60, A). These are not recognized on outcrops, and are unevenly distributed through one or multiple close-spaced fault zones. Pseudotachylytes occur as single discrete fault-veins and injection-vein branches, which together form complex networks along strike of fault zones. The amount of pseudotachylyte along individual faults can be high or low, and vary from sample to sample, making it hard to generalize the appearance of these.

Fault-veins range in thickness from <1mm to a maximum of 380mm, the latter constrained from the field (figure 37, B, chapter 4), whereas the sampled faults typically display widths in between <1-4mm. Fault-vein size is considerably reduced by drainage into the wall rock through injection veins and as releasing bend pull-apart segments. These constitute a large volume of melt observed along fault zones. The typical geometrical relationship between fault- and injection veins (figure 3, chapter 1) is occasionally preserved, however, for most fault zones this is not the case and they form anastomosing networks that run subparallel to faults, often bridging several fault planes (figure 60, B). Observations from the field have shown similar relationships where the interplay between several close-spaced faults produce comparable features (figure 36, D and figure 37, A, chapter 4), supporting efficient drainage from fault planes on a large scale. Field relations have also shown examples of cross-cutting pseudotachylyte of different generations that might indicate a polyphase slip history (figure 40, chapter 4). On the smaller scale this manifests as re-injection, modification and offset over and along pre-existing veins (figure 60, C).

The mineralogy of the investigated thin sections containing faults are consistent with previously described pl-spl-lherzolite and spl-melagabbro where ol ≈ opx > cpx > pl > spl. It is difficult to separate between the two due to abundant granulation and alteration. All phases are thoroughly fractured and occasionally hydrated through commonly present veins of srp. Breakdown of pl has usually run to completion in the vicinity of faults. Some samples display

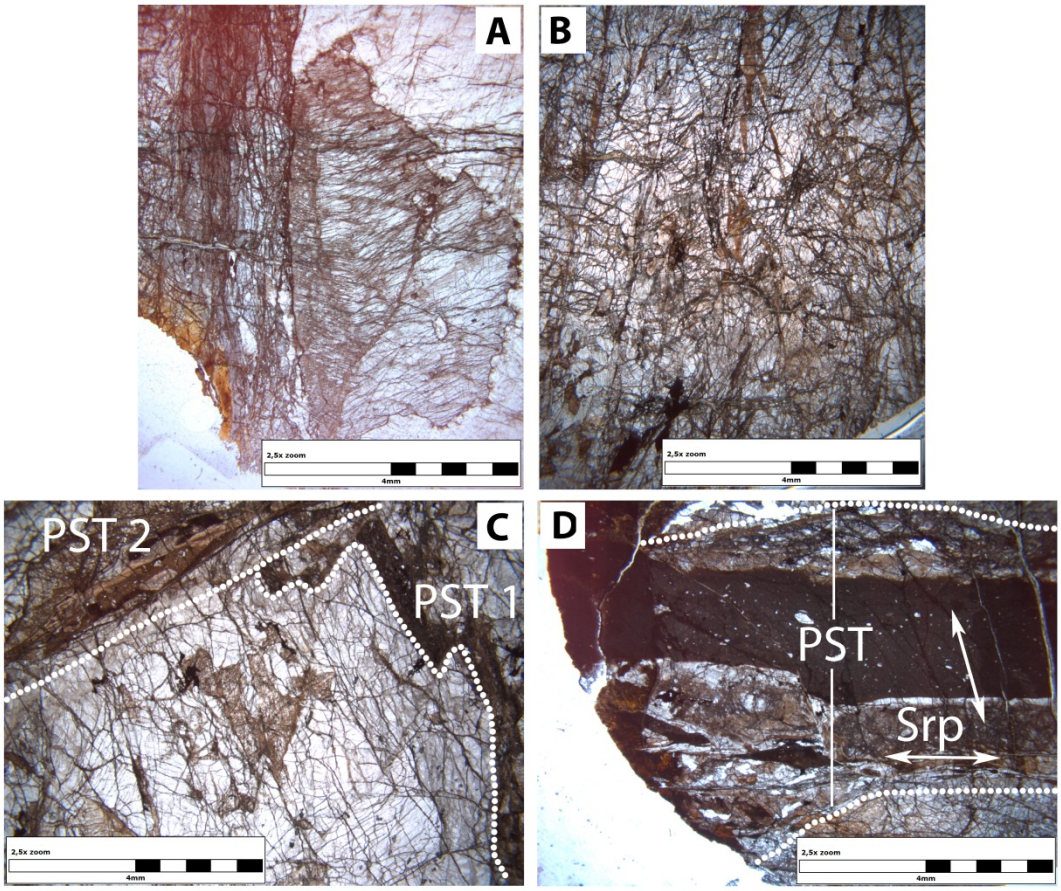

Figure 60: Micrographs in plane-polarised light of common features along faults. A) Fault zone cutting individual mineral grains with numerous hair-thin anastomosing fault- and injection veins. Note the folded cleavages in the cpx grain. From sample COR-28-05. B) Fault-and injection veins bridging several fault planes. Note the highly variable amount of pseudotachylyte along individual faults. From sample COR-04-06. C) Two generations of pseudotachylyte, evident by offset, different color and margins. From COR-13-06. D) Fault-vein (3mm wide) and associated fault zone on opposite ends containing variable amounts of pseudotachylyte along minute faults, pull-apart segments and injection-veins. Veins of srp align subparallel to the fabric and at a steep angle to it. This relationship can be observed on all four micrographs. From sample COR-05-06C.

few if any hydrous phases while others are completely altered. The most hydrated samples have been avoided in terms of investigation by EBSD. Intermediate amounts of hydration is restricted to fractures that typically run subparallel to the dominating fabric and fault-veins, in addition along recent faults that offset individual pseudotachylyte veins at a steep angle (figure 60, D).

The appearance of faulted peridotite deviates largely from the least altered host rocks. Relict texture can be found at distance from the fault zones, depending on sample width. Wide and/or several damage zones may inhibit investigation of the texture, but when observed it is typically modified and locally retains characteristics described in the previous section. The vague, inconsistent compositional banding and protogranular texture are rarely observed, and there have been found no apparent trend in grain sizes for individual phases as observed in the

least altered spl-melagabbro and pl-spl-lherzolite. Grain sizes are highly variable through the extent of the sampled faults but commonly increase from individual faults into the distal domains (figure 61, B and appendix 3).

Fault zone margins

The contact from host rock to a fault zone is characterized by two type of margins; one that truncates wall rock grains (figure 60, A, and figure 61, A and B) and one that is characterized by a strong reduction in grain size, starting a few grain widths from the distal margin of generation surfaces (figure 61). The latter domain contains peeled-off wall rock clasts enveloped in a matrix of very fine grained material, adjacent to fault(s). Peeled-off clasts align subparallel to these and are highly sheared. The fine-grained domain terminates, away from generation surfaces, into domains of larger tabular grains (figure 61, B) or a brecciated zone (figure 61, C). The interface separating fine-grained fault zone and tabular wall rock typically strikes subparallel to fault-veins. The other type of host rock-fault zone interface has sharp

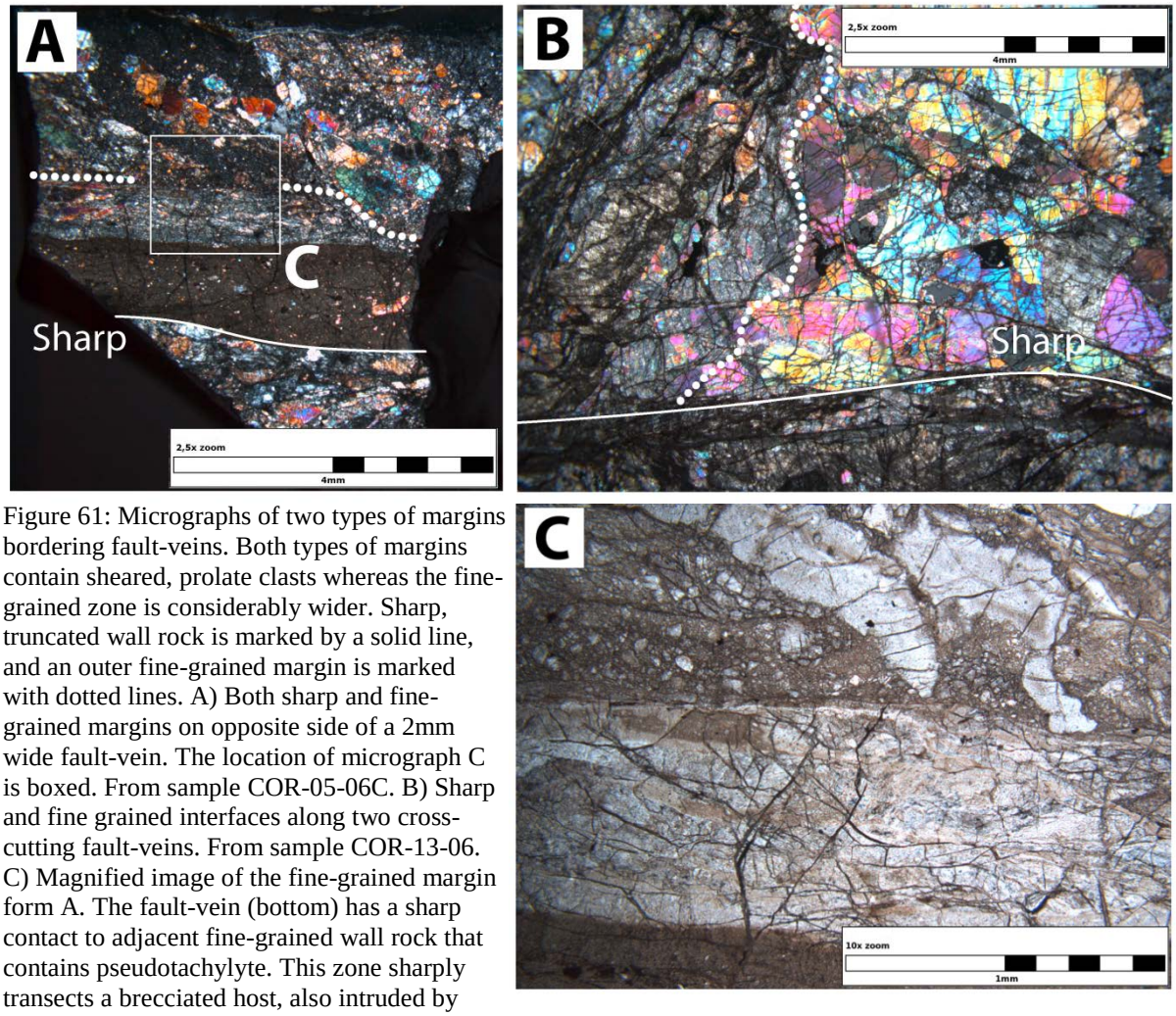

Figure 61: Micrographs of two types of margins bordering fault-veins. Both types of margins contain sheared, prolate clasts whereas the fine-grained zone is considerably wider. Sharp, truncated wall rock is marked by a solid line, and an outer fine-grained margin is marked with dotted lines. A) Both sharp and fine-grained margins on opposite side of a 2mm wide fault-vein. The location of micrograph C is boxed. From sample COR-05-06C. B) Sharp and fine grained interfaces along two cross-cutting fault-veins. From sample COR-13-06. C) Magnified image of the fine-grained margin form A. The fault-vein (bottom) has a sharp contact to adjacent fine-grained wall rock that contains pseudotachylyte. This zone sharply transects a brecciated host, also intruded by injection veins from a second fault-plane.

contacts to the host rock that may truncate individual mineral grains. These interfaces occasionally contain peeled-off clasts that show a common SPO (figure 61, A and B). Injection veins and pockets of melt are commonly found intruding both truncated and fine-grained fault zone margins.

Many fault zones display both type of margins, one on opposite side (figure 61, A), while some seems to have developed either fine grained or sharp margins to wall rock on both sides (figure 60, B, figure 60, D, respectively). Even though the fine grained fault zone margin is marked by a decrease in grain size, there is an irregular distribution of grain sizes within the zone to generation surfaces, varying from <10µm to 5mm along the long axis of prolate wall rock fragments. Ol constitute a large portion of both peeled-off clasts and fine grained material, and is easily recognized in these zones. Other phases are severely modified and 'smeared' as trails and clusters in between ol grains in the direction of slip surfaces. Identification of these phases is commonly halted by the strong fabric (figure 62). Large ol clasts are highly sheared and often isolated by converging fault planes and/or 'smeared' minerals on both ends. These clasts show pronounced undulatory extinction and variable development of tilt walls.

In both type of fault zone margins peeled-off and sheared clasts with various sizes typically rest onto fault planes. These clasts are occasionally imbricated and commonly draped by trails of very fine-grained material and/or melt (figure 61, B, figure 62). 'Smeared' phases are pl, cpx and opx. Spl also attest to modification within these domains. Pl is hardly recognizable within and adjacent to fault zones. Here, carlsbad twins have not been observed and the

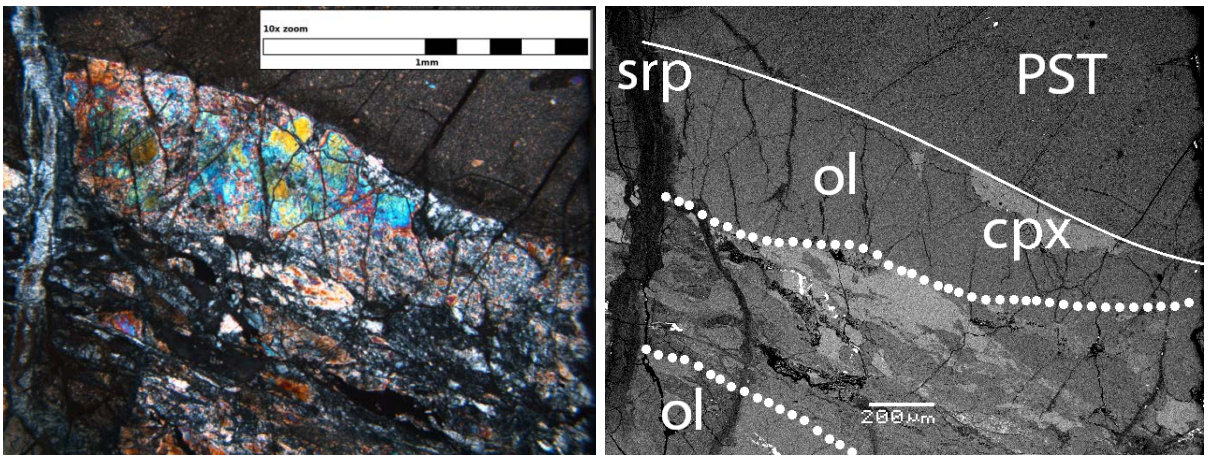

Figure 62: Micrograph in cross-polarized light and BSE image of fine grained wall rock adjacent to a pseudotachylyte fault-vein. The domain between the dotted lines shows crushed and sheared ol together with 'smeared' and elongate grains of opx, cpx, pl and spl enveloping pockets of pseudotachylyte. The 2mm ol wall rock fragment has an intact interior bordered by numerous fine grains. From sample COR-05-06C.

alteration towards a more ab-rich component and has usually run to completion, producing completely cloudy grains. These have developed extremely interlobate grain boundaries and appear as increasingly elongated trails in the vicinity of faults.

Kinking and twinning of both pyroxenes are occasionally encountered within and adjacent to both types of wall rock-fault vein interfaces. However, both phases are more frequently profoundly folded both in the distal and proximal areas relative to faults, apparent by cleavage planes and cpx/opx immiscibility (figure 60, A, figure 63 and figure 65, A). Opx or cpx grains that reside inside fault zones or terminate at fault-veins show a gradient in strain towards the fault plane(s), indicating the direction of slip along it (figure 60 A, figure 63). Rarely, offset over individual grains in truncated wall rock can be observed and used to estimate the length of slip along the fault plane/zone. An example of an offset ol grain is shown on figure 64. The ol grain on figure 64 display lamellas evident by uneven extinction angles oriented at a high angle to the fault-vein. These resemble deformation twins, however, twin-like features have not been widely addressed in literature for ol (Brothers, 1959a, b). Deformation lamellas in ol have been observed in samples COR-07-06 and COR-04-06 adjacent to fault-veins.

In distal areas, some grain widths from the outer fault zone margins, intense deformation vanes rapidly. Wall rock commonly exhibits a slight elongation onto faults that weakens at increasing distance into wall rock. In distal areas, in the extent of thin sections, wall rock retains a protogranular texture with some grain boundary migration. Ol locally possess modified polygonal junctions. Opx and cpx appear similar to those in distal host ultramafics (figure 53, figure 54), with the addition of occasionally highly folded and sheared grains at scattered locations (figure 65, A). Pl retains a cloudy appearance and highly interlobate grain boundaries. In locations where pl is not severely broken down, several grains record extensively sweeping grain boundaries with adjacent ol (figure 65, B).

Fractures and sheared bands

The faulted samples contain numerous fractures and sheared bands like those observed in the host ultramafics. Again two populations are found; one striking subparallel to pseudotachylyte fault-veins and one that strike at a high angle to these. Those that sit at high angles are offset by faults, occasionally recognized as elongate clasts within individual peeled-off wall rock grains. Such bands will be assessed in the next section.

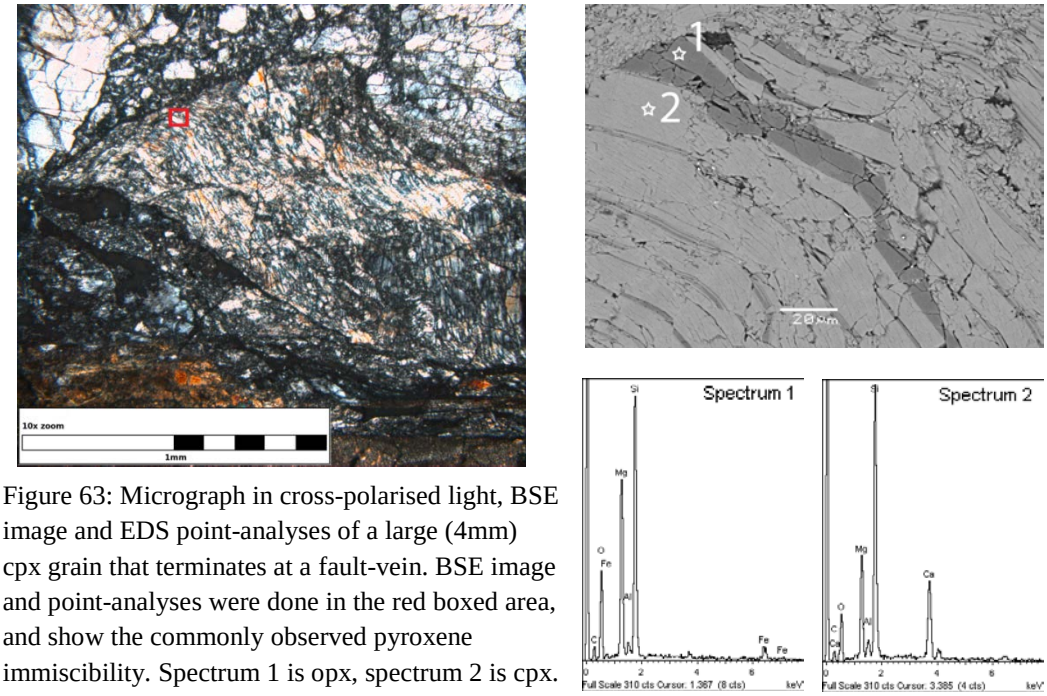

Figure 63: Micrograph in cross-polarised light, BSE image and EDS point-analyses of a large (4mm) cpx grain that terminates at a fault-vein. BSE image and point-analyses were done in the red boxed area, and show the commonly observed pyroxene immiscibility. Spectrum 1 is opx, spectrum 2 is cpx. Images and analyses from sample COR-05-06C.

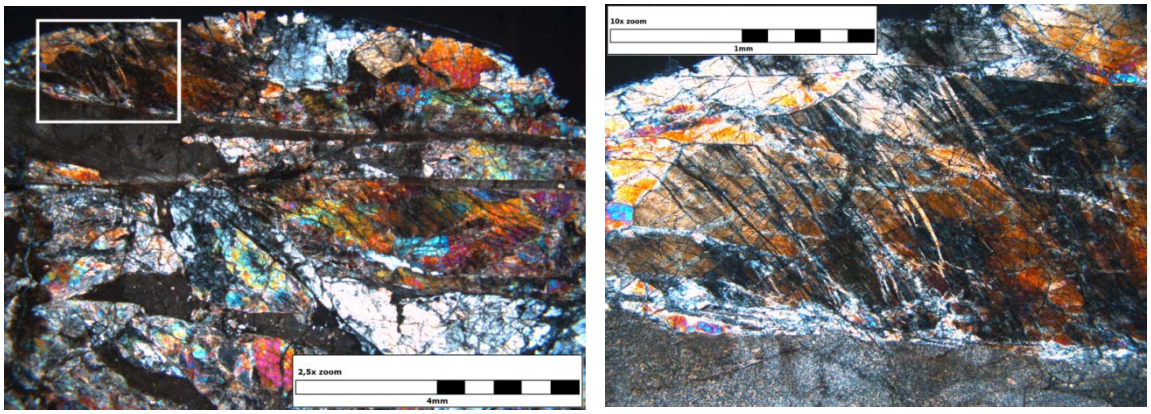

Figure 64: Micrographs in cross-polarised light of an ol grain transected by a fault-vein. The offset is approximately 8mm. The area in the white frame is magnified on the right hand side micrograph. Here, note deformation lamellas in ol and the sharp contact to the pseudotachylyte separated by a fine-grained seam. From sample COR-07-06.

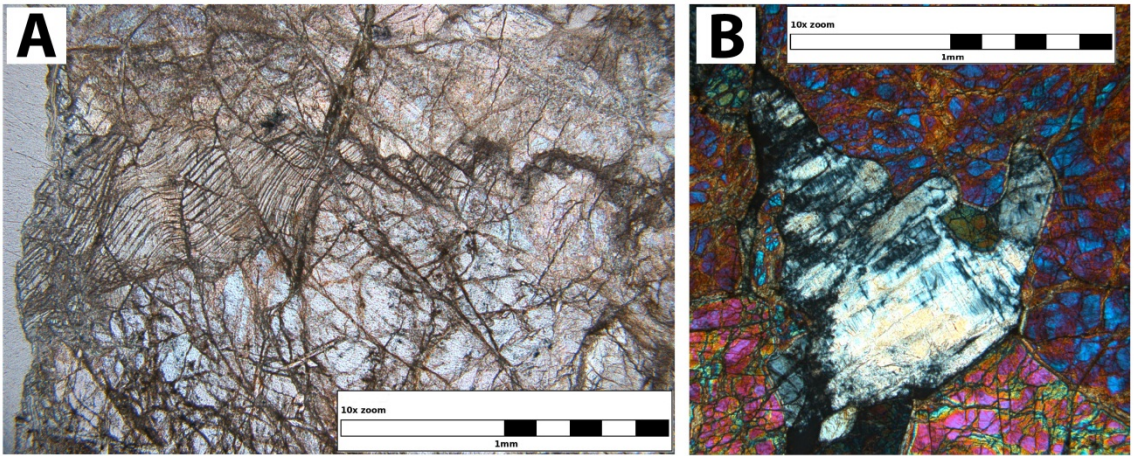

Figure 65: Micrographs in plane-polarised light of grains in distal domains, away from faults. A) Highly sheared and folded opx grain, resembling boudins. From COR-09-03. B) Relatively intact pl displaying highly interlobate grain boundaries. From sample COR-04-06.

EBSD analyses of wall-rock along pseudotachylyte fault-veins

EBSD was done on truncated wall rock, in fine grained wall rock-fault zone margins, over single discrete fault-veins and along intragranular sheared bands that align subparallel to these features. Analyses was done on two sampled faults (COR-04-06 and COR-05-06C), which together contain all fault-vein characteristics described above. The sampling locations and orientation of the respective faults are shown on figure 32 and figure 39 in chapter 4.

The aim was to investigate, and if possible quantify a progressive reduction in grain size towards fault-veins, and map the orientation of porphyroclasts within fault zones and orientation in adjacent wallrock. Subsequently, based on the results, try to constrain deformation mechanism(s) in the studied domains. Initial mapping was set up to index the two dominant phases (ol and opx), however, most of the areas selected for orientation mapping in the vicinity of faults has low total amounts of indexing. Indexation of ol adjacent to faults was relatively successful. Analyses have been investigated by purely indexing ol.

Fault sample COR-04-06

Truncated wall rock, as previously emphasized, are characterized by cut-off grains and prolate, sheared grains without a fine-grained matrix resting directly onto generation surfaces. Sample COR-04-06 contains numerous thin fault strands and sheared/fractured bands distributed within two narrow (<5mm) subparallel fault-zones (see appendix 3). The apparent offset along the fault zone is 0.8cm, and strain-averaged stresses are estimated to 40MPa (Andersen et al., 2008). EBSD analyses were done over the most distally located fault zone margin, towards wall rock (figure 66). The outer margin of one of the fault zones (area 2.1) as well as the width of the single fault (area 2.2) were investigated and are presented individually (figure 66). Outside fault zones in distal areas the sample largely retains a protogranular, massive texture with large equant grains of ol and opx with small amounts of cpx and pl. Dislocation walls in ol, folding of opx and cpx and highly interlobate grain boundaries in pl are usually encountered.

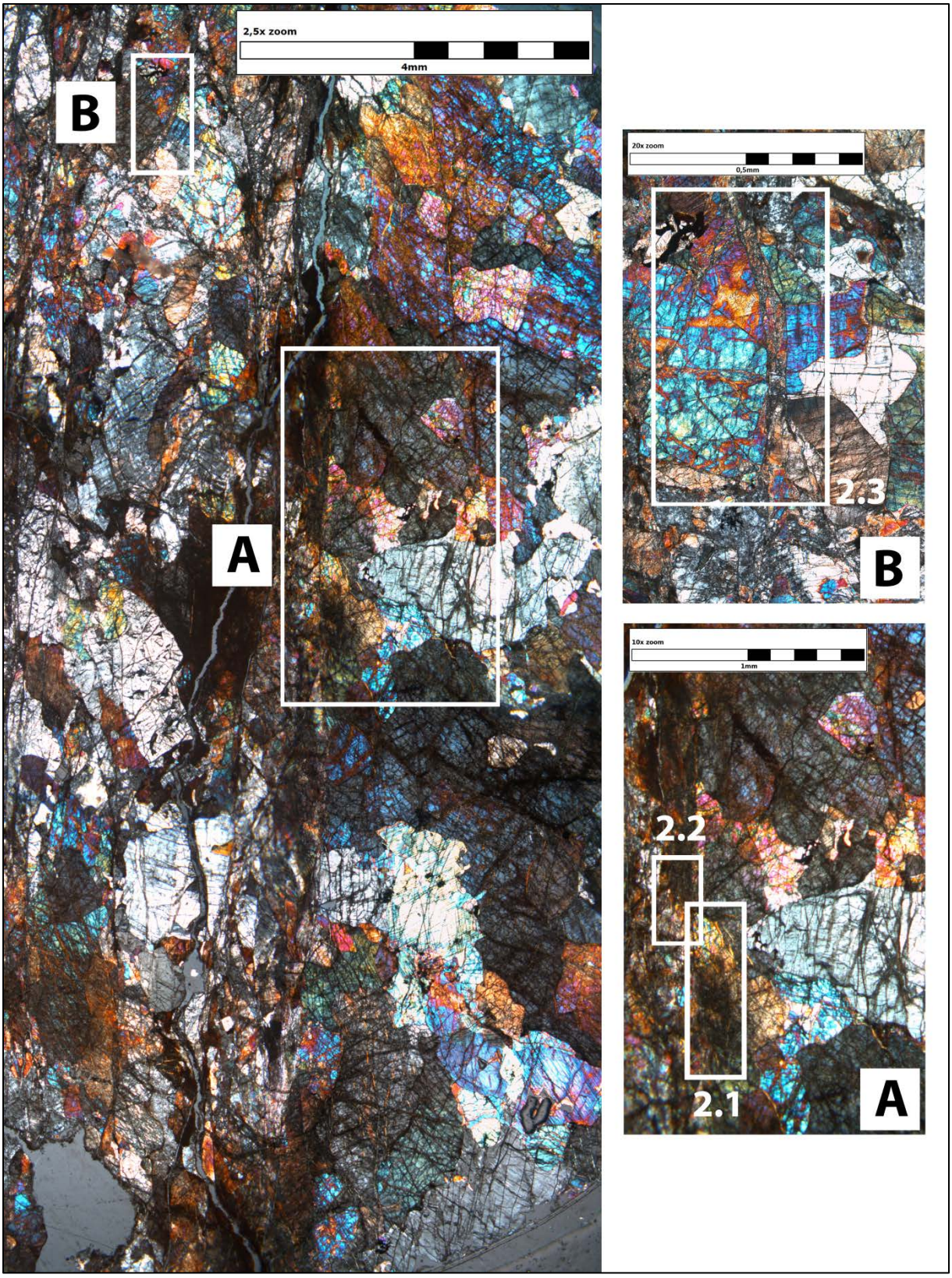

Figure 66: Photomerged section of micrographs in cross-polarized light, portraying one of the fault zones that transect the sample. Note the abundance of fractures and fine-grained bands that strike subparallel to fault(s). The boxed areas are magnified on the right-hand side. Areas selected for EBSD are numbered and indicated with white boxes. These are treated in their respective sections. The large photomerged micrograph is not completely to scale. Images from sample COR-04-06.

Area 2.1

The distal margin, relative the fault zone highlighted on figure 66, A, was selected for EBSD analysis due to abundant presence of ol. It displays truncated wall rock devoid of a fine grained matrix and peeled-off clasts in vicinity of the fault margin. The dataset was cropped into two sections, individually displaying wall rock and porphyroclasts, and the orientation of these. The datasets are displayed on figure 67. Grain size statistics are presented in figure 68, see text for details. The scan area relative to the macrofabric can be seen on figure 66 and in appendix 3. The acquisitional parameters and the properties of the post-processed datasets are displayed in table 4.

Software	EDAX/TSL
Step size	2.0µm
Working distance	8.0mm
Wall rock	Cropped map
Avg. angular misfit	1.22°
Avg. image quality	63.58
Indexed fraction	0.67
#Indexed points/grains	110750/294
Clasts	Cropped map
Avg. angular misfit	1.39°
Avg. image quality	47.17
Indexed fraction	0.11
#Indexed points/grains	10057/260

Table 4: Acquisitional parameters and properties for area 2.1.

The scan area (figure 67) display sharply truncated wall rock ol and peeled-off clasts resting in a nonindexed area. The nonindexed area represents the fault strand, extending from wall rock out of the dataset. Wall rock ol are criss-crossed by nonindexed fractures, separated by relatively planar nonindexed grain boundaries that arrange in modified polygonal triple junctions. The clasts within the fault define a SPO subparallel to the fault margin. The largest clasts display nonindexed fractures similar to that in wall rock. There is an interesting transition along the fault margin from top to bottom on the entire scan area displayed on figure 67. Some grains are cut straight off whereas the central region displays a progressive trend in both grain sizes and the elongation of these, towards the fault margin. In order to separate between wall rock and clasts, the band of minute grains in proximity of the fault margin were defined to belong to wall rock. The distance from the minute clasts to larger clasts, resting in the distal area of the fault, correlates with their distance from truncated grains. Both wall rock and clasts record similar, although poor orientations of the three principle crystallographic axes relative to the macroscopic fabric. The pole figures show few intensity maxima that correlate to the four dominant colour-coded orientations on the IPF+IQ maps. This questions any present LPO. However, the projections are not completely random. Poles to [010] align in a girdle subparallel to the fault, whereas poles to [001] and [100] scatter. Conspicuously, orientations of [010] subparallel to the defining fabric was also found in the host ultramafic, sample COR-06-03D, figure 59.

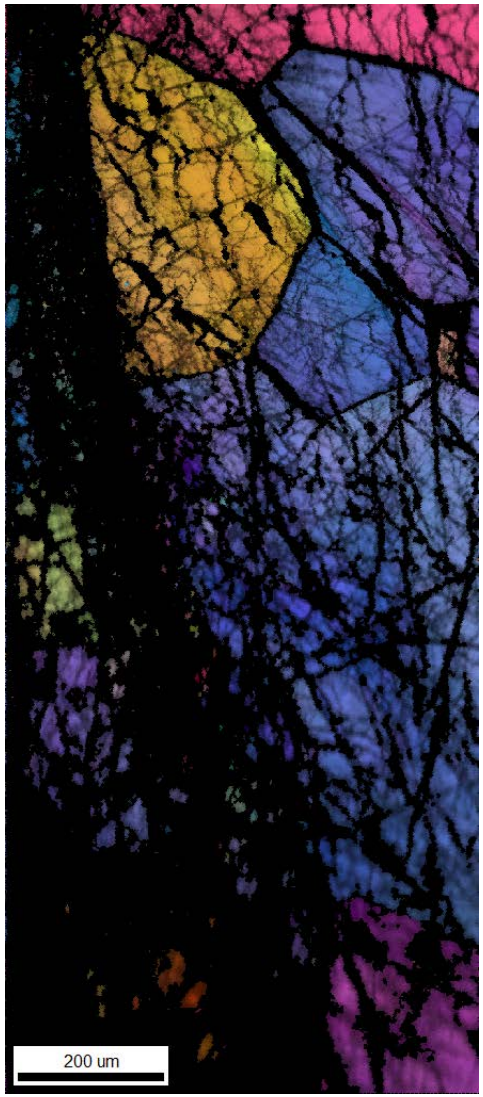

Color Coded Map Type: Inverse Pole Figure [001]

olivine

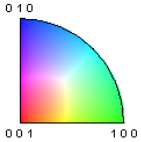

Wall rock

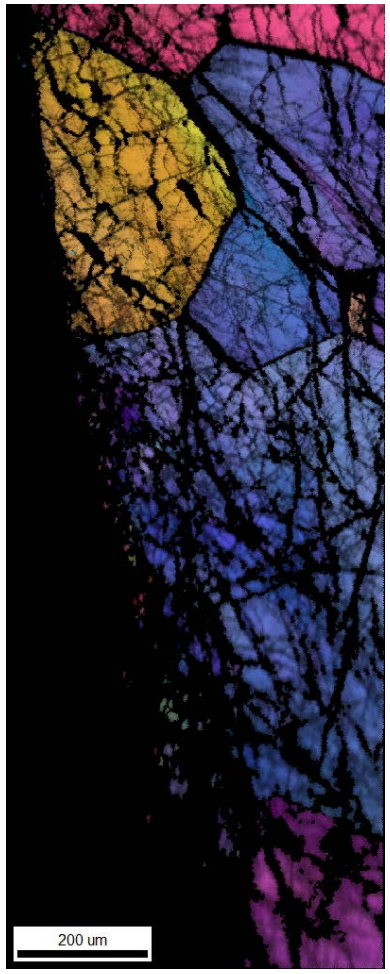

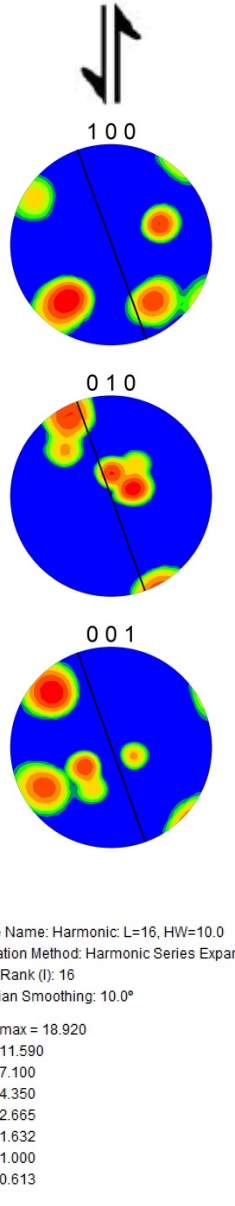

Texture Name: Harmonic: L=16, HW=10.0
Calculation Method: Harmonic Series Expansion
Series Rank (l): 16
Gaussian Smoothing: 10.0°

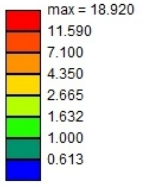

Clasts

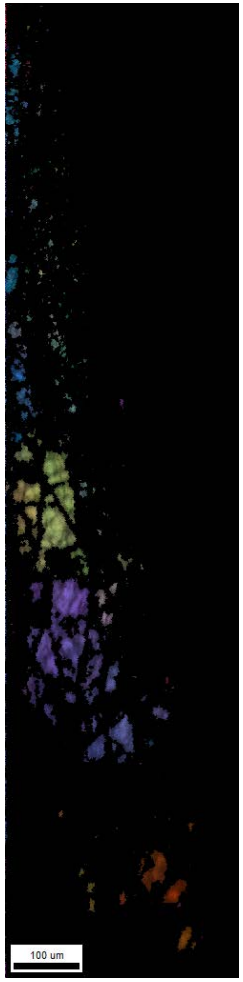

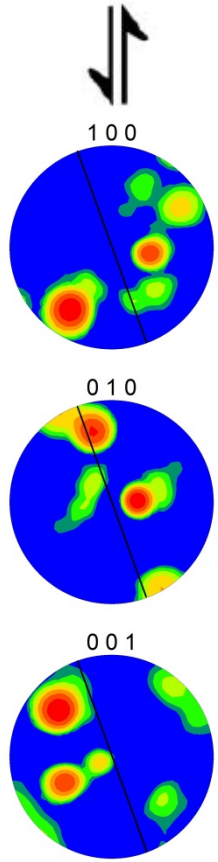

Texture Name: Harmonic: L=16, HW=10.0
Calculation Method: Harmonic Series Expansion
Series Rank (l): 16
Gaussian Smoothing: 10.0°

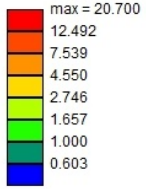

Figure 67: Area 2.1; IPF+IQ maps and contoured PF of truncated wall rock ol and peeled-off clasts. The IQ+IPF maps are colour-coded according to the unit triangle. The calculation parameters and the intensity of the PF are shown below the respective PF. The solid line on the PF displays the orientation of the fault plane, and the reference direction is marked by shear direction. See text for discussion.

In order to investigate the transitional, central domain this part of the dataset was cropped into three identically large sections (1-3, figure 68) from the distal to proximal side of the fault margin. The sections and their statistical grain size (diameter) distributions are presented on figure 68. Due to the curvature of the fault plane the true distribution of grains included in the statistics are not absolute, and restrict correlation between the three. It does, however, give an indication of the distribution from the most distal (1) to most proximal (3) area of the fault, with a mixed area in between (2) (look at the three sections on figure 68 and compare to the margin of the fault plane). From the most distal to proximal side of the fault plane there are increasing number of small grains, especially those <10µm. Domain (2) include grains at the fault-margin and display variable sizes with a large amount of small (<10µm) grains. However, the average grain size diameter from all cropped sections, including the constraints discussed, do show a progressive reduction from dataset (1) through (2) to (3).

Area 2.2

The same fault strand was targeted to investigate the highly dismembered material within it (figure 66, A). Optical microscopy in area 2.2 has shown that the wall rock on both margins is ol and that the ratio of minerals to pseudotachylyte is high within the fault. The material within the fault is largely constituted by highly fragmented and undulose ol and opx with minor trails of pl, transected by fractures filled with srp.

The dataset was cropped into two parts, individually displaying wall rock and porphyroclasts. These are displayed on figure 69. The scan area relative to the macrofabric can be seen on figure 66 and in appendix 3. Acquisitional parameters and properties of the post-processed datasets are displayed in table 5.

Software	EDAX/TSL
Step size	3.0µm
Working distance	12.0mm
Wall rock	Cropped map
Avg. angular misfit	1.39°
Avg. image quality	47.5
Indexed fraction	0.13
#Indexed points/grains	32125/175
Clasts	Cropped map
Avg. angular misfit	1.41°
Avg. image quality	38.74
Indexed fraction	0.02
#Indexed points/grains	2615/194

Table 5: Acquisitional parameters and properties for area 2.2.

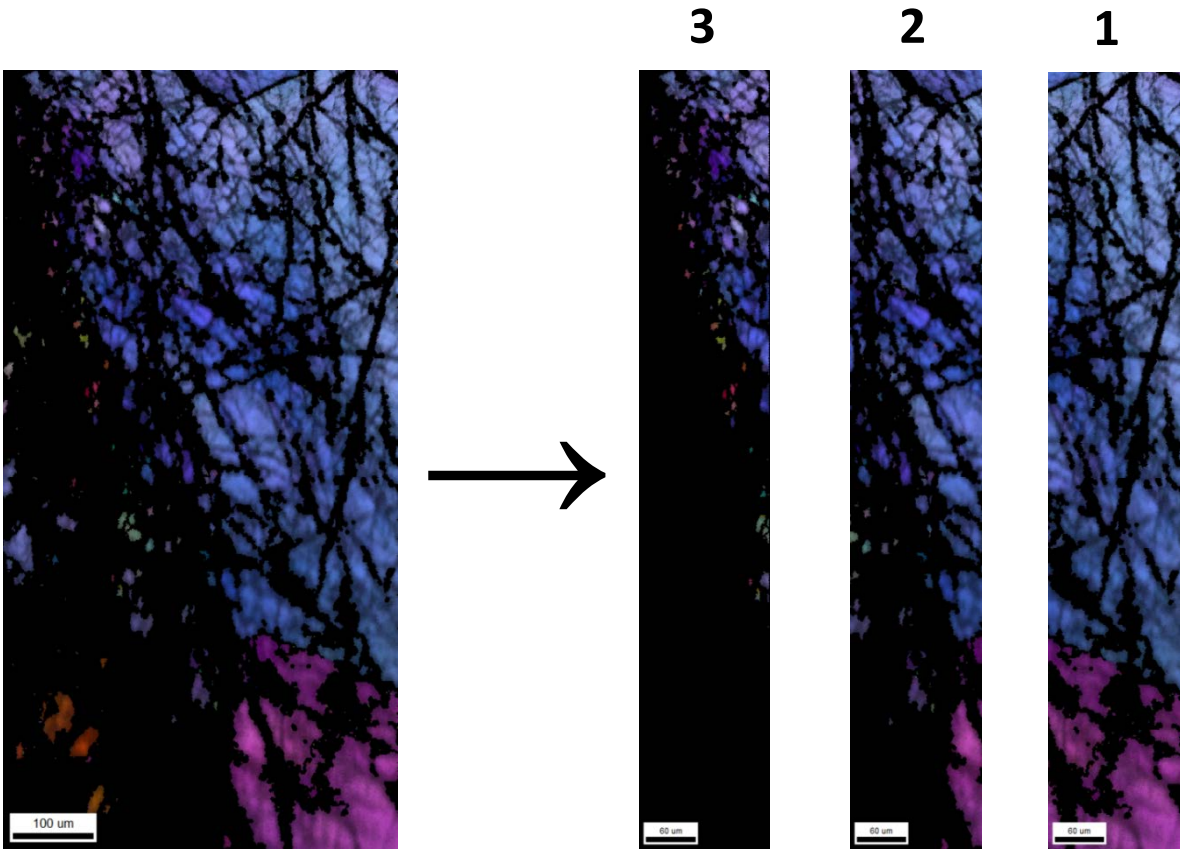

3

Chart: Grain Size (diameter)

Edge grains excluded from analysis

Diameter [microns]	Number
4.63399	52
7.96186	27
11.2897	7
14.6176	5
17.9454	3
21.2733	1
24.6012	1
27.929	1
31.2569	1
34.5848	0
37.9126	0
41.2405	1
44.5684	0
47.8962	0
51.2241	0
54.552	0
57.8798	1
61.2077	0
64.5355	0
67.8634	1

Average	
Number	8.89954
Standard Deviation	10.1664

2

Chart: Grain Size (diameter)

Edge grains excluded from analysis

Diameter [microns]	Number
4.2084	27
6.68509	32
9.16177	7
11.6385	7
14.1151	4
16.5918	1
19.0685	3
21.5452	0
24.0219	1
26.4986	4
28.9753	1
31.4519	1
33.9286	0
36.4053	0
38.882	0
41.3587	0
43.8354	0
46.312	0
48.7887	0
51.2654	1

Average	
Number	9.24858
Standard Deviation	8.08752

1

Chart: Grain Size (diameter)

Edge grains excluded from analysis

Diameter [microns]	Number
4.81202	37
8.49593	5
12.1798	5
15.8638	0
19.5477	2
23.2316	2
26.9155	2
30.5994	1
34.2833	0
37.9672	0
41.6511	0
45.335	0
49.019	0
52.7029	0
56.3868	1
60.0707	1
63.7546	1
67.4385	0
71.1224	0
74.8063	1

Average	
Number	11.6648
Standard Deviation	16.1931

Figure 68: Cropped IQ+IPF maps and grain size diameter statistics from the central, transitional domain in area 2.1. Edge grains are excluded from the calculations. From the distal area (1) to the proximal area (3), relative to the fault, there are increasing numbers of small grains. The smallest recorded grains are 4,2µm, whereas the step size used was set to 2.0µm (table 4).

The scan area (figure 69) shows that the indexation of ol clasts within the fault is extremely low (table 5). Opx and pl constitute some of the nonindexed volume, however the small indexation of ol is atypical from previously acquired datasets. The fault sharply truncates two ol grains on either side. The wall rock grains colour-coded red and yellow (figure 69) are the same truncated grains from the previous dataset (figure 67). The offset on the fault strand, based on separation of these two grains is approximately 0.5mm. Clasts in the fault strand range in size from 40-3µm (the step size) with a dominant proportion of clasts <10µm. These show a SPO subparallel to fault margins.

Both wall rock and clasts within the small fault strand show apparently strong and similar orientations of their three principle crystallographic axes (figure 69). There is a larger scatter for clasts. However, the amount of individual grains used for projection from both wall rock and clasts are very low and may not properly represent a LPO. The number of grains used for projection from wall rock orientations are 194 (table 5), however, when counted on the IPF+IQ map there are actually only two separated grains. This is reflected on the contoured PF.

On comparing area 2.1 (figure 67) and area 2.2 (figure 69), along the very same fault, shows that wall rock and clasts in area 2.2 seemingly has developed a strong orientation on either [100](010) or [010](100) as suggested by Ave'Lallemant and Carter (1970). Poles to [001] largely project out of the dataset. These orientations are devoid in area 2.1, further questioning the validity of a strong LPO in area 2.2.

Color Coded Map Type: Inverse Pole Figure [001]

olivine

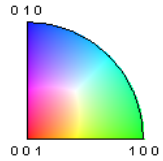

Wall rock

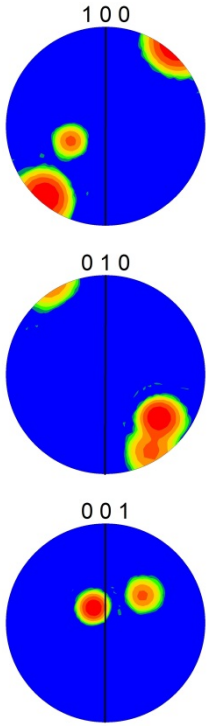

Texture Name: Harmonic: L=16, HW=10.0
Calculation Method: Harmonic Series Expansion
Series Rank (l): 16
Gaussian Smoothing: 10.0°

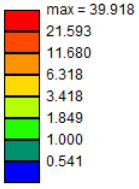

Clasts

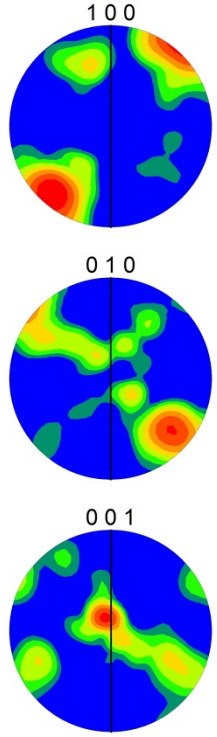

Texture Name: Harmonic: L=16, HW=10.0
Calculation Method: Harmonic Series Expansion
Series Rank (l): 16
Gaussian Smoothing: 10.0°

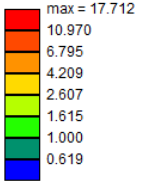

Figure 69: Area 2.2; IPF+IQ maps and contoured PF of truncated wall rock ol and peeled-off clasts. The IPF maps are colour-coded according to the unit triangle. The calculation parameters and the intensity of the projections are shown below the respective PF. The solid line on the PFs displays the orientation of the fault plane, and the reference direction is marked by the shear direction (arrows). See text for discussion.

Area 2.3

Sample COR-04-06 contains numerous fractures and sheared bands (figure 66) previously described in samples without pseudotachylytes (figure 51 and figure 52).

Software	EDAX/TSL
Step size	1.0µm
Working distance	12.0mm
Wall rock	Cropped map
Avg. angular misfit	1.30°
Avg. image quality	55.84
Indexed fraction	0.521
#Indexed points/clasts	899920/5116
Clasts	Cropped map
Avg. angular misfit	1.36°
Avg. image quality	47.81
Indexed fraction	0.17
#Indexed points/clasts	34496/1385

Table 6: Acquisitional parameters and properties for area 2.3.

Such fractures and bands are evident as planar features offsetting individual grains, and as wider (<0,5mm) zones with prolate clasts. In sample COR-04-06, both types of bands strike subparallel to the two fault zones that transect the sample. Area 2.3 was done over a <0.2mm wide fracture with prolate clasts of ol, opx, cpx and pl (figure 66, B). The band does not contain any trace of pseudotachylyte. The dataset was cropped into two parts, individually displaying wall rock and clasts in the fracture. The datasets are displayed on figure 70. The scan area relative to the macrofabric can be seen on figure 66 and in appendix 3. Acquisitional parameters and properties of the post-processed datasets are displayed in table 6.

The IQ+IPF map of the entire dataset (figure 70) display large ol grains transected by a variably indexed fracture containing prolate clasts. Wall rock ol attest to planar nonindexed grain boundaries, and are separated by fractures and patches with not indexed phases. Nonindexed large grains are constituted by opx, pl, and spl (figure 66, B). Narrow fractures within ol, opx and pl host rock grains are filled with srp. The fracture with clasts transects the host at a sharp interface and contains elongated, at times imbricated ol that range in diameter from 40-5µm with a dominant portion of clasts <20µm. The band has thin nonindexed margins of srp. The lower half of band is not indexed and largely contains opx and pl (figure 66, B).

Scan area 2.3 contains numerous indexed and oriented ol grains in the fracture (see table 6), and the orientation of these correlate to the wall rock. The number of grains used for projection in wall rock is amplified by abundant fractures. The IPF map and PF for wall rock display four dominant colour-coded grains and four intensity maxima, respectively. There is a scatter in maxima intensity for the clasts relative to wall rock. For both domains, [001] axes align subparallel to the macroscopic fabric defined by the two fault zones and to

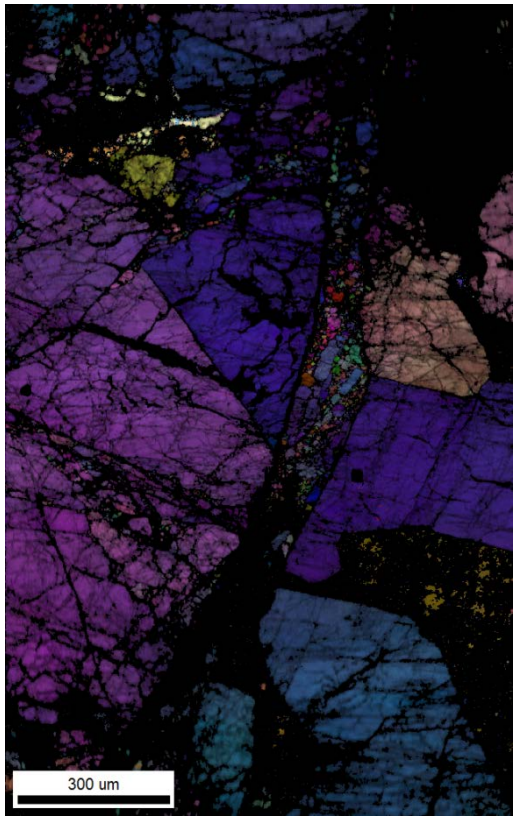

Color Coded Map Type: Inverse Pole Figure [001]

olivine

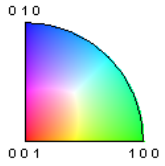

Wall rock

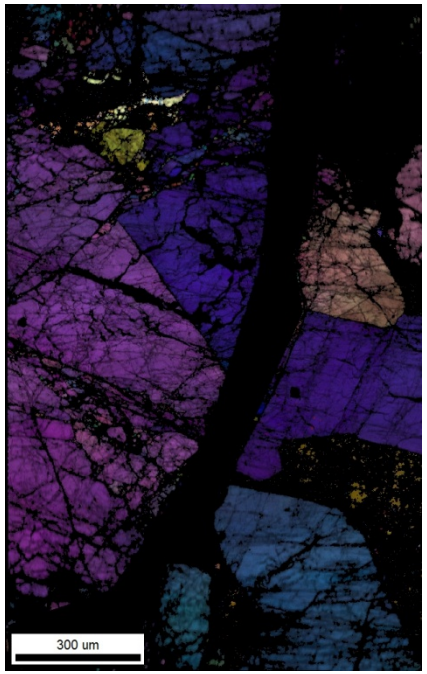

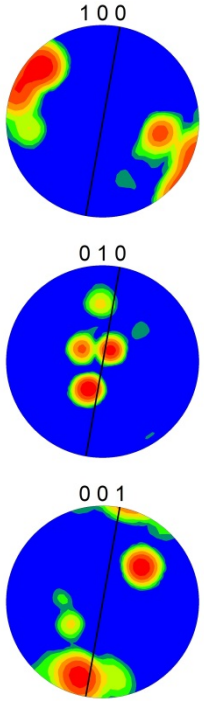

Texture Name: Harmonic: L=16, HW=10.0
Calculation Method: Harmonic Series Expansion
Series Rank (l): 16
Gaussian Smoothing: 10.0°

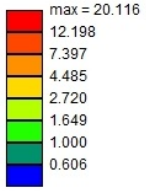

Clasts

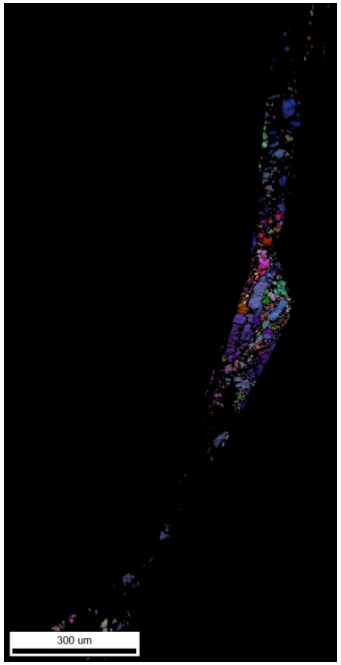

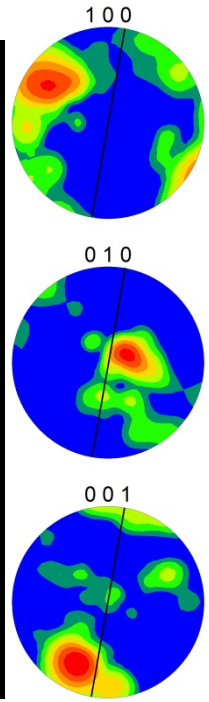

Texture Name: Harmonic: L=16, HW=10.0
Calculation Method: Harmonic Series Expansion
Series Rank (l): 16
Gaussian Smoothing: 10.0°

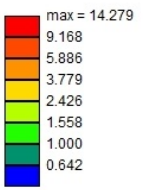

Figure 70: Area 2.3; IPF+IQ maps and contoured PF of wall rock ol and an intragranular fracture containing prolate clasts. The IPF maps are colour-coded according to the unit triangle. The calculation parameters and the intensity of the projections are shown below the respective PF. The solid line on the PF displays the orientation of intragranular fracture, and the reference direction is marked by shear direction (arrows). See text for discussion.

the fracture (figure 66), with [100] axes normal to these. Axes of [010] largely project into/out of the dataset (figure 70). The apparent strong LPO might represent activity on [001](100), as proposed by Ave'Lallemant and Carter (1970).

COR-04-06 EBSD wrap-up

The three areas investigated with EBSD in sample COR-04-06 display poor, if any, to apparent well developed LPO for ol in the mapped sections. All mapped sections were investigated along the same fault zone reference surface, and faults and fractures sharply truncate wall rock in all investigated areas. Clasts share a SPO subparallel to these features. In all datasets, both wall rock and clasts, in either faults or fracture individually display similar crystallographic orientations. One slip system has been observed for area 2.3 along the intragranular sheared fracture. Wall rock in area 2.1 display [010] axes that align subparallel to the fault zones, this is consistent with previously investigated host rock sample COR-06-03D. Area 2.2 may indicate slip along [100](010) or [010](100), however this is highly uncertain due to few indexed grains.

Fault sample COR-05-06C

The sample displays a <1,5cm fault zone that constitute most of the extent of the thin section (figure 71, appendix 3). The apparent slip is estimated to 18.3cm and estimated strain-averaged stress is 135MPa (Andersen et al., 2008). Two prominent subparallel pseudotachylyte fault-veins ranging from 3mm-0.5mm are enveloped by associated damage zones in highly deformed, fine grained fault zone margins (figure 71). Numerous hair-thin fault veins are found within these margins. Minor preserved patches of host rock are preserved in distal parts of the sample, away from the fault zone. These attest to severely modified textures where polygonal junctions are rarely observed (figure 71).

As previously emphasized, fine grained fault zone margins are characterized by a strong reduction in grain size that separate wall rock and slip surfaces. Within these, larger sheared and prolate clasts align subparallel to generation surfaces and are enveloped by fine-grained trails, 'smeared' phases and/or converging fault planes. In sample COR-05-06C, highly undulose ol constitute the dominant portion of dismembered material and wall rock fragments within these margins. Pl is commonly completely broken down and attests to high degree of grain boundary mobility, frequently' injecting' along fractures and fault zones.

EBSD analyses were done at spaced intervals within the distal side of a fine grained fault zone margin, relative to pseudotachylyte fault-veins. This fault margin and the location of analyses along it are displayed on figure 71, A. The width of the margin is elaborate due to large, ~8mm sheared grains of ol and opx, which halts assessment of its lateral continuity. The two large ol and opx grains are highly deformed, witnessed by numerous subgrains in ol and faults imbricating the large opx grain (figure 71). Both phases are elongated subparallel to the fine grained fault zone margin. The ol grain contains several cataclastic bands that sit at a high angle to fault-veins. Thin fault-veins within the fine grained zone transect the large ol grain at its lower rim. Area 3.1 was done along the interface between an ol subgrain and fault-veins, whereas areas 3.2 and 3.3 were done on sheared clasts within the fine grained margin (figure 71, A).

Area 3.4 was done in the internal fault zone that separates the two wide pseudotchylyte fault-veins (figure 71, B). This area is adjacent to a fracture that has injection veins ramifying off it (figure 71), representing a concealed generation surface by almost complete drainage of pseudotachylyte. The brecciated aggregate of ol, opx and pl has been described on figure 61, C.

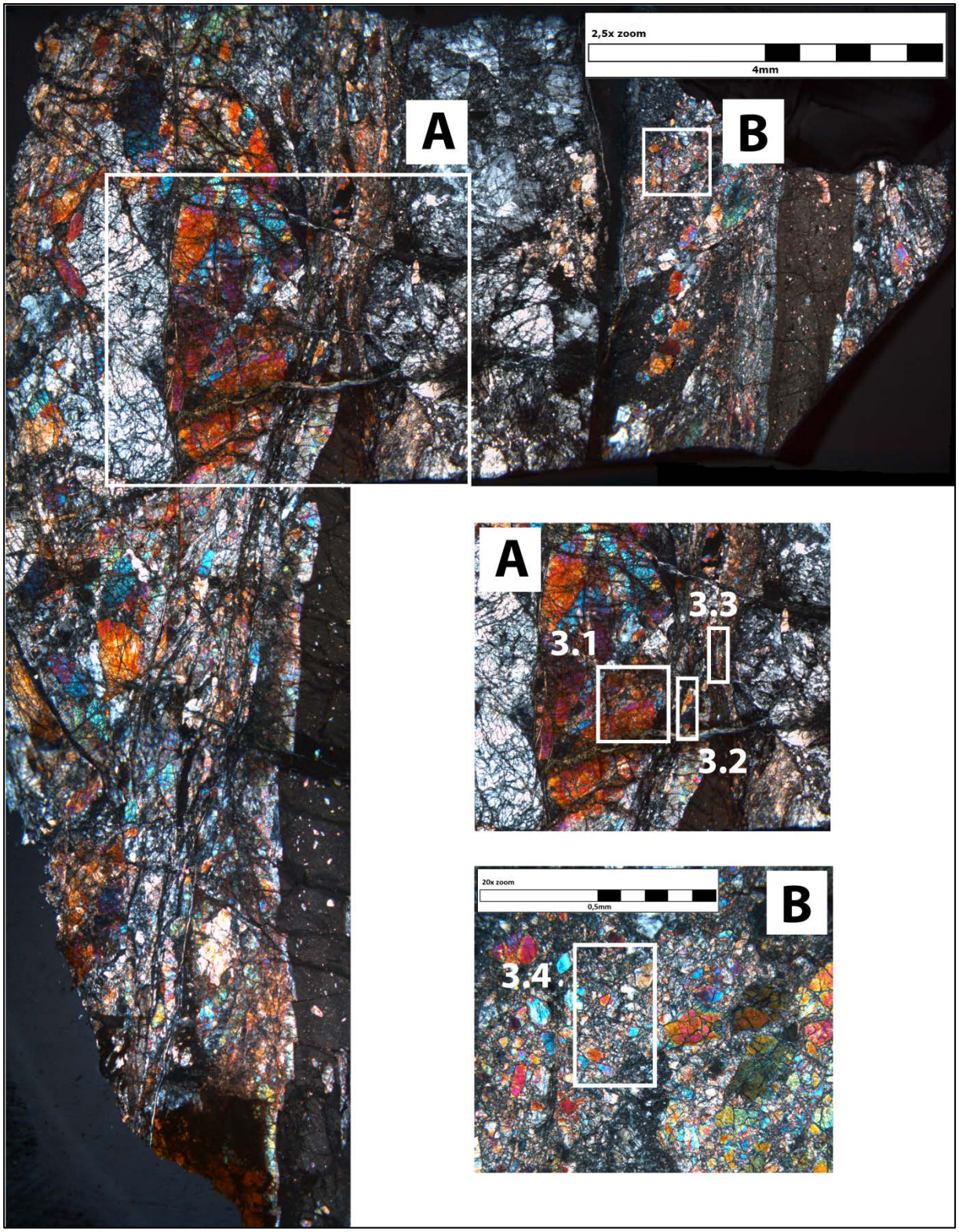

Figure 71: Photomerged section of micrographs in cross-polarised light, portraying a distal, fine grained fault zone margin (left) and the internal damage zone relative to pseudotachylyte fault-veins. The wide, distal fine grained margin is difficult to trace, halted by the size of the sample and by two large ol and opx grains, highlighted in A. Note injection veins ramifying off of the fracture adjacent to area B. Areas selected for EBSD are numbered and indicated with white boxes. These are treated in their respective sections. The large photomerged micrograph is not completely to scale. From sample COR-05-06C.

Area 3.1

The interface between the large (~8mm) ol grain and fault vein(s) within the fine grained fault zone (figure 71, A) was mapped. Exploration of any progressive development in grain size and orientation from distal to proximal side in the subgrain was done, relative to the fault zone. Area 3.1 was cropped and highlighted into four datasets. These individually display the ol subgrain (termed wall rock) and clasts in the fine grained zone, displayed on figure 72. A fracture with clasts and the margin of the ol wall rock, relative to fault zone are highlighted maps and displayed on figure 73. Investigation of grain sizes over the analysed area is presented on figure 74. See below for descriptions. The scan area relative to the macroscopic fabric is displayed on figure 71 and in appendix 3. The acquisitional parameters and properties of the post-processed datasets are displayed in table 7.

Software	EDAX/TSL
Step size	1.0µm
Working distance	10.0mm
Wall rock	Cropped map
Avg. angular misfit	1.38°
Avg. image quality	45.05
Indexed fraction	0.291
#Indexed points/clasts	371722/7588
Clasts	Cropped map
Avg. angular misfit	1.27°
Avg. image quality	39.73
Indexed fraction	0.008
#Indexed points/clasts	1995/146
Clasts in fracture	Highlighted map
Avg. angular misfit	1.34°
Avg. image quality	42.82
Indexed fraction	-
#Indexed points/clasts	22058/699
Wall rock margin	Highlighted map
Avg. angular misfit	1.30°
Avg. image quality	41.79
Indexed fraction	-
#Indexed points/clasts	9955/483

Table 7: Acquisitional parameters and properties of datasets in area 3.1.

The IQ+IPF map of the analysed area (figure 72) display one of the subgrains in the large ol grain. It is cut at the top, bottom and to the left by nonindexed veins of srp, and to the right by the nonindexed fine grained fault zone with pseudotachylyte (figure 71). Wall rock is internally crisscrossed by nonindexed fractures filled with srp (figure 72). A fracture with elongate clasts transects wall rock. It extends from central left to right on the IQ+IPF map, evident by an array of colour-coded grains that differ from the colour-coding of surrounding grains. These share a SPO subparallel to the direction of the fracture.

The nonindexed, fine grained fault zone contains a very small fraction of indexed clasts (table 7). These range in diameter from 20-1.0µm (the step size) and share a SPO subparallel to the margin of the wall rock. An interesting feature is that no part of the wall rock margin is

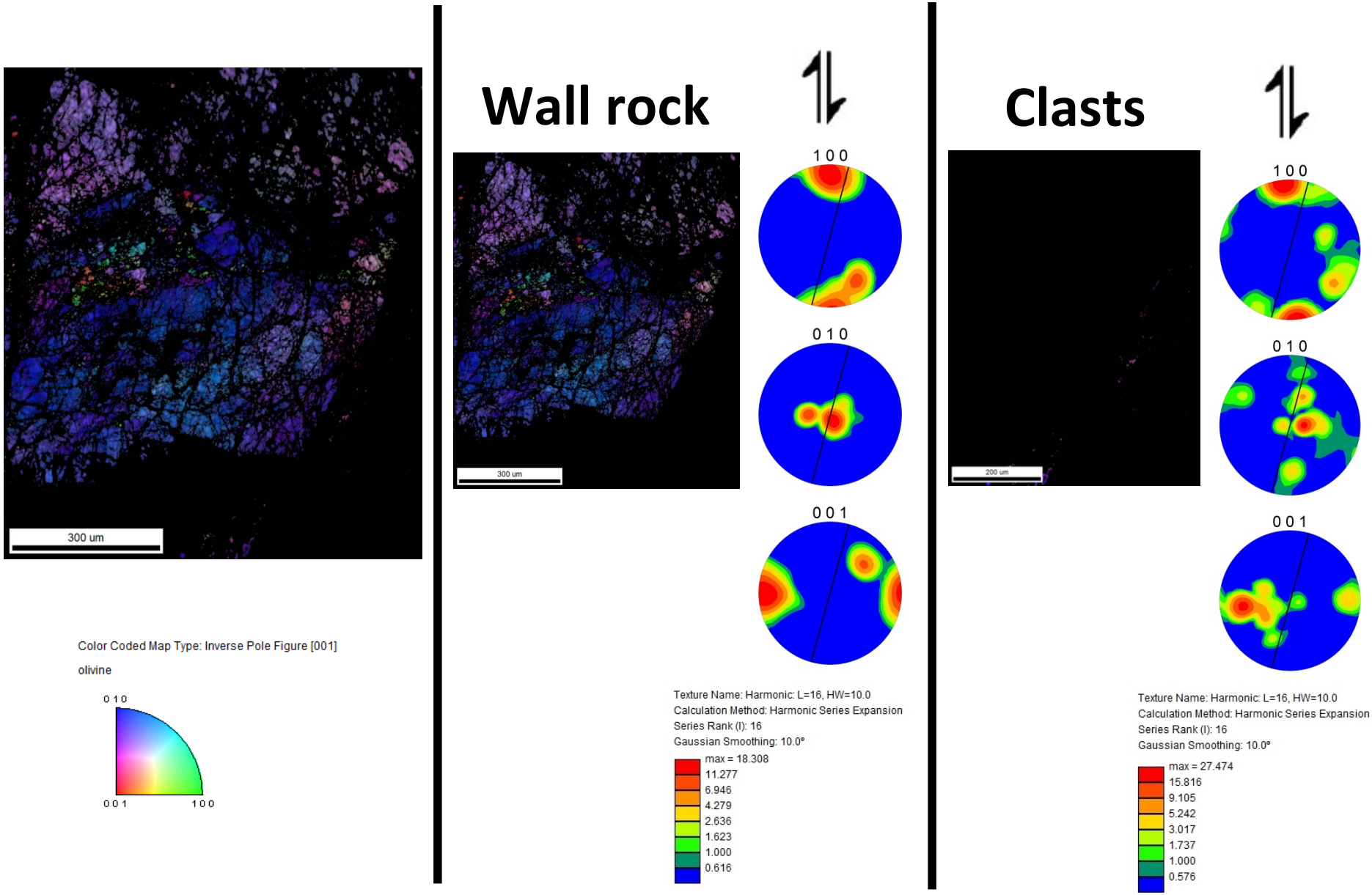

Figure 72: Area 3.1; IQ+IP maps and contoured PF of truncated wall rock ol and peeled-off clasts. The IPF maps are colour-coded according to the unit triangle. The calculation parameters and the intensity of the projections are shown below the respective PF. The solid line on the PF displays the orientation of the fault plane, and the reference direction is marked by shear direction (arrows). See text for discussion.

truncated like that found in sample COR-04-06, on figure 67 and figure 69. In the ol subgrain (figure 72), from distal to proximal side in wall rock, ol separated by veins of srp progressively elongate in vicinity to the fine grained fault zone. A population of small grains that rest directly on the interface to the fine grained fault zone margin deviates in orientation from that in wall rock. Both wall rock and clasts in the fault zone display relatively similar orientations for the three principle crystallographic axes in ol (figure 72). The number of grains used for projection in wall rock (table 7) is sufficient to suggest a LPO where poles to [100] align subparallel to the macroscopic fabric (figure 71) with poles to [001] normal to these. Poles to [010] largely project out of the analysed area, proposing activity on the [100](001) slip system as proposed by Ave'Lallemant and Carter (1970).

Clasts in the fracture transecting wall rock, and the population of small grains located on the wall rock margin to the fault zone was highlighted and treated individually. This was done due to their orientations deviating from that in bulk wall rock. Highlighting was done using IPF maps for easier selection of individual grains. The highlighted maps are presented on figure 73. Grains that arrange at the highlighted wall rock margin and clasts in fracture (figure 73) display orientations almost identical to wall rock (figure 72). The clasts at the wall rock margin show similar orientation of poles to [100], whereas [010] and [001] are oriented differently. Nonetheless, both domains correlate to the overall texture found in wall rock.

In order to investigate grain size distribution in the ol subgrain, relative to the fault zone, the dataset was cropped into four identically large sections. The sections and their statistical grain size (diameter) distributions are presented on figure 74. Grains terminating at the edges of the sections were not included in the statistics. Due to the curvature of the fault plane, uneven distribution of srp veins and internal features in the ol subgrain, the true distribution of grains included in the statistics are not absolute and restrict correlation between the four areas. The sections have huge differences in the amount of indexed material, and sections (1) and (2) include fine grained clasts in the fracture. However, the statistics give an indication of the distribution from the most distal (1) to most proximal (4) section relative to the fault. From distal to proximal side of the fault zone there is an abrupt decrease in the largest grains identified and used for calculation, coupled with an increasing range of grains <10µm (figure 74). The average grain size diameter from all cropped sections, including the constraints discussed, show a progressive reduction from the distal (1) to proximal (4) side relative to the fault zone, both in diameter and two-dimensional surface.

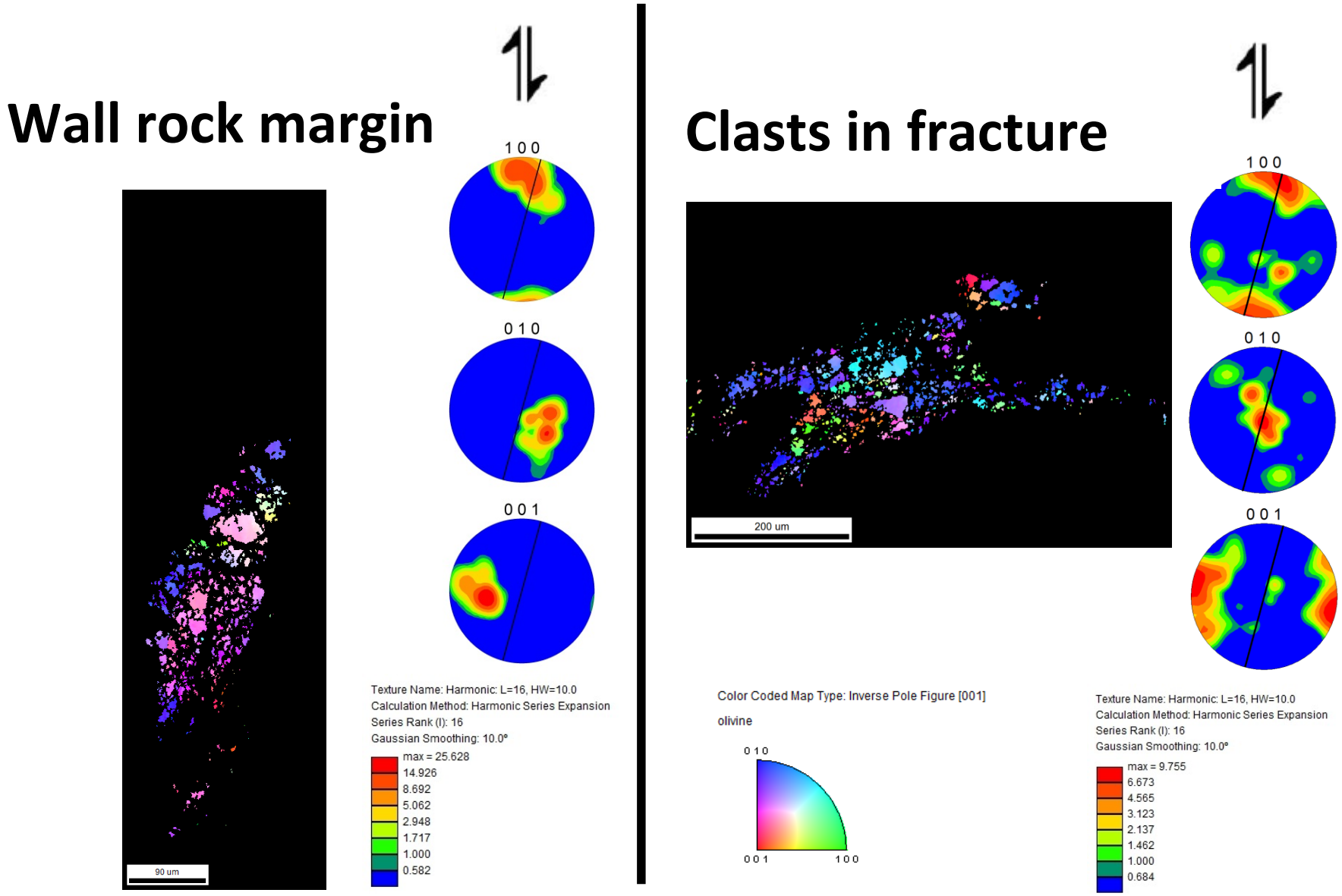

Figure 73: Area 3.1; IPF maps and contoured PF of clasts at the interface between wall rock and fine grained fault zone, and of clasts in a fracture in wall rock. The IPF maps are colour-coded according to the unit triangle. The calculation parameters and the intensity of the projections are shown below the respective PF. The solid line on the PF displays the orientation of the fault plane, and the reference direction is marked by shear direction (arrows). See text for discussion.

1

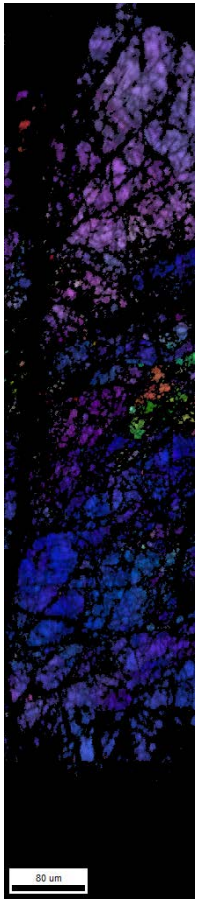

Chart: Grain Size (diameter)

Edge grains excluded from analysis

Diameter [microns]	Number
1.9776	1603
4.25267	265
6.52773	93
8.8028	59
11.0779	24
13.3529	17
15.628	5
17.9031	10
20.1782	9
22.4532	3
24.7283	3
27.0034	4
29.2784	2
31.5535	1
33.8286	2
36.1036	3
38.3787	1
40.6538	1
42.9289	0
45.2039	0
47.479	0
49.7541	0
52.0291	1
54.3042	0
56.5793	0
58.8543	0
61.1294	1
63.4045	0
65.6796	0
67.9546	0
70.2297	2
72.5048	0
74.7798	0
77.0549	0
79.33	0
81.605	0
83.8801	1
86.1552	0
88.4303	0
90.7053	0
92.9804	0
95.2555	0
97.5305	0
99.8056	0
102.081	0
104.356	0
106.631	0
108.906	0
111.181	0
113.456	1

Average	
Number	3.0063
Standard Deviation	5.58287
Area	47.6794

2

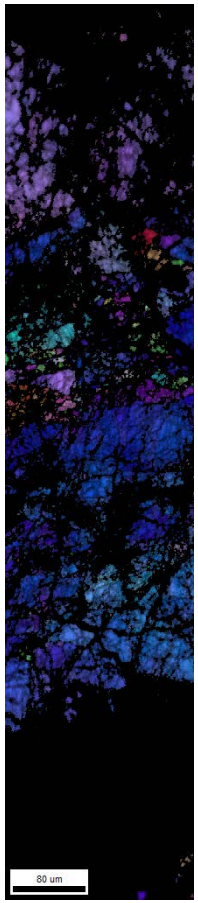

Chart: Grain Size (diameter)

Edge grains excluded from analysis

Diameter [microns]	Number
1.8885	1692
3.98538	241
6.08226	101
8.17914	52
10.276	21
12.3729	14
14.4698	13
16.5667	9
18.6635	8
20.7604	4
22.8573	2
24.9542	6
27.0511	0
29.148	3
31.2448	2
33.3417	4
35.4386	1
37.5355	0
39.6324	2
41.7292	1
43.8261	2
45.923	0
48.0199	1
50.1168	1
52.2136	0
54.3105	0
56.4074	2
58.5043	0
60.6012	0
62.698	0
64.7949	0
66.8918	0
68.9887	0
71.0856	0
73.1824	0
75.2793	0
77.3762	0
79.4731	0
81.57	0
83.6669	0
85.7637	0
87.8606	0
89.9575	0
92.0544	0
94.1513	0
96.2481	0
98.345	0
100.442	0
102.539	0
104.636	1

Average	
Number	2.80429
Standard Deviation	5.11336
Area	39.0344

3

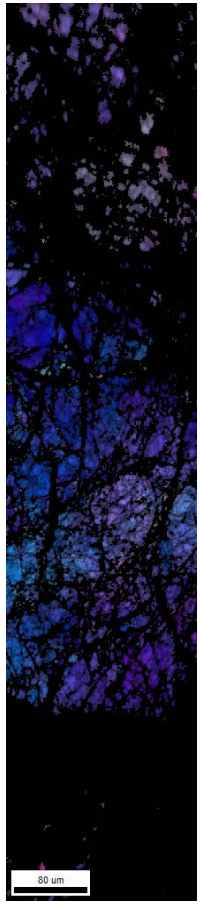

Chart: Grain Size (diameter)

Edge grains excluded from analysis

Diameter [microns]	Number
1.5893	1479
3.08778	292
4.58625	140
6.08473	71
7.58321	51
9.08169	22
10.5802	11
12.0786	8
13.5771	9
15.0756	10
16.5741	8
18.0725	7
19.571	9
21.0695	7
22.568	2
24.0665	0
25.5649	6
27.0634	2
28.5619	2
30.0604	0
31.5588	0
33.0573	1
34.5558	0
36.0543	0
37.5528	0
39.0512	0
40.5497	1
42.0482	2
43.5467	1
45.0451	0
46.5436	0
48.0421	0
49.5406	0
51.039	2
52.5375	0
54.036	1
55.5345	1
57.033	0
58.5314	0
60.0299	0
61.5284	0
63.0269	0
64.5253	0
66.0238	1
67.5223	0
69.0208	0
70.5192	1
72.0177	0
73.5162	0
75.0147	1

Average	
Number	2.90512
Standard Deviation	5.15062
Area	34.4197

4

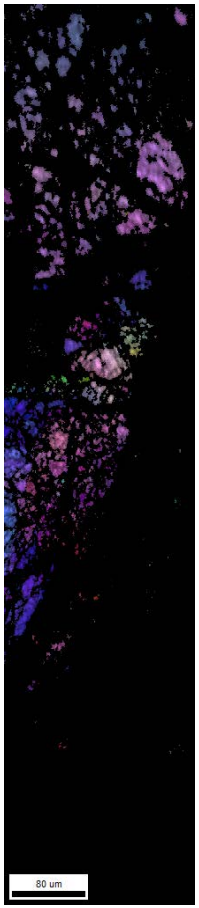

Chart: Grain Size (diameter)

Edge grains excluded from analysis

Diameter [microns]	Number
1.34876	950
2.36615	161
3.38355	92
4.40094	72
5.41833	39
6.43573	22
7.45312	24
8.47052	14
9.48791	8
10.5053	9
11.5227	4
12.5401	7
13.5575	4
14.5749	4
15.5923	3
16.6097	3
17.6271	2
18.6445	3
19.6619	3
20.6792	0
21.6966	1
22.714	3
23.7314	0
24.7488	2
25.7662	2
26.7836	0
27.801	0
28.8184	0
29.8358	2
30.8532	0
31.8706	0
32.888	0
33.9054	1
34.9228	0
35.9402	0
36.9576	0
37.975	0
38.9923	1
40.0097	0
41.0271	0
42.0445	0
43.0619	0
44.0793	0
45.0967	0
46.1141	0
47.1315	0
48.1489	0
49.1663	0
50.1837	0
51.2011	1

Average	
Number	2.52827
Standard Deviation	3.77583
Area	19.5886

Figure 74: Cropped IQ+IPF maps and grain size diameter statistics in wall rock from distal (1) to proximal (4) side relative to the fault zone. Edge grains are excluded from calculations. From the distal area (1) to the proximal area (4), relative to the fault, there are increasing numbers of small grains. The smallest recorded grains are 1.3µm, whereas the step size used was set to 1.0µm (table 7).

Area 3.2

The same fault zone was analysed away from area 3.1 into the fault zone (figure 71, A). This was done to capture peeled-off clasts almost devoid in the fault zone in area 3.1. The scan area relative to the macroscopic fabric is displayed on figure 71 and in appendix 3. The acquisitional parameters and properties of the post-processed datasets are displayed in table 8, and the dataset is displayed on figure 75.

Software	EDAX/TSL
Step size	1.0µm
Working distance	13.0mm
Avg. angular misfit	1.42°
Avg. Image quality	47.32
Indexed fraction	0.025
#Indexed points/grains	35599/3147

Table 8: Acquisitional parameters and properties for area 3.2.

The amount of indexed ol, shown in table 8, again records poor indexation within a fault zone. Opx, cpx, pl, pseudotachylyte and veins of srp occupy a fraction of the nonindexed areas, but the amount of ol is remarkably low. The outline of indexed clasts resembles dismembered and peeled-off fragments from wall rock (figure 75). These share a SPO subparallel to fault margins. Clasts range in diameter from 50-1µm (the step size), but are commonly <20µm. The PF show several intensity maxima and scattered projections. Poles to [100] project both subparallel and normal to fault margins, and poles to [010] and [001] largely project out of the dataset. The IPF show that poles to [100] have strong intensity maxima normal to fault zone margins. Poles to [010] and [001] have intermediate but clustered orientations, shown on the IPF. This suggest activity on [010](100) or [001](100) as suggested by Ave'Lallemant and Carter (1970).

There is significant scatter around the intensities for all three principle crystallographic axes, questioning the strength of any LPO.

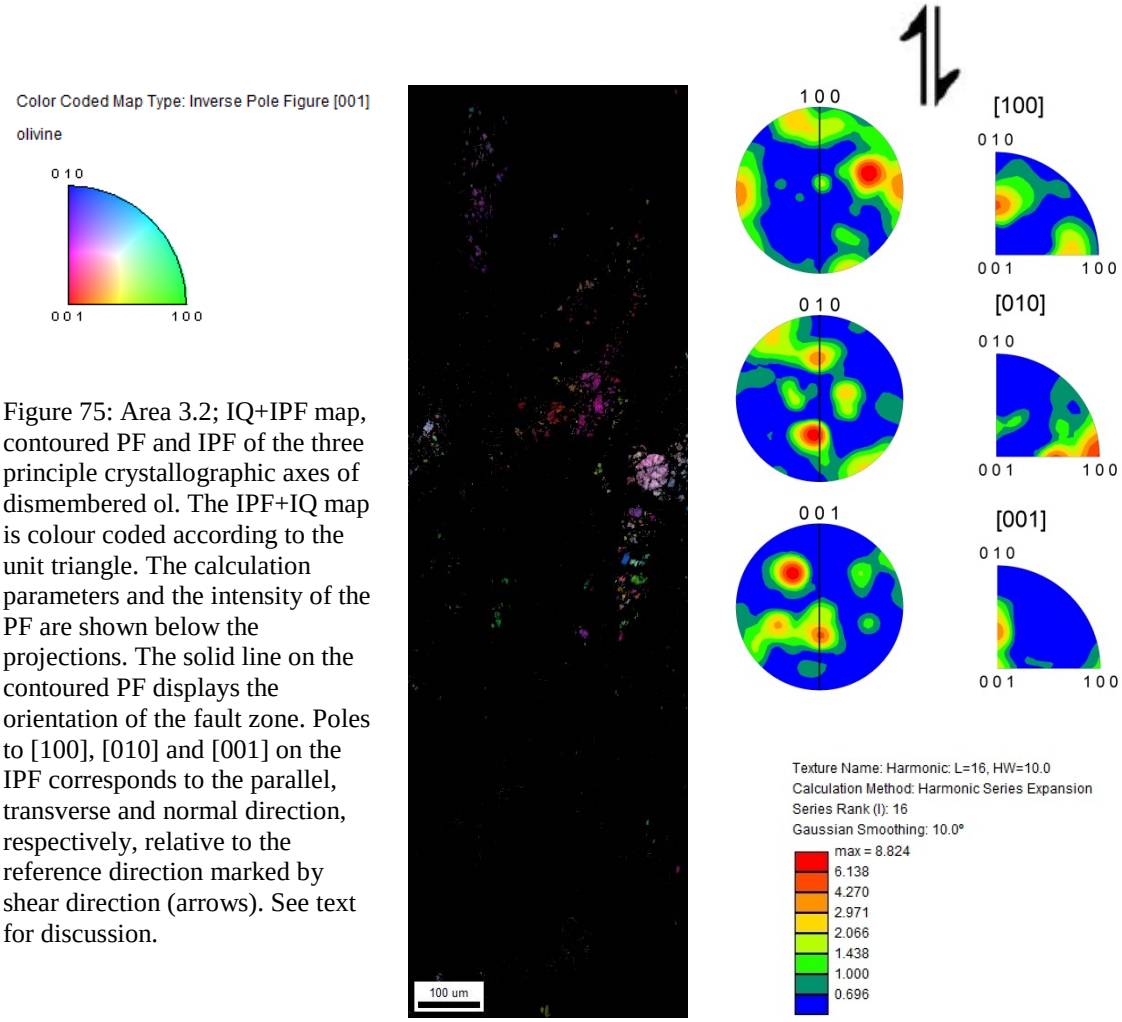

Figure 75: Area 3.2; IQ+IPF map, contoured PF and IPF of the three principle crystallographic axes of dismembered ol. The IPF+IQ map is colour coded according to the unit triangle. The calculation parameters and the intensity of the PF are shown below the projections. The solid line on the contoured PF displays the orientation of the fault zone. Poles to [100], [010] and [001] on the IPF corresponds to the parallel, transverse and normal direction, respectively, relative to the reference direction marked by shear direction (arrows). See text for discussion.

Area 3.3

Another analysis was done within the fine grained fault zone, adjacent to area 3.2. The scan area relative to the macroscopic fabric is displayed on figure 71 and in appendix 3. The mapped area captures the interior of a pseudotachylyte fault-vein and a highly sheared ol porphyroclast next to it (figure 76). The dataset was cropped in two sections; one of indexed ol in pseudotachylyte and one of indexed ol in the fault zone. The cropped dataset from pseudotachylyte is moved to the chapter assessing pseudotachylytes, whereas clasts in the fault zone are presented here. The entire dataset and the cropped section of area 3.3, relative to the pseudotachylyte, are shown on figure 76. The acquisitional parameters and properties of the post-processed dataset from the cropped fault zone are displayed in table 9.

Software	EDAX/TSL
Clasts	Cropped map
Step size	0.5µm
Working distance	13.0mm
Avg. angular misfit	1.47°
Avg. Image quality	52.53
Indexed fraction	0.119
#Indexed points/grains	143977/4366

Table 9: Acquisitional parameters and properties for area 3.3.

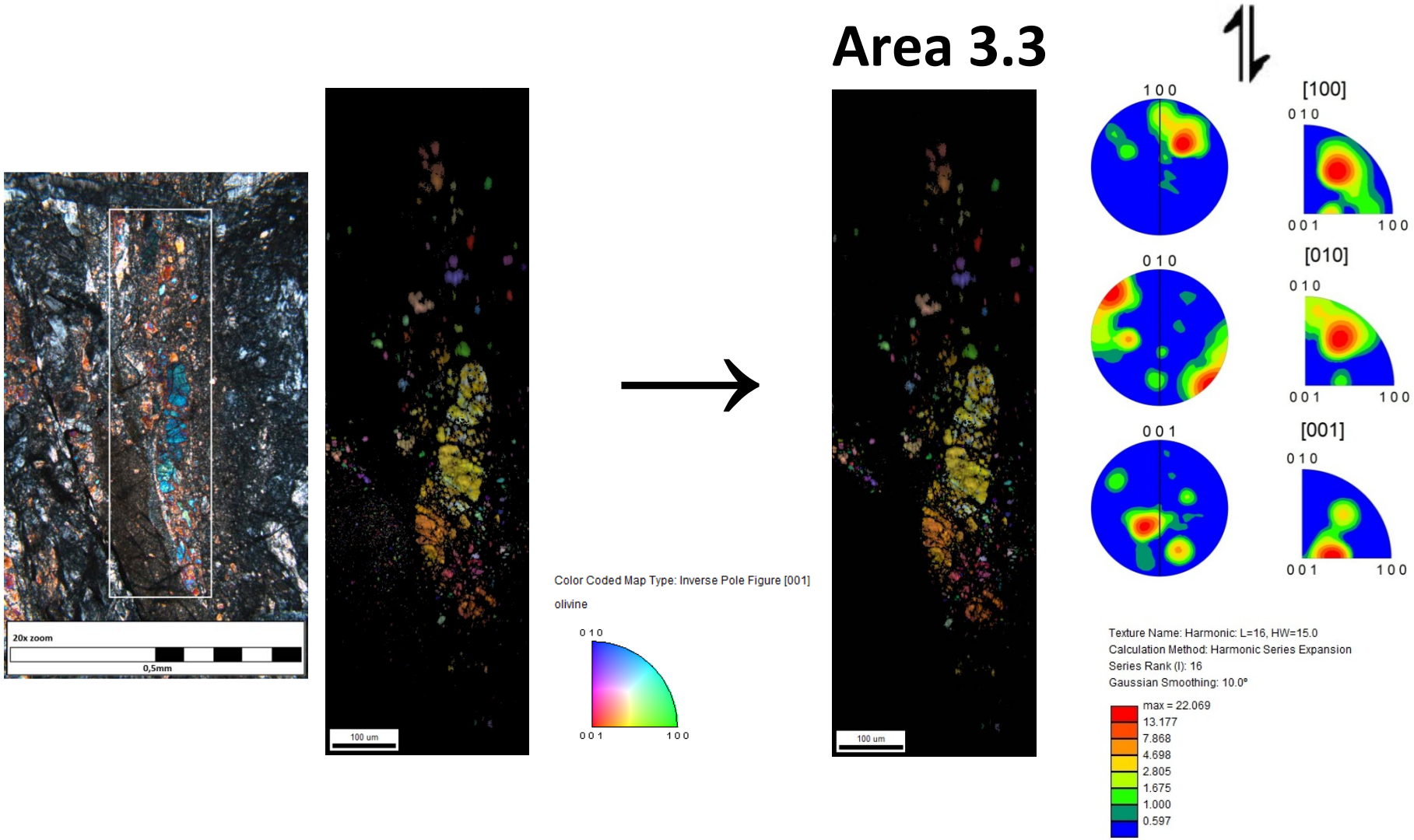

Figure 76: Area 3.3; Micrograph in cross-polarised light, IQ+IPF maps and contoured PF and IPF of the three principle crystallographic axes of ol. The entire dataset and the cropped section of area 3.3 is indicated with an arrow. The IPF+IQ maps are colour coded according to the unit triangle. The calculation parameters and the intensity of the PF are shown below the projections. The solid line on the contoured PF displays the orientation of the fault zone. Poles to [100], [010] and [001] on the IPF corresponds to the parallel, transverse and normal direction, respectively, relative to the reference direction marked with shear direction (arrows). See text for discussion.

Ol in the fault zone are poorly indexed (table 9). The large sheared clast (figure 76) is approximately 0.7cm long and display comminuted margins. It is internally separated by aggregates of small grains that rest in nonindexed fractures. Total clast sizes range from 70-0.5µm (the step size) with a dominant portion <20µm. All clasts share a SPO subparallel to fault margins. The PF and IPF show few intensity maxima where poles to [010] are aligned normal to the fault margins. The IPF show that a high fraction of poles to [001] are aligned with the sample normal, more so than poles to [100]. This might indicate activity on the [100](010) slip system as proposed by Ave'Lallemant and Carter (1970). The projections are not definite and slip on [001](010) is not excluded.

This dataset was the only dataset where pseudosymmetry clean-up was not successful using EDAX/TSL. Pseudosymmetry is evident in the large peeled-off clast as domains that share similar orientations that deviate from that of the porphycorlast itself (figure 77). The amount of misorientation is visualized on the misorientation profile. The angular relationship is an artefact in the acquisition and indexing algorithms, producing hexagonal pseudosymmetry (60°) around the a-axis due to oxygen stacking (Fliervoet et al., 1999). This will slightly effect crystallographic projections.

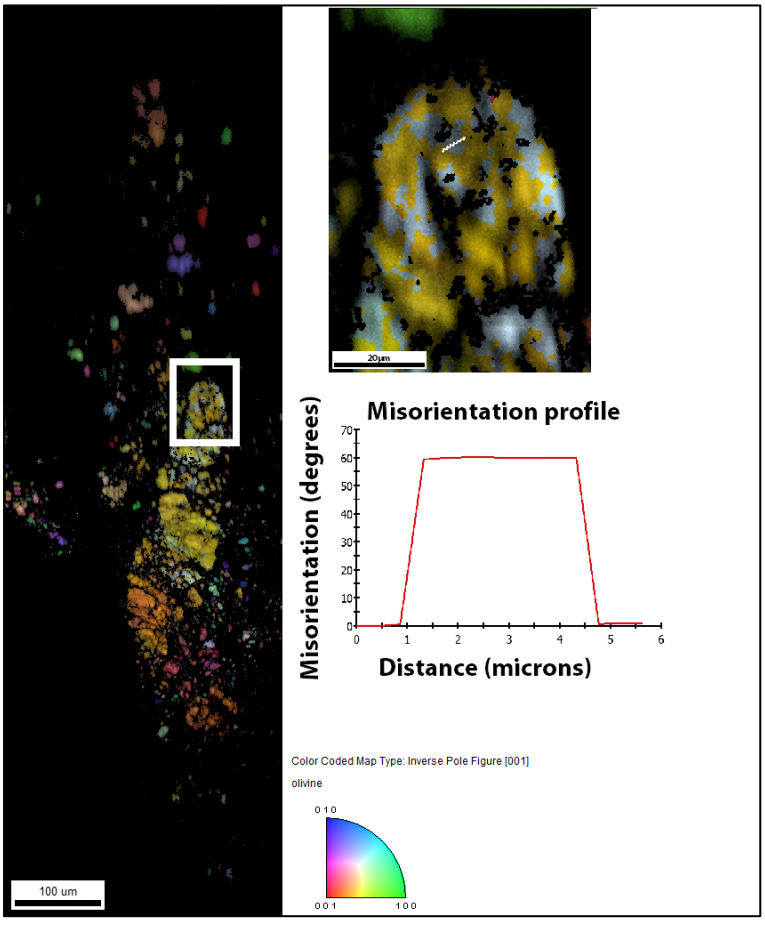

Figure 77: Area 3.3; IQ+IPF maps and misorientation profile over misindexed domains in a peeled-off wall rock clast. The IQ+IPF maps are colour coded according to the unit triangle. The white squared area is magnified on the upper right IQ+IPF map. The misorientation profile shows the amount of misorientation from bottom left to upper right, along the white line on the magnified IQ+IPF map. Blue pixels are misindexed 60° relative to their host.

Area 3.4

The brecciated zone displayed on figure 71, B was chosen for analysis. The scan area relative to the macroscopic fabric is displayed on figure 71 and in appendix 3. This breccia has also been discussed on figure 61, C. The dataset is displayed on figure 78. The acquisitional parameters and properties of the post-processed dataset are displayed in table 10.

Software	HKL Channel 5
Step size	2.0µm
Working distance	12.0mm
Mean angular misfit	0.73°
Avg. band contrast	58.61
Indexed fraction	0.274
#Indexed points	73829

Table 10: Acquisitional parameters and properties for area 3.4.

Area 3.4 display angular to rounded clasts that rest in a nonindexed matrix of opx and pl (figure 71, B). The clasts share a vague SPO subparallel to the fault zone (figure 78 and figure 71). Several grains records misindexing evident on the IPFC map. Due to the limited stay at the University of Liverpool, later post-processing could not be done. Misindexing is due to ol hexagonal pseudosymmetry that is confined to rotations of 60° around the a-axis due to oxygen stacking (e.g. Fliervoet et al., 1999). This can be seen as a peak on the misorientation angle distribution for neighbouring (correlated) pixels (figure 78).

The misorientation profile suggests a LPO, based on a higher frequency of low-angle misorientations for uncorrelated grains than the theoretical random distribution (Wheeler et al., 2001). High-angle misorientations for uncorrelated grains are slightly lower than what is expected in a random distribution. Correlated grains largely have low misorientations, and a low frequency of high angle misorientations. There is a vague alignment of crystallographic axes on the PF where poles to both [010] and [001] arrange perpendicular to each other, subparallel to the macroscopic fabric. Assessment of the IPF show that poles to [010] axes follow the sample parallel, more so than poles to [001], that are skewed towards the transverse direction. Poles to [100] consistently project along the sample normal. This suggest activity on [010](001) over [001](010), as proposed by Ave'Lallemant and Carter (1970).

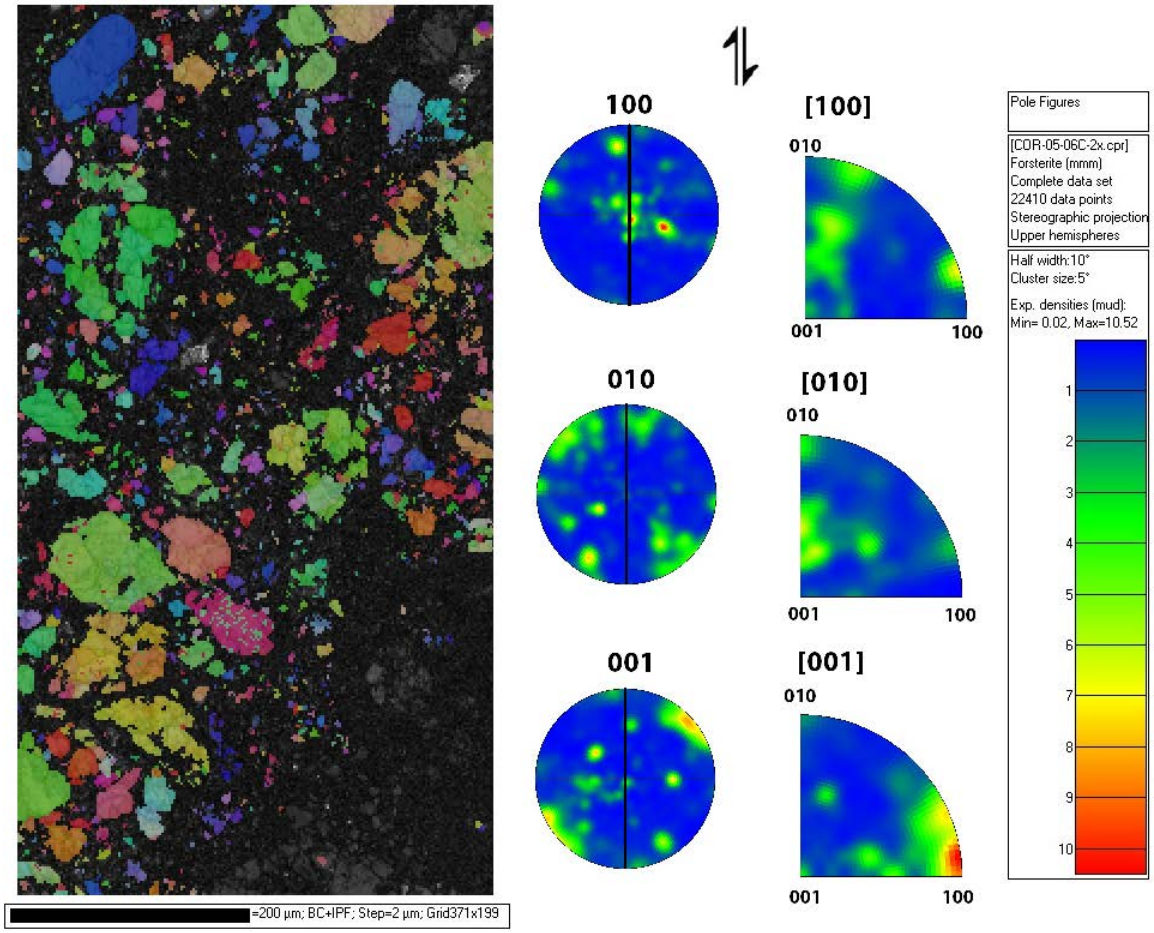

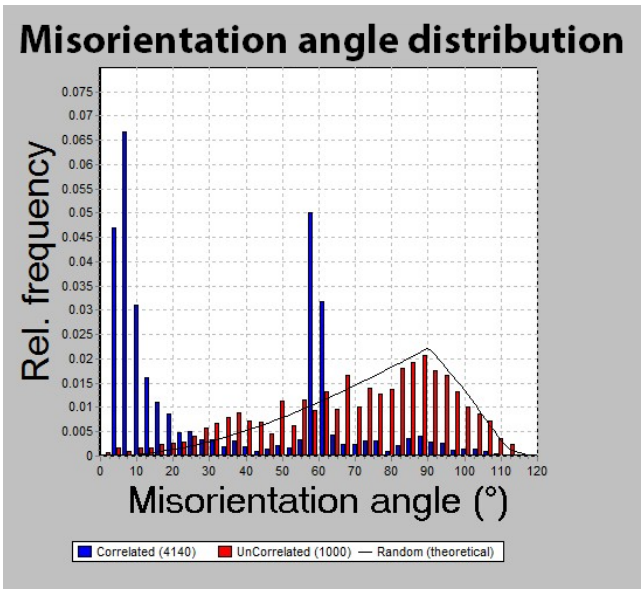

Figure 78: Area 3.4; BC+IPFC map, contoured PF and IPF for the three principle crystallographic axes in ol and misorientation angle distribution. The solid line on the PF displays the orientation of the fault zone. Poles to [100], [010] and [001] on the IPF follow the parallel, transverse and normal direction, respectively, relative to the reference direction marked by shear direction (arrows). The misorientation angle distribution displays the amount of misorientation for correlated (neighbouring) and uncorrelated (random pairs) relative to the theoretical random for the orthorhombic crystal system.

Dislocations in olivine

In order to decorate dislocations in ol, sample COR-04-06 was polished and oxidized in air (e.g. Karato, 1987; Kohlstedt et al., 1976). A standard 30µm petrographic thin section was then prepared with the previously polished face in contact with the glass slide.

The decorated thin section has a reddish colour which is confined to ol grains (figure 79). This is a result of chemical diffusion towards or away from dislocation cores and grain boundaries, precipitating hem-mag and silica-rich phases (Karato, 1987). Initial investigation with the optical microscope, also visible in hand specimen, is the increasing red tone from distal to proximal side of faults. Dislocations were observed with a SEM using backscattered electron images. Dislocations were explored at three locations; in the distal (1), intermediate (2) and proximal (3) areas relative to the outer margin of a fault zone that transects the sample. Decorated dislocations and grain boundaries are evident as bright features, indicating an increase in the mean atomic number near dislocation cores and grain boundaries (e.g. Kohlstedt et al., 1976). The approximate locations of the investigated areas are marked on figure 79.

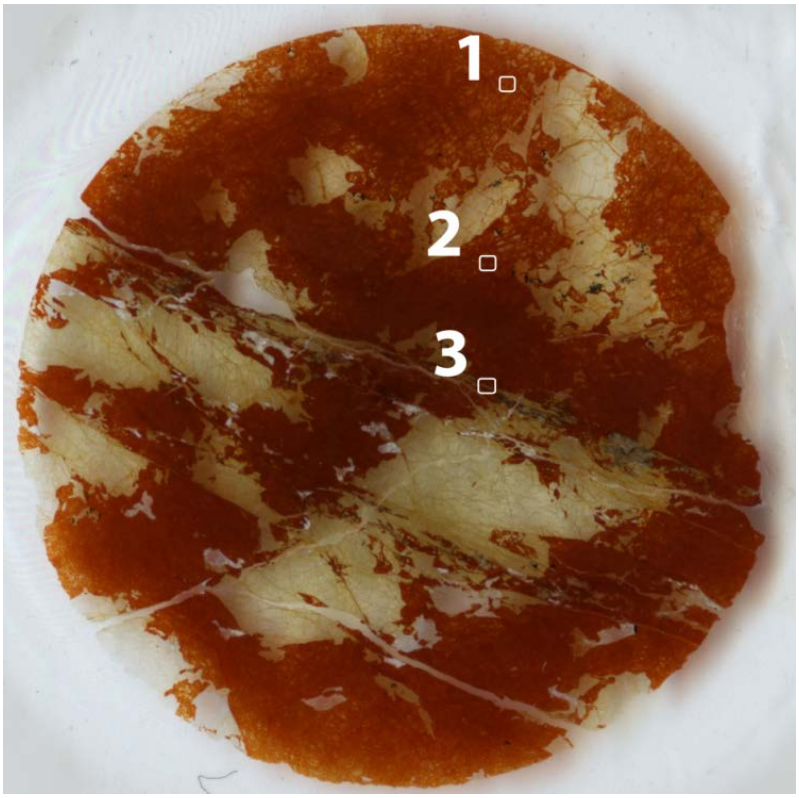

Figure 79: Scan of the oxidized thin section from sample COR-04-06. Ol grains have inherited a reddish color that progressively darkens from sample rim towards fault veins. Other phases than ol retain their original color and internal features. The marked areas correspond to the approximate locations of BSE imaging and are assessed in their respective sections.

The free dislocation density (ρ) can be estimated using equation 7;

$$\rho = \sum l / V \qquad \text{(Equation 7)}$$

where $\sum l$ is the total length of dislocations in a volume V (e.g. Jung and Karato, 2001). The dislocation density can be used to estimate the differential stress, where the density versus stress relationship follows equation 8;

$$\rho = \alpha b^{-2} (\sigma / \mu)^2 \qquad \text{(Equation 8)}$$

where α is a nondimensional constant, b is the length of the burgers vector, σ is the stress and μ is the shear modulus. The physical basis for the relationship is the force balance between applied stress and the stress field around a dislocation (e.g. Poirier, 1985).

Area 1

The distal area, away from faults (figure 79, 1) commonly displays dislocations that have arranged into planar features (figure 80). These are probably tilt walls, twist walls and subgrain boundaries (e.g. Passchier and Trouw, 2005). Dislocations have been observed to align at spaced, uneven intervals or as dense networks. Some grains show little of these features. Dislocation walls that arrange along dense networks (figure 80, A), on closer observation (figure 80, B) displays two prominent directions that intersect at a high angle. These are marked and separated by white and grey arrows. Dense networks of dislocation walls contain numerous laterally inconsistent arrays.

Some grains are almost devoid of dislocation walls (figure 80, C). Here they form single and discrete features, unevenly spaced with areas of no dislocation arrangements. Again, two principle orientations of dislocations have been identified. It should be noted that none of the images on figure 80 was taken at sufficient magnification to determine dislocation densities, and that the magnification conceals the true dislocation structure.

Most grains display dark, spherical voids highlighted by circles on figure 80, A. These are visible in all BSE images from all area 1 to 3.

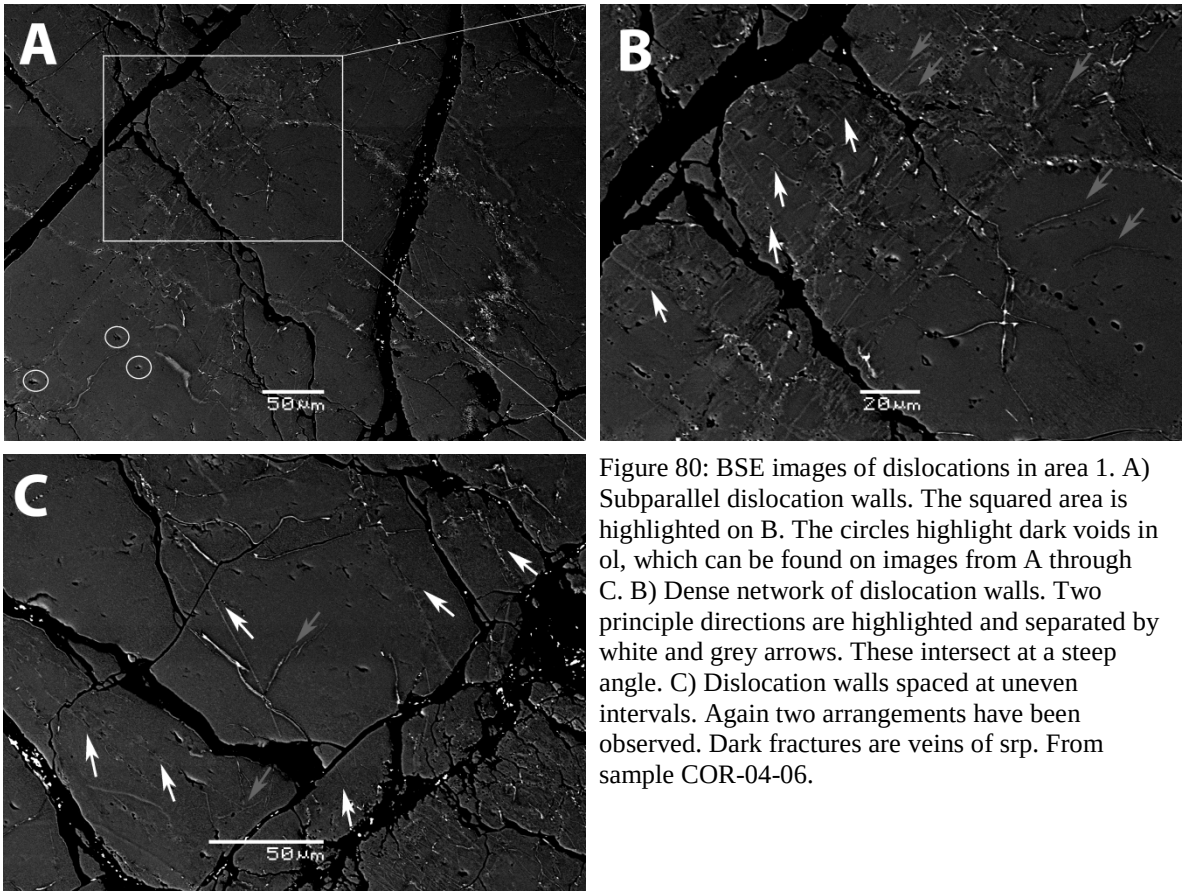

Figure 80: BSE images of dislocations in area 1. A) Subparallel dislocation walls. The squared area is highlighted on B. The circles highlight dark voids in ol, which can be found on images from A through C. B) Dense network of dislocation walls. Two principle directions are highlighted and separated by white and grey arrows. These intersect at a steep angle. C) Dislocation walls spaced at uneven intervals. Again two arrangements have been observed. Dark fractures are veins of srp. From sample COR-04-06.

Area 2

The second explored area (figure 79, 2) is located in between the most distally investigated area and fault-veins, and share many similarities with area 1. Some grains are relatively free of dislocations (figure 81, A), whereas other grains contain networks of criss-crossing dislocation walls (figure 81, B). In figure 81, A, only one population of dislocations has been identified and share an approximate orientation with those marked with grey arrows in area 1. Dark voids are found in all investigated areas and occasionally cluster, as seen on figure 81, A. These are associated with a bright Z-contrast which indicate that dislocations or dense phases may assemble around these (e.g. Wenk and Bulakh, 2008).

Networks of dislocations walls arrange and intersect with approximate directions to that found in the most distally investigated area 1 (figure 81, B). The two populations display both long and shorter, linked up dislocation walls. An interesting feature in this area (figure 81, B) is two distinct domains, within the same grain, that record different appearance of dislocations.

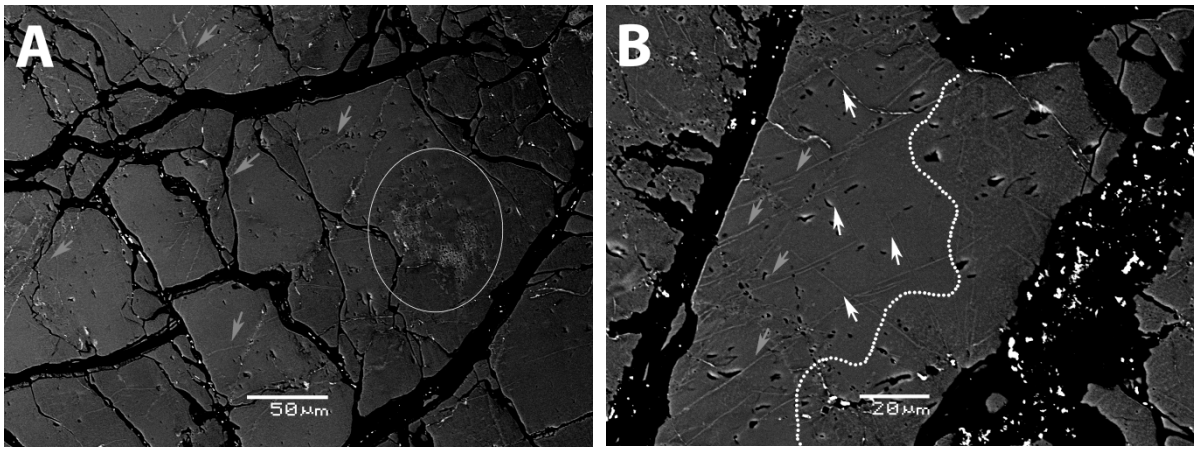

Figure 81: BSE images of dislocations in area 2. A) Ol relatively devoid of dislocations. Some dislocation walls are highlighted by grey arrows, with an orientation accordingly to those in area 1. The circle highlights a cluster of dark voids associated with a high Z-contrast. B) Networks of mutually criss-crossing dislocations. Their orientation is similar to that in area 1. The dotted line marks the boundary between two distinct domains. The domain on the right-hand side show numerous free dislocations and wavy, poorly developed arrangements that intersect. Dark fractures are veins of srp. From sample COR-04-06.

Free dislocations have here been identified as numerous points with a high Z-contrast (e.g. Jung and Karato, 2001). These are associated with wavy and diffuse dislocation walls. These walls intersect with orientations and angles similar to that found in both area 1 and 2. Unfortunately, no images were taken at a magnification sufficient to determine dislocation densities. The low magnification conceals the true dislocation structure.

Area 3

The proximal area relative to fault-veins (figure 79, 3) defines the outer margin of one of the fault zones that transect the sample. In figure 82 two thin (100-10µm) fault-veins truncate wall rock and dislocations have been imaged adjacent to these.

Dense networks of subparallel, close-spaced dislocation walls intersect at a high angle similar to that in area 1 and 2. The spacing between the two arrangements is found to be much lower than that in previously imaged areas (figure 82, A). Dislocation walls are bordered by free dislocations and minor dislocation walls that intersect at a multitude of angles. Adjacent- and between the two fault-veins (figure 82, B) is a change in dislocation arrangement from that in figure 82, A. Dislocations walls are wavy and an apparent lower number of free dislocations, relative to figure 82, A, has been observed. Dark voids are found in truncated wall rock and pseudotachylyte (figure 82, B).

No dislocation densities could be determined due to low quality of the high resolution images.

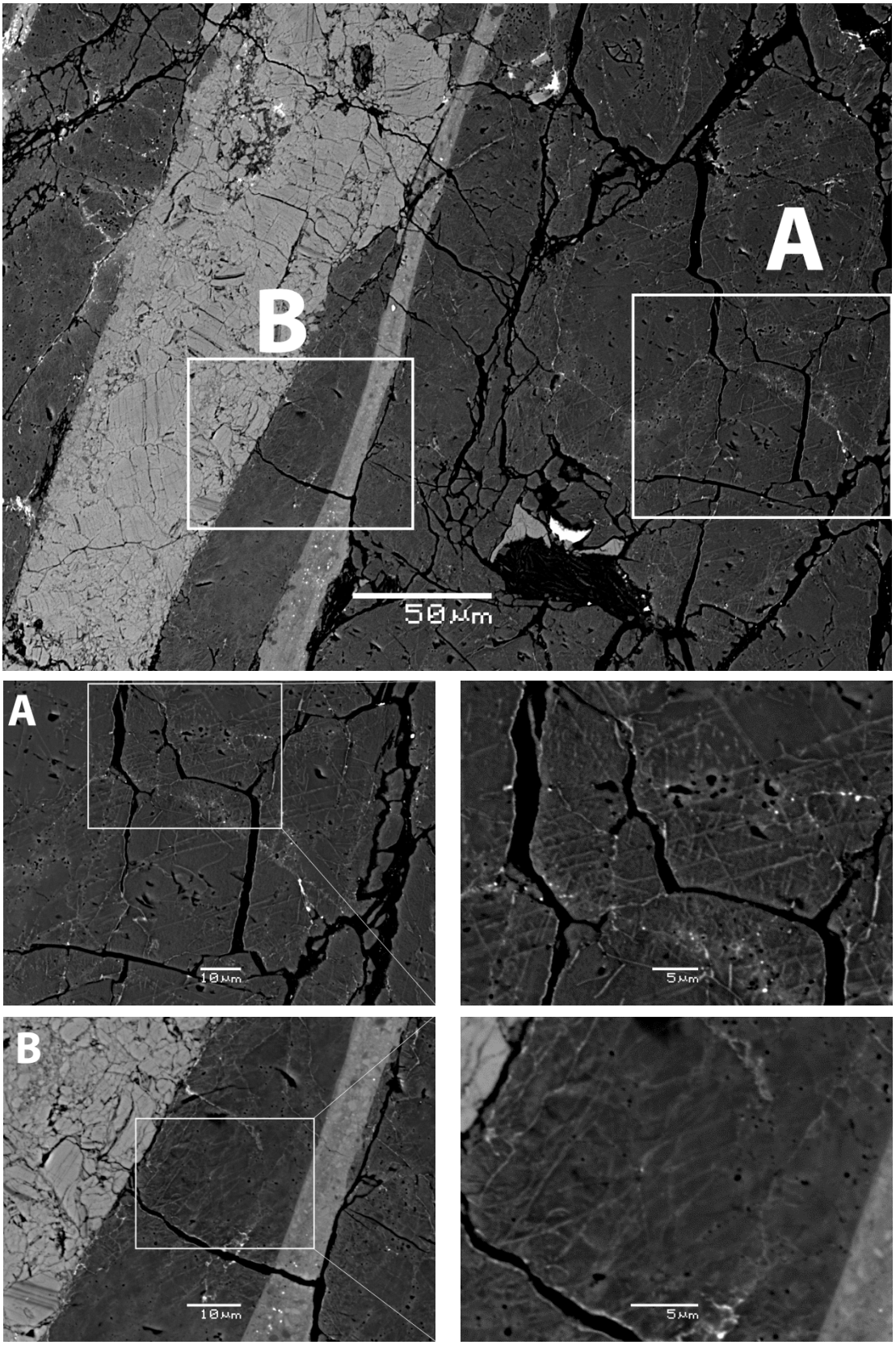

Figure 82: BSE images of dislocations in area 3. Two subparallel fault-veins (100-10µm) truncate wall rock. Dark voids are found in all investigated areas. A) Close-spaced dislocations walls (<10µm) that intersect in several directions, bordered by free dislocations and minor dislocation walls. The squared image is magnified on the right-hand side. B) Wavy dislocation walls with apparent fewer free dislocations, compared to that in A. The squared image is magnified on the right-hand side. Dark fractures on all images are veins of srp. From sample COR-04-06.

Pseudotachylyte - mineralogy and texture

The pseudotachylytes preserved within peridotite take on a wide range of appearances. Pseudotachylyte veins are found variably distributed in fault zones where the width of individual veins differ from outcrop to outcrop (figure 37, page 66) and between samples (figure 60, page 87). Fault-veins may truncate individual mineral grains (figure 64, page 91) or have fine-grained zones in wall rock towards their margins (figure 61, page 88). Injection-veins ramify off of generation surfaces (figure 61, A), constitute pockets along strike (figure 60, D) and occasionally bridge multiple slip surfaces (figure 60, B). Based on similarities and differences between the pseudotachylytes themselves there are several textural and mineralogical characteristics that have repeatedly been observed.

Both fault- and injection veins are readily identified as dark, cryptocrystalline to glassy, brown to black coloured veins under the optical microscope. Most sampled ultramafic pseudotachylyte are texturally zoned with ultra-fine grained, colour banded margins and variable content of porphyroclasts from margin to vein centre (figure 62, figure 71). In spite of different margins in wall rock, the interface between pseudotachylyte veins and wall rock is very sharp, characterized by an abrupt change in texture due to the extremely fine-grained pseudotachylyte (figure 83, A). BSE images and EDS point analyses show that the very fine matrix is typically constituted by newly formed subhedral to euhedral crystallites <10µm in diameter (figure 83, B). These are dominantly ol and opx. Cr-spl occurs in pseudotachylyte veins as peeled-off wall rock fragments. Ol crystallites are consistently zoned with Mg-rich cores and Fe-rich rims (Andersen and Austrheim, 2006), evident on figure 83, B.

Pseudotachylyte, together with wall rock, is criss-crossed by fractures filled with srp (e.g. figure 82 and figure 83). Pseudotachylyte contain numerous small (<1µm) cavities that represents porosity in the veins (figure 83, C). Here, fibrous patches are frequently observed, recording devitrification of the pseudotachylyte to srp and clc (Andersen and Austrheim, 2006; Deseta et al., submitted). Crystallites are here, on figure 83, C, unaffected by later hydration. Pseudotachylyte may also retain frequently observed flow structures, in spite of later serpentinization in both fault- and injection veins (figure 84).

There are commonly textural differences between wide and thin pseudotachylyte veins. Quench- and subsequent time for crystallization differ on the amount of melt that has been generated (Andersen and Austrheim, 2006). Veins thicker than a few millimetre may in addition to small (<10µm) crystallites contain micro-porphyritic domains that have

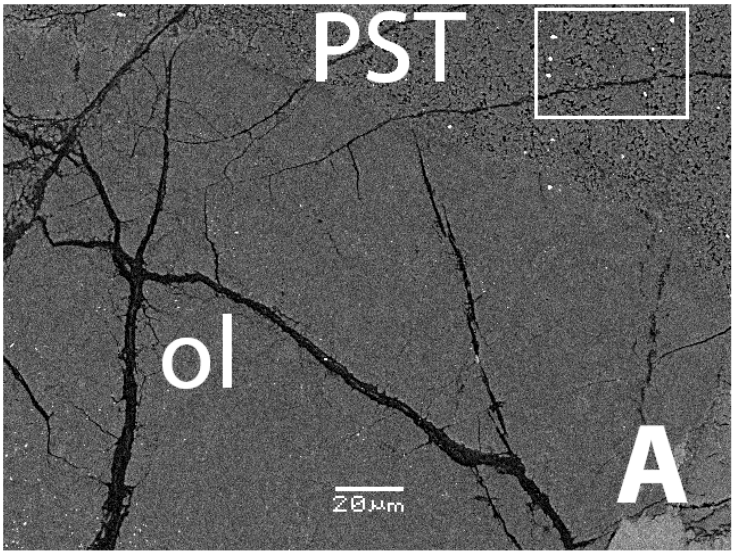

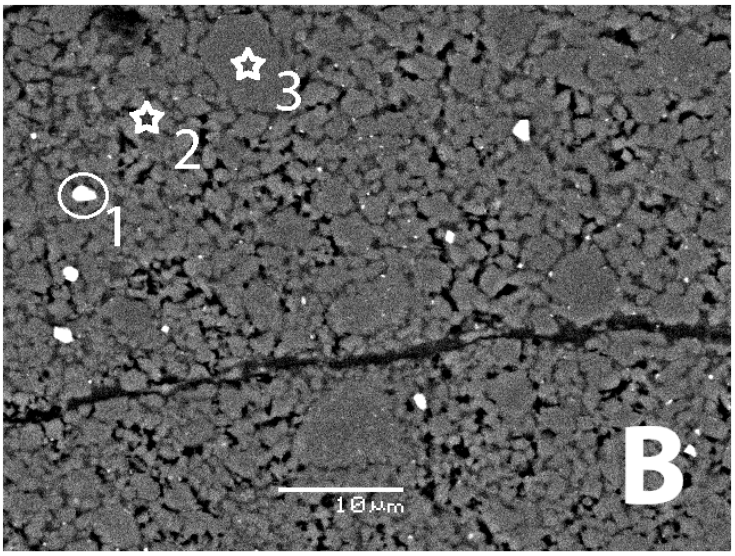

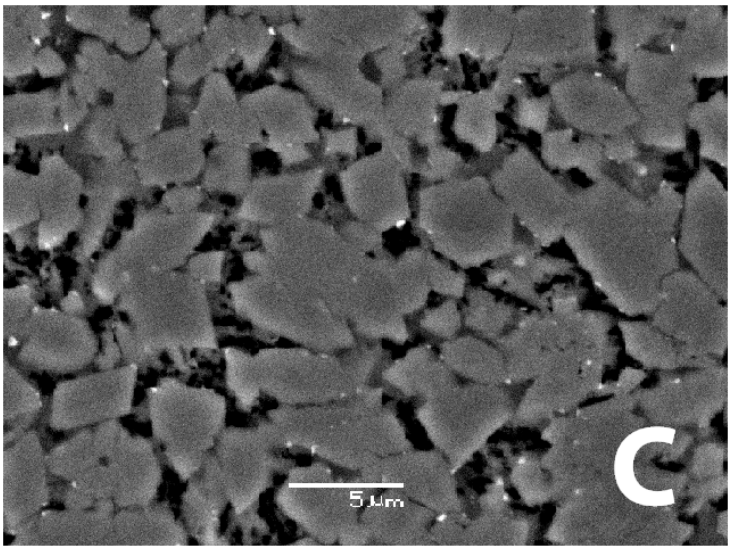

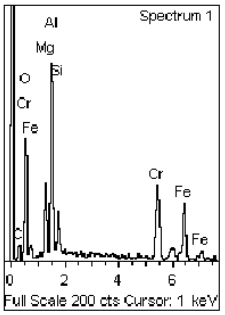

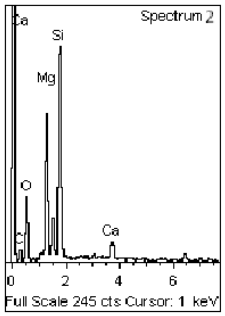

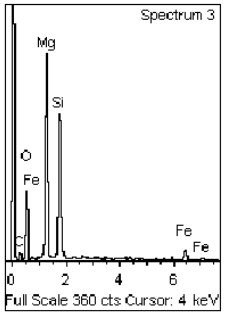

Figure 83: BSE images and EDS point analyses of mineralogy and texture close to the interface between a pseudotachylyte fault-vein and wall rock. A: Pseudotachylyte fault-vein truncating an ol grain. The squared area is displayed on B. B) EDS point analyses of minerals and crystallites in pseudotachylyte. Spectrum 1 (circled bright mineral) is Cr-spl. Spectrum 2 (dark grey crystallite) is opx. Spectrum 3 (dark grey crystallite) is ol. C) Euhedral to subhedral ol and opx. Note the chemical zoning in ol with Fe-rim to Mg-core (darker) and small <2µm cavities and fibrous patches between crystallites. The fractures that transect all imaged areas are filled with srp. Images and analyses from sample COR-05-06C.

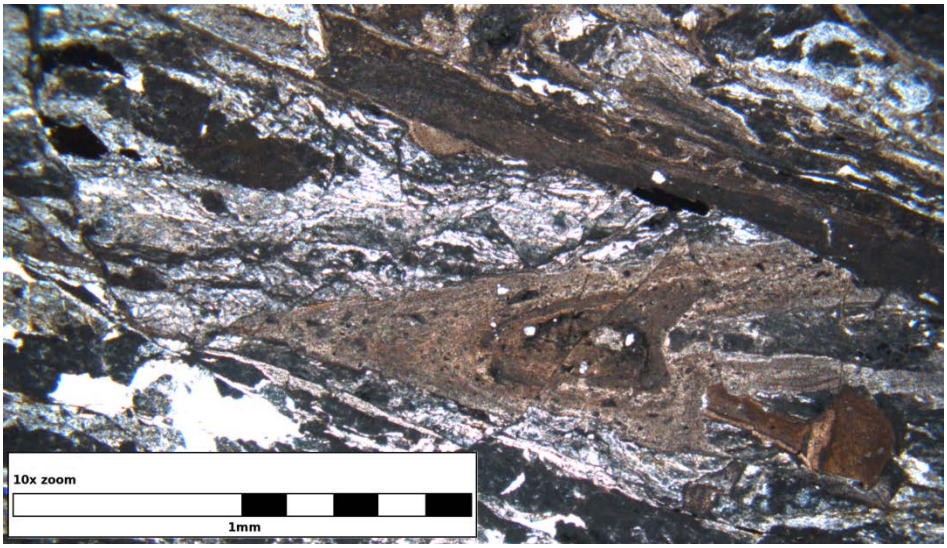

Figure 84: Micrograph in plane-polarised light of preserved flow structures in pseudotachylyte fault- and injection veins in serpentinized peridotite. The difference in colour between these indicates reactivation along the generation surface and re-injection into wall rock. From sample COR-47-01.

progressively developed from vein margin towards vein core. Figure 85 displays an injection vein with a width of ~6cm that contain micro-porphyritic domains and several generations of re-injection. The micro-phenocrysts are cpx crystallized directly from the frictional melt (Andersen and Austrheim, 2006). These are strongly poikilitic to dendritic and range in size up to 500µm (figure 85, A). The length of dendrites typically increases with increasing vein-width, and are best developed in the core of pseudotachylyte veins. Dendrites contain ol and opx inclusions in their cores (figure 85, B). Recently intruded veins are evident by different colour and texture from that in the host (figure 85). These are devoid of micro-porphyritic domains and display colour banded margins.

Ultramafic pseudotachylyte fault- and injection veins contain variable amounts of peeled-off wall rock clasts. In all investigated samples their composition mirrors that in adjacent wall rock mineralogy. Both the amount and sizes of porphyroclasts in ultramafic pseudotachylyte commonly show ol > opx > cpx. Porphyroclasts in fault-veins share a SPO subparallel to fault-vein margins, whereas clasts in injection-veins have no apparent preferred orientation. Clast size varies from vein to vein from barely identifiable in matrix to several millimetres along their long axis (figure 86, A). Porphyroclasts have highly variable sizes (5mm-<10µm along their long axes) and commonly display thermally rounded margins in both fault (figure 86, A) and injection veins. Porphyroclasts frequently display undulose extinction (figure 86, A, figure 86, C). Peeled-off wallrock fragments of ol occasionally attest to recrystallization in

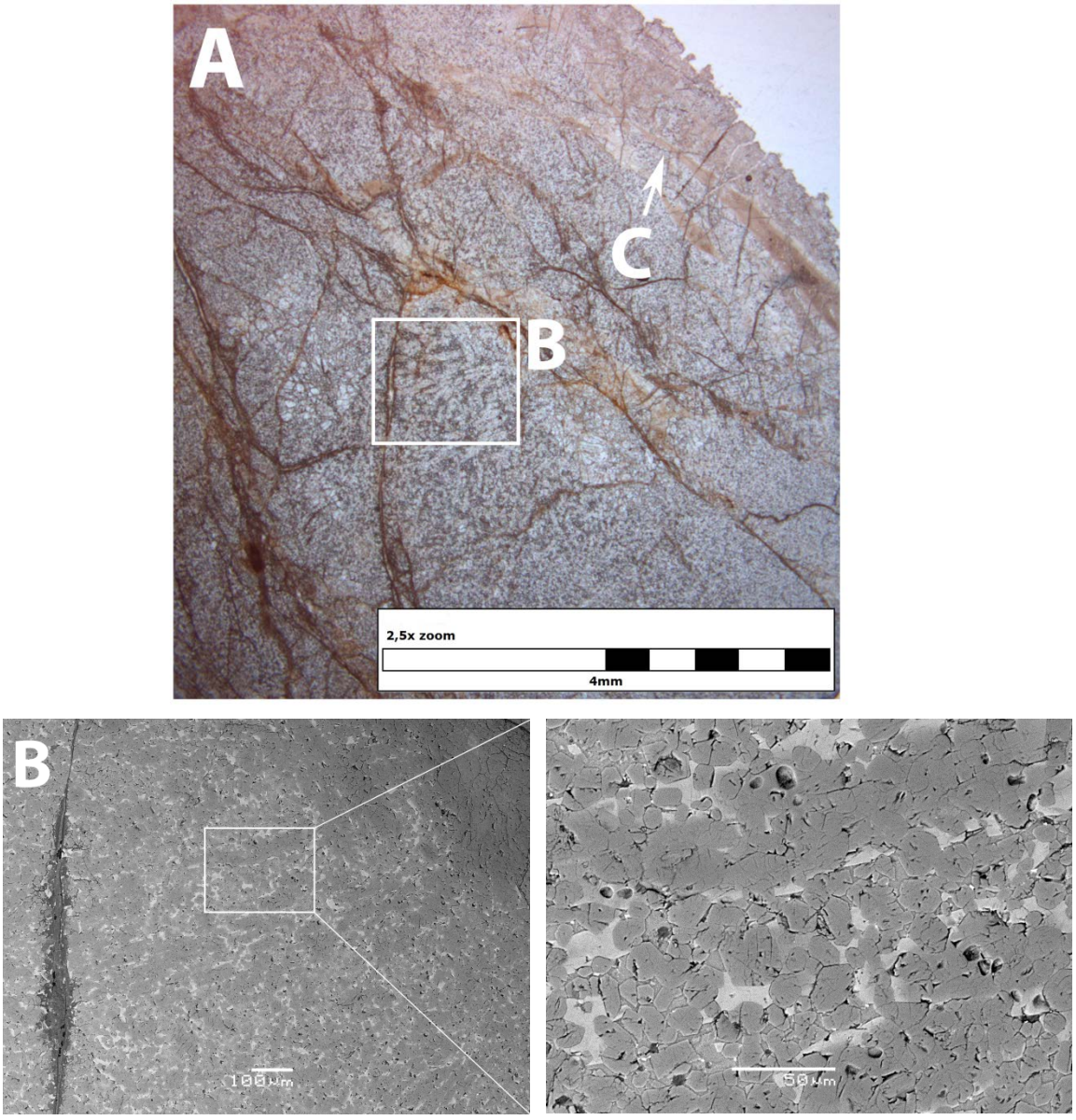

Figure 85: Micrograph in plane-polarised light and BSE images of textures in an injection vein. The sampling location is displayed on figure 32. A) Injection vein with micro-porphyritic domains, re-injected by thinner veins. The squared area is shown on BSE image B and the arrow points to the location of BSE image C. B) BSE image of slightly recrystallized, large (<500µm) dendritic porphyrites. The phenocrysts are cpx with abundant inclusions of opx and ol (undistinguishable on BSE images). Note the dark voids. The squared area is magnified on the right-hand side. C) Interface along re-injected pseudotachylyte. The recently intruding pseudotachylyte display small <10µm crystallites that are not recrystallized. Fractures on all images are veins of srp associated with mag. Images from sample COR-6/12.

both weakly and strongly recrystallized pseudotachylyte matrixes. Figure 86, C shows a remnant ol clast in a 6cm wide injection vein. The ol clast is bordered by neoblasts. It is evident that pseudotachylyte veins and porphyroclasts do attest to variable amount of recrystallization (figure 86) and hydration (figure 84). Individual pseudotachylyte veins do not record varying texture or alteration along them, but large differences are found from sample to sample. Wall rock fragments that rest in serpentinized pseudotachylyte attest to significant serpentinization which has commonly run to completion.

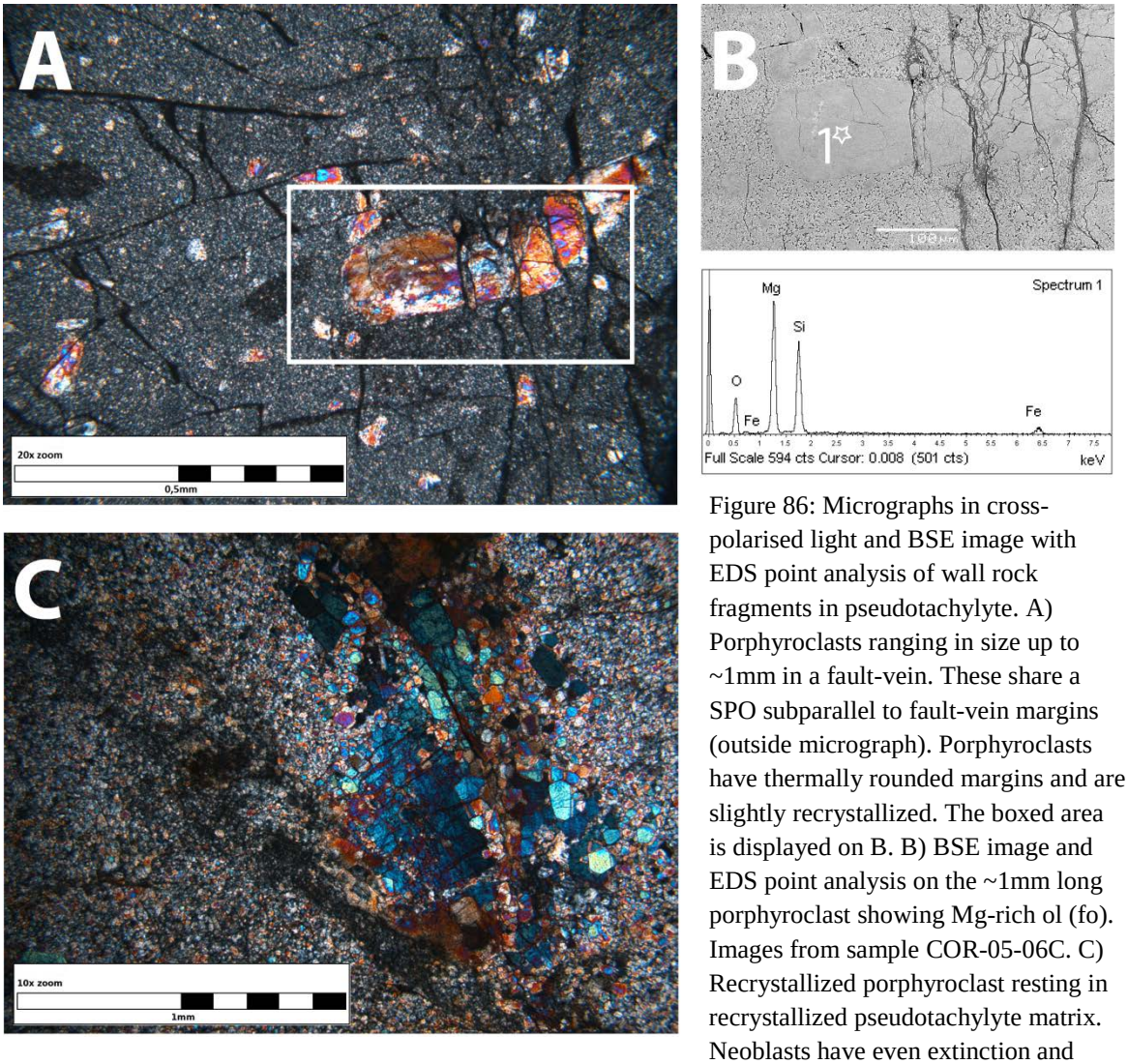

Figure 86: Micrographs in cross-polarised light and BSE image with EDS point analysis of wall rock fragments in pseudotachylyte. A) Porphyroclasts ranging in size up to ~1mm in a fault-vein. These share a SPO subparallel to fault-vein margins (outside micrograph). Porphyroclasts have thermally rounded margins and are slightly recrystallized. The boxed area is displayed on B. B) BSE image and EDS point analysis on the ~1mm long porphyroclast showing Mg-rich ol (fo). Images from sample COR-05-06C. C) Recrystallized porphyroclast resting in recrystallized pseudotachylyte matrix. Neoblasts have even extinction and share a LPO based on interference colours. Image from COR-6/12. All fractures are veins of srp with associated mag.

EBSD on pseudotachylyte fault- and injection veins

One pocket of pseudotachylyte in a fine-grained wall rock margin (area 4.1) and one fault vein (area 4.2) were investigated in sample COR-05-06C using EBSD.

Area 4.1

A pocket of pseudotachylyte in a fine grained wall rock margin, adjacent to a 3mm wide fault-vein was investigated. The scan area relative to the macroscopic fabric can be seen on figure 87 and in appendix 3. The dataset is displayed on figure 88 and the acquisitional parameters and properties of the post-processed dataset are displayed in table 11.

Software	HKL Channel 5
Step size	0.5µm
Working distance	12.0mm
Mean angular misfit	0.56°
Avg. band contrast	58.61
Indexed fraction	0.269
#Indexed points	47565

Table 11: Acquisitional parameters and properties for area 4.1

Assessment of the IPFC map displays one dominant band in the centre of the analysed area, subparallel to the fault vein on figure 87. The indexed grains in the band are very small (<<10µm), indicating that these are crystallites. The adjacent, scattered indexation in a nonindexed volume is constituted by tectonic mixing of minerals in the fine grained wall rock. The PF show few maxima with huge scatter (figure 88), but align poles to [001] subparallel to the macroscopic fabric (figure 87). The IPF confirms that poles to [001] align parallel to the sample reference, and that poles to [010] largely align in the transverse direction. This suggests activity on [001](010) as proposed by Ave'Lallemant and Carter (1970).

Figure 87: Micrograph in cross-polarised light of a fault vein (far right) and an adjacent fine grained wall rock zone. Area 4.1 is done over a pocket of pseudotachylyte in this zone. Image from COR-05-

However, poles in the normal direction scatter on the IPF. The misorientation angle distribution shows that both correlated and uncorrelated grains largely follow the theoretical random. There is a discrepancy of high-angle misorientations for correlated grains, and slightly more misoriented at a small angle. The peak at 60° is ol having hexagonal pseudosymmetry (e.g. Fliervoet et al., 1999).

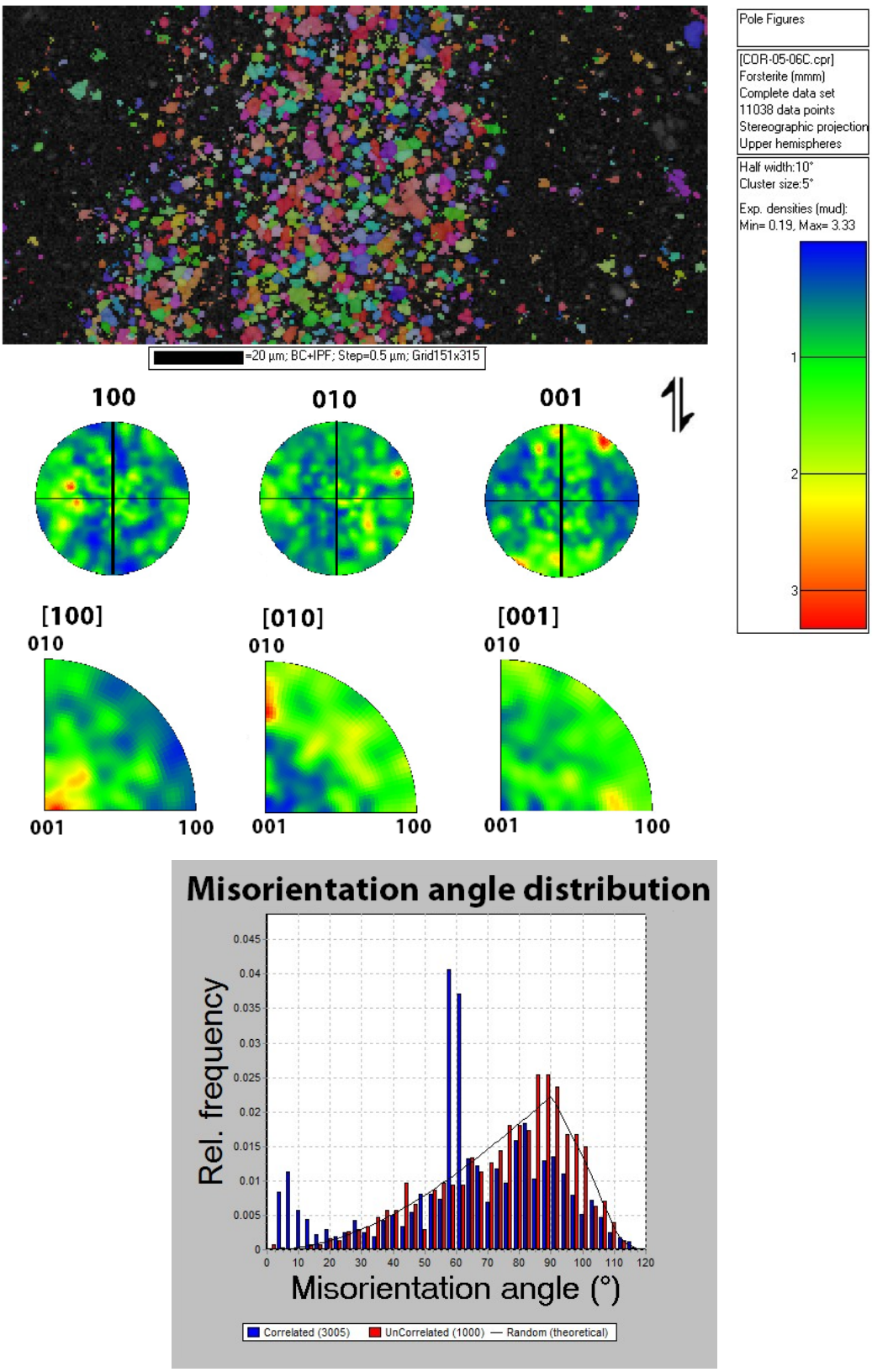

Figure 88: Area 4.1; BC+IPFC map and contoured PF and IPF for the three principle crystallographic axes in ol. The solid line displays the orientation of the fault zone. Poles to [100], [010] and [001] on the IPF follow the parallel, transverse and normal direction, respectively, relative to the reference direction indicated by the shear direction (arrows). The misorientation angle distribution displays the amount of misorientation for correlated (neighbouring) and uncorrelated (random pairs) relative to the theoretical random for the orthorhombic crystal system. The calculation parameters and the intensity for the PF are shown on the right-hand side.

Area 4.2

Area 4.2 is the remainder of the cropped dataset from area 3.3 (figure 76). The scan area relative to the macroscopic fabric can be seen on figure 71 and in appendix 3. The dataset is displayed on figure 89 and the acquisitional parameters and properties of the post processed dataset are displayed in table 12.

Software	EDAX/TSL
Crystallites	Cropped map
Step size	0.5µm
Working distance	13.0mm
Mean angular misfit	1.48°
Avg. image quality	40.85
Indexed fraction	0.039
#Indexed points/grains	12529/2253

Table 12: Acquisitional parameters and properties for area 4.2.

Grain size diameters were calculated to constrain the amount of clasts and crystallites in the fault-vein, due to the low magnification of the scan area. The grain sizes show that no indexed grains are larger than 5.8µm in diameter (figure 89), suggesting that these are crystallites similar, to that in area 4.1 (figure 88). The PF and IPF display a consistent arrangement with poles to [100] subparallel to the fault zone, poles to [010] normal to the fault zone and poles to [001] project along the reference normal. This suggests activity on [100](010) as proposed by Ave'Lallemant and Carter (1970).

Due to the fine grain sizes, a misorientation angle distribution was calculated for this dataset. The distribution show that correlated grains largely follow the theoretical random, with more grains misoriented at low angles. Uncorrelated grains have a discrepancy of low-angle misorientations and are frequently misoriented at an angle of 80-90°, more so than the theoretical random.

Chart: Grain Size (diameter)

Edge grains excluded from analysis

Diameter [microns]	Number
0.659833	1265
0.929425	261
1.19902	181
1.46861	161
1.7382	115
2.00779	83
2.27738	63
2.54698	38
2.81657	28
3.08616	13
3.35575	11
3.62534	9
3.89493	2
4.16453	3
4.43412	1
4.70371	3
4.9733	3
5.24289	2
5.51249	0
5.78208	1

Average	
Number	1.02205
Standard Deviation	0.702461
Area	2.14353

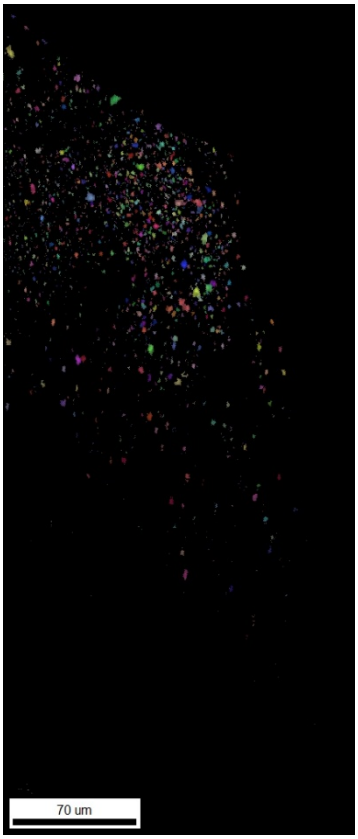

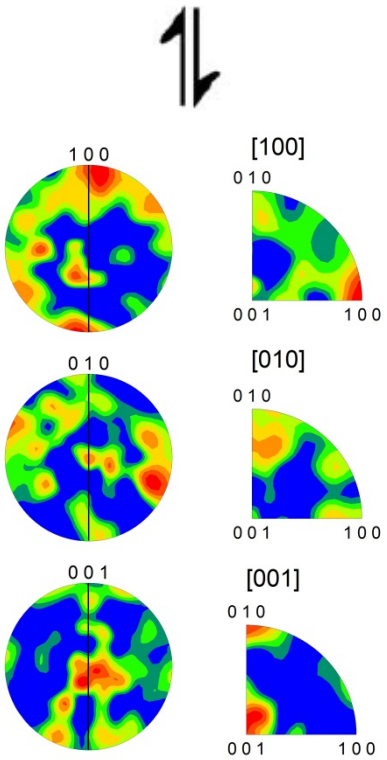

Color Coded Map Type: Inverse Pole Figure [001]

olivine

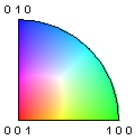

Texture Name: Harmonic: L=16, HW=30.0
Calculation Method: Harmonic Series Expansion
Series Rank (l): 16
Gaussian Smoothing: 10.0°

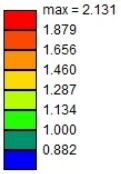

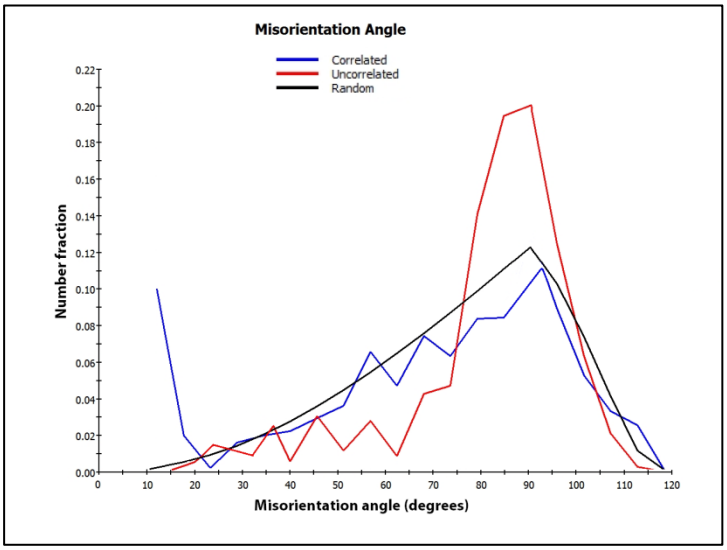

Figure 89: Area 4.2; IQ+IPF map, contoured PF and IPF, grain size statistics and misorientation angle distribution. The IPF map is colour coded according to the coded unit triangle. The solid line on the PF displays the orientation of the fault vein. Poles to [100], [010] and [001] on the IPF follow the parallel, transverse and normal direction, respectively, relative to the reference direction indicated by the shear direction (arrows). The calculation parameters and the intensity for the PF are shown below the projections.

6. Discussion

The Corsican peridotites experienced subduction to approximately 50 km (or deeper), where peak regional metamorphism are estimated from 420°C at 1.9-2,6GPa (Ravna et al., 2010) to 500-540°C at 2.3GPa (Brovarone et al., 2011b). The peridotites largely consist of ol and opx with variable amount of cpx with subsidiary pl and spl. The investigated samples display approximately even amounts and distribution of ol and opx+cpx for both host- and fault rocks.

Deformation of the lithospheric mantle is considered to be controlled by ol, which is the most abundant mineral. Its rheology is usually softer than opx+cpx (e.g. Karato and Wu, 1993; Rutter and Brodie, 1988). Thus, the rheology of the oceanic lithosphere is probably dominated by that of polycrystalline ol. This is supported by observations from the Corsican samples COR-06-03D, COR-10/12 and COR-04-06 where opx+cpx largely retain their mechanical framework. They display low degree of recrystallization through kinking, twinning and minor development of tilt walls (figure 52, A, figure 53, figure 56, C). All phases have grain boundary migration, but ol display a wider array of grain sizes and shapes.

Micrographs, EBSD plots and decorated dislocations presented in this thesis, point towards ol having deformed under conditions of crystal plasticity. The interpretation is based on textural criteria of weak to intense undulose extinction, development of tilt walls and subgrains (figure 57, figure 80), neoblasts (figure 58), and rare but strong LPO (figure 72). Observations in pseudotachylyte-devoid samples (COR-06-03D and COR-10/12) attest to altered equilibrium textures (figure 51) whereas fault sample COR-05-06C display intense deformation where relict textures are obliterated (figure 71). Fault sample COR-04-06 is more akin to host ultramafics, retaining a coarse and equant grain size that is sharply truncated by minor faults (figure 66). This attests to similar initial textures and for both host- and faulted spl-melagabbro and pl-spl-lherzolite. This is reasonable, given that all samples have been sampled within a few hundred meters of each other (figure 32).

Ol grain sizes and shapes in the investigated thin sections are highly variable. A reduction in grain size has been observed using the optical microscope on approaching faults (figure 61). Both truncated and fine grained fault margins attest to a reduction in grain size as shown by investigation using EBSD (figure 68 and figure 71). Wall rock ol elongates in the vicinity of faults, based on the amount of offset (figure 66, figure 73). The microstructure in samples with pseudotachylyte resembles host ultramafics in distal domains, away from faults. Ol in host ultramafics are typically coarse, but are vaguely elongated subparallel to an inconsistent

compositional banding. Host ultramafics and wall rock along faults record tilt walls and neoblasts in ol. Based on the maximum grain sizes observed in the two host ultramafics, ol and cpx+opx are in the order of ~8mm along their long axes.

Polycrystalline aggregate in a rock can deform plastically by two main processes (chapter 2). (1) Change in grain shape by diffusion creep. (2) Change in shape by dislocation creep. LPO and SGR-recrystallization indicate that a combination of generating, mobilizing and redistributing dislocations have been important at some stage in deformation (e.g. Passchier and Trouw, 2005). The next section focuses on the complex behaviour of LPO development in ol.

Assessment of lattice preferred orientations in olivine

The areas analysed with EBSD display nonexistent to strong LPO in ol. Assessment of the texture in several datasets is halted due to coarse grain sizes of ol, and magnification at which EBSD data was acquired. This will be discussed later. Datasets that certainly show LPO display medium to strong preferred orientations. A consistent development for the type of LPO has been found in all elements within the analysed areas, e.g. wall rock and clasts along faults. Wall rock ol typically displays stronger orientations than that in clasts. Datasets that display none or weak development of orientation typically show scattered intensity maxima and/or girdles along some of the principle axes. Equally, a consistent development for the type of maxima/girdles has been found for all elements in these datasets, where the orientation of clasts scatter more relative to that in wall rock.

The early studies of Ave'Lallemant and Carter (1970) identified and classified a large number of slip systems in ol, including [100](010), [100](001), [100](0kl) and [001](kl0) as shown on figure 23, page 45. Slip systems largely accommodate the total strain and controls overall LPO development. This is an important issue in ol where there are only three independent slip systems (Jung et al., 2006). The relative contribution of differently activated slip systems depends on the relative easiness of activation for the individual slip system. The conditions that activate and eventually cause transitions between these, for all minerals, are derived from experimental studies where temperature, strain rate, confining pressure and presence of volatiles is controlled. These factors are suggested to control the relative strength between differently activated slip systems (Drury, 2005; Karato and Jung, 2003). In turn, the relative importance of the controlling parameters has significant effects on crystal-plastic deformation

in ol (Mackwell et al., 1985; Mei and Kohlstedt, 2000). Recent experimental studies have expanded on the behaviour of ol using a range of deformational conditions.

Previous experimental studies on LPO in olivine

Ol has a very complex crystal-plastic behaviour that is strongly dependent on temperature. Out of the classified fabrics, slip with the Burgers vector (b) along [100] is considered 'easy,' while slip with b=[001] is considered 'hard'(Drury, 2005). This can be explained by equation 6 on page 44, and that the CRSS is significantly different for the two slip directions. Experimentally derived slip systems in dry ol at 1,5GPa was classified by Ave'Lallemant and Carter (1970) that suggested a linear relationship between temperature and strain rate. Slip with b=[100] only occurred at elevated temperatures (figure 23). Thus, 'easy' and 'hard' slip directions might be explained by the effect of temperature in dry ol, where at low (<1000°C) constant temperature, lowering the strain rate promoted a transition from slip along b=[001] to b=[100]. On the other hand, Passchier and Trouw (2005) have argued that at temperatures below 1000°C, only partial girdles of the three principle crystallographic axes develop in ol.

Optical and transmission electron microscope observations of experimentally and naturally deformed peridotites as well as single crystals has been compiled by Tommasi et al. (2000), and references therein. The type of observed LPO are displayed in table 13. Naturally deformed peridotites mostly displayed activity on the high temperature [100](0kl). LPO patterns suggesting activation on [001](hk0) were restricted to low temperature, high-stress deformation, supporting Ave'Lallemant and Carter (1970).

A large amount of water can be dissolved in ol, up to 8900ppm at 12GPa (Smyth et al., 2006), where confining pressure controls the amount of water that can be dissolved in the lattice (Kohlstedt et al., 1996). Experimental studies by Karato (1995); Mackwell et al. (1985) suggested that slip with b= [001] ('hard' direction) becomes easier with the addition of water at both high and low confining pressures. Experimental studies by Jung et al. (2006) and references therein, investigated the effect of LPO development in ol by varying stress and the amount of water at constant temperature (T~1470K-1570K) and pressure (0.5-2.0GPa). This correlates roughly to the asthenosphere-lithosphere isotherm at 1300°C. They found that all earlier classified slip systems may develop at asthenospheric temperatures, by varying the stress and amount of water. Four fabric types of LPO were proposed. The typical pole figure for each type of LPO and the conditions they developed under is shown in figure 90.

Temperature	σ_1 Orientation	Dislocations	Slip Systems	Remarks
600°C	$[101]_c$	screw, **b** = [001]; edges very short	(?)[001]	
800°C	$[101]_c$ and $[011]_c$	screw and edge, **b** = [001]	(100)[001], {110}[001], and (010)[001]	
800°C	$[110]_c$	screw and edge, **b** = [010] screw and edge, **b** = [100]	(100)[010] (010)[100]	high-strain domains low-strain domains high flow stress (1.28 GPa)
1000°C	$[101]_c$	screw and edge, **b** = [001], some loops; fewer **b** = [100]	(100)[001], {110}[001], secondary (001)[100]	
1000°C	$[011]_c$	screw and edge, **b** = [001], some loops	(010)[001]	
1000°C	$[110]_c$	screw and edge, **b** = [100], some loops	(010)[100]	flow stress similar to $[101]_c$
> 1150°	$[101]_c$	screw and edge **b** = [100], screw segments longer than edge segments; few screw **b** = [001]; (100) subgrain boundaries	(001)[100], secondary (100)[001]	intermediate strength orientation at high temperature, it becomes the softest one at high f_{O_2}
> 1150°	$[011]_c$	screw and edge, **b** = [001], loops of (010)[001]; screw **b** = [100], subgrain walls in (010); [100] organization	(010)[001] and (010)[100]	hardest orientation at high temperature
> 1150°	$[110]_c$	screw and edge **b** = [100], numerous loops in the (010) plane; [100] organization	(010)[100]	softest orientation at high temperature
> 1150°	$[110]_c$ and $[101]_c$		{031}[100], {021}[100], and {011}[100]?	only observed in forsterite

Table 13: Observations from naturally and experimentally deformed peridotites in different crystallographic orientations. Ol dominantly deforms by slip on [100](0kl) and [001](hk0) systems. Modified from Tommasi et al. (2000) and references therein.

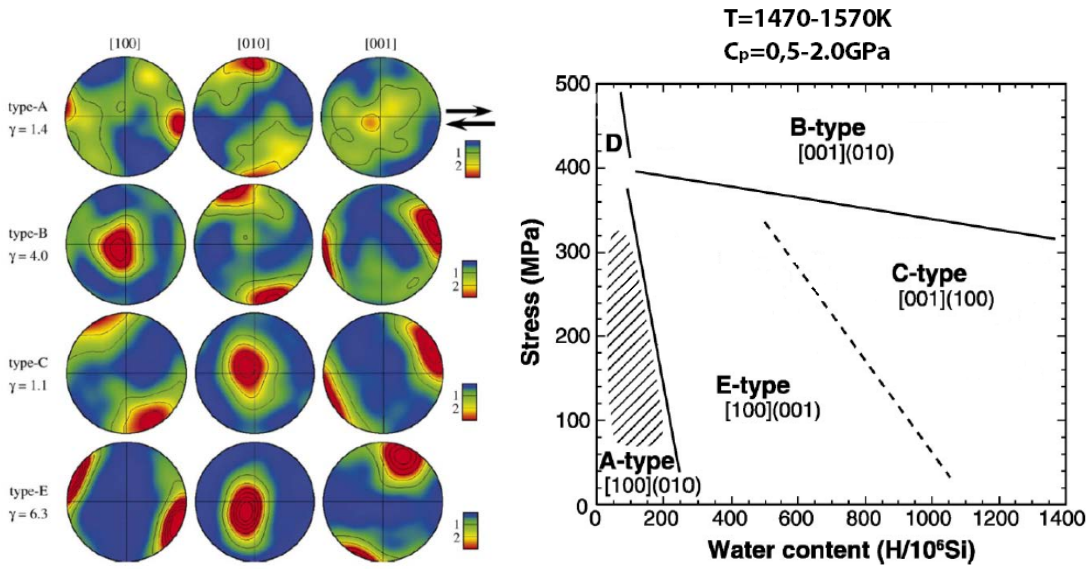

Figure 90: Left: Typical pole figures of LPO type A, B, C and E from experimentally deformed ol aggregates. East-west direction corresponds to shear direction, and north (south) corresponds to the shear-plane normal. Right: Fabric diagram of ol at T~1470-1570K (T/T_m ~0.7-0.75) and 0.5-2.0GPa showing the dominant fabric as a function of stress and water content (C_{OH}). Modified from Jung et al. (2006).

The experimental data support that addition of water promote slip with b= [001], from [100](010) to [100](001) and finally [001](100) at constant, high temperature. A supplement to the same study has predicted that the boundary from type-B to type-C is sensitive to temperature, as well as stress (Katayama and Karato, 2006).

It should be noted that experimental studies are haltered by limitations of the apparatus. Deformation paths are restricted to axial compression, plane compression and simple shear. Experiments are commonly confined to constant strain rates, constant temperatures and pressures, and a pre-defined amount of volatiles. Applying and relaxing temperature and pressure often follows a linear relationship. Altogether, most experiments simulate steady-state flow (e.g. Jung et al., 2006; Karato and Wu, 1993; Tommasi et al., 2000).

Natural peridotites lack sufficient strain markers to allow strain quantification, and strain paths in naturally deformed peridotites are poorly developed (e.g. Mercier and Nicolas, 1975; Tommasi et al., 2000). They probably follow numerous strain paths where pressure, stress, temperature and water content vary over geological time, as do the geometry of the stress field. For the Corsican samples with pseudotachylyte, fault-vein margins have been used as a reference frame for the finite strain. The textural criteria described for host- and fault rocks, and the occurrence of pseudotachylyte attest to conditions that cannot together be explained by steady-state flow.

Assessment of EBSD data and clean-up

The analyses of Alpine peridotite and pseudotachylyte from Corsica were done at two separate laboratories, using different calibration of the SEM and different software packages. Slight differences are found between the two types of datasets, while some complications are consistent for EBSD analyses. For example, only ol has been indexed in this thesis.

Large grain sizes in texturally equilibrated peridotite impede representative crystallographic projections, because few grains used for projection give a poor representation of the overall fabric. This is reflected by several intensity maximum on pole figures and inverse pole figures. Some projections show partial girdles along principle crystallographic axes for indexed ol, some are random, whereas others show a strong LPO. This has been found in datasets containing host rock, truncated wall rock and within fault zones. The total number of grains acquired in individual datasets is controlled by the magnification at which EBSD datasets were mapped, second to selecting proper areas for analysis. The maximum scan area using EDAX/TSL was approximately 1x1.5 mm, whereas ol grain sizes in host ultramafic and

truncated wall rock typically are >>0.1 mm. Further, indexing of solely ol in largely polyphase rock halts the number of grains that can be acquired in individual datasets. In general, analyses on fault zones have suffered from low amounts of indexing relative to that in host rock.

At high magnification and a small step size the software readily identifies and indexes crystallites in pseudotachylyte veins (figure 88). At low magnification, when retaining a small step size, recording EBSPs in small grains is difficult. If these are recorded and identified, simulated bands often give a poor fit (EDAX/TSL: low confidence index) and are readily eliminated by clean-up procedures. Intuitively, by increasing the total number of EBSPs from individual small grains, a better fit of their orientation can be acquired. This is because the simulated fit onto the EBSPs is limited by only having a few points within individual grains. Consequently, the data must be considered with great care to avoid errors in interpretations.

EBSD analyses on host rock sample COR-06-03D have shown good fractions of indexed ol in datasets (areas 1.1 – 1.3). On the other hand, analyses done on truncated wall rock, in fault zones and on pseudotachylyte have given very low fractions of indexed ol (areas 2.1 – 4-2). The clean-up procedures have readily removed misindexed pixels, which contribute to lowering the fraction of indexed material. In both host- and fault rocks, misindexing have been confined to pseudosymmetry in ol, phases other than ol and along grain boundaries of ol. Adjacent to truncated wall rock and in fault zones there is high degree of tectonic mixing of phases, accounting for lower total indexed fractions. In pseudotachylyte, both ol and opx largely contribute to the total volume (figure 83), halting proper assessment of the texture.

Successful indexation of ol in host rock sample COR-06-03D has given image qualities (IQ) / band contrasts (BC) that range from maximum 96.38 in area 1.1 (table 1), to a minimum of 77.91 in area 1.3 (table 3). Indexation of ol in truncated wall rock along fault zones has generally given lower values, from a maximum of 63.58 in area 2.1 (table 4) to a minimum of 45.05 in area 3.1 (table 7). For all acquired datasets, the IQ/BC of clasts that reside in fault zones or in fractures is lower than that for wall rock in the same dataset (table 4, 5, 6 and 7). The observation that intensities of acquired EBSPs are progressively reduced from host rock to fault zones points to increasingly distorted crystal lattices. Crystal lattices can be distorted due to strain, but also from melting, which both increase in the vicinity of faults.

Indexing of grain boundaries is ambitious (chapter 2). In addition, the Corsican samples are commonly fractured and hydrated, where srp initiate at grain boundaries. The low amount of

indexation here could also reflect the low viscosity of the ultramafic melt (Andersen and Austrheim, 2006; Suzuki and and collaborators, 2001), possibly wetting grain boundaries.

EBSD data: Forskningsparken, UiO / University of Liverpool

There are systematic differences between the datasets acquired at Forskningsparken, UiO and at the University of Liverpool. The data from Liverpool shows that mean angular deviations of computer-simulated bands are approximately 1° lower. In addition, BC in ol is generally higher for the same type of analysed area compared to datasets from Forskningsparken, UiO (compare table 11 and table 12).

The data from Liverpool was acquired using high vacuum, whereas data from UiO was acquired at low vacuum conditions. At low vacuum, the mean free path of electrons changes as a function of pressure. Primary electrons will readily experience elastic and inelastic interactions (appendix 2) with gas in the SEM-chamber before interacting with the sample, producing skirting-effects (e.g. Reed, 2005). This eventually distorts intensities of individual diffraction bands, and produces stronger background signals. There could also have been differences between the two symmetry databases that were used to index the EBSPs, leading to different fit onto the captured diffraction patterns.

EDAX/TSL: Confidence index, grain dilation and misorientation angle distribution

Treatment and post processing of raw data largely affects the outcome of final EBSD maps, and more importantly the projections from post processed orientation data. As pointed out in chapter 2 on clean-up procedures, the confidence index (CI) has largely been used to post process datasets acquired using EDAX/TSL. This has implications on calculating misorientation angle distributions.

Pixels with low CI (≤0.15) were excluded from datasets. This increases the total fraction of nonindexed pixels. Misorientation angle distributions utilizes grains that touch (correlated) and randomly selected pairs of grains (uncorrelated). Misindexing, as previously pointed out, occurred along grain boundaries. On calculating misorientation angles in post-processed datasets the distribution makes little sense, because grain boundaries are effectively nonindexed, and few grains touch. On calculating these distributions *without* applying a CI threshold, on a dataset that displayed strong LPO (area 3.1), misorientation angles largely followed the theoretical random. This is shown on figure 91.

This gives information on pixels with low CI. Such pixels are small and numerous, and pixels with CI close to zero have no ideal orientation relative to the recorded EBSP (TexSEM, 2009). The software does not compare every single pixel in the dataset but collects a representative amount for correlated and uncorrelated grains (TexSEM, 2009). The huge number of low CI pixels largely contributes to the calculation, and their orientation is essentially random.

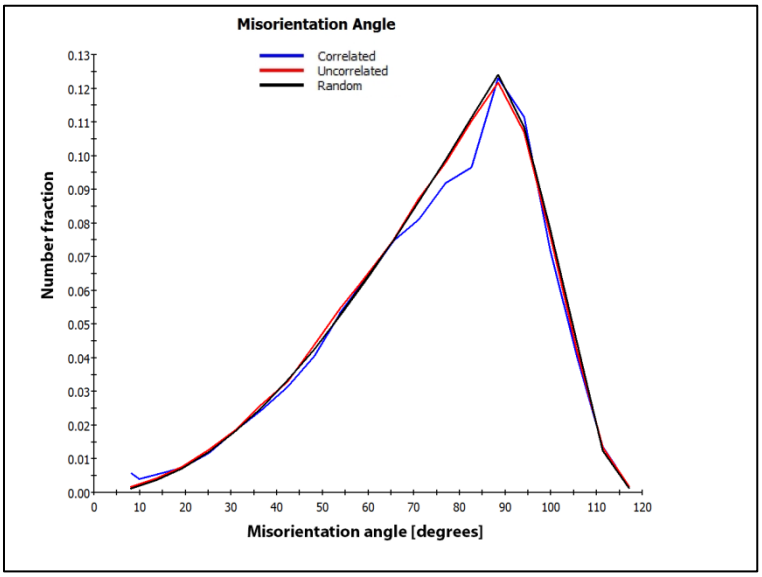

Figure 91: Misorientation angle distribution from area 3.1 without applying a CI threshold at 0.15. The dataset displays a strong LPO. Both correlated and uncorrelated grains largely follow the theoretical random distribution.

A grain dilation method was avoided since control on the dilated grain size in comparison to the recorded IQ could not be assessed. This is the reason why misorientation angle distributions have been excluded from all but one EDAX/TSL dataset. The dataset where misorientation angles were calculated display close spaced crystallites (figure 89).

This is unfortunate, since such calculations potentially contain valuable information. Misorientation angles can for example be applied to quantitatively describe fabric strength by calculating the M-index (Skemer et al., 2005). This calculation provides a number from 0 to 1, where 0 is random, which consequently increase with increasing fabric strength. Due to the absence of misorientation angle distributions using EDAX/TSL and the limited time using HKL Channel 5, such calculations could not be included.

Correlation of observed textures in Corsican peridotite

The acquired datasets of ol in the Corsican peridotites have been compared to experimental results by Ave'Lallemant and Carter (1970); Jung et al. (2006); Tommasi et al. (2000). Their results (figure 23, table 13 and figure 90) have been used as a qualitative proxy for the amount of water, temperature and stress during development of the recorded LPO. These have been compared to the texture found in the respective samples and areas chosen for EBSD. Generation of ultramafic pseudotachylyte requires that peridotite is locally heated to at least ~1750°C (Andersen and Austrheim, 2006), from ambient temperatures of 420-540°C (Brovarone et al., 2011b; Ravna et al., 2010). It is assumed that the main role of confining pressure is to modify the relative easiness of slip systems before and during deformation, through a change in water fugacity. The notation (type-A to E) used by Jung et al. (2006) has been incorporated where strong LPO are recorded. Orientations where intensity maximum or girdles with b=[010] align parallel to the macroscopic fabric have experimentally been found to form at low temperatures (<1000°C) in high strain domains (table 13) (Tommasi et al., 2000). The margins of fault zones have been used to represent macroscopic fabric in samples with pseudotachylyte, and the compositional banding has been used for host ultramafic rock.

Equilibrated textures and truncated wall rock

Sample COR-06-03D

- Area 1.3

The host spl-melagabbro (COR-06-03D) display weak girdles with poles to [010] subparallel to the vague compositional banding. Scattered maxima for the six intensities on the pole figure are described on page 84 and shown on figure 59. Based on the projections from this area and on comparison to the overall textures, it is unlikely that these ol deformed in a very high strain regime (table 13) where b=[010]. The sampled host rock was sampled approximately 20 m or more from major faults. It exhibits protogranular, modified equilibrated textures with straight to lobate grain boundaries that join up in modified triple junctions (figure 51, A, figure 52 and figure 56, B). Opx frequently record kinking and slight folding (figure 53 and figure 54). Kinking can only accommodate a limited amount of strain (e.g. Passchier and Trouw, 2005). Ol grain sizes in sample COR-06-03D are highly variable (8-<1mm) but commonly <4mm, probably due to SGR-recrystallization and recovery as shown in area 1.1 and 1.2 (figure 57 and figure 58). Opx display grain sizes up to 8 mm. The relationship between formation of pseudotachylyte and SGR-recrystallization, producing

high-angle grain boundaries and a reduction in grain size in ol in distant host rock may not be related.

Sample COR-04-06

This sample display textures similar to sample COR-06-03D, transected by two thin fault zones. The fault zones contain multiple fault strands with pseudotachylyte and fractures that strike subparallel to each other. The apparent offset on the faults is estimated to 0.8cm, and the strain-averaged stresses are estimated to a minimum of 40MPa (Andersen et al., 2008). EBSD analyses were done over distal fault- and truncated wall rock, relative to the fault zones (area 2.1 and area 2.2) and between the two fault zones (area 2.3).

- Area 2.1

Wall rock truncated by a thin fault in area 2.1 show several intensity maxima. These arrange a girdle of poles to [010] subparallel to the fault (figure 67, page 95). On the other hand, poles to [010] align normal to the compositional banding that elongate onto the fault strand (figure 66), dissimilar to COR-06-03D. Four intensity maxima on the IPF map represent four dominant grain orientations, and do not give a proper assessment the fabric. Poles to [100] and [001] scatter. Grain boundaries in truncated wall rock are similar to that found in distal wall rock and host ultramafics, with straight to curved interfaces that link up in modified polygonal junctions (figure 66). Kinked opx or pl has not been found in the extent of the thin section. Opx is frequently slightly folded conjointly with cpx, progressively so in the vicinity of faults. Ol wall rock grain sizes vary (8-<1mm) but are generally coarse and equant, similar to that in host ultramafic COR-10/12 (figure 51, B). Ol exhibit subgrain boundaries and undulouse extinction like that occasionally encountered in both host ultramafics.

The cropped ‘transitional’ margin (figure 68) displays a reduction in grain size from wall rock towards fault margin. There are numerous nonindexed voids in wall rock. Assessment of the micrograph (figure 66, A) display a brown discolouration enveloping the location of the ‘transitional’ domain. The discolouration can also be observed along wide, open fractures that transect the sample, where the discolouration extends into adjacent wall rock (figure 66). The brown discolouration may be intimately associated with fracturing, halting indexation of wall rock, and comprise the apparent grain size reduction.

- Area 2.2

Crystallographic orientations in ol truncated by a thin fault (figure 66, A) are poorly determined due to very few indexed grains in wall rock. Here, two ol grains are offset approximately 300µm. The apparent strong LPO on [100](010) (type-A) or [010](100), and strong poles to [001] (figure 69, page 99) is highly dissimilar from that in adjacent mapped area 2.1 on figure 67. Development of LPO must be considered over a large population of grains, and it is unlikely that crystal-plasticity is so localized that the adjacent, overlapping dataset does not display the same orientation. The two grains separated by the fault likely exhibit an arbitrary orientation that coincides with an experimentally derived slip system. Peeled-off clasts inherit the orientation from their parent and show the same orientation. The texture in the sample, as previously highlighted, is similar to that in the two host ultramafics. No interpretation on activated slip system has been suggested in this area due to this.

BSE imaging of dislocations in wall rock, adjacent to the fault that truncates area 2.1 and 2.2 progressively arranges in dense networks of dislocation walls (figure 80, 81 and 82, pages 118-120). There has been observed increasing numbers of both dislocation walls and free dislocations from distal to proximal side of the fault. Similar dislocation networks to that on figure 82, A, have been found in experiments on ol ("*cellular structures*"), however on a smaller scale and devoid of significant recovery (e.g. De Ronde et al., 2005; Druiventak et al., 2011). De Ronde et al. and Druiventak et al. suggested that low-temperature plasticity accounted for the structures, resulting in high elastic strains. Within the pseudotachylyte as shown on figure 82, B, an ol-clast retains networks of dislocations. These are wavy and may display a lower number of free dislocations. Observations of dislocations suggest that after seismic relaxation, crystal plasticity ceased and movement of dislocations is restricted. This supports the absence of a LPO for clasts in area 2.2.

It is interesting that wall rock in area 2.1 and 2.2 align poles to [010] subparallel to fault zones in spite of the poor number of grains used for projection. This is similar to that in the host ultramafic, where poles to [010] align subparallel to the vague banding, in area 1.3. The two fault zones in sample COR-04-06 transect the vague banding at a steep angle (figure 66).

- Area 2.3

A fracture truncating wall rock in area 2.3 display apparent strong LPO on [001](100) as shown on figure 70, page 101. Clasts in the fracture are elongated and align subparallel to the

direction of the fracture. The strong projections suggest that this could be a type-C LPO. Four individual indexed grains in wall rock are not conclusive, similar to the interpretation from area 2.2. A possibility is that the wall rock developed the LPO prior to fracturing, and that clasts largely inherited the orientation, although scattered (figure 70). Wall rock ol arrange with planar to curved grain boundaries and some intracrystalline distortion, evident on the IPF map, similar to that in area 1.3, 2.1 and 2.2.

Wall rock fragments and fine-grained fault zone margins

Sample COR-05-06C

Sample COR-05-06C is transected by a fault zone with an apparent slip of 18.3 cm and estimated minimum strain averaged stresses of 135MPa (Andersen et al., 2008). The protogranular, equilibrated texture is obliterated as shown on figure 71. Two pseudotachylyte fault-veins (1-4 mm wide) and associated damage zones are dominant features in the sample. Relict equilibrated texture can be found in the most distal areas in the thin section, outside of the fault zone. EBSD analyses were done within the fault zone and no assessment of the distal texture has been done. The mapped sections in this sample display highly sheared clasts (areas 3.1, 3.2 and 3.3) and a brecciated ol-opx-pl aggregate (area 3.4).

- Area 3.1

As in the previously assessed datasets, area 3.1 show similar crystallographic orientations for wall rock and clasts, the latter more scattered (figure 72, page 106). The dataset displays one of many subgrains in a sheared, coarse ol grain (8 mm along its long axis), from distal to proximal side, relative to thin fault-veins (figure 71, A). A relatively well developed, strong SPO and LPO has been found for both wall rock and clasts, suggesting activity on the [100](001) (type-E) slip system. The presence of defined subgrains in the ol (figure 71, A) suggests dislocation creep, and the dataset possibly represents a true LPO. Experimental deformation on ol has found that this slip system develops at high temperatures (≥1000°C) (Ave'Lallemant and Carter, 1970; Jung et al., 2006; Tommasi et al., 2000) as shown in table 13 and on figure 23 and figure 90. The temperature along the slip surfaces (figure 71, A) on formation must have been at a minimum of 1750°C (Andersen and Austrheim, 2006). It is considered that deformation in ol under high temperatures readily activates [100](010) (type-A), whereas [100](001) (type-E) is activated when ol contains an intermediate amount of water (Jung et al., 2006). This is supported by BSE imaging of dark voids, possibly fluid

inclusions in sample COR-04-06 (figure 80, 81 and 82) and COR-6/12 (figure 85, B). Most of the pseudotachylyte from the peridotites in Corsica exhibits these (Andersen and Austrheim, 2006; Deseta et al., submitted).

The highlighted wall rock margin (figure 73) display a prominent slip direction with b=[100], similar to that in the host grain, whereas poles to [010] and [001] arrange differently. A rotation of approximately 45° around the a-axis, into the fault, can account for the projections. The reduction in grain size in wall rock, from distal to proximal side of the fault zone (figure 74) is not associated with discolouration like that in area 2.1. The average grain diameter does not change significantly from the distal (1) to proximal (4) side, since small grains are abundant in all cropped sections. However, the average size of the two-dimensional surfaces of grains experiences a strong reduction, since there are fewer large grains. The wall rock witnesses a progressive elongation of ol that are separated by nonindexed fractures. The highlighted clasts in the fracture that transect the mapped area (figure 73) have similar orientations to that in wall rock, suggesting that these are deformed conjointly with their host. This observation, coupled with the rotation of the wall rock margin into the fault zone suggests that these features are contemporaneous, or possibly pre-dates generation of pseudotachylyte. Intense heat generation along the slip surface may facilitate recrystallization in adjacent wall rock and possibly re-arrange wallrock clasts. Grain size of recrystallized grains in the ol subgrain is probably not determined by a balance of grain-size reduction and growth during steady-state dislocation creep. This is required for the application of a grain size paleopiezometer (e.g. Derby and Ashby, 1987; Warren and Hirth, 2006). Instead, the grain size reduction is probably transient; related to generation of pseudotachylyte.

- Area 3.2

Area 3.2 display trails of dominantly small <20 µm ol clasts where the outline of these could represent larger, peeled-off and dismembered wall rock fragments. The indexation is very low and the crystallographic projections scatter largely around several intensity maxima (figure 75, page 106). The projections suggests activity on [010](100) or [001](100) (type-C). The clasts most likely correlates to the high temperatures suggested in area 3.1. Observations in an injection vein (figure 86) attest that ol porphyroclasts can completely recrystallize if high temperatures is sustained for relatively short periods of time (minutes to hours). This may induce recrystallization of wall rock fragments after detachment from their host, modifying

clast shape, size, as well as LPO. Possibly, peeled-off wall rock fragments inherit an arbitrary orientation within fault zones. This may account for the scattered projections.

- Area 3.3

Area 3.3 displays a peeled-off and sheared wall rock clast 0.7 cm along its long axis and smaller, scattered fragments as shown on figure 76, page 112. Clasts share a SPO subparallel to faults. Crystallographic projections indicate activity on [100](010) (type-A) over [001](010) (type-B). Given the estimated strain-averaged stresses of minimum 135MPa, type-B seems improbable, but may possibly be an underestimation of stresses during coseismic deformation. A possibility arises from figure 73 of the rotated wall rock margin in area 3.1. A rotation of 90° around [100] on peeled-off clasts derived from a crystal with type-E LPO will produce type-A orientation. Vice versa, a 90° rotation around [100] on a crystal with type-A LPO will produce type-E orientation. All three proposed orientations (type-A, B and E) may develop at high temperature, which is likely if the indexed ol represents peeled-off clasts, like that in area 3.2, from a common parent grain similar to area 3.1.

- Area 3.4

Area 3.4 displays a cataclastic, brecciated aggregate of ol, pl and opx found adjacent to a generation surface concealed by almost complete drainage of pseudotachylyte (figure 71, B). Indexed ol grains have rounded margins and show a vague SPO subparallel to the drained generation surface. The crystallographic orientations of these are elaborate. The misorientation angle distribution supports the presence of a LPO (figure 78, page 115).

Assessment of the IPF suggests activity on [010](001) over [001](010) (type-B). Crushed and brecciated aggregates have been associated with pseudotachylyte (figure 61, C). Brecciated zones could be precursor to generation of pseudotachylyte, developing LPO to accommodate strain at lower temperature than that required for melting. On the other hand, the generation surface concealed by drainage of pseudotachylyte may have brecciated the rock, questioning the minimum estimated stresses of 135MPa. The role of stress concentration at a propagating fault tip (e.g. Twiss and Moores, 2007) could possibly explain type-B concurrent with generation. Both proposed slip systems have experimentally been associated with high strain domains and high stresses, respectively (Jung et al., 2006; Tommasi et al., 2000). There is not enough data to speculate further.

Pseudotachylyte

- Area 4.1

Area 4.1 is interpreted to display crystallites formed in a pseudotachylyte pocket that aligns subparallel to fault veins (figure 87, page 126). The amount of ol within the vein far exceeds nonindexed areas, suggesting that ol is the dominant mineral in the pseudotachylyte matrix. The projections display several intensity maxima with huge scatter (figure 88). The projections suggest activity on [001](010) (type-B). This seems, however, unreasonable for crystallites that nucleated after post-seismic stress-drop.

The misorientation angle distribution shows that uncorrelated grains generally follow the theoretical random distribution, although with higher frequencies of high-angle misorientations. Uncorrelated grains lack higher frequencies of low-angle misorientations, relative to the theoretical random (figure 78, page 115 for comparison). This suggests that some other mechanism might explain the LPO. Injection veins and pockets of pseudotachylyte are found intruding into fine grained wall rock adjacent to fault veins, indicating that their formation postdates development of such margins. In order to explain type-B LPO, high differential stresses are needed at high temperatures of >1150°C, where 1300° correlates to the nucleation temperature of the crystallites (Andersen and Austrheim, 2006). Such stresses are, however, unlikely after seismic stress-drop.

One possibility could be that as crystallites nucleate, they favourably nucleate (or rotate) to minimize surface energy at ol-ol interfaces, which is aided when melt is present (Wheeler et al., 2001). Neighbouring crystallites may subsequently tile on the relatively flat (010) faces. There is not sufficient data to support this. Imaging of crystallites in a fault-vein in the same sample have shown euhedral to subhedral crystals (figure 83), but imaging of dislocation-free crystallites in the injection vein would be required in order to completely exclude intracrystalline deformation.

- Area 4.2

Area 4.2 is a cropped section from dataset 3.3, and is interpreted to display pseudotachylyte crystallites in a fault-vein (figure 89, page 129). The projections are highly scattered but display intensity maxima that may indicate activity on [100](010) (type-A). Ueda et al. (2008) reported type-A fabric ol in pseudotachylyte fault-veins in mylonitized peridotite from Balmuccia, Italy. They suggested that ductile shear localization, followed by seismic slip

produced pseudotachylyte, and subsequent ductile shear mylonitized and produced [100](010) fabric within the fault-vein. The fault-vein in area 4.2 does not show evidence for mylonitization. Imaging of the very same vein has shown euhedral-to subhedral crystallites (figure 83).

Ol crystallites in area 4.2 display a remarkably similar misorientation angle distribution, and also align poles to [010] normal to the macroscopic fabric like that in area 4.1. A similar interpretation to that in area 4.1 is assumed here.

Summary of observed LPO

Table 14 lists the Corsican samples and estimated conditions during deformation and generation of pseudoatchylyte. The interpreted fabric elements are from Jung et al. (2006); Tommasi et al. (2000) and minimum strain-averaged stresses are from Andersen et al. (2008). The temperatures associated with generation of pseudotachylyte are schematically drawn on figure 92. Temperatures are estimates from temperature profiles during dike solidification (Turcotte and Schubert, 2002), based on congruent melting of peridotite from ambient conditions of 1.5GPa and 470°C, to 1750°C (ΔT=1280°C) (Andersen et al., 2008). It is assumed that the temperature adjacent to a fault vein is close to the temperature in the vein, and that the temperature adjacent to an injection-vein follows ambient+½ΔT (Turcotte and Schubert, 2002). Wall rock is assumed to stay at ambient conditions. This means that the

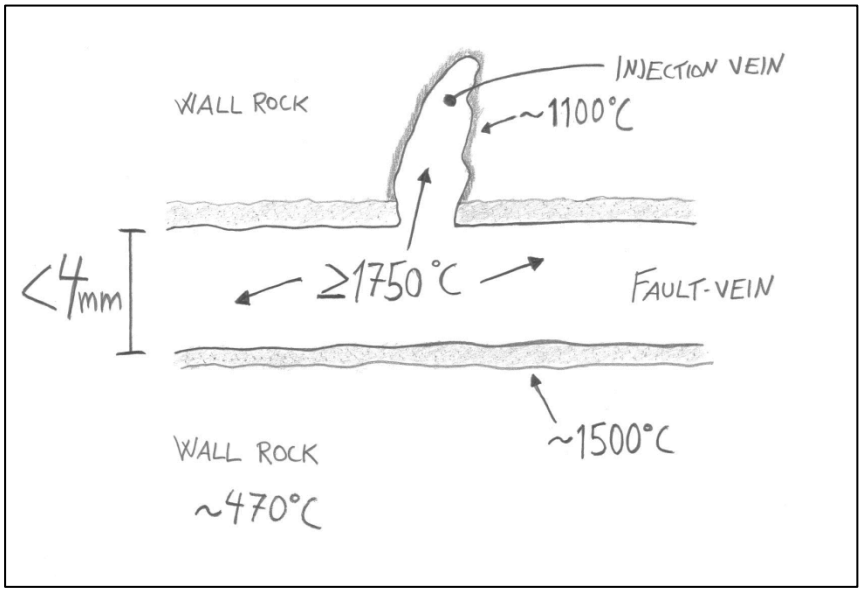

Figure 92: Schematically drawn fault-and injection vein representative for samples COR-04-06 and COR-05-06C. Assumptions on temperatures in are estimates from temperature profiles during dike solidification from Turcotte and Schubert (2002). Congruent melting of peridotite requires temperatures of minimum 1750°C at 1.5GPa (Andersen et al., 2008). See text for discussion.

temperature adjacent to fault- and associated injection veins and pockets must have been very high during generation of pseudotachylyte. Such temperatures correlate well with the experiments conducted by Jung et al. (2006). Sample COR-05-06C record all possible slip systems on figure 90, except fabric D (table 14), close to- and within fault zones. This suggests that the peridotites contained a sufficient amount of water, and/or that stresses did not reach 400MPa. LPO of possible type-B has been observed in two datasets which suggest that stresses possibly exceeded 300MPa, or that these developed at higher temperatures (Katayama and Karato, 2006). This raises a question regarding the minimum strain-averaged stresses on this sample by Andersen et al. (2008).

Areas 3.2, 3.3 and 3.4 are wall rock fragments resting in fault-zones and record multiple solutions, some of them type-B LPO. Two of these datasets record possible slip with b=[010], which by Tommasi et al. (2000) was associated with low temperature in high strain domains. The slip planes are different in the two which may suggest that porphyroclasts inhibits an arbitrary orientation after detaching from wall rock. However, all acquired datasets in this thesis have shown that wall rock and adjacent clasts have the same orientation. It is not

Sample	Scan area	Fabric	Wall rock	Clasts	Fault-vein	Injection-vein	T (°C)	Min. σ (MPa)
COR-06-03D	Area 1.3	-	X	-	-	-	~470	-
COR-04-06	Area 2.1	-	X	X	-	-	~1500	40
	Area 2.2	-	X	X	-	-	~1500	40
	Area 2.3	- (C?)	X	-	-	-	~470	40
COR-05-06C	Area 3.1	E	X	X	-	-	~1500	135
	Area 3.2	C ([010](100)?)	-	X	-	-	~1500	135
	Area 3.3	A? B?	-	X	-	-	~1500	135
	Area 3.4	B ([010](001)?)	-	X	-	-	?	135
	Area 4.1	- (B?)	-	-	?	?	≥1750	-
	Area 4.2	- (A?)	-	-	X	-	≥1750	-

Table 14: Overview of the Corsican samples and areas for EBSD analyses. Activated slip systems in sample COR-05-06C are elaborate, but are associated with high temperatures and/or high stresses. See text for discussion of the assumed conditions of formation.

unlikely that type-B LPO and slip with b=[010] could somehow be related, since these are associated with high stresses and high strains, respectively. The strong type-E LPO in wall rock, area 3.1, is suggested to be concurrent with generation of pseudotachylyte, and has developed within a single grain. It has become evident that indexing in sample COR-06-03D and COR-04-06 has proven difficult due to coarse grain sizes. LPO development increases with increasing strain (Passchier and Trouw, 2005), and sufficient strain is necessary for LPO alignment with the shear direction (Warren et al., 2008). This may explain why sample COR-05-06C has developed a strong fabric and sample COR-04-06 retains coarse, equilibrated fabrics. The minimum estimated stresses between the two samples vary with several magnitudes (table 14).

Analysed crystallites in pseudotachylytes have shown that these have preferred orientations, whereas the misorientation angle distributions do not associate these with intracrystalline deformation.

Overprinting relationships

The pyroxene end-members, primary ol and Cr-spl are typical for spl-lherzolite of mantle origin (e.g. Winter, 2010). The variable pl-content suggests that it has been refertilized at a later stage (Rampone et al., 1995). The host ultramafics retain modified protogranular, equilibrated fabrics where grain sizes have been observed up to 8mm for ol and opx. Spl is mostly located along grain boundaries and at triple junctions. Prominent recrystallization of ol in host rocks into finer bands (figure 51, A) may be derived from deformation during high-temperature crystal-plasticity, since alternating coarse- and fine grained textures are commonly found in exhumed peridotite (Mercier and Nicolas, 1975). High temperatures are required to sustain recrystallization in ol (Druiventak et al., 2011; Li et al., 2004) and do not concur with the regional peak metamorphism.

Low-temperature crystal plasticity is recorded by kinking and curvature of immiscibility lamellas in opx and cpx, twinning in pl, opx and cpx and common undulous ol (Matysiak and Trepmann, 2012; Passchier and Trouw, 2005). Minor development of tilt walls and subgrain boundaries in ol may accompany low-temperature plasticity (figure 57 and figure 58). Dislocations in sample COR-04-06 attest to local high dislocation density in distant wall rock (figure 81, B). Numerous tilt-walls arrange in subparallel networks and intersect. Recrystallization processes are amplified by water (e.g. De Ronde et al., 2005; Mackwell et

al., 1985), which may be abundant in subduction zones, and similar microstructures have probably evolved throughout in the Corsican peridotites.

On approaching fault-vein margins, cpx+opx commonly show intense curvature of exsollution lamellas (figure 63 and figure 65, A), pl has reacted and broken down and spl attest to modification (figure 62). Ol show progressively higher densities of free dislocations (figure 82) and rarely display strong LPO (figure 74). The association with deformation and pseudotachylyte generation might be spatially related, as previously commented. Deformation 'lamellas' resembling mechanical twins in ol (figure 64) have been observed adjacent to two fault-veins. These might have developed concurrent to massive release of energy by earthquake faulting. Parallel fractures in garnet has been related to energy by stress-concentration during earthquake faulting (Austrheim et al., 1996), and might relate to the structures found in ol adjacent to faults.

Pseudotachylyte fault-and injection veins are found intruding commonly present fine grained fault zone margins (figure 61, A, B and figure 71). Such margins have been observed to truncate brecciated aggregates (figure 61, C). There is lack of exposed breccias in the samples, maybe because pseudotachylyte is intimately associated with these and obliterates the former texture. Breccias or fine-grained zones have not been observed extending into host ultramafics, and may explain why they are devoid of pseudotachylyte. Such zones have possibly accommodated later strain localization and may be favourable sites for pseudotachylyte generation. Observations from area 3.1 have shown that a change in grain size may accompany, or possibly pre-date generation of pseudotachylyte. Here, ol wall rock contains clasts in a fracture, where clasts have developed similar LPO to that in wall rock(figure 73). This can be extrapolated to area 2.3, where LPO was not considered due to few indexed grains in wall rock, whereas both clasts and wallrock display a strong LPO. The fracture may possibly pre-date deformation, where clasts are deformed conjointly with the host. The fracture strike subparallel to fault veins, and may also represent a favourable site for generation of pseudotachylyte. In host ultramafics, thin fractures and sheared bands occasionally transect all phases (figure 52) but are devoid of a fine matrix.

The investigated faults COR-04-06 and COR-05-06 display ~1 mm and <4 mm wide fault-veins, respectively, whereas elsewhere in the peridotite bodies fault-veins commonly range from 1-3cm (figure 37, A) up to 38cm (figure 37, B). Spray (1992) determined that fracture toughness and grain size of fusing minerals in the host rock play an important role on the

volume of generated pseudotachylyte. The association of thin fault-veins obliterating earlier, fine-grained cataclastic or syndeformational zones agree with his work. The amount of melt generation may also be associated with the amount of slip, 0.8cm for COR-04-06 and 18.6cm for COR-05-06C. A larger offset would likely fuse more material.

During post-seismic relaxation there has not been much structural modification of the pseudotachylyte veins in sample COR-05-06C and COR-6/12. This is evident by euhedral crystallites (figure 83), preserved spherulites and dendrites (figure 85), and a lack of higher frequencies of low-angle misorientations for uncorrelated grains (figure 88 and figure 89). Even completely hydrated pseudotachylyte may preserve the original quench-texture, including spherulites, dendrites and chilled margins (Andersen and Austrheim, 2006; Austrheim and Andersen, 2004).

Thin fault-veins have been observed to mutually criss-cross along fault zones (figure 36, D) indicating reactivation, and/or truncate quenched and cooled fault-veins at a steep angle (figure 60, C). Earthquakes are universally associated with aftershock sequences, and occur due to stress redistribution in the vicinity of slipped regions. The rate of magnitude and recurrence of aftershocks on a seismic source follow Omori's law and the Gutenberg-Richter frequency-magnitude scaling, respectively (e.g. Kisslinger, 1996). Large earthquakes have larger aftershocks and more aftershocks.

On outcrop-scale, the large fossil MOHO-parallel fault (figure 41) clearly represents a mainshock where numerous aftershocks are distributed in the adjacent rocks. An array of later faults have been observed to truncate pseudotachylyte (figure 40) and possibly represents one of numerous aftershocks. These can be large on outcrop scale (figure 37, B) or small, even on thin-section scale (figure 60, C and figure 61, B), and they have different orientations. The investigated fault samples COR-04-06 and COR-05-06C probably represent aftershocks from redistribution of stress in the peridotite.

Effect of water

The identified LPO (table 14) found in wall rock in area 3.1 and possibly area 2.3 suggest that ol contained water dissolved in crystal lattices during deformation. In addition, none of the recorded LPO shows type-D, although possible type-B has been found in two datasets. This is consistent with reports from Andersen and Austrheim (2006); Deseta et al. (submitted) where estimates of porosity and water-bearing matrix in the ultramafic pseudotachylyte suggests up to ~4wt% H_2O. The preservation of primary texture and mineralogy of crystallites and micro-

phenocrysts (figure 83 and figure 85) suggest that fluid was originally dissolved in the ultramafic melt, not introduced at a later stage. Thus, water must have been present and locally dehydrated surrounding wall rock on seismic rupture. The dark voids found in BSE images probably represent fluid inclusions in wall rock ol and pseudotachylyte (figure 82 and figure 85, B).

Deformation aids and partly controls recrystallization by raising the energy of the system. This is achieved by increasing dislocation densities, and by allowing fluids to react with new volumes of rock (Austrheim et al., 1996). At the same time, metamorphic reactions affect deformation through changes in rheology and density (De Ronde et al., 2005). Water is known to greatly reduce the melting temperature in solid materials (e.g. Winter, 2010) and might enhance the volume of melts generated during seismicity. On outcrop-scale, pseudotachylytes are more commonly seen in the peridotite than in gabbro. This is supported by (Deseta et al., submitted) who also found that pseudotachylyte in peridotite is more hydrous than in gabbro.

Water enhances the rate and extent of grain boundary mobility, and probably plays a more important role than SGR under wet conditions (e.g. Jung and Karato, 2001; Mackwell et al., 1985; Mei and Kohlstedt, 2000). The LPO of ol can in turn be modified by grain boundary migration. Grain boundary migration has been observed for all phases in both spl-melagabbro and pl-spl-lherzolite (e.g. figure 56 A, and C, figure 58, figure 65, B). The LPO investigated here, however, is mainly a function of the magnification at which EBSD data was obtained.

Origin of water

Petrological studies have suggested that water content in the mantle below oceanic spreading axes (<120km depth) contain 400-1200ppm H/Si^6 (Hirth and Kohlstedt, 1996; Kohlstedt et al., 1996). According to figure 90, at approximately asthenospheric temperatures, the dominant ol fabrics will here either be type-E or type-C, dependent on the water content. At decreasing depths, ol grains are ‘dried out’ because water is strongly partitioned into the melt. This is shown on figure 93. This leaves residual grains that are depleted in water, eventually constituting the upper oceanic lithosphere. The upper oceanic lithosphere has been constrained texturally (from LPO) and seismologically (from anisotropy) to consist of ol having deformed on the [100](010) dry type-A fabric (figure 90) (e.g. Karato and Wu, 1993; Tommasi et al., 2000). If we can assume that the Corsican peridotites rested in the old, cold Tethyan oceanic basin at a depth of ~10km, the confining pressure must have been in the order of 0.3GPa prior to subduction (using ρgh where ρ=3000 kg/m3, h=10 km and

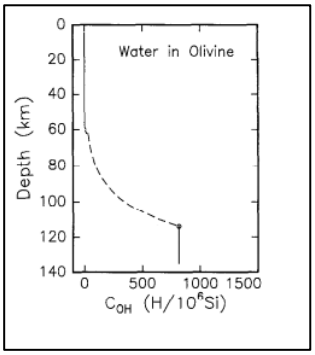

Figure 93: Estimated water content in ol versus depth beneath a mid-ocean ridge. From Hirth and Kohlstedt (1996).

g=gravitational constant). The solubility of water at this depth is approximately 250 H/10^{6}Si (Hirth and Kohlstedt, 1996) given that there are efficient pathways for fluid transport to this depth. This correlates to a type-A LPO when stresses are <100MPa (figure 90). The degree of serpentinization prior to subduction is not constrained. Observations of inclusions of tlc, clc and srp in opx and ol show evidence of hydration prior to subduction and prograde metamorphism (Austrheim and Andersen, 2004; Deseta et al., submitted).

Two of the LPO found in this study might suggest deformation on type-A fabric, however, these are from peeled-off clasts resting in a fault zone and pseudotachylyte crystallites (area 3.3 and area 4.2) and may not represent a pre-existing fabric. Ol LPO evolution and LPO variations suggest that a pre-existing (or absent) LPO influences the strain necessary for LPO alignment with the shear direction (Warren et al., 2008). In addition, the presence of additional phases affects the behaviour of ol slip systems during deformation (Kaminski and Ribe, 2002). The strong type-E LPO (area 3.1) indicate that water must have been in the order of 200-800 H/Si^6 if the observed LPO formed during coseismic deformation. This is reasonable, given its appearance with subgrains, intragranular clasts, alignment with the shear direction and consistent LPO. If area 2.3 record type-C LPO, despite the issues discussed, this implies that the amount of dissolved water in ol must have been even higher (Jung et al., 2006).

The time scale to modify pre-existing fabrics is an important issue in regions where dominant fabric types change spatially, such as in subduction zones. At increasing depths during subduction, increasing confining pressure will increase the diffusivity of water in ol. Water can be supplied from in-situ or extrinsic dehydration through reactions 1-5 on page 15,

allowing ol to develop preferential slip from [100](010) (type-A) to [100](001) (type-E) and [001](100) (type-C).

Suggested mechanisms for intermediate-depth seismicity

The two main proposed mechanisms for intermediate-depth seismicity (dehydration embrittlement and self-localizing shear heating) have been reviewed in chapter 1. Microtextural observations in the Corsican peridotites are elaborate, but so far have not been successful in constraining one or the other. The investigated samples are highly dissimilar. The EBSD analyses carried out so far are quite limited and a number of problems with interpretations have become evident.

It is reasonable to conclude that free water was available in the peridotites during coseismic deformation. Water dissolves in ol as a function of availability and confining pressure (e.g. Mackwell et al., 1985). Peridotites are largely impermeable rocks (e.g. Kostenko et al., 2002) and require pathways in order for water to infiltrate and interact. Ol, opx and cpx records inhomogeneous low-temperature crystal plasticity in host ultramafics. This is largely attributed to glide of dislocations, evident through twinning, kinking and undulouse extinction. A progressive number of dislocations adjacent to fault in sample COR-04-06 have been observed. Dislocations can be pinned by impurities, inclusions, and intersecting dislocations (Wenk and Bulakh, 2008). A pile-up of dislocations may lead to intragranular work hardening, nucleation of microcracks and is known to trigger brittle failure (e.g. Druiventak et al., 2011; Hirth and Lothe, 1992; Twiss and Moores, 2007). Coalescing microcracks may not be associated with seismicity alone, but may be an efficient way of fracturing the peridotite at depth, allowing fluid percolation. The pathways of fluids are not well constrained, and on the contrary may possibly migrate into the mantle wedge (e.g. Peacock, 2009; Reynard, 2012). There are no direct observations of dislocation pinning in relation to microfractures in the Corsican samples. Dark voids in sample COR-04-06 are found to be enveloped by dense phases or possibly dislocations (figure 81, A), but the origin of the dark voids is not constrained, nor the high z-contrast features that envelop these. However, a strain hardening mechanism operating in the lower-temperature range may add to the traditional faulting at the outer rise, transporting zones of weakness in the downgoing slab.

Previous work in Corsica has not been able to document dehydration embrittlement reactions that may be the direct cause of embrittlement and seismic faulting. Locally, dehydration reactions within pseudotachylyte have been observed by the breakdown of tlc to secondary ol

as described on page 60, but this is generated by the heat from solidification of pseudotachylyte and hence post-dates the seismic faulting (Austrheim and Andersen, 2004). Dehydration embrittlement cannot, however, be excluded as a mechanism for producing earthquakes. Intragranular work hardening and faulting at the outer rise could make dehydration reactions at depth exploit fracture networks and increase pore fluid pressures. The peridotite most likely contained free water during deformation, both dissolved in crystals and as an intergranular fluid. The origin of the fluid is not constrained.

Self-localizing shear heating is a mechanism for catastrophic failure of viscoelastic materials (Braeck and Podladchikov, 2007). Its potential relevance for earthquake faulting was demonstrated by John et al. (2009). Inherited in this model was that the rock undergoes ductile deformation, which in turn produces heat (equation 2, page 18), which feeds back in a manner that results in more deformation and heating in a progressively localized domain. Ultimately this results in complete material failure, melting and faulting. The hall-mark of self-localizing shear heating is therefore evidence for viscous deformation as a precursor to faulting and melting (John et al., 2009).

7. Conclusion

The microstructure of the investigated Corsican peridotites has been assessed in terms of processes related to earthquake-driven deformation using the relatively new technique of EBSD. Due to the limited time available for the study there has been some issues regarding the data acquisition and post processing. EBSD work has not been done on these rocks before and the study therefore has a character of a pilot investigation.

The new results are:

- The strength of the peridotite is mostly determined by the strength of olivine. Olivine display variable extent of recrystallization while orthopyroxene and clinopyroxene largely retain their mechanical framework.
- The peridotites record highly inhomogeneous crystal-plasticity. Samples gathered in proximity of each other frequently display mechanical twinning and kinking in host rock, and development of strong lattice preferred orientations in fault rocks. LPO in olivine along faults are associated with high temperatures and possibly very high stresses.
- Co-seismic deformation in the peridotite occurred in the presence of free water. Water may have triggered and amplified recrystallization in vicinity of faults, possibly by easing the direction of slip in olivine. Pseudotachylyte fault veins may be associated with pre-existing or syn-deformational weaknesses in the peridotite, however, melting commonly destroy evidence for precise observation.
- After seismic stress-drop the peridotite largely returned to ambient conditions and experienced rapid exhumation. Well preserved pseudotachylyte attest to little post seismic deformation in the studied localities.
- There are difficulties with comparing the observed textures to experimental studies. The coexistence of ductile deformation and pseudotachylytes cannot be assessed in terms of steady-state flow. The texture in host rock has not been resolved in this thesis. It is a necessity, as it holds the reference to which co-seismic deformation products can be compared.
- Correlation between analysed areas and samples has proven difficult. The peridotites have a complex thermal history and samples are highly dissimilar. It has become evident that interpretations are limited due to unrepresentative EBSD datasets.

- Acquisition, post-processing and interpretation of EBSD data has been learned using two separate software packages in different laboratories. However, a much more comprehensive EBSD-study is necessary to provide a more detailed explanation of the microstructure and an understanding of the deformation mechanism(s) related to the co-seismic faulting.

8. Further work

EBSD software has been developed with the capability to process and analyse large datasets (HKL, 2007). In order to constrain the texture in the peridotite, several datasets at a low magnification and a coarse step size could be stitched together. This should be done on samples both devoid of pseudotachylyte and from fault zones with coarse-grained, truncated wall rock into more distant wall rock. This will give insight into overall LPO, it will reduce the amount of erroneous data (hence provide misorientation angle distributions using EDAX/TSL) and give possible links to overall water content and stresses.

Indexation of opx should be incorporated. It has been found that the strength of opx LPO decreases with increasing water content, and has a correlation with the strength of the LPO of ol (Jung et al., 2010).

Stitched maps at a high magnification and low step size should be conducted within pseudotachylyte fault- and injection veins. The crystallographic projections acquired for these in this thesis are elaborate. The orientation of crystallites may assess conditions that post-date seismic event(s), since these show little sign of modification. Imaging of dislocations in crystallites should be done.

Fabric elements and microstructures found in peridotite should subsequently be compared with those in structurally overlying gabbros.

Assessment of stresses during coseismic faulting can be constrained with high-resolution TEM or BSE imaging of dislocations in wall rock adjacent to faults. Grain sizes are typically coarse and proper assessment of suited grains is key. TEM should be applied on deformation ‘lamellas’ in ol adjacent to fault veins, to see if the orientation of these is related to a preferential slip direction.

It should not be concealed that the selection of areas prior to analyses could have been better in this study.

9. References

Almendinger, R., 2013, Stereonet 8; http://www.geo.cornell.edu/geology/faculty/RWA/programs/stereonet.html.

Andersen, T. B., and Austrheim, H., 2006, Fossil earthquakes recorded by pseudotachylytes in mantle peridotite from the Alpine subduction complex of Corsica: Earth and Planetary Science Letters, v. 242, no. 1-2, p. 58-72.

Andersen, T. B., Austrheim, H., Deseta, N., Ashwal, L. D., and Silkoset, P., submitted, Evidence for large subduction earthquakes along the fossil MOHO in Alpine Corsica, p. 1-7.

Andersen, T. B., Mair, K., Austrheim, H., Podladchikov, Y. Y., and Vrijmoed, J. C., 2008, Stress release in exhumed intermediate and deep earthquakes determined from ultramafic pseudotachylyte: Geology, v. 36, no. 12, p. 995-998.

Austrheim, H., and Andersen, T. B., 2004, Pseudotachylytes from Corsica: fossil earthquakes from a subduction complex: Terra Nova, v. 16, no. 4, p. 193-197.

Austrheim, H., and Boundy, T. M., 1994, Pseudotachylytes Generated during Seismic Faulting and Eclogitization of the Deep Crust: Science, v. 265, no. 5168, p. 82-83.

Austrheim, H., Erambert, M., and Boundy, T. M., 1996, Garnets recording deep crustal earthquakes: Earth and Planetary Science Letters, v. 139, no. 1-2, p. 223-238.

Ave'Lallemant, H. G., and Carter, N. L., 1970, Syntectonic Recrystallization of Olivine and Modes of Flow in Upper Mantle: Geological Society of America Bulletin, v. 81, no. 8, p. 2203-2220.

Barcheck, C. G., Wiens, D. A., van Keken, P. E., and Hacker, B. R., 2012, The relationship of intermediate- and deep-focus seismicity to the hydration and dehydration of subducting slabs: Earth and Planetary Science Letters, v. 349, p. 153-160.

Barron, A., 2012, Physical Methods in Chemistry and Nano Science, Connexions, Rice University, p. 702.

Brace, W. F., and Byerlee, J. D., 1966, Stick-Slip as a Mechanism for Earthquakes: Science, v. 153, no. 3739, p. 990-&.

Braeck, S., and Podladchikov, Y. Y., 2007, Spontaneous thermal runaway as an ultimate failure mechanism of materials: Physical Review Letters, v. 98, no. 9.

Braeck, S., Podladchikov, Y. Y., and Medvedev, S., 2009, Spontaneous dissipation of elastic energy by self-localizing thermal runaway: Physical Review E, v. 80, no. 4.

Bridgman, P. W., 1945, Polymorphic Transitions and Geological Phenomena: American Journal of Science, v. 243A, p. 90-97.

Brindley, G. W., and Hayami, R., 1965, Kinetics and Mechanism of Formation of Forsterite (Mg2sio4) by Solid State Reaction of Mgo and Sio2: Philosophical Magazine, v. 12, no. 117, p. 505-&.

Brothers, R. N., 1959a, Flow Orientation of Olivine: American Journal of Science, v. 257, no. 8, p. 574-584.

-, 1959b, A Penetration-Twin in Olivine: American Mineralogist, v. 44, no. 9-10, p. 1086-1089.

Brovarone, A. V., Beltrando, M., Malavieille, J., Giuntoli, F., Tondella, E., Groppo, C., Beyssac, O., and Compagnoni, R., 2011a, Inherited Ocean-Continent Transition zones in deeply subducted terranes: Insights from Alpine Corsica: Lithos, v. 124, no. 3-4, p. 273-290.

Brovarone, A. V., Groppo, C., Hetenyi, G., Compagnoni, R., and Malavieille, J., 2011b, Coexistence of lawsonite-bearing eclogite and blueschist: phase equilibria modelling of Alpine Corsica metabasalts and petrological evolution of subducting slabs: Journal of Metamorphic Geology, v. 29, no. 5, p. 583-600.

Brunet, C., Monie, P., Jolivet, L., and Cadet, J. P., 2000, Migration of compression and extension in the Tyrrhenian Sea, insights from Ar-40/Ar-39 ages on micas along a transect from Corsica to Tuscany: Tectonophysics, v. 321, no. 1, p. 127-155.

Burnley, P. C., and Green, H. W., 1989, Stress Dependence of the Mechanism of the Olivine Spinel Transformation: Nature, v. 338, no. 6218, p. 753-756.

Cavazza, W., Zattin, M., Ventura, B., and Zuffa, G. G., 2001, Apatite fission-track analysis of Neogene exhumation in northern Corsica (France): Terra Nova, v. 13, no. 1, p. 51-57.

Christensen, D. H., and Ruff, L. J., 1988, Seismic Coupling and Outer Rise Earthquakes: Journal of Geophysical Research-Solid Earth and Planets, v. 93, no. B11, p. 13421-13444.

Clarke, G. L., and Norman, A. R., 1993, Generation of Pseudotachylite under Granulite Facies Conditions, and Its Preservation during Cooling: Journal of Metamorphic Geology, v. 11, no. 3, p. 319-335.

Cornelis, K., and Dutrow, B., 2008, Mineral Science, John Wiley & Sons, Inc., 675 p.:

Cowan, D. S., 1999, Do faults preserve a record of seismic slip? A field geologist's opinion: Journal of Structural Geology, v. 21, p. 995-1001.

Curewitz, D., and Karson, J. A., 1999, Ultracataclasis, sintering, and frictional melting in pseudotachylytes from East Greenland: Journal of Structural Geology, v. 21, no. 12, p. 1693-1713.

Day, A. P., and Quested, T. E., 1999, A comparison of grain imaging and measurement using horizontal orientation and colour orientation contrast imaging, electron backscatter pattern and optical methods: Journal of Microscopy-Oxford, v. 195, p. 186-196.

De Ronde, A., Stunitz, H., Tullis, J., and Heilbronner, R., 2005, Reaction-induced weakening of plagioclase-olivine composites: Tectonophysics, v. 409, p. 85-106.

Derby, B., and Ashby, M. F., 1987, On Dynamic Recrystallization: Scripta Metallurgica, v. 21, no. 6, p. 879-884.

Deseta, N., Ashwal, L. D., and Andersen, T. B., submitted, Intermediate-depth seismicity initiated by thermal runaway, detailed petrographic and microtextural observations from blueschist facies pseudotachylytes, Cape Corse, Corsica, p. 45.

Di Toro, G., Nielsen, S., and Pennacchioni, G., 2005, Earthquake rupture dynamics frozen in exhumed ancient faults: Nature, v. 436, no. 7053, p. 1009-1012.

Di Toro, G., and Pennacchioni, G., 2004, Superheated friction-induced melts in zoned pseudotachylytes within the Adamello tonalites (Italian Southern Alps): Journal of Structural Geology, v. 26, no. 10, p. 1783-1801.

Dingley, D. J., and Randle, V., 1992, Microtexture Determination by Electron Back-Scatter Diffraction: Journal of Materials Science, v. 27, no. 17, p. 4545-4566.

Druiventak, A., Trepmann, C. A., Renner, J., and Hanke, K., 2011, Low-temperature plasticity of olivine during high stress deformation of peridotite at lithospheric conditions - An experimental study: Earth and Planetary Science Letters, v. 311, no. 3-4, p. 199-211.

Drury, M. R., 2005, Dynamic recrystallization and strain softening of olivine aggregates in the laboratory and the lithosphere: Deformation Mechanisms, Rheology and Tectonics: From Minerals to the Lithosphere, v. 243, p. 143-158.

Duda, R. O., and Hart, P. E., 1972, Use of Hough Transformation to Detect Lines and Curves in Pictures: Communications of the Acm, v. 15, no. 1, p. 11-&.

DuPont, 2005, Material safety data sheet, DuPont air products NanoMaterials L.L.C., p. 5.

Durand-Delga, M., Peybernes, B., and Rossi, P., 1997, Evidence to support the proximity of the Balagne ophiolitic complex (Haute-Corse, France) to the European continental margin during the Jurassic: Comptes Rendus De L Academie Des Sciences Serie Ii Fascicule a-Sciences De La Terre Et Des Planetes, v. 325, no. 12, p. 973-981.

Egal, E., 1992, Structures and Tectonic Evolution of the External Zone of Alpine Corsica: Journal of Structural Geology, v. 14, no. 10, p. 1215-1228.

Egal, E., and Caron, J. M., 1988, Polyphase Tectonics in the Autochthonous Eocene at the Western Front of the Balagne Thrust Sheets (Corsica): Bulletin De La Societe Geologique De France, v. 4, no. 2, p. 315-321.

Egydio-Silva, M., and Mainprice, D., 1999, Determination of stress directions from plagioclase fabrics in high grade deformed rocks (Alem Paraiba shear zone, Ribeira fold belt, southeastern Brazil): Journal of Structural Geology, v. 21, no. 12, p. 1751-1771.

Etchecopar, A., and Vasseur, G., 1987, A 3-D Kinematic Model of Fabric Development in Polycrystalline Aggregates - Comparisons with Experimental and Natural Examples: Journal of Structural Geology, v. 9, no. 5-6, p. 705-717.

Evans, B. W., 1999, Phase relations of epidote blueschists: Lithos, v. 25, p. 3-23.

Fliervoet, T. F., Drury, M. R., and Chopra, P. N., 1999, Crystallographic preferred orientations and misorientations in some olivine rocks deformed by diffusion or dislocation creep: Tectonophysics, v. 303, no. 1-4, p. 1-27.

Fournier, M., Jolivet, L., Goffe, B., and Dubois, R., 1991, Alpine Corsica Metamorphic Core Complex: Tectonics, v. 10, no. 6, p. 1173-1186.

Frank, F. C., 1980, The Frank-Read Source: Proceedings of the Royal Society of London Series a-Mathematical Physical and Engineering Sciences, v. 371, no. 1744, p. 136-138.

Frohlich, C., 2006, Deep earthquakes, Cambridge, Cambridge University Press.

Goldschmidt, V. M., 1943, Om friksjonsglass (pseudo-tachylitt) i fjellkjeden: GFF, v. 65, p. 83-84.

Google Earth™, 2013, IGN France

Green, H. W., and Burnley, P. C., 1989, A New Self-Organizing Mechanism for Deep-Focus Earthquakes: Nature, v. 341, no. 6244, p. 733-737.

Green, H. W., and Houston, H., 1995, The Mechanics of Deep Earthquakes: Annual Review of Earth and Planetary Sciences, v. 23, p. 169-213.

Hacker, B. R., Peacock, S. M., Abers, G. A., and Holloway, S. D., 2003, Subduction factory - 2. Are intermediate-depth earthquakes in subducting slabs linked to metamorphic dehydration reactions?: Journal of Geophysical Research-Solid Earth, v. 108, no. B1.

Hasegawa, A., Umino, N., and Takagi, A., 1978, Double-planed deep seismic zone and upper-mantle structure in the Northeastern Japan Arc: Geophysical Journal International, v. 54, no. 2, p. 281-296.

Hiltner, P. A., and Krieger, I. M., 1969, Diffraction of Light by Ordered Suspensions: Journal of Physical Chemistry, v. 73, no. 7, p. 2386-&.

Hirth, G., and Kohlstedt, D. L., 1996, Water in the oceanic upper mantle: Implications for rheology, melt extraction and the evolution of the lithosphere: Earth and Planetary Science Letters, v. 144, no. 1-2, p. 93-108.

Hirth, J. P., and Lothe, J., 1992, Theory of dislocations: Krieger Publishing Company, Malabar, Florida, p. 515.

HKL, O. I., 2007, HKL Channel 5 Manual, Oxford Instruments HKL, p. 475.

Hobbs, B. E., and Ord, A., 1988, Plastic Instabilities - Implications for the Origin of Intermediate and Deep-Focus Earthquakes: Journal of Geophysical Research-Solid Earth and Planets, v. 93, no. B9, p. 10521-10540.

Humphreys, F. J., and Hatherley, M., 1995, Recrystallization and related annealing phenomena: Elsevier Science, New York, p. 498.

Jaroslow, G. E., Hirth, G., and Dick, H. J. B., 1996, Abyssal peridotite mylonites: Implications for grain-size sensitive flow and strain localization in the oceanic lithosphere: Tectonophysics, v. 256, no. 1-4, p. 17-37.

Jensen, L. N., and Starkey, J., 1985, Plagioclase Microfabrics in a Ductile Shear Zone from the Jotun Nappe, Norway: Journal of Structural Geology, v. 7, no. 5, p. 527-539.

Jessell, M. W., 1987, Grain-Boundary Migration Microstructures in a Naturally Deformed Quartzite: Journal of Structural Geology, v. 9, no. 8, p. 1007-1014.

John, T., Medvedev, S., Rupke, L. H., Andersen, T. B., Podladchikov, Y. Y., and Austrheim, H., 2009, Generation of intermediate-depth earthquakes by self-localizing thermal runaway: Nature Geoscience, v. 2, no. 2, p. 137-140.

Jolivet, L., Daniel, J. M., and Fournier, M., 1991, Geometry and Kinematics of Extension in Alpine Corsica: Earth and Planetary Science Letters, v. 104, no. 2-4, p. 278-291.

Jolivet, L., Dubois, R., Fournier, M., Goffe, B., Michard, A., and Jourdan, C., 1990, Ductile Extension in Alpine Corsica: Geology, v. 18, no. 10, p. 1007-1010.

Jolivet, L., Faccenna, C., Goffe, B., Burov, E., and Agard, P., 2003, Subduction tectonics and exhumation of high-pressure metamorphic rocks in the Mediterranean orogens: American Journal of Science, v. 303, no. 5, p. 353-409.

Jung, H., Green, H. W., and Dobrzhinetskaya, L. F., 2004, Intermediate-depth earthquake faulting by dehydration embrittlement with negative volume change: Nature, v. 428, no. 6982, p. 545-549.

Jung, H., and Karato, S. I., 2001, Effects of water on dynamically recrystallized grain-size of olivine: Journal of Structural Geology, v. 23, no. 9, p. 1337-1344.

Jung, H., Katayama, I., Jiang, Z., Hiraga, I., and Karato, S., 2006, Effect of water and stress on the lattice-preferred orientation of olivine: Tectonophysics, v. 421, no. 1-2, p. 1-22.

Jung, H., Park, M., Jung, S., and Lee, J., 2010, Lattice Preferred Orientation, Water Content, and Seismic Anisotropy of Orthopyroxene: Journal of Earth Science, v. 21, no. 5, p. 555-568.

Kaminski, E., and Ribe, N. M., 2002, Timescales for the evolution of seismic anisotropy in mantle flow: Geochemistry Geophysics Geosystems, v. 3.

Karato, S., 1987, Scanning Electron-Microscope Observation of Dislocations in Olivine: Physics and Chemistry of Minerals, v. 14, no. 3, p. 245-248.

-, 1995, Effects of Water on Seismic-Wave Velocities in the Upper-Mantle: Proceedings of the Japan Academy Series B-Physical and Biological Sciences, v. 71, no. 2, p. 61-66.

Karato, S., and Wu, P., 1993, Rheology of the Upper Mantle - a Synthesis: Science, v. 260, no. 5109, p. 771-778.

Karato, S. I., and Jung, H., 2003, Effects of pressure on high-temperature dislocation creep in olivine: Philosophical Magazine, v. 83, no. 3, p. 401-414.

Katayama, I., and Karato, S., 2006, Effect of temperature on the B- to C-type olivine fabric transition and implication for flow pattern in subduction zones: Physics of the Earth and Planetary Interiors, v. 157, no. 1-2, p. 33-45.

Kearey, P., Klepeis, K. A., and Vine, F. J., 2009, Global Tectonics, Blackwell Publishing, 482 p.:

Kelemen, P. B., and Dick, H. J. B., 1995, Focused Melt Flow and Localized Deformation in the Upper-Mantle - Juxtaposition of Replacive Dunite and Ductile Shear Zones in the Josephine Peridotite, Sw Oregon: Journal of Geophysical Research-Solid Earth, v. 100, no. B1, p. 423-438.

Kelemen, P. B., and Hirth, G., 2007, A periodic shear-heating mechanism for intermediate-depth earthquakes in the mantle: Nature, v. 446, no. 7137, p. 787-790.

Killick, A. M., 1990, Pseudotachylyte generated as a result of a drilling "burn-in": Tectonophysics, v. 171, p. 221-227.

Kirby, S. H., Stein, S., Okal, E. A., and Rubie, D. C., 1996, Metastable mantle phase transformations and deep earthquakes in subducting oceanic lithosphere: Reviews of Geophysics, v. 34, no. 2, p. 261-306.

Kisslinger, C., 1996, Aftershocks and fault-zone properties: Advances in Geophysics, Vol 38, v. 38, p. 1-36.

Kohlstedt, D. L., Goetze, C., Durham, W. B., and Vandersande, J., 1976, New Technique for Decorating Dislocations in Olivine: Science, v. 191, no. 4231, p. 1045-1046.

Kohlstedt, D. L., Keppler, H., and Rubie, D. C., 1996, Solubility of water in the alpha, beta and gamma phases of (Mg,Fe)(2)SiO4: Contributions to Mineralogy and Petrology, v. 123, no. 4, p. 345-357.

Kohlstedt, D. L., Nichols, H. P. K., and Hornack, P., 1980, The Effect of Pressure on the Rate of Dislocation Recovery in Olivine: Journal of Geophysical Research, v. 85, no. Nb6, p. 3122-3130.

Kostenko, O., Jamtveit, B., Austrheim, H., Pollok, K., and Putnis, C., 2002, The mechanism of fluid infiltration in peridotites at Almklovdalen, western Norway: Geofluids, v. 2, no. 3, p. 203-215.

Kunze, K., Adams, B. L., Heidelbach, F., and Wenk, H. R., 1994, Local Microstructural Investigations in Recrystallized Quartzite Using Orientation Imaging Microscopy: Proceedings of the 10th International Conference on Textures of Materials, Pts 1 and 2 - Icotom-10, v. 157-, p. 1243-1249.

Lahondere, D., and Guerrot, C., 1997, Sm-Nd dating of Alpine eclogittic metamorphism in Corsica: evidence for Late Cretaceous subduction beneath the Corsican-Sardinian block: Geologie de la France, v. 3, p. 3-11.

Lavier, L. L., and Manatschal, G., 2006, A mechanism to thin the continental lithosphere at magma-poor margins: Nature, v. 440, no. 7082, p. 324-328.

Lay, T., Ammon, C. J., Kanamori, H., Xue, L., and Kim, M. J., 2011, Possible large near-trench slip during the 2011 M-w 9.0 off the Pacific coast of Tohoku Earthquake: Earth Planets and Space, v. 63, no. 7, p. 687-692.

Lay, T., Kanamori, H., Ammon, C. J., Nettles, M., Ward, S. N., Aster, R. C., Beck, S. L., Bilek, S. L., Brudzinski, M. R., Butler, R., DeShon, H. R., Ekstrom, G., Satake, K., and Sipkin, S., 2005, The great Sumatra-Andaman earthquake of 26 December 2004: Science, v. 308, no. 5725, p. 1127-1133.

Lee, R. W., and Kirby, S. H., 1984, Experimental Deformation of Topaz Crystals - Possible Embrittlement by Intracrystalline Water: Journal of Geophysical Research, v. 89, no. Nb6, p. 4161-4166.

Li, L., Weidner, D., Raterron, P., Chen, J. H., and Vaughan, M., 2004, Stress measurements of deforming olivine at high pressure: Physics of the Earth and Planetary Interiors, v. 143, p. 357-367.

Lin, A. M., 1994, Glassy Pseudotachylyte Veins from the Fuyun Fault Zone, Northwest China: Journal of Structural Geology, v. 16, no. 1, p. 71-83.

Lister, G. S., and Hobbs, B. E., 1980, The Simulation of Fabric Development during Plastic-Deformation and Its Application to Quartzite - the Influence of Deformation History: Journal of Structural Geology, v. 2, no. 3, p. 355-370.

Liu, L., 1983, Phase transformations, earthquakes and the descending lithosphere: Physics of the Earth and Planetary Interiors, v. 32, p. 226-240.

Lund, M. G., 2002, Metamorphism, earthquakes and fracturing of the deep continental crust: Unpubl. PhD, Univ. Oslo, p. 169.

Mackenzie, J. K., and Thomson, M. J., 1957, Some Statistics Associated with the Random Disorientation of Cubes: Biometrika, v. 44, no. 1-2, p. 205-210.

Mackwell, S. J., Kohlstedt, D. L., and Paterson, M. S., 1985, The Role of Water in the Deformation of Olivine Single-Crystals: Journal of Geophysical Research-Solid Earth and Planets, v. 90, no. Nb13, p. 1319-1333.

Maggi, M., Rossetti, F., Corfu, F., Theye, T., Andersen, T. B., and Faccenna, C., 2012, Clinopyroxene-rutile phyllonites from the East Tenda Shear Zone (Alpine Corsica, France): pressure-temperature-time constraints to the Alpine reworking of Variscan Corsica: Journal of the Geological Society, v. 169, no. 6, p. 723-732.

Magloughlin, J. F., 1992, Microstructural and Chemical-Changes Associated with Cataclasis and Frictional Melting at Shallow Crustal Levels - the Cataclasite Pseudotachylyte Connection: Tectonophysics, v. 204, no. 3-4, p. 243-260.

Magloughlin, J. F., and Spray, J. G., 1992, Frictional Melting Processes and Products in Geological-Materials - Introduction and Discussion: Tectonophysics, v. 204, no. 3-4, p. 197-206.

Mainprice, D., and Nicolas, A., 1989, Development of Shape and Lattice Preferred Orientations - Application to the Seismic Anisotropy of the Lower Crust: Journal of Structural Geology, v. 11, no. 1-2, p. 175-189.

Malavieille, J., Molli, G., Vitale Brovarone, A., and Beyssac, O., 2011, CorseAlp 2011 Field Trip Guidebook.

Mariani, E., Prior, D. J., McNamara, D., Pearce, M. A., Seaton, N., Seward, D., Tatham, D., and Wheeler, J., 2008, Instrumental Techniques Applied to Mineralogy and Geochemistry, *in* Subías, I. a. B., B., ed., Volume 5: Madrid, Sociedad Española de Mineralogía, p. 7-21.

Masch, L., Wenk, H. R., and Preuss, E., 1985, Electron-Microscopy Study of Hyalomylonites - Evidence for Frictional Melting in Landslides: Tectonophysics, v. 115, no. 1-2, p. 131-160.

Mattauer, M., and Proust, F., 1975, New Data on Structural Evolution of Alpine Belt in Corsica: Comptes Rendus Hebdomadaires Des Seances De L Academie Des Sciences Serie D, v. 281, no. 22, p. 1681-1684.

Matysiak, A. K., and Trepmann, C. A., 2012, Crystal-plastic deformation and recrystallization of peridotite controlled by the seismic cycle: Tectonophysics, v. 530, p. 111-127.

Mei, S., and Kohlstedt, D. L., 2000, Influence of water on plastic deformation of olivine aggregates 2. Dislocation creep regime: Journal of Geophysical Research-Solid Earth, v. 105, no. B9, p. 21471-21481.

Mercier, J. C. C., and Nicolas, A., 1975, Textures and Fabrics of Upper-Mantle Peridotites as Illustrated by Xenoliths from Basalts: Journal of Petrology, v. 16, no. 2, p. 454-487.

Michard, A., and Martinotti, G., 2002, The Eocene unconformity of the Brianconnais domain in the French-Italian Alps, revisited (Marguareis massif, Cuneo); a hint for a Late Cretaceous-Middle Eocene frontal bulge setting: Geodinamica Acta, v. 15, no. 5-6, p. 289-301.

Mohn, G., Manatschal, G., Muntener, O., Beltrando, M., and Masini, E., 2010, Unravelling the interaction between tectonic and sedimentary processes during lithospheric thinning in the Alpine Tethys margins: International Journal of Earth Sciences, v. 99, p. S75-S101.

Molli, G., 2008, Northern Apennine-Corsica orogenic system: An updated overview: Geological Society, London, Special Publications, v. 298, p. 413-442.

Molli, G., and Tribuzio, R., 2004, Shear zones and metamorphic signature of subducted continental crust as tracers of the evolution of the Corsica Northern Apennine orogenic system: Flow Processes in Faults and Shear Zones, v. 224, p. 321-335.

Molli, G., Tribuzio, R., and Marquer, D., 2006, Deformation and metamorphism at the eastern border of the Tenda Massif (NE Corsica): a record of subduction and exhumation of continental crust: Journal of Structural Geology, v. 28, no. 10, p. 1748-1766.

Morishita, T., 1998, Possible pseudotachylyte from the Horoman peridotite complex of the Hidaka belt, Hokkaido, northern Japan: J. Geol. Soc. Jpn., v. 104, p. 18-23.

Obata, M., and Karato, S., 1995, Ultramafic Pseudotachylite from the Balmuccia Peridotite, Ivrea Verbano Zone, Northern Italy: Tectonophysics, v. 242, no. 3-4, p. 313-328.

Ogawa, M., 1987, Shear Instability in a Viscoelastic Material as the Cause of Deep-Focus Earthquakes: Journal of Geophysical Research-Solid Earth and Planets, v. 92, no. B13, p. 13801-13810.

Pacheco, J. F., Sykes, L. R., and Scholz, C. H., 1993, Nature of Seismic Coupling Along Simple Plate Boundaries of the Subduction Type: Journal of Geophysical Research-Solid Earth, v. 98, no. B8, p. 14133-14159.

Passchier, C. W., 1982, Pseudotachylyte and the Development of Ultramylonite Bands in the Saint-Barthelemy Massif, French Pyrenees: Journal of Structural Geology, v. 4, no. 1, p. 69-79.

Passchier, C. W., and Trouw, R. A., 2005, Microtectonics, Springer, 366 p.:

Peacock, S. M., 2001, Are the lower planes of double seismic zones caused by serpentine dehydration in subducting oceanic mantle?: Geology, v. 29, no. 4, p. 299-302.

-, 2009, Thermal and metamorphic environment of subduction zone episodic tremor and slip: Journal of Geophysical Research-Solid Earth, v. 114.

Pec, M., Stunitz, H., and Heilbronner, R., 2012, Semi-brittle deformation of granitoid gouges in shear experiments at elevated pressures and temperatures: Journal of Structural Geology, v. 38, p. 200-221.

Peron-Pinvidic, G., and Manatschal, G., 2009, The final rifting evolution at deep magma-poor passive margins from Iberia-Newfoundland: a new point of view: International Journal of Earth Sciences, v. 98, no. 7, p. 1581-1597.

Poirier, J. P., 1985, Creep of crystals: Cambridge Univ. Press, New York.

Post, R. L., 1977, High-Temperature Creep of Mt Burnet-Dunite: Tectonophysics, v. 42, no. 2-4, p. 75-110.

Prior, D. J., Boyle, A. P., Brenker, F., Cheadle, M. C., Day, A., Lopez, G., Peruzzo, L., Potts, G. J., Reddy, S., Spiess, R., Timms, N. E., Trimby, P., Wheeler, J., and Zetterstrom, L., 1999, The application of electron backscatter diffraction and orientation contrast

imaging in the SEM to textural problems in rocks: American Mineralogist, v. 84, no. 11-12, p. 1741-1759.

Prior, D. J., Mariani, E., and Wheeler, J., 2009, EBSD in the Earth Sciences: Applications, Common Practice, and Challenges, *in* Schwartz, A. J., Kumar, M., Adams, B. L., and Field, D. P., eds., Electron Backscatter Diffraction in Materials Science, Springer US, p. 345-360.

Raleigh, C. B., and Paterson, M. S., 1965, Experimental Deformation of Serpentinite and Its Tectonic Implications: Journal of Geophysical Research, v. 70, no. 16, p. 3965-&.

Rampone, E., Hofmann, A. W., Piccardo, G. B., Vannucci, R., Bottazzi, P., and Ottolini, L., 1995, Petrology, Mineral and Isotope Geochemistry of the External Liguride Peridotites (Northern Apennines, Italy): Journal of Petrology, v. 36, no. 1, p. 81-105.

Ranero, C. R., Morgan, J. P., McIntosh, K., and Reichert, C., 2003, Bending-related faulting and mantle serpentinization at the Middle America trench: Nature, v. 425, no. 6956, p. 367-373.

Ravna, E. J. K., Andersen, T. B., Jolivet, L., and De Capitani, C., 2010, Cold subduction and the formation of lawsonite eclogite - constraints from prograde evolution of eclogitized pillow lava from Corsica: Journal of Metamorphic Geology, v. 28, no. 4, p. 381-395.

Reed, S. J. B., 2005, Electron Microprobe Analysis and Scanning Electron Microscopy in Geology, Cambridge University Press.

Reimold, W. U., Gibson, R. L., and Henkel, H., 2008, Scientific comment on "Muundjua et al., 2007: Magnetic imaging of the Vredefort impact crater, South Africa, EPSL 261, 456-468" Discussion: Earth and Planetary Science Letters, v. 273, no. 3-4, p. 393-396.

Reynard, B., 2012, Serpentine in active subduction zones: Lithos.

Reynard, B., Nakajima, J., and Kawakatsu, H., 2010, Earthquakes and plastic deformation of anhydrous slab mantle in double Wadati-Benioff zones: Geophysical Research Letters, v. 37.

Rice, J. R., 2006, Heating and weakening of faults during earthquake slip: Journal of Geophysical Research-Solid Earth, v. 111, no. B5.

Rollet, N., Deverchere, J., Beslier, M. O., Guennoc, P., Rehault, J. P., Sosson, M., and Truffert, C., 2002, Back arc extension, tectonic inheritance, and volcanism in the Ligurian Sea, Western Mediterranean: Tectonics, v. 21, no. 3.

Rosbaud, P., and Schmid, E., 1925, On strain hardening of crystals in alloys and cold working: Zeitschrift Fur Physik, v. 32, p. 197-225.

Rossi, P., and Rouire, J., 1980, Corse - Carte Géologique de la France: BRGM - Service Géologique National, scale 1:250000.

Rupke, L. H., Morgan, J. P., Hort, M., and Connolly, J. A. D., 2004, Serpentine and the subduction zone water cycle: Earth and Planetary Science Letters, v. 223, no. 1-2, p. 17-34.

Rutter, E. H., and Brodie, K. H., 1988, The Role of Tectonic Grain-Size Reduction in the Rheological Stratification of the Lithosphere: Geologische Rundschau, v. 77, no. 1, p. 295-307.

Savage, J. C., 1969, Mechanics of Deep-Focus Faulting: Tectonophysics, v. 8, no. 2, p. 115-&.

Schmid, S. M., 1994, Textures of geological materials: computer model predictions versus emprical interpretations based on rock deformation experiments and field studies: Bunge H.J., Siegesmund, S., Skrotzki, W., Weber, K., (eds) Textures of geological materials. DGM Informationsges, Oberursel, p. 279-301.

Scholz, C. H., 2002, The Mechanics of Earthquakes and Faulting, Cambridge University Press, 471 p.:

Schwartz, A. J., Kumar, M., Adams, B. L., and Field, D. P., 2009, Electron Backscatter Diffraction in Materials Science, Springer, 406 p.:

Shand, S. J., 1916, The pseudotachylyte of parijs (Orange Free State), and its relation to "Trap-shotten gneiss" and "Flinty crush-rock": Geological Society of London Quarterly Journal, v. 72, p. 198-217.

Shelley, D., 1979, Plagioclase Preferred Orientation, Foreshore Group Metasediments, Bluff, New-Zealand: Tectonophysics, v. 58, no. 3-4, p. 279-290.

Sibson, R. H., 1975, Generation of Pseudotachylyte by Ancient Seismic Faulting: Geophysical Journal of the Royal Astronomical Society, v. 43, no. 3, p. 775-&.

-, 1980, Transient Discontinuities in Ductile Shear Zones: Journal of Structural Geology, v. 2, no. 1-2, p. 165-&.

Sibson, R. H., and Toy, V. G., 2006, The habitat of fault-generated pseudotachylyte: Presence vs. absence of friction-melt: Earthquakes: Radiated Energy and the Physics of Faulting, v. 170, p. 153-166.

Skemer, P., Katayama, B., Jiang, Z. T., and Karato, S., 2005, The misorientation index: Development of a new method for calculating the strength of lattice-preferred orientation: Tectonophysics, v. 411, no. 1-4, p. 157-167.

Smyth, J. R., Frost, D. J., Nestola, F., Holl, C. M., and Bromiley, G., 2006, Olivine hydration in the deep upper mantle: Effects of temperature and silica activity: Geophysical Research Letters, v. 33, no. 15.

Soustelle, V., Tommasi, A., Demouchy, S., and Ionov, D. A., 2010, Deformation and Fluid-Rock Interaction in the Supra-subduction Mantle: Microstructures and Water Contents in Peridotite Xenoliths from the Avacha Volcano, Kamchatka: Journal of Petrology, v. 51, no. 1-2, p. 363-394.

Spear, F. S., 1993, Metamorphic phase equilibria and pressure-temperature-time paths, Washington, D.C., Mineralogical Society of America, 799 p.:

Spray, J. G., 1987, Artificial Generation of Pseudotachylyte Using Friction Welding Apparatus - Simulation of Melting on a Fault Plane: Journal of Structural Geology, v. 9, no. 1, p. 49-60.

-, 1988, Generation and Crystallization of an Amphibolite Shear Melt - an Investigation Using Radial Friction Welding Apparatus: Contributions to Mineralogy and Petrology, v. 99, no. 4, p. 464-475.

-, 1992, A Physical Basis for the Frictional Melting of Some Rock-Forming Minerals: Tectonophysics, v. 204, no. 3-4, p. 205-221.

-, 1995, Pseudotachylyte Controversy - Fact or Friction: Geology, v. 23, no. 12, p. 1119-1122.

Stüwe, K., 2007, Geodynamics of the Lithosphere: An Introduction, Springer London, 493 p.:

Suzuki, A., and and collaborators, 2001, Viscosity of komatiite magma at high pressure: Bayerishes Geoinstitut Annual Report, http://www.bgi.uni-bayreuth.de/annual_report/navigat.php3?year=2001.

Swanson, M. T., 1992, Fault Structure, Wear Mechanisms and Rupture Processes in Pseudotachylyte Generation: Tectonophysics, v. 204, no. 3-4, p. 223-242.

Tao, X. D., and Eades, A., 2005, Errors, artifacts, and improvements in EBSD processing and mapping: Microscopy and Microanalysis, v. 11, no. 1, p. 79-87.

TexSEM, L., 2009, OIM Analysis 6.1 Manual, TexSEM Laboratories, p. 483.

Tichelaar, B. W., and Ruff, L. J., 1993, Depth of Seismic Coupling Along Subduction Zones: Journal of Geophysical Research-Solid Earth, v. 98, no. B2, p. 2017-2037.

Tommasi, A., Mainprice, D., Canova, G., and Chastel, Y., 2000, Viscoplastic self-consistent and equilibrium-based modeling of olivine lattice preferred orientations: Implications for the upper mantle seismic anisotropy: Journal of Geophysical Research-Solid Earth, v. 105, no. B4, p. 7893-7908.

Tullis, J., 1977, Preferred Orientation of Quartz Produced by Slip during Plane Strain: Tectonophysics, v. 39, no. 1-3, p. 87-102.

Turcotte, D. L., and Schubert, G., 2002, Geodynamics, Cambridge University Press.

Twiss, R. J., and Moores, E. M., 2007, Structural Geology, W.H. Freeman and Company, 736 p.:

Ueda, T., Obata, M., Di Toro, G., Kanagawa, K., and Ozawa, K., 2008, Mantle earthquakes frozen in mylonitized ultramafic pseudotachylytes of spinel-lherzolite facies: Geology, v. 36, no. 8, p. 607-610.

Venables, J. A., and Harland, C. J., 1973, Electron Backscattering Patterns - New Technique for Obtaining Crystallographic Information in Scanning Electron-Microscope: Philosophical Magazine, v. 27, no. 5, p. 1193-1200.

Verma, H. R., 2007, Atomic and Nuclear Analytical Methods: XRF, Mössbauer, XPS, NAA and B63Ion-Beam Spectroscopit Techniques, Berlin, Heidelberg: Springer-Verlag Berlin Heidelberg, p. 365.

Vernon, R. H., 2004, A Practical Guide to Rock Microstructure, Cambridge University Press, 594 p.:

Viganò, A., Tumiati, S., Recchia, S., Martin, S., Marelli, M., and Rigon, R., 2011, Carbonate Pseudotachylytes: Evidence for Seismic Faulting along Carbonate faults: Terra Nova, v. 23, p. 187-194.

Warren, J. M., and Hirth, G., 2006, Grain size sensitive deformation mechanisms in naturally deformed peridotites: Earth and Planetary Science Letters, v. 248, no. 1-2, p. 438-450.

Warren, J. M., Hirth, G., and Kelemen, P. B., 2008, Evolution of olivine lattice preferred orientation during simple shear in the mantle: Earth and Planetary Science Letters, v. 272, no. 3-4, p. 501-512.

Weertman, J., and Weertman, J. R., 1975, High-Temperature Creep of Rock and Mantle Viscosity: Annual Review of Earth and Planetary Sciences, v. 3, p. 293-315.

Wenk, H. R., and Bulakh, A., 2008, Minerals: Their Constitution and Origin, Cambridge University Press, 635 p.:

Wheeler, J., Prior, D. J., Jiang, Z., Spiess, R., and Trimby, P. W., 2001, The petrological significance of misorientations between grains: Contributions to Mineralogy and Petrology, v. 141, no. 1, p. 109-124.

Whitney, D. L., and Evans, B. W., 2010, Abbreviations for names of rock-forming minerals: American Mineralogist, v. 95, no. 1, p. 185-187.

Wilkinson, A. J., and Hirsch, P. B., 1997, Electron diffraction based techniques in scanning electron microscopy of bulk materials: Micron, v. 28, no. 4, p. 279-308.

Winter, J. D., 2010, Principles of Igneous and Metamorphic Petrology, Pearson Education, Inc., 702 p.:

Zhou, W., and Wang, Z. L., 2007, Scanning Microscopy for Nanotechnology Techniques and Applications, Springer, 522 p.:

http://neic.usgs.gov/neis/eq_depot/2011/eq_110311_c0001xgp/neic_c0001xgp_h.html

Appendix 1

Mineral abbreviations by (Whitney and Evans, 2010).

Minerals:

Ab – albite

An - anorthite

Atg – antigorite

Cal – calcite

Clc - clinochlore

Car – carphiolite

Chl – chlorite

Cpx - clinopyroxene

Czo – clinozoisite

Di – diopside

En – enstatite

Ep – epidote

Fa – fayalite

Fo – forsterite

Fs – ferrosillite

Grt – garnet

Gln – glaucophane

Hem – hematite

Lws – lawsonite

Mag – magnetite

Ol – olivine

Omp - omphacite

Opx – orthopyroxene

Pl – plagioclase

Prh - prehnite

Qz – quartz

Srp – serpentine

Spl – spinel

Tlc – talc

Wo - wollastonite

Zeo – zeolite

Zo - zoisite

Nonminerals:

PST - pseudotachylyte

Appendix 2

In the following sections are brief descriptions of the instrumentation and setup of the scanning electron microscope, and a review on electron-specimen interactions and detection relevant to the analytical work that has been done. The following summaries are based on Barron (2012); Cornelis and Dutrow (2008); Reed (2005); Schwartz et al. (2009); Verma (2007); Wenk and Bulakh (2008).

SEM instrumentation

Scanning electron microscopy is a method of imaging and nondestructive qualitative phase determination of micron-sized volumes at the surface of materials. In an SEM, high-energy electrons are bombarded onto the sample and act as the source for analysis which can be collected through an array of different detectors (EDS, SE, BSE and cathodoluminescence detectors) after interacting with the sample surface and interior. The instrument can roughly be divided into three parts; the electron gun, the optical column and a sample chamber which hosts the mounting stage and the multitude of detectors. Figure A.1 sums up the general assembly within an SEM. An important factor for all three segments is that they are to be kept in vacuum. Vacuums are needed to prevent electrical discharge in the gun assembly and to allow the electrons to travel within the instrument unimpeded.

The source of electrons in the SEM is emitted from a filament which is held at a negative potential and subsequently accelerated towards the sample. There are two classes of emission sources; thermionic emitters and field emitters. Thermionic emitters use an electrical current to heat up the filament, typically a tungsten (W) cathode or a lanthanum hexaboride (LaB_6) cathode, prompting electrons to be more readily detached from its surface by the aid of an electric field. In a field emission gun the filament is kept at a huge electrical potential gradient, so large that the work function of the material is overcome and electrons are drawn off of the filament. The stream of detached electrons is focused into a narrow band by the aid of electrostatic fields and accelerated by an anode positioned at the top of the optical column (figure A.1). This anode is associated with the accelerating voltage, which determines the velocity at which the electrons travel down the column and onto the sample.

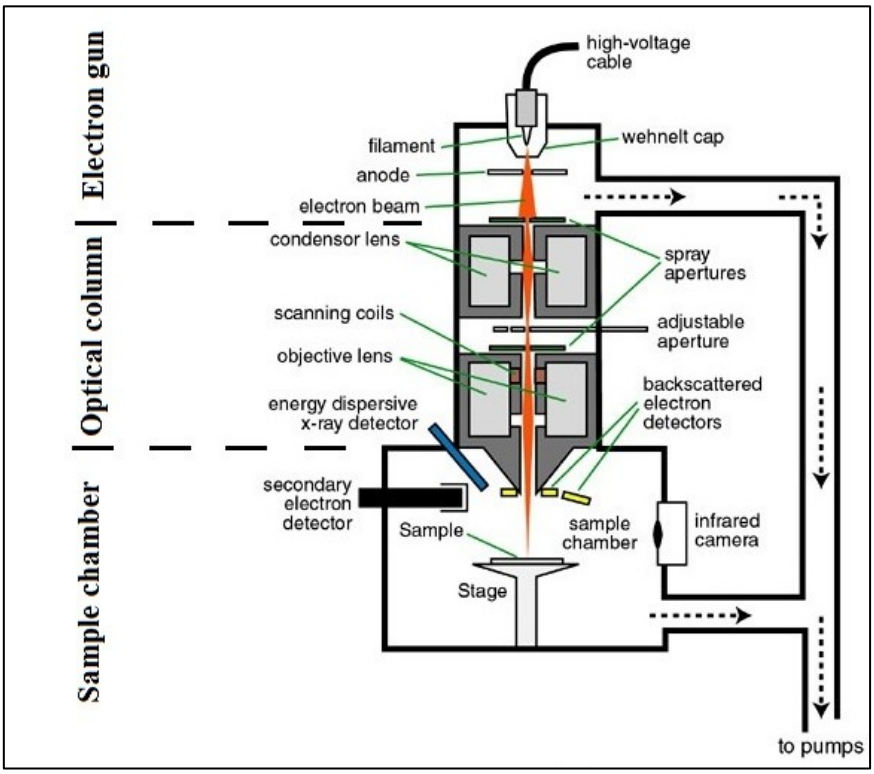

Figure A.1: Schematic overview of the assembly within a scanning electron microscope. Modified from Barron (2012).

The path of electrons is altered by an array of magnetic electron lenses (condenser lenses and objective lenses) positioned down the optical column (figure A.1). Interaction with these fields causes electrons to be deflected towards the axis, where the amount of deflection is controlled by the strength of the current in the condenser lenses. The diameter of the beam, referred to as the *spot size*, is limited by interchangeable apertures positioned at intervals from beneath the electron gun to just above the final condenser lens, which act as the final objective lens. The objective lens is the last component manipulating the electron beam. It is responsible for rastering the beam over the surface of the specimen and is synchronized with the scan of the viewing monitor, thus controlling the magnification. When electrons impinge upon the sample surface these experience a series of interactions with the atoms residing in it and, depending on their energies after ejection, are gathered by the array of appointed detectors.

Electron-specimen interactions and detection
Electron-specimen interactions are divided into two categories; elastic and inelastic scattering.

Inelastic scattering
Inelastic scattering events are those where electrons of the primary beam lose a detectable amount of energy ($E<E_{primary}$) through collision with a nucleus or electron of an atom in the specimen. On colliding, the primary electron undergoes a change in direction and transfer energy onto the specimen. This give rise to a series of possible ejecta in the form phonon excitation (heat production), plasmon production (secondary electrons), Brehmsstrahlung (continuous X-ray radiation), ejection of outer shell electrons (Auger electron production) and inner orbital electron ionization (characteristic X-ray production and cathodoluminescence).

Secondary electron (SE) imaging and phase determination by energy-dispersive X-ray spectroscopy (EDS) has been done during the course of this thesis and concern inelastic scattering. X-rays are produced when primary electrons generated in the electron gun collides and ejects electrons from atoms within the sample (figure A.2). This leaves vacancies in the orbitals which is swiftly (10^{-15}s) replaced by electrons from one of the outer orbitals, where the outer-shell electrons lose a specific amount of energy in order to occupy the closer shell of higher binding energy.

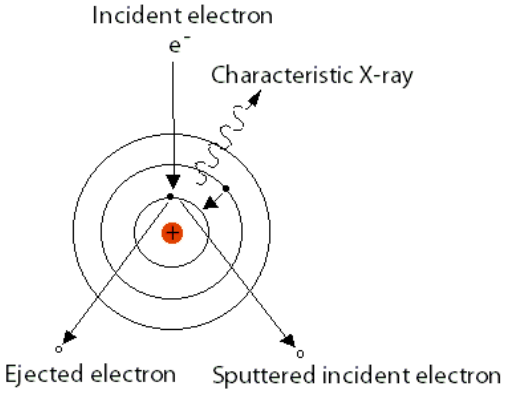

Figure A.2: Inelastic scattering of a primary electron by collision with an electron in an atom in the sample. The generation of characteristic X-rays occurs by replacing the void with an electron from one of the outer orbitals. Modified from Barron (2012).

Each electron transfer represents a loss in potential energy for the atom which is radiated as a *characteristic X-ray* with energy corresponding to equation A.E.1:

$$E_{photon} = E_{outer\ shell} - E_{inner\ shell} \qquad \text{Equation A.E.1.}$$

X-rays of different energies are divided by the amplitude of their pulse where the number of charges created in the EDS detector per incident photon with energy E_{photon} is given by equation A.E.2:

$$n = E_{photon}/\varepsilon \qquad \text{Equation A.E.2.}$$

where n is the number of charges produced, E is the energy of the incoming photon and ε is a constant at 3,8eV. The EDS detector records X-rays of all ionization energies created simultaneously, within the extent of the spot size, and produces an output in the form of a plot of intensity versus X-ray photon energy (figure A.3). Different elements have allowed and nonallowed transitions producing spikes characteristic of the element in which the allowed

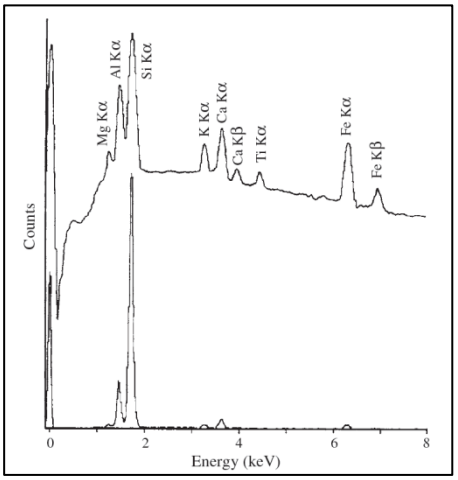

Figure A.3: Energy-dispersive X-ray spectrum of an alumina silicate consisting of a histogram of counts per channel. From Reed (2005).

transitions took place. Analysis of the X-ray emission spectrum produces qualitative results about the elemental composition of the specimen within the extent of the spot size.

Some of the electrons that are ejected out of their orbitals by collision of primary electrons, after undergoing additional scattering events while traveling through the specimen, may emerge from the surface of the sample. These ejected electrons are *secondary electrons* (SE) and are used for surface (topographic) imaging. The fraction of secondary electrons produced is relatively independent of the atomic number of the scattering atoms and is given through equation A.E.3:

$$\delta = n_{SE}/n_{beam}$$ Equation A.E.3.

where n is the number of electrons for both cases and δ is a constant depending on the element. Ejected SE has energies less than 50eV and need to be accelerated in order to produce output from a detector. A positive potential is applied to a thin metal coating in front of a photomultiplicator which enhances and records the ejected electrons.

Elastic scattering

Elastic scattering events are those where primary electrons comes close to the nuclei of atoms in the specimen and alters their path with minimal loss in electron velocity ($E \approx E_{primary}$) due to the large mass of the nuclei compared with that of the electrons (figure A.4).

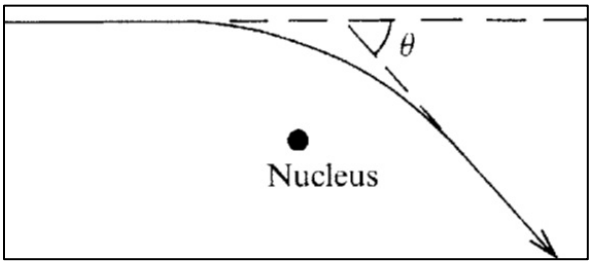

Figure A.E.4: Elastic scattering: an incident electron is deflected (without significant energy loss) by the attractive force experienced in passing close to a positively charged nucleus. From Reed (2005).

Backscattered electron imaging and electron backscatter diffraction has been done during the course of this thesis and concern elastic scattering. Fundamentally, elastic scattering changes the incident electron trajectory and is comprised by two components: coulombic interaction of the incident electron with a nucleus (Rutherford scattering) and interaction with internucleic electron cloud. The angular deflection γ as is given by equation A.E.4:

$$\tan\left(\frac{\gamma}{2}\right) = Z/(1.4pE)$$ Equation A.E.4.

where p is the minimum distance (in nm) between the undeflected electron path and the nucleus. Following this equation elastic scattering is greatest for heavy elements (high Z) and low electron energies, and electrons that pass close to the nucleus will be scattered through larger angles than those that pass more distantly. There is a finite probability of an incident electron being deflected through an angle greater than 90° and emerge from the surface of the target. This event may occur once or through multiple smaller deflections and may change the path of a primary electron up to 180°. The incident electron beam diameter is larger than the

atomic spacing, so by interaction with a population of nuclei in the specimen, incident primary electrons will be scattered within the sample with all possible trajectories. The scattered electron intensities will be a function of scatter angle, where low angle interactions conserve a tiny fraction more energy relative to high-angle interactions. If the primary electron leaves the sample surface, it is ejected as a *backscattered electron* (BSE).

The fraction of incident electrons which leave the specimen in this way is known as the backscatter coefficient (η) and is given through equation A.E.5:

$$\eta = n_{BSE}/n_{beam} \qquad \text{Equation A.E.5.}$$

where n is the number of electrons for both cases. The backscatter coefficient is strongly dependent on atomic number, because of the increasing probability of high-angle deflection with increasing Z (figure A.5). The relationship between η and Z takes the form shown on figure X for normal-incidence electrons.

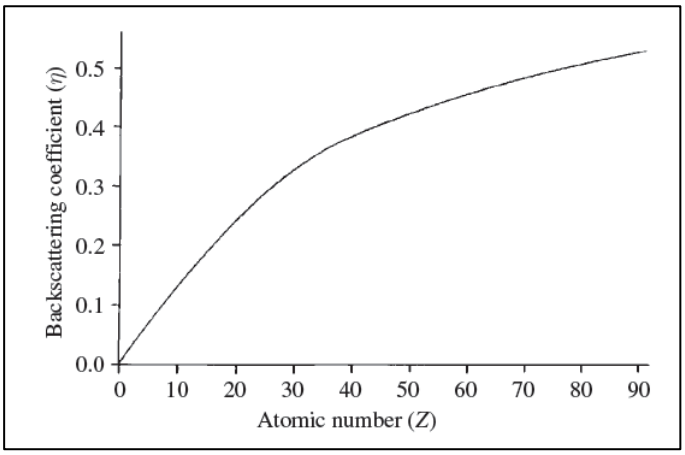

Figure A.5: Backscattering coefficient (η) versus atomic number. The backscatter coefficient is the fraction of incident electrons that leave the target and is almost independent of incident electron energy. From Reed (2005).

For backscatter electron imaging, concerning purely normal-incidence electrons, the amount of backscattered electrons emitted from a specimen area is recorded by a backscatter detector positioned adjacent to the bottom of the optical column (figure A.1). The amount of deflected electrons per area is detected and displayed in greyscale where dark annotation correspond to low atomic number and bright areas correspond to areas of high atomic number.

However, for EBSD, η is greater due to an oblique angle of incidence and does not record the same type of contrast in atomic number over the analysed area.

Activation volume

In order for the SEM to create an image the electrons that impinge upon the sample surface must interact with the sample in one of the aforementioned ways (and several others not mentioned in detail here) and escape from the sample and be detected. The *activation volume* is a function of the electrons ability to escape from the interior of the sample, dependant on their energies (figure A.6). Low energy electrons (secondary electrons, Auger electrons) derived from inelastic interactions can only eject from the uppermost few nanometres of the sample and gives information about the topography and morphology of the sample surface. High-energy electrons (backscattered electrons) derived from elastic interactions can eject from greater depths in the sample (<2µm) and give information of the chemical composition and its architecture. Continuous X-rays (Brehmsstrahlung) and characteristic X-rays have higher energies and are able to escape from greater depths in the sample.

The extent of the activation volume is dependent on incident electron energy where penetration depth generally increases with increasing accelerating voltages.

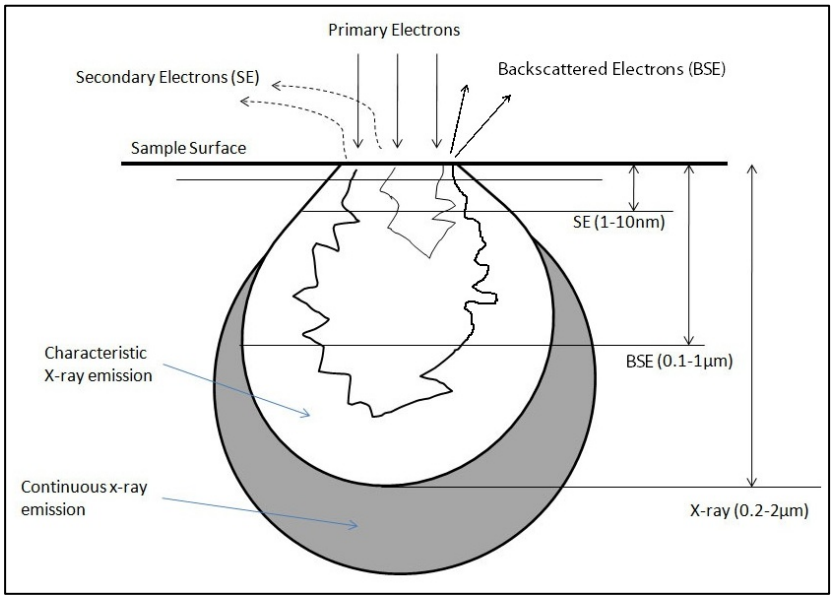

Figure A.6: Interaction volume for electrons and X-rays in crystalline samples. The energy of ejected electrons and X-rays is a function of their penetration depth. Modified from (Barron, 2012).

Appendix 3

COR-06-03D

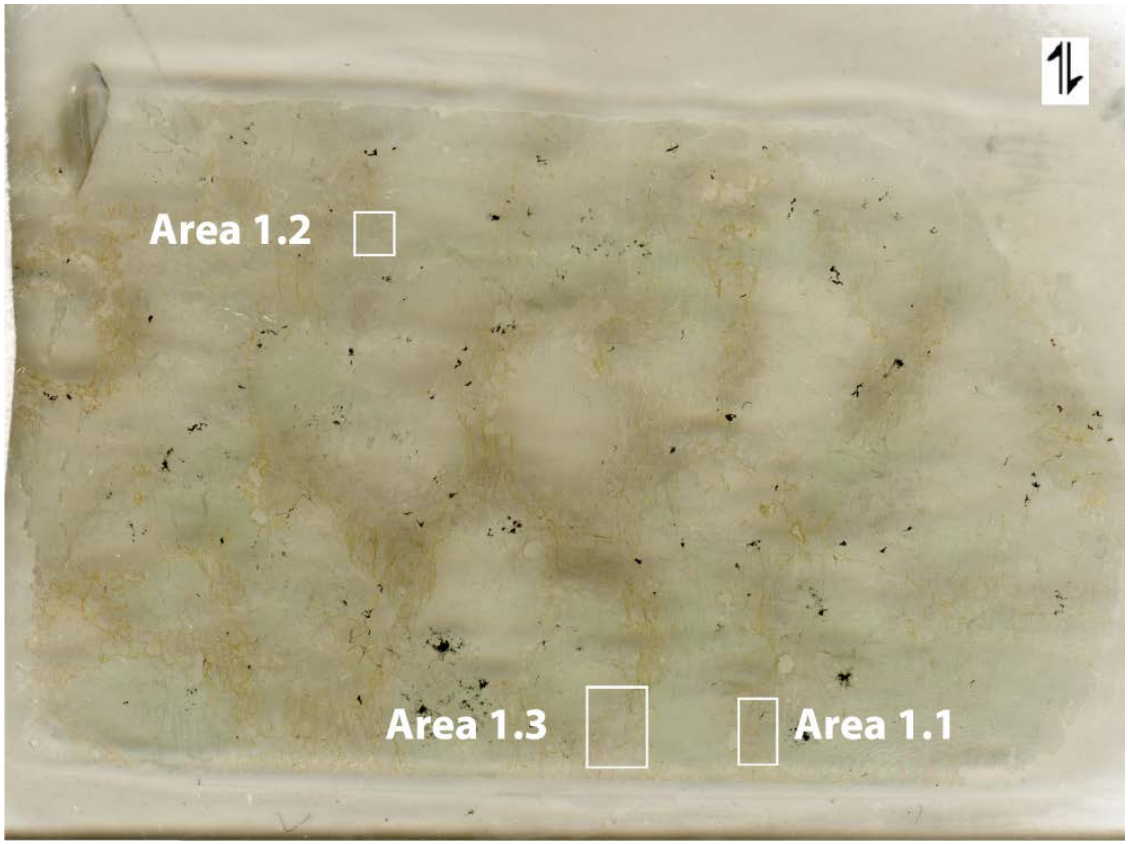

Spl-melagabbro. Protogranular with some grain boundary migration. A vague compositional banding can be observed (roughly N-S on image). Opx grain sizes ≤8 mm. Ol, cpx and pl are distributed in intervening bands that are fractured and associated with discolouration. Areas for EBSD analyses are boxed and the reference direction is marked with shear direction (arrows).

COR-04-06

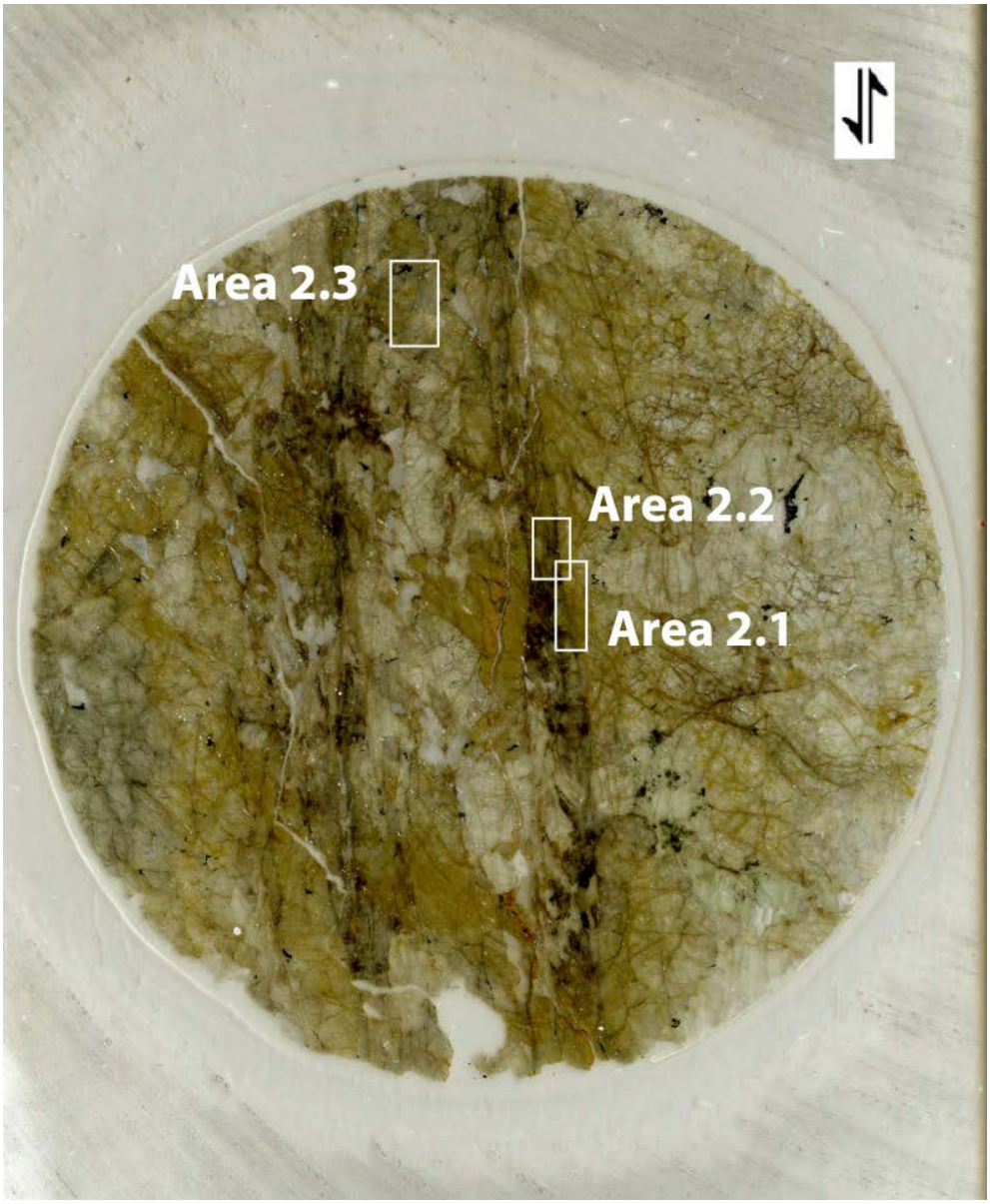

Area 2.1	Page 95
Area 2.2	Page 99
Area 2.3	Page 101

Two subparallel fault zones transect- and truncate grains in unclassified peridotite with protogranular textures and some grain boundary migration. Apparent offset is 0.8cm and minimum estimated strain-averaged stresses are 40MPa (Andersen et al., 2008). A vague compositional banding can be observed (E-W on image). Areas for EBSD analyses are boxed and the reference direction is marked with shear direction (arrows).

COR-05-06C

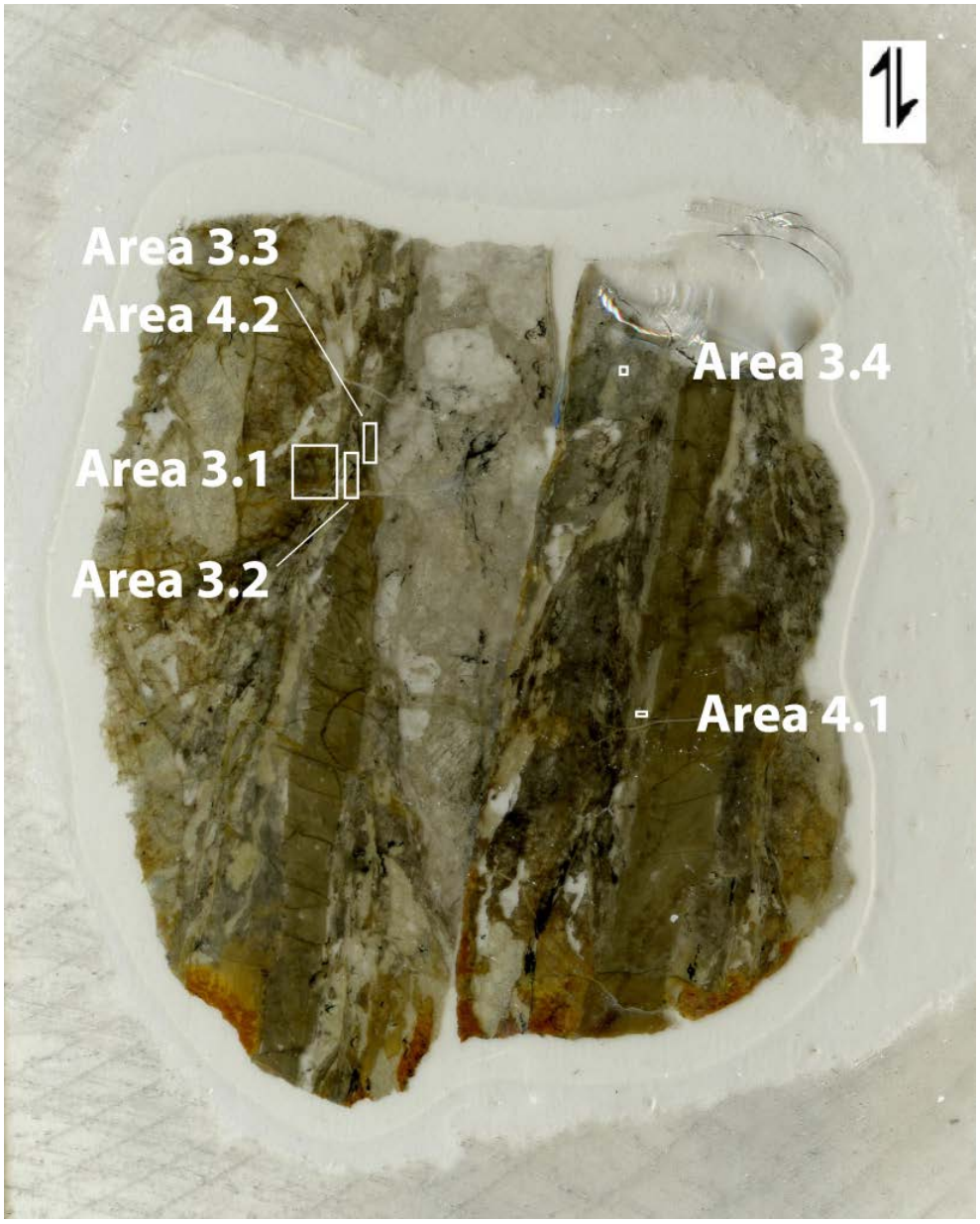

Two subparallel fault-veins (<4 mm wide) and associated damage zones transect unclassified peridotite. Relict protogranular texture can be observed in the most distal (E-W) areas of the sample. Compositional banding is not recognizable. Apparent offset is 18.3 cm and minimum estimated strain-averaged stresses are 135MPa (Andersen et al., 2008). Areas for EBSD analyses are boxed and the reference direction is marked with shear direction (arrows).

Appendix 4

List of figures

List of tables